A Novel Diagnostic Technique for The Quantification of Lithium-ion Battery Degradation Modes Under In-operando Conditions

Imperial College London – Department of Mechanical Engineering

Ryan Prosser
PhD Thesis

Supervisor: Dr. Yatish Patel

Co-supervisor: Prof. Gregory J Offer

Statement of Originality

The work in this thesis is entirely my own except where explicitly referenced or acknowledged.

Ryan Prosser

Copyright Declaration

Abstract

Reliable and frequent diagnostics of lithium-ion batteries is critical to extending battery life and by extension reducing the total cost of ownership of electric vehicles. State-of-the-art quantitative diagnostic techniques almost all require open circuit voltage versus state of charge profiles for them to be used; unfortunately, these measurements are rarely available in normal device operation. Therefore, this thesis contains the theory and experimental validation of a novel diagnostic technique which is usable in conditions seen under normal device operation. The technique uses cell heat generation rate versus time as its diagnostic signal and can predict electrode capacities and the lithium inventory of the cell.

From experimental validation of the diagnostic technique, its predicted outputs are compared to a state-of-the-art open circuit voltage model-based technique. Thorough analysis of the identifiability of the parameters shows that the novel diagnostic technique is capable of robustly predicting the positive electrode capacity to a similar accuracy as the state-of-the-art technique for high-powered and high energy cells if a reduced order diffusion model is included in the technique.

Not only has a diagnostic technique capable of quantifying positive electrode capacity been developed, but a framework for evaluation of any diagnostic technique's efficacy has also been developed. This work is missing from the diagnostic literature and can hopefully be used by the academic community to help build better diagnostic techniques which will in turn help extend battery lifetime and reduce the total cost of ownership of electric vehicles.

Acknowledgements

I would like to begin these acknowledgements by thanking both my supervisors Dr Yatish Patel and Prof. Greg Offer whose guidance and mentorship helped me greatly throughout both my undergraduate degree and PhD. From the beginnings of working with both during my final year as a mechanical engineering student on my final year project through to the end of my PhD. I'd like to thank both not only for the academic mentorship but also for creating a camaraderie within the Electrochemical Science and Engineering research group.

I've made a long list of great friends throughout my PhD who've helped the oftentimes stressful life of a PhD student more bearable with their social company. I'd like to give thanks in particular to Alastair, Joe, Idris, Gavin, Max and Oisin for providing me with great memories (and plenty of nights where the memories are blurry). I hope that we'll stay in touch for many years to come.

I'd also like to give special thanks to Dr Ian Campbell and Dr Yan Zhao for inviting me to join them at their company Breathe Battery Technologies after working closely with both throughout the duration of my PhD. Their mentorship through PhD and continued mentorship in my professional career has and is an invaluable gift that I am incredibly grateful for.

Finally, and most of all, I would like to thank Joanne and Hugh; or mam and dad as I call them. You've been on the emotional rollercoaster that is a PhD with me from day one and I can't ever thank you enough for your support. I love you both.

Project Outputs

Journal Articles (3) First Author (1)

“Lithium-Ion Diagnostics: The First Quantitative In-Operando Technique for Diagnosing Lithium Ion Battery Degradation Modes under Load with Realistic Thermal Boundary Conditions”

Ryan Prosser, Gregory J. Offer, Yatish Patel

Journal of The Electrochemical Society, vol. 168, no. 3, p. 030532, Mar. 2021.

“Lithium ion battery degradation: what you need to know”

Jacqueline S. Edge, Simon O’Kane, Ryan Prosser, Niall D. Kirkaldy, Anisha N. Patel, Alastair Hales, Abir Ghosh, Weilong Ai, Jingyi Chen, Jiang Yang, Shen Li, Mei-Chin Pang, Laura Bravo Diaz, Anna Tomaszewska, M. Waseem Marzook, Karthik N. Radhakrishnan, Huizhi Wang, Yatish Patel, Billy Wu and Gregory J. Offer

Phys. Chem. Chem. Phys., vol. 23, no. 14, pp. 8200–8221, 2021.

“The Cell Cooling Coefficient as a design tool to optimise thermal management of lithium-ion cells in battery packs”

Alastair Hales, Ryan Prosser, Laura Bravo Diaz, Gavin White, Yatish Patel, Gregory J. Offer

Journal of e-Transportation, vol. 6, 2020.

Table of Contents

List of commonly used symbols

Below is a list of commonly used symbols and their meaning. All symbols are introduced in the text where they first appear. Note that the below is not an exhaustive list of symbols but includes those which are used at multiple places throughout the thesis.

Symbol	Description
C_i	Capacity of entity i (Amp-hours)
G	Gibbs free energy (Joules)
H	Enthalpy (Joules)
I	Cell current (Amps)
mCp	Heat capacity (Joules / Kelvin)
Q	Charge (Amp-hours)
q	Heat rate (Watts)
R	Thermal Resistance (Watts / Kelvin) OR Particle radius (Metres)
r	Particle radial coordinate (metres)
S	Entropy (Joules)
T	Temperature (Kelvin)
t	Time (seconds)
U	Open circuit voltage (Volts)
V	Cell terminal voltage (Volts)
x	Lithiation fraction (dimesionless)

List of common Abbreviations

Abbreviations	Definition
BOL	Beginning of life
CC	Constant current
CCC	Cell cooling coefficient
CN	Crank Nicholson
CV	Constant voltage
FIM	Fisher information matrix
ICA	Incremental capacity analysis
LAM	Loss of active material
LLI	Loss of lithium inventory
NE	Negative electrode
OCV	Open circuit voltage
PE	Positive electrode
SOC	State of charge
SPM	Single particle model

List of Figures

List of Tables

1. Introduction

1.1 The rise and rise of lithium-ion batteries

In recent history, development in portable electronics has led to a great rise in use and consumption of lithium-ion batteries (LIBs) in a wide range of applications. The applications for LIBs range from portable electronics, such as mobile phones and laptops, through to being used in storing surplus energy produced by renewable sources. Suffice to say LIBs have become central to the average person's life in the developed world and societies reliance on them has seen the global demand for LIBs rapidly rise. Figure 1 shows the total gigawatt-hour (GWh) demand for LIBs by sector, which is expected to exponentially increase in the next 10 years. This growth is expected to come primarily from the electric vehicle (EV) market and to a lesser extent, the stationary storage market. Until recently, consumer electronics has dominated demand for LIBs with EVs only recently catching up. From this, it would not be unreasonable to speculate that due to the global uptake in EVs, LIBs will become one of the most widely used pieces of technology in history.

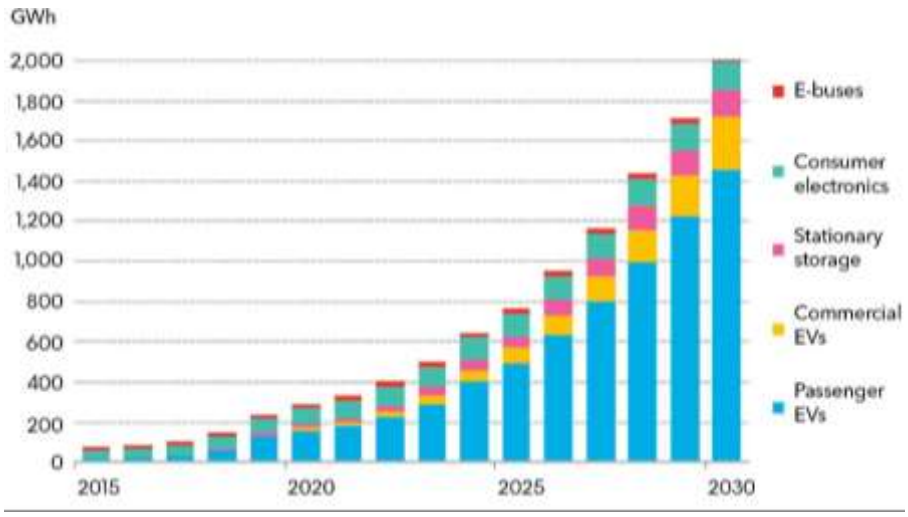

Figure 1: Historic and predicted GWh demand by use for LIBs show that demand is set to grow exponentially over the next decade due to increased uptake of EVs. Reproduced with permission from [1].

Why would one choose an LIB over a different battery chemistry? Figure 2 shows a Ragone plot for various battery chemistries. The plot gives the range of specific power and energy that different battery chemistries are reported to have. It is seen that for a given specific power, the specific energy of an LIB is superior to other battery technologies. Put simply, for a given power requirement of an application, LIBs can store more energy per kilogram than other battery types. It is also seen that LIBs have a wide range of specific energy and power. This means there are very high-powered LIBs which are useful for short bursts of high power, and very high-energy LIBs which can store large amounts of energy for low power applications. This wide range of energy and power options combined with the better specific energy than other technology has seen the LIB emerge as the frontrunner for the choice in powering modern electrical systems.

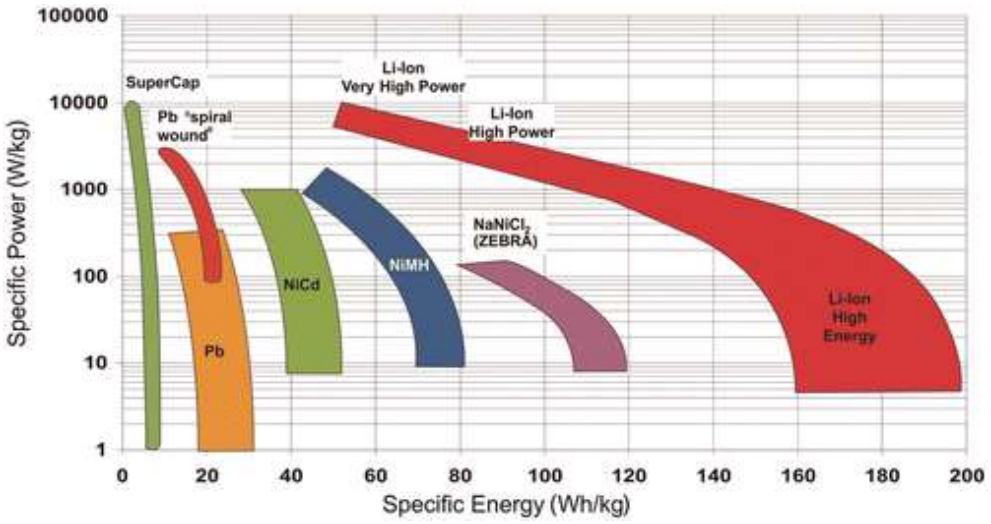

Figure 2: Ragone plot of various battery technologies showing superior performance of LIBs over other battery technologies for a wide range of power and energy demands reproduced with permission from [2].

While consumer electronics and stationary storage will certainly impact demand for LIBs, the main driver in projected demand is the EV market whose competition is the internal

combustion engine vehicle (ICEV) market. According to the International Energy Agency (IEA), the EV market, which includes battery EVs (BEVs) and plug-in hybrid EVs (PHEVs), accounted for 2.6% of global car sales in 2019 [3], still a fraction of the ICEV market. However, this is set to rapidly change over the next two decades, Bloomberg New Energy Finance's electric vehicle outlook suggest that a staggering 54 million EVs will be sold each year by 2040, 58% of global passenger vehicle sales [4]. Figure 3 is taken from an insight article produced by Deloitte where it can be seen that the number of ICEVs sold will begin to decrease from around 2025 while the total number of EVs sold is expected to continue to grow exponentially [5]. The report from Deloitte shows that EVs will account for an astonishing 1 in 3 passenger and light duty vehicles sold by as early as 2030.

Figure 3: Projected data shows EVs will account for 1 in 3 passenger and light duty vehicle sold globally by 2030 reproduced with permission from [5].

The rapid increase in EV sales can be attributed to a reduction in the price to produce battery packs as well as regional and local policy on reducing carbon emissions from ICEVs. The price of producing a battery pack has historically meant that EV "sticker" price, the price consumers pay, was much higher than that of similar ICEVs. The historical average price of

battery packs is shown in Figure 4 which is taken from an article produced by Bloomberg. In 2010 the average price of a LIB pack was above $1,100 per kilowatt-hour (kWh) and from Figure 4 it is seen that this number has fallen by a staggering 89% in the last decade [6]. This cost is set to reach a milestone number of $100/kWh by 2023 [4], which is the price which automakers should be able to produce EVs at the same price as similar ICEVs with no government subsidies [6]. At this milestone EV battery pack cost, there would be no economic reason to produce or own an ICEV over an EV when considering the initial price.

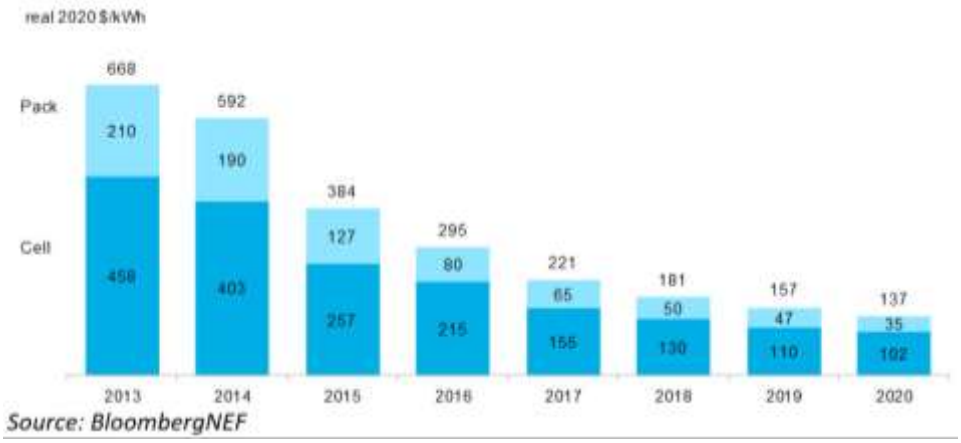

Figure 4: EV battery pack prices ($/kWh) have fallen at an average compound rate of 19% a year over the last decade due to increasing order sizes and reduction in production costs. Reproduced from [6] *with permission requested.*

Due to economies of scale and higher factory utilisation, countries which sell more EVs and produce more batteries are typically able to produce cheaper battery packs. Figure 5 shows passenger EV sales by country, provided in a blog post by S&P Global Market Intelligence [7]. It shows that China was the largest producer of passenger EVs until 2019 largely due to a government policy induced demand for passenger electric vehicles and subsequent investment in battery manufacturing capability [7]. However, Europe has surpassed China as the largest seller of EVs due to ambitious emissions targets set by regulatory bodies and complete bans on sales of ICEVs by 2030 or soon thereafter for some countries [8]. These

policy shifts force European car makers to shift to electric platforms for their vehicles, meaning that they are beginning to benefit from economies of scale in their production of EVs and hence can offer a lower price to consumers. The constant reduction in cost for end user will be the main driver in the uptake of EVs and in realising the projected demands for LIBs over the next decade.

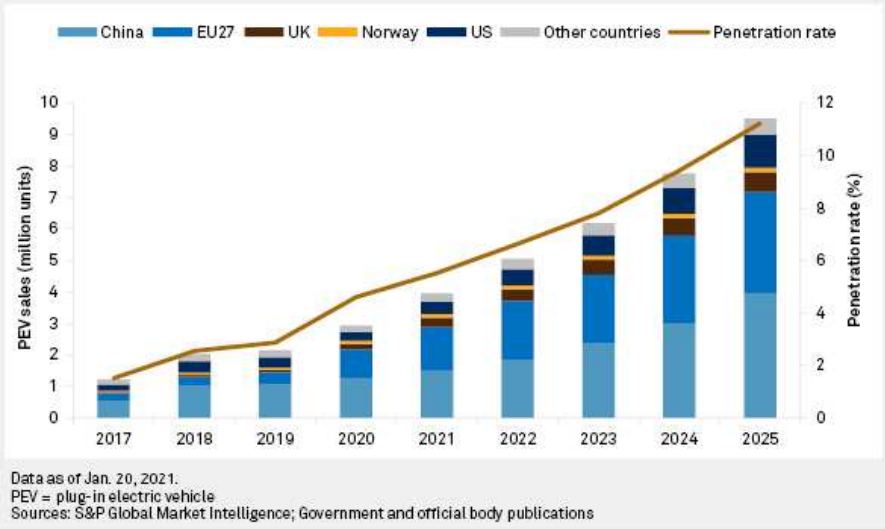

Figure 5: China is currently the world's largest market for EVs, but Europe is expected to overtake in near future. Reproduced with permission from [7].

1.2 Thesis aims

It has been shown that a key factor in the rising demand of LIBs is the decreasing cost of producing EV battery packs. The average cost of production is rapidly approaching the $100/kWh milestone which is the cost which would make the price of EVs comparable to ICEVs in their initial purchase [9]. Economies of scale in manufacturing and improvements in pack design are the main drivers of this “sticker” price reduction. However, am arguably more important metric is the total cost of ownership, defined as the total yearly cost of owning an EV from beginning to end of the vehicle’s life. Decreasing the total cost of ownership can be achieved by either decreasing the initial price of the vehicle, or by extending the lifetime of the battery pack. Extending pack lifetime is difficult as it generally requires advancements in fundamental understanding of LIBs, complex mathematical modelling and long-term testing which all take significant amounts of time and effort. Despite this, as the rate of decrease in battery pack price per kWh slows, it will be necessary to extend battery life to continue to decrease the total cost of ownership of EVs.

Extending battery lifetime can be achieved in several ways; advancing in battery materials, over-engineering the battery pack, by adding more cells or additional cooling power, or by controlling the battery’s boundaries of operation to adapt to changes in the battery’s internal states. For example being able to manage charging current to prevent lithium plating is reliant on having accurate information about a batteries state-of-health. The former two options would likely add cost to production of the battery pack which doesn’t align with the goal of reducing total cost of ownership. Adaptively controlling the boundaries of operation of the battery on the other hand adds very little cost to the battery pack. Extending battery life through adaptive control has three facets, understanding what

the internal state of the battery is, understanding how the state will change over time and understanding how the evolution of the state changes for different operating conditions. The terms given to these fields of research are diagnostics, prognostics and optimal control respectively. Ultimately it is optimal control which extends battery life; however, it is impossible to effectively perform optimal control with poor levels of diagnostic or prognostic information.

This thesis focusses on the diagnostic part of this problem and aims to develop a novel diagnostic technique which can be used in almost any load cycle and thermal condition. This is complementary to other diagnostic techniques which are typically performed under equilibrium conditions – more on this in a later chapter. It is accepted by the author of this thesis that diagnostics by itself is insufficient to extend the lifetime of LIBs. However, it is the bedrock from which all prognostics and optimal control strategies are built upon. Therefore, all effort in this thesis will go toward developing a diagnostic technique which:

- Must give results which are able to quantify some internal, otherwise unobservable state of a battery which changes throughout its lifetime as a result of degradation.
- Must be able to be performed under conditions seen in normal battery operation.
- Must be robust to operating conditions such as temperature, load and working environment.
- Must be applicable to any battery chemistry and form factor.
- Must use only readily available measurements of the cell; voltage, current and temperature and data parameterisable from the battery system at beginning of life.

1.3 Knowledge Gap and Research Questions

Many diagnostic techniques exist for LIBs, however quantifying degradation modes under conditions seen in reality without the use of significant amounts of degradation data is a gap in the science. There is a research question associated with each criterion set out in the previous section which the work in this thesis aims to address simultaneously. From these criteria, a singular catch-all research question is formulated:

"Is it possible to quantify battery degradation mode amounts under general operating conditions using only voltage, current and temperature measurements?"

Breaking this down slightly further – "quantify battery degradation", the technique should provide numbers and not qualitative analysis. "general operating conditions", the technique should not be restricted to open circuit conditions and should work throughout the lifetime of the cell without updating some other model. "voltage, current & temperature measurements", these are the quantities that are measured by typical BMS systems.

The sub research questions for this master research question are formulated throughout the body of this thesis rather than at this point so as not to detract from the overarching goal of the work produced during this PhD.

1.4 Thesis Structure

With the given criteria for the perfect diagnostic technique set out above, the structure of this thesis given below.

Chapter 1: Introduction

This section outlines the motivation for the work and the scope of work. A review of the trends of the LIB market is given as well as the current problems facing the sector in general. From this, the scope of the work is outlined and the research question underpinning the work is formulated

Chapter 2: Literature Review

The literature review is split into three main parts; a general review of battery operating principles, followed by battery degradation and finally an in-depth review on state-of-the-art diagnostic techniques is performed.

Chapter 3: Theory for the novel diagnostic technique

In depth theory on how the new diagnostic technique operates. This includes the fundamental operating principles which make this technique possible as well an in-depth review of the optimisation routine that is implemented in this technique.

Chapter 4: Implementation of the diagnostic technique – experimental evaluation

This chapter contains the first implementation of the diagnostic technique. It first outlines the experimental measurements that are taken, thermal models based on the experimental set up and what validation experiments are performed. Following this, an in-depth analysis on the performance of the technique and the benchmark technique is performed.

Chapter 5: Improvement of technique – application to high energy and degraded cells

This chapter contains theory the theory which is required to improve the diagnostic techniques efficacy when diffusion effects are significant in a cell. Once the theory is established, a set of experimental tests are performed to evaluate the performance of the

changes and then the results are analysed and the final form of the diagnostic technique is presented.

The work presented in this thesis is novel and is not adapted from any other works, all work was carried out by myself with input and guidance from my supervisors. Chapters 2, 3 & 4 contain work that is published in academic journals of which I an author of. I would like to acknowledge that the respective journals hold the copyright to these publications and I, as an author have the rights to insert and/ or reproduce the said publications for my personal use in the form of a thesis which is to be published strictly for non-commercial use. Entries in these chapters may be, in full or in part, included verbatim from said publications.

2 Literature Review

This chapter contains the already established research concerned with this thesis. Firstly, the background and working principles of a lithium-ion battery are given. Secondly an introduction to degradation of lithium-ion batteries is given, covering only the most prevalent degradation mechanisms seen in normal lithium-ion operation as well as degradation modes. In the final section of the literature review, current state-of-the-art work is reviewed which is in the field of quantitative diagnostics of lithium-ion cell degradation. The quantitative diagnostics field is vast with a very large number of academic works published every year. Therefore, only the works which are immediately relevant to this thesis are reviewed in detail.

2.1 Basic Operating Principles

2.1.1 Components and their function

A lithium-ion battery is a collection of galvanic cells which contain a positive and negative electrode. Both electrodes undergo reversible half-cell reactions with lithium ions in the form given in Eq. (1) where X is the electrode material. During discharge, the negative electrode is oxidised and releases an electron and a positive lithium ion, while the positive electrode is reduced and gains an electron and a lithium molecule. This electron is then passed from the negative electrode, around an external circuit to do electrical work and then is reabsorbed into the positive electrode. Conversely, during charge the electrodes switch roles and electrons enter the negative electrode and leave the positive electrode. When a lithium ion reacts with the electrode – reduction - intercalation occurs. The process

of intercalation means that the lithium atom diffuses through the lattice of the electrode material, from its surface to its centre. The reverse process of deintercalation occurs during the oxidation reaction. A schematic showing the transport of lithium ions and electrons is given in Figure 6.

$$X(s) + Li^+ + e^- \rightleftharpoons LiX(s) \quad (1)$$

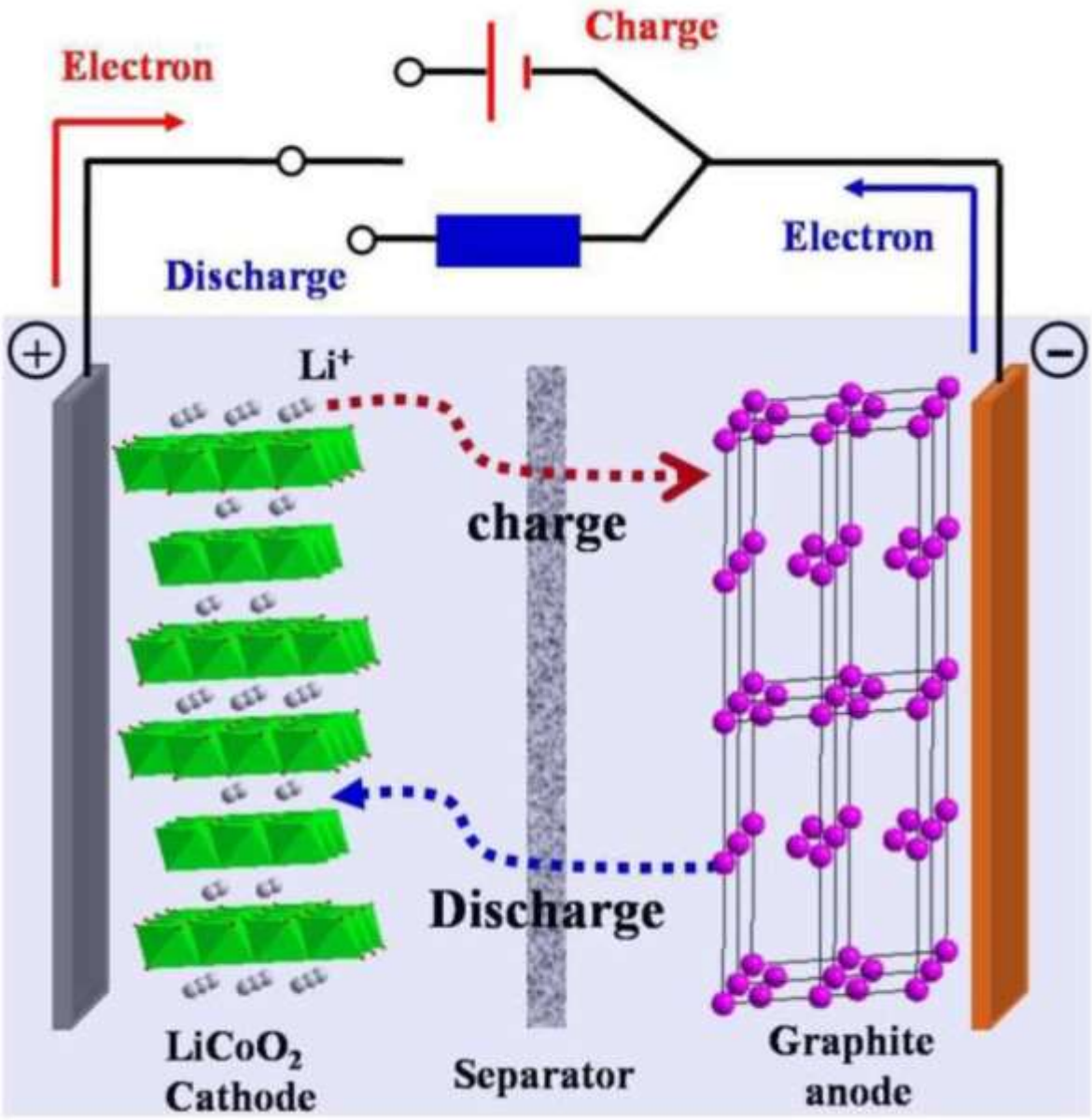

Figure 6: Schematic showing the transport of lithium ions and electrons for charging and discharging in a lithium ion battery. Reproduced with permission from [10].

Electrode particles are not electrically conductive and as such a conductive path is needed to facilitate the electron transport from the active particle to the external circuit. The electrode particles held together with a medium known as a binder. The binder contains conductive additives which provides a path from the electrode particle to another component of a battery, the current collector. A current collector is a thin sheet of metal, usually copper for the negative electrode and aluminium for positive electrode [11], which then is welded to the terminal of a battery to complete the electronic circuit from terminal to electrode particle.

Similarly, ions of lithium cannot be transported without an ionically conductive material. The medium that conducts ions in a galvanic cell is an electrolyte. Electrolytes have the property of being ionically conductive but electrically insulating meaning the electrons cannot flow through them. Electrolytes contain a salt and a solvent. The most common salt in lithium ion cells is reported to be lithium hexafluorophosphate, $LiPF_6$, and the most common solvent is ethylene carbonate, EC [12]. Electrolytes used in lithium ion batteries are usually organic solvents which are known to be toxic to humans and flammable. Thus, there is a safety risk posed by the use of these compounds as electrolytes [13]. To reduce the safety risk posed by these electrolytes, much attention has been given to solid state batteries which replace the liquid electrolyte with a polymer based one to mitigate these dangers [14] but this technology is not widely adopted in applications yet.

If the electrodes with binder and electrolyte are allowed to touch each other, a short circuit reaction would occur where the electrons would conduct from the negative electrode to the positive electrode and the lithium atoms would flow in the opposite direction. This would

mean that no electrons are transferred through the external circuit to do electrical work. To stop this, a separator is placed between the electrodes which is permeable to the lithium ions but is electronically insulating. As well as electrically insulating, good mechanical strength is also a requirement to avoid tearing and puncturing if a battery is subject to physical damage [14]. A schematic of a lithium ion battery with the inclusion of the separator is given in Figure 7 [15].

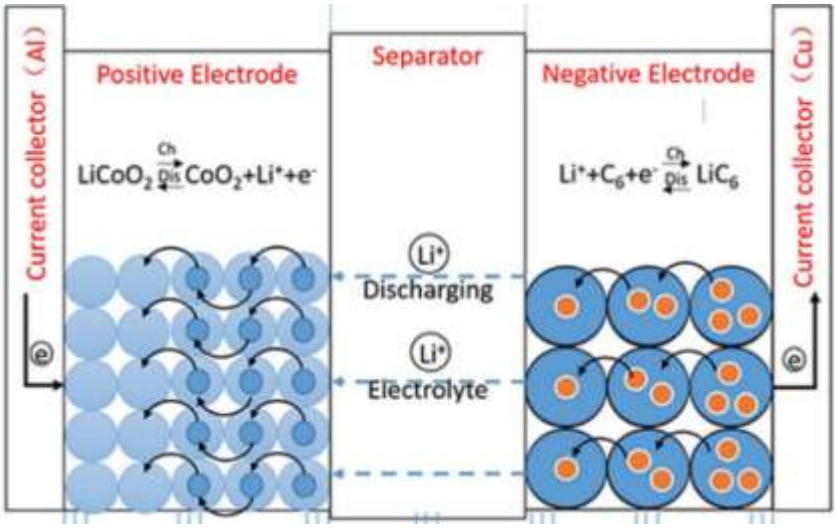

Figure 7: Schematic of a lithium ion battery showing how the separator allows lithium ion movement but keeps the electrodes apart to stop short circuit. Reproduced with permission from [15].

2.1.2 Thermodynamics and cell properties

The most common property that comes to mind with a battery is the voltage. The voltage of a battery is defined as the change in Gibbs free energy that occurs when one Coulomb of the species – lithium in this case - reacts, this is given in Eq. (2). Here ΔG is the change in Gibbs free energy of the system per mole of reacting species, n is the number of electrons per molecule of the reacting species – 1 in the case of lithium - and F is Faradays number which has units of Coulombs per mole. A positive voltage means that an electric current will

flow from positive to negative terminal if the two terminals of the cell are connected. This implies the discharge reaction is spontaneous – no external work needs to be done to make the reaction occur. This then explains the presence of the negative sign in Eq. (2) as for a reaction to be spontaneous, the change in Gibbs free energy must be negative. The relation given in Eq. (2) is the cell voltage under equilibrium conditions, i.e. when no current is flowing. This is known as the open circuit voltage (OCV) of the cell.

$$E_{cell} = -\frac{\Delta G}{nF} \tag{2}$$

The change in Gibbs free energy of a reaction is the chemical potential of the product species subtracted from the chemical potential of the reactants. The chemical potential is a quantity related to the material and species under reaction. This implies that different combinations of materials have different electrochemical cell voltages. Often for lithium-ion batteries, different materials are compared verses a Li/Li^+ reference electrode. This leads to a table of OCVs for common electrode materials and is given in Table 1 which is adapted from [16] and shows the average cell OCVs for common electrode materials versus lithium metal. The top 4 rows correspond to common negative electrode materials, and the bottom 4 rows correspond to common positive electrode materials. From an energy density point of view, the higher the cell voltage the better and so why do we not only see cells with a lithium cobalt oxide (LCO) positive electrode and a lithium metal negative electrode? The answer is that energy density is not the only factor and things like cycle life, thermal stability and cost all play a part in the selection of material pairings for a cell. There are many review papers which discuss in detail the merits and drawbacks of different electrode materials and this short section is not meant to be an in depth discussion on different battery materials. If

the reader would like more information on properties of different electrode materials then Nitta et al. [16] provide a good overview of the characteristics of different battery materials as well as their strengths and weaknesses. Information on specific battery materials can be found in [17]–[20].

Table 1: Voltages versus lithium for common lithium-ion cell electrodes. Adapted from [16].

Electrode material	**Average Voltage vs Li/Li^+ (V)**
Li metal	0
Graphite	0.14
Lithium titanate (LTO)	1.58
Silicon	0.4
Nickel cobalt aluminium (NCA)	3.7
Nickel manganese cobalt (NMC)	3.7
Lithium cobalt oxide (LCO)	3.8
Lithium iron phosphate (LFP)	3.4

The term average voltage is used in Table 3 to refer to the OCV of the electrode material. Average implies that the OCV of the electrode is not always at the value given in Table 3 which is indeed the case. The electrode's chemical potential and hence its OCV are dependent on the chemical composition and crystal structure of the electrode. As lithium intercalates into the electrode its chemical composition and crystal structure change which causes the electrode and hence the cell voltage to change. As more lithium intercalates with an electrode, the lower its potential versus lithium gets. On discharge, the negative electrode is delithiated and the positive electrode is lithiated resulting in the cell OCV decreasing and vice versa on charge.

The increasing and decreasing of OCV with charging / discharging leads to the concept of cell capacity which is the total electric charge transferred by the cell from its lowest allowable voltage to its highest. The cell state-of-charge (SoC) is the fraction of charge that the cell has stored at any time out of its total amount of charge it can store at its upper voltage limit compared to its lower voltage limit. The OCV of the cell can be found at each SoC point and gives rise to the most popular thermodynamic property of a lithium-ion cell, the OCV profile. The OCV profile is usually plotted with SoC on the x-axis and OCV on the y-axis. There are other thermodynamic quantities which form their respective profiles which will be examined in due course throughout this thesis.

2.1.3 Considerations under load

So far, properties of the cell have been discussed when the cell is under equilibrium conditions – when there is no current applied. When a cell is under load, its voltage behaviour changes due to cell kinetics and dynamics. These changes can be thought of as inefficiencies in the cell and lead to less energy being delivered than the theoretical amount of energy stored in the battery during discharging. Similarly on charge, the amount of energy stored is less than the energy supplied due to these inefficiencies. These inefficiencies are often thought of as cell internal resistances and come from various sources.

The first source of resistance is the Ohmic resistance of the cell. Electronic Ohmic resistance is caused by the electron transport through the current collectors and tab welds as well as the effective resistance of the binder material in the solid phase that conducts electrons from reaction site – at the particle of the electrode – to the current collector in the anode

and vice versa in the cathode. There is also ionic Ohmic resistance from the conductance of the electrolyte which causes a voltage drop by moving a current of ions through the electrolyte.

The second source of resistance is due to the reaction kinetics at the interface between electrolyte and electrode particle. The Butler-Volmer equation is given in Eq. (3) and gives the relationship between the net current per unit area and the overpotential at the electrode surface, η_s [21]. There is a Butler-Volmer relationship at each electrode with their own parameters. The definitions and descriptions of the remaining terms are given in Table 2. The Butler-Volmer equation has two parts, the first term relates to the anodic reaction and the second term to the cathodic. At equilibrium – when i is 0 – both anodic and cathodic reactions occur at equal rates and hence there is no net current. For large positive overpotentials, the anodic current dominates, and for large negative overpotentials the cathodic current dominates [22].

$$i = i_0 \left(\exp\left(\frac{\alpha_a F}{RT} \eta_s \right) - \exp\left(-\frac{\alpha_c F}{RT} \eta_s \right) \right) \quad (3)$$

Table 2: Terms in the Butler - Volmer equation and their physical descriptions

Symbol and name	Description
i_0 – exchange current density	The magnitude of background current that occurs at rest, can be thought of as the gain between overpotential and current
α_a / α_c – anodic / cathodic exchange coefficients	Represent the bias toward anodic / cathodic reaction. The sum of these terms is the number of the electrons involved in the reaction. For lithium ion; $\alpha_a + \alpha_c = 1$
T – temperature	Temperature at which the reaction occurs at.
F – Faraday's number	Coulombs of charge in a mole of electrons

R – molar gas constant	-

The overpotential in the Butler-Volmer equation represents the difference between the electrode potential compared to the equilibrium electrode potential – the electrode OCV in the previous chapter which is a function of SoC. The electrode potential is given as the difference in potential between the electrode surface, ϕ_s, and the electrolyte, ϕ_e. The overpotential is then calculated by Eq. (4) [22]. A schematic of how the voltage between negative and positive current collector varies is given in Figure 8. In this schematic, the different overpotentials are shown, it is seen that the negative solid phase potential, ϕ_s, decreases from left to right and at the separator the potential drops by the overpotential ΔV_η^- and the equilibrium potential ΔV_U^- to the surface electrolyte potential, ϕ_e . A Ohmic voltage drop then occurs across the electrolyte ΔV_e before a further reaction overpotential drop at the positive electrode, ΔV_η^+. The positive electrode equilibrium voltage is then added, ΔV_U^+, and finally the solid phase potential of the positive electrode causes a further decrease in voltage until the positive electrode current collector. The overall equation for the terminal voltage of the cell, V, is given in Eq. (5) [22].

$$\eta_s = \phi_s - \phi_e - U \tag{4}$$

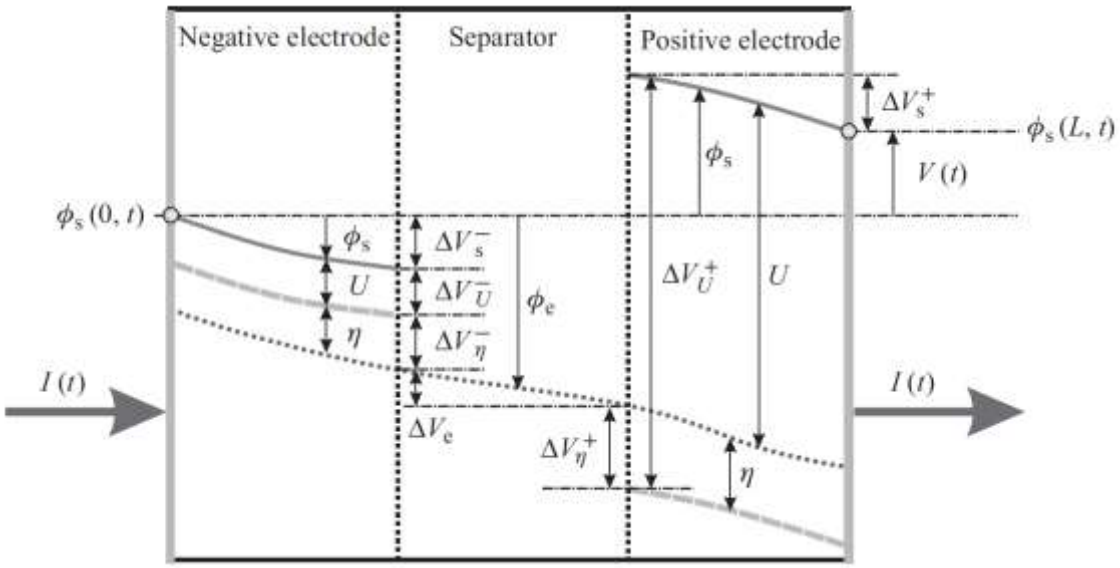

Figure 8: Schematic on how the voltage changes between current collectors in a cell, reproduced from [22] *with permission requested.*

$$V = V_U^+ - V_s^- - V_U^- - V_\eta^- - V_e - V_\eta^+ - V_s^+ \tag{5}$$

The third common source of resistance relates the time it takes for intercalated lithium to diffuse through the active material particle. This means that the surface concentration of the electrode particle is different to the average concentration in the particle. This has the effect of changing ϕ_s and hence η_s to even higher values for the anodic reaction, and lower for the cathodic reaction causing an even bigger difference in the terminal voltage to the cell OCV.

2.2 Lithium-ion Battery Degradation

A lithium-ion battery's performance diminishes over time due to a phenomenon called degradation. Lithium-ion degradation results in two main engineering consequences; a loss of capacity and a loss of power. The loss of capacity means that the battery is unable to store the same amount of capacity as it was at its beginning of life, known as beginning of life (BoL) capacity. The loss of power means that for a given current, the battery is unable to supply as high a voltage as it was at its beginning of life due to increases in battery resistance. This results in a lower power delivered by the cell. The combination of these two engineering consequences impacts the usable capacity of the battery, the amount of capacity which can be accessed from the battery under a nominal current. This decrease in usable capacity leads to a definition of the state of health (SoH) of the battery which is given as the current usable capacity as a fraction of the BoL usable capacity.

While the capacity fade and power fade are the results of lithium-ion degradation, to understand degradation and make improvements in battery technology, an understanding of the causes of degradation is crucial. Therefore, the remainder of this chapter will be dedicated to the causes of degradation and the interplay between these causes of degradation. This includes degradation mechanisms, which are the chemical and physical changes which occur within the battery itself. The field of degradation mechanisms is vast and so rather than trying to address all the information in this field, this thesis aims to cover the absolute minimum that is required to understand the degradation without overcomplicating the subject. This also includes degradation modes which group effects of different degradation mechanisms and give a useful middle ground between the degradation mechanisms and engineering consequences.

Lithium-ion degradation is often presented as a very complex topic; the domain of hard-core electrochemists, materials scientists, and those with an IQ of 140+. Degradation is often summarised by figures like the one presented in

Figure 9 [23]. These figures present a wide range of degradation mechanisms, many of which do not occur under nominal conditions, with no context and often ill-explained diagrams of what each mechanism is and how it occurs. Further to this, there are an incredibly large number of review papers on lithium-ion battery degradation which often times try to cite as many references as possible. For context, searching Web of Science for "Lithium-ion battery degradation" and filtering to review papers yields 90 results from 2021 alone. From a small sample of these papers, a reference count of 200-300 published works is not uncommon.

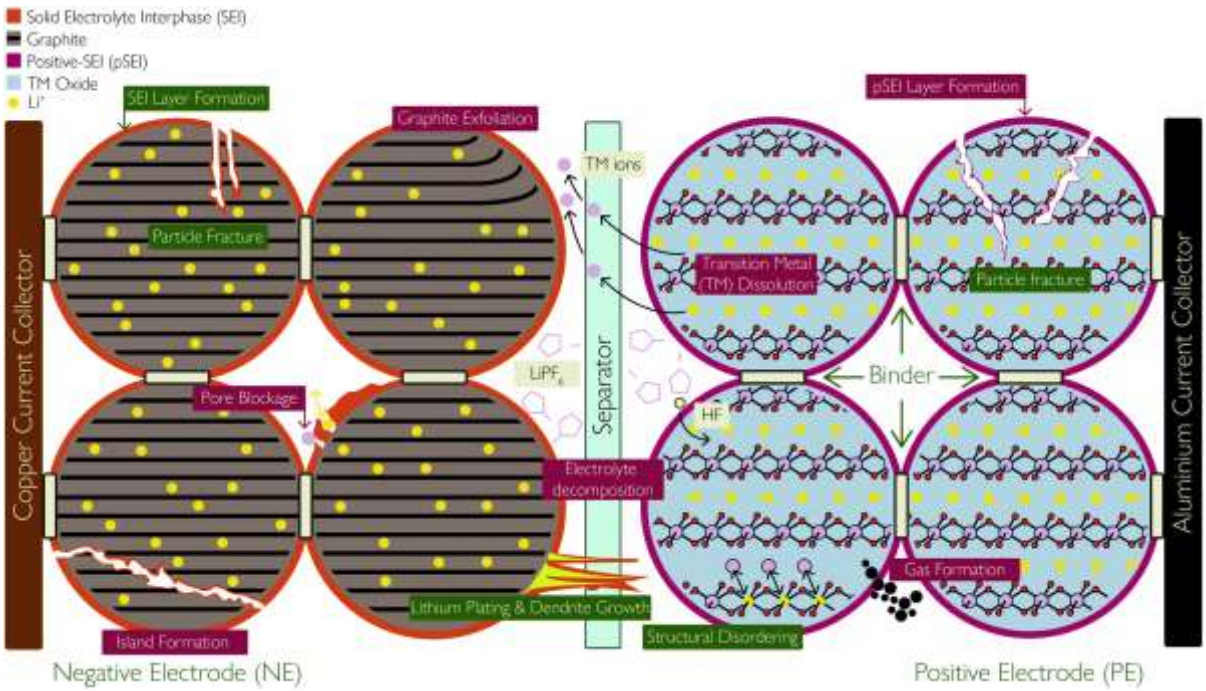

Figure 9: A typical representation of lithium-ion battery degradation found in literature. The figure shows a wide range of degradation mechanisms without giving any links between mechanisms. Figure taken from J. S. Edge et al., "Lithium ion battery degradation: what you need to know," Phys. Chem. Chem. Phys., vol. 23, no. 14, pp. 8200–8221, 2021.[23].

Clearly there is a tendency to overcomplicate the field of lithium-ion degradation. Granted, the intricate details of the mechanisms of the degradation may well be a complicated topic. However, in the interest of the reader's (and writer's) sanity, here lithium-ion degradation will be presented in the simplest possible way which gives the reader everything they need to know to follow the rest of this thesis. In this section, only a subset of degradation mechanisms are addressed. These are mechanisms which occur under nominal battery use and as such mechanisms which result from overcharge, overdischarge and cell overheating are not covered. The mechanisms which will be addressed are typically those which lead to further degradation consequences, what will be known as primary mechanisms. There will also be discussion of a small subset of secondary mechanisms which are those which occur as a consequence of primary mechanisms.

2.2.1 Negative Electrode Degradation

Solid Electrolyte Interphase Growth

There are several degradation mechanisms which take place at the negative electrode, the most notable of which is solid electrolyte interphase (SEI) growth. SEI growth occurs when electrolyte comes into contact with the surface of the negative electrode. This forms a passivating layer over the electrode particle surface which then becomes a physical barrier for lithium ions to diffuse through, causing a rise in cell impedance. The SEI reaction occurs when solvent molecules of the electrolyte reach the surface of the electrode in the presence of lithium ions. The low voltage of the negative electrode, below the voltage stability limit of the electrolyte , means there is an appreciable rate of reaction between the solvent molecules and the negative electrode [24], [25]. Examination of SEI composition has also

revealed that in the majority of SEI compounds lithium is also present, meaning that during this reaction lithium atoms are also consumed from the system [26], [27].

The growth part of SEI layer growth degradation stems from the increasing thickness of this layer by more electrolyte solvent molecules and lithium ions reaching the surface of the negative electrode over time [28], [29]. This is depicted in Figure 10 which is taken from Tahmasbi et al [28]. It is observed in literature that elevated temperatures increase the rate of SEI layer growth [30]. This observation can be explained by the strong temperature dependence on diffusion rate, a higher temperature means a faster rate of diffusion of solvent molecules through the existing SEI layer and to the surface of the electrode. A high SoC also increases the rate of SEI growth [30]. This is because high SoCs mean low negative electrode potential which facilitates a faster rate of reaction between the solvent and the surface of the electrode.

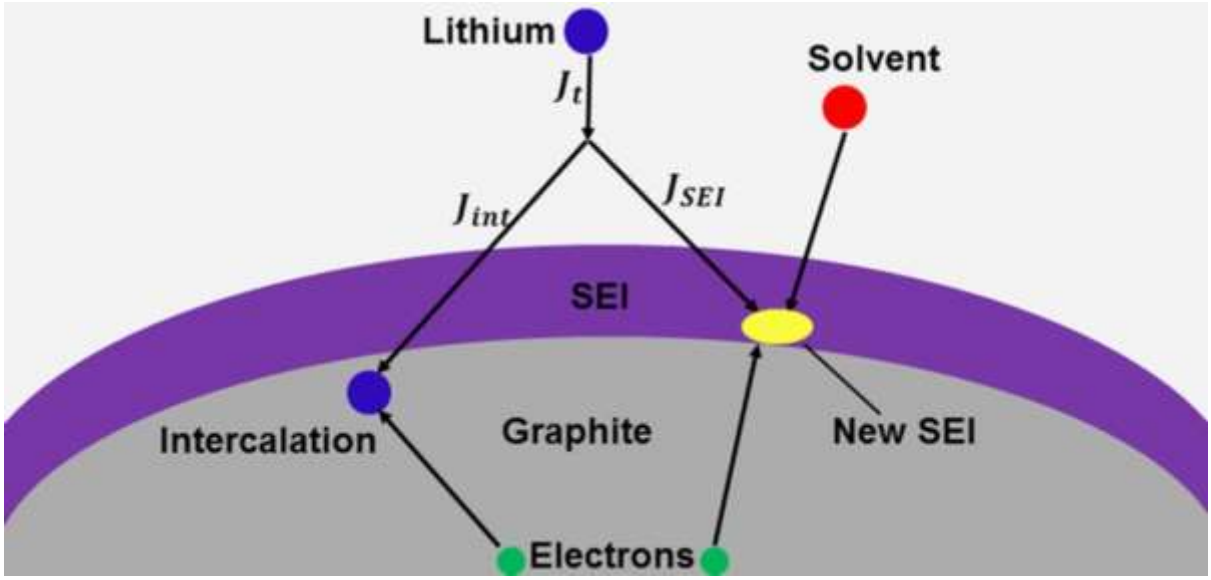

Figure 10: Mechanism of SEI layer growth as a reaction between electrolyte solvent, lithium ions and electrons at the surface of the electrode. Reproduced with permission from [28]

SEI layer growth is the prominent degradation mechanism in calendar ageing, which is aging which occurs when a cell is left at rest for prolonged periods of time. An investigation on the rates of SEI layer growth was performed by Ecker et al. [30]. In this work, cells were charged to various SoCs and stored at various temperatures and their usable capacities over time tracked. The experiment echoes the points made above, the higher SoC cells exhibited higher rates of calendar ageing and hence SEI layer growth compared to those at lower SoCs. Cells which were at higher temperatures also exhibited higher rates of calendar ageing than those which were at lower temperatures.

SEI layer growth by the mechanism described above is a continuous process which can occur at high rates under the right (or wrong!) conditions and its impact is felt over long periods of time. However, more acute forms of negative electrode degradation take place during cell cycling, especially aggressive cell cycling. These are predominantly lithium plating and particle cracking.

Lithium Plating

Lithium plating is a phenomenon whereby metallic lithium is deposited on the surface of the negative electrode. This occurs when it is more energetically favourable for the lithium to electroplate on the surface of the electrode, rather than intercalate into the particle. This can happen when the electrode surface reaches the lithium saturation limit; when the graphite layers at the surface are unable to accommodate more lithium atoms [31]. When this happens the reaction potential between the liquid phase and the solid phase drops

below a threshold, commonly stated to be 0V in the literature, and the lithium ions plate onto the surface of the negative electrode which is known as kinetic plating [32]. Lithium plating is not wholly irreversible; once the surface of the electrode is not saturated with lithium atoms, some of the plated lithium can be intercalated into the active material. Additionally, some lithium becomes dead lithium by reacting with the solvent in the electrolyte to form islands of substance similar to SEI, this is shown in Figure 12.

A stripping reaction, the opposite of the plating reaction, can also occur on subsequent discharges [33]. It is unclear on what proportion of the plated lithium is intercalated or stripped, but there is some permanent plated lithium left over after stripping and intercalation. Fig shows the surface of a negative electrode, made of graphite which has undergone plating [33]. The lithium has not been stripped or re-intercalated into the electrode meaning it is permanently lost from the cyclable inventory of lithium.

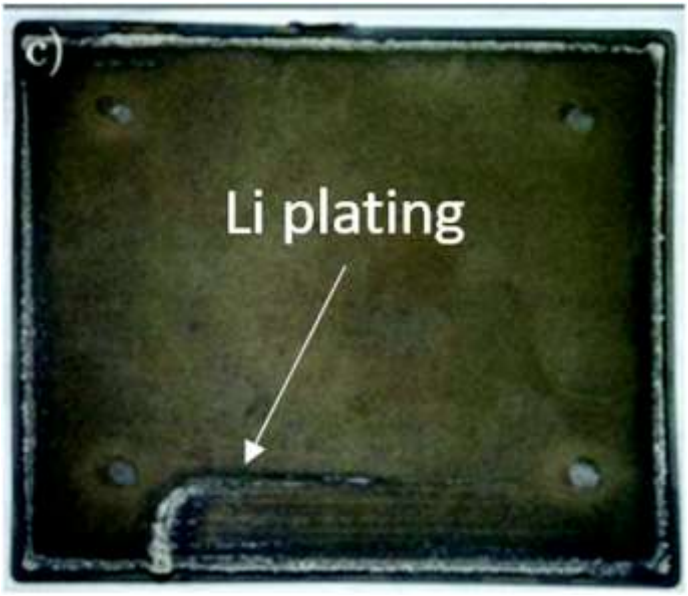

Figure 11: Graphite electrode which has undergone significant amounts of plating (arrowed). Taken from I. D. Campbell, M. Marzook, M. Marinescu, and G. J. Offer, "How Observable Is Lithium Plating? Differential Voltage Analysis to Identify and

Quantify Lithium Plating Following Fast Charging of Cold Lithium-Ion Batteries," J. Electrochem. Soc., vol. 166, no. 4, pp. A725–A739, Mar. 2019. [33]

Lithium plating can occur in two ways, as a distributed sheet of lithium across the surface of the electrode, or more concerningly, as dendrites which can lead to puncturing of the separator and a subsequent internal short circuit [33]. The latter of these obviously poses a safety risk to the battery, but to the best of the authors knowledge, no battery fire events have been attributed to internal short circuits caused by dendritic plating. However, the rapid reacting of electrolyte with the plated lithium can form flammable gas which does put the cell at a higher risk of catching fire [34].

Much more common and mundane is the trapping of plated lithium by the rapid reaction of electrolyte with the plated lithium due to the low potential of the metallic lithium [34]. This reaction causes the lithium below the surface of the newly formed SEI to become trapped and no longer electrochemically active. This effect is twofold for degradation; the plated lithium itself is lost and more SEI layer is formed in this reaction which causes more loss of lithium atoms. This is shown in the schematic in Figure 12 which is taken from Edge et al. and was adapted from Zhao et al. [35].

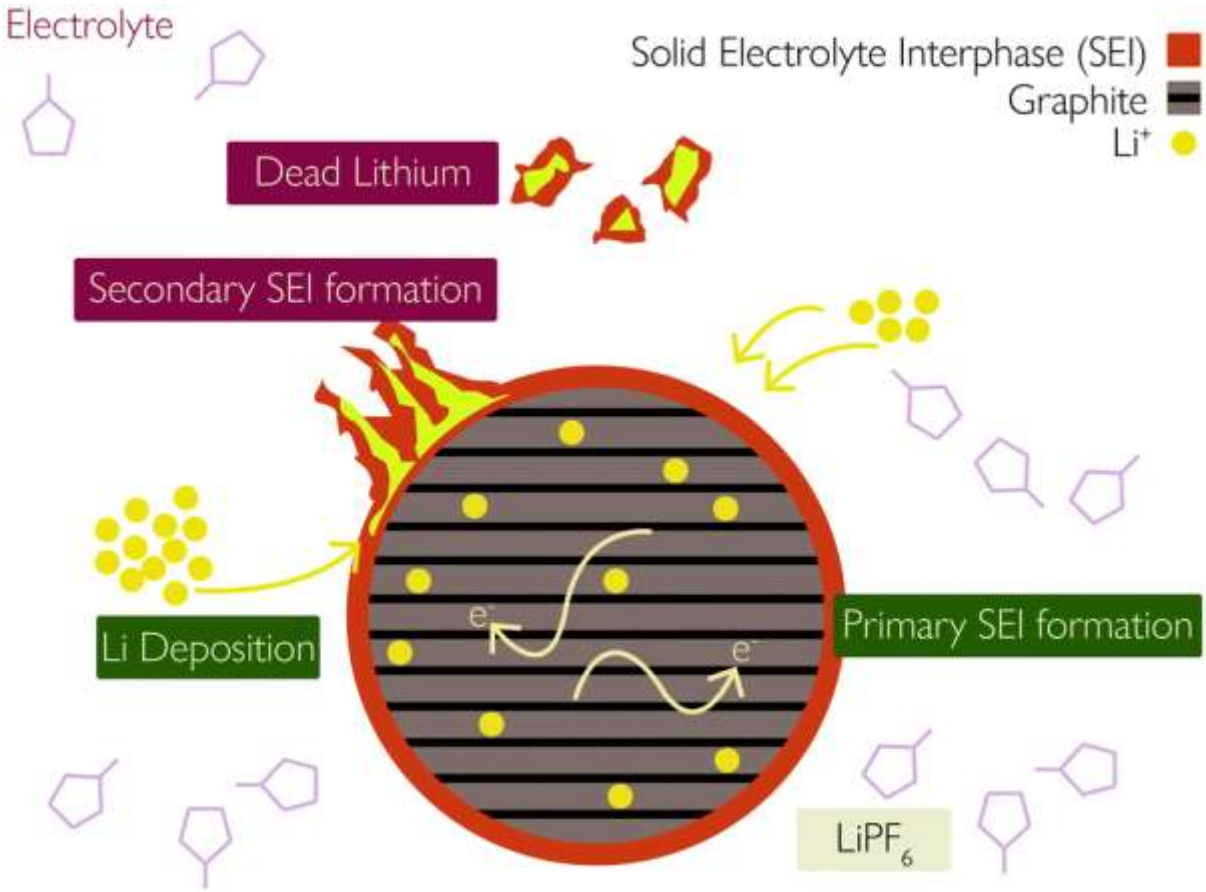

Figure 12: Schematic of the process of lithium plating and subsequent trapping by SEI formation. Adapted from X. G. Yang, Y. Leng, G. Zhang, S. Ge, and C. Y. Wang, "Modeling of lithium plating induced aging of lithium-ion batteries: Transition from linear to nonlinear aging," J. Power Sources, vol. 360, pp. 28–40, Aug. 2017. [35]

As stated above, the mechanism of plating is related to the concentration of the lithium in the graphite being close to its saturation limit [31], and the reaction potential between the liquid and solid phase being below zero [32]. This means that lithium plating is especially prevalent during battery charging, especially fast charging [33]. During fast charging, the high current means that there is a build up of lithium atoms at the surface of the electrode giving a two-fold effect. The surface potential of the electrode is much lower, meaning that the overpotential generated by the kinetic reaction would more likely be lower than the threshold of 0V vs Li/Li^+ causing plating. Similarly, as the lithium concentration of the negative electrode surface is very high during high currents, the particle is more likely to be

at its concentration limit. Low temperatures achieve a similar effect by limiting the rate of diffusion of lithium through the particle and hence making it more likely that the surface of the particle is at the concentration limit or that the potential between solid and liquid phase is less than 0V.

Particle Cracking

Mechanical stresses are exerted on particles when lithium atoms intercalate into them [36]. Charging and discharging leads to a constant application and release of tensile and compressive stresses in the particle which leads to cracks forming and growing in the particles [37]. If a crack grows to be too large, it can cause complete fracture and can mean that some of the particle becomes electrically isolated in a process known as island formation [38]. This disconnected piece of electrode then becomes unavailable for electrochemical activity, meaning the capacity of the electrode is decreased. Additionally, if there is lithium inside the disconnected piece of electrode, that lithium becomes trapped, reducing the amount of cyclable lithium in the system. When a new crack forms, new electrode surface is exposed to the electrolyte. This new surface is quickly covered in SEI layer as the solvent in the electrolyte reacts with the electrode surface. Therefore, particle cracking leads to an accelerated rate of SEI layer growth. The early, middle, and advanced stages of particle fracture are shown in Figure 13 [23]. In early stages, cracks nucleate in the particle, and are then covered in newly formed SEI. Subsequently the crack propagates and finally the particle completely fractures leading to island formation.

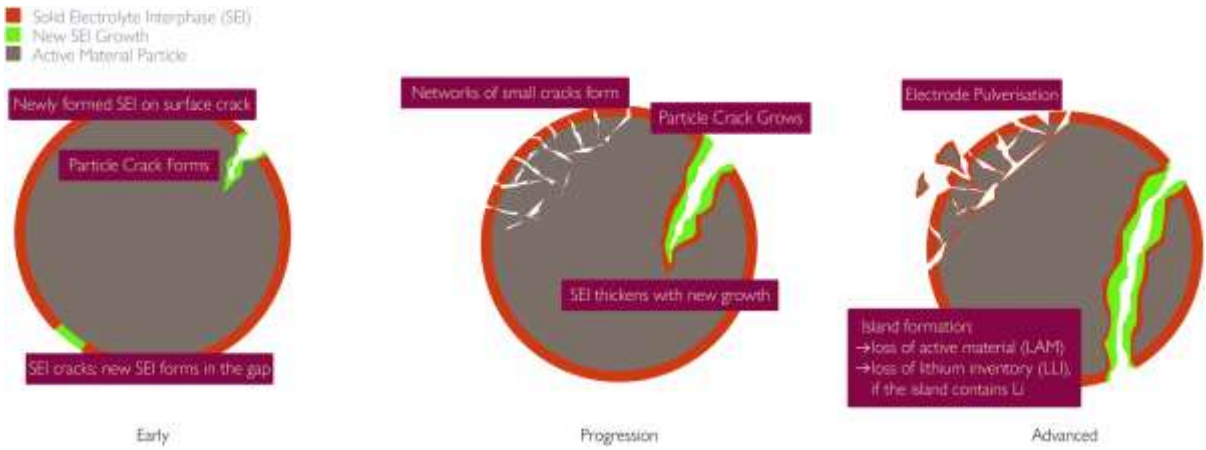

Figure 13: Figure showing the different phases of particle fracture. Early stages show crack initiation, then crack progression followed by complete fracture and subsequent island formation. Figure taken from [1] J. S. Edge et al., "Lithium ion battery degradation: what you need to know," Phys. Chem. Chem. Phys., vol. 23, no. 14, pp. 8200–8221, 2021. [23]

The amount of stress generated in the particle is proportional to the strain that is applied to the particle during lithium insertion [39]. This strain is proportional to the gradient of the concentration of lithium in the particle, i.e. the difference in concentration between neighbouring regions of the particle. A larger concentration gradient arises from two main factors, higher current and lower temperatures. Higher currents mean that the surface of the particle fills up with lithium atoms faster causing a larger gradient in the particle. A lower temperature means that the rate of diffusion of lithium through the particle is slower, causing a larger gradient in the particle. Therefore, fast charging / discharging and low temperature charging/ discharging can cause significant particle cracking.

As well as the concentration gradient effect, different materials exhibit different amounts of volumetric expansion / contraction when they undergo (de)intercalation. An extreme example of a material whose volume change is very large is silicon. Silicon has a very high specific capacity, 4200mAh/g compared to 372mAh/g for graphite [40]. However, silicon

also has a very large volume change as it is lithiated; 320% compared to 12% for graphite [40]. This volume change occurs as lithium alloys with the silicon atom which forms different compounds with different unit-cell sizes [41]. This large change in volume increases the rate of particle fracture in the electrode and hence reduces the cycle life of the material [42].

2.2.2 Positive electrode related

Structural Decomposition

Positive electrode degradation occurs mainly because the compounds which they consist of are generally unstable due to their high potential against the electrolyte [43]. There are several mechanisms by which these reactions can occur and of course the prevalent mechanisms depend on the chemistry of the positive electrode. However, despite there being a variety of mechanisms by which these reactions occur the effects of these reactions can be distilled into a small number of common outcomes. As already mentioned, positive electrode materials are generally unstable, structurally as well as chemically. This instability means that the crystal structure of the electrode can itself change; known as structural disordering, or the atoms can react with compounds in the electrolyte and are then lost from the electrode; known as transition metal dissolution.

Transition metal dissolution and structural disordering can occur via several mechanisms. However, common to all these mechanisms is the consumption of part of the crystal structure to form a positive electrode solid electrolyte interphase (pSEI) layer. The pSEI layer, much like the SEI layer, inhibits charge transfer and increases the resistance of the cell. Similarly, because some of the electrode is consumed in these reactions, there is a loss of theoretical capacity of the positive electrode. One common mechanism that the pSEI can

form is through the decomposition of the layered transition metal structure into an amorphous rock-salt compound which is electrochemically inert [44]. This rock-salt layer is one form of pSEI which causes a shrinking of the active material particle due to its consumption [45]. Similarly, to the negative electrode SEI the pSEI will also grow if new positive electrode surface is exposed to the electrolyte and the surface reacts with the electroyte, specifically nickel which reacts quickly if exposed to electrolyte [23]. In the positive electrode, when the electrolyte comes into contact with the active material it causes chemical decomposition of the electrode itself. The chemical decomposition involves some transition metal species reacting with fluorine in the electrolyte to form pSEI. This reaction is given in Eq. [46], [47] where M is the transition metal species and R is the residual electrode species that do not react to form the pSEI. This reaction involves the direct consumption of electrode material, leading to a reduced capacity of the positive electrode. Conversely, SEI growth on the negative electrode does not directly consume electrode material.

$$2H^+ + 2F^- + MO - R = MF_2(pSEI) + H_2O + R$$

The rate at which the mechanisms to form pSEI happen are typically related to the lithiation state of the electrode. The mechanism of formation of the rock-salt layer has been found to happen more readily at low positive electrode lithiations [48] which is a high cell SOC. As well as lithiation states, the ratios of the transition metals also plays a part in which mechanisms are dominant. Chemistries which are relatively higher in cobalt will be more structurally stable but will be more chemically unstable and more readily react with compounds in the electrolyte [23]. The opposite is true for manganese rich chemistries

which are chemically stable but more likely to decompose into a rock-salt phase to form pSEI by the mechanism described above [25]. Finally, nickel rich chemistries are prone to a mechanism which involves the movement of nickel ions into the intercalation sites for lithium resulting in a loss of electrode capacity [49]. Temperature also plays a large role in the rates of all of the above reactions with elevated temperatures increasing the rates of each mechanism [48], [50].

Particle Cracking

Particle cracking is not unique to the negative electrode, the positive electrode also undergoes particle cracking via the same mechanisms as the negative electrode. The exacerbating conditions are cold temperatures and high currents, just like the negative electrode. The difference between the two electrodes particle cracking is the consequences of the particle cracking. In the negative electrode when electrolyte comes into contact with new material SEI forms.

2.2.3 Electrolyte related

Electrolyte consumption and decomposition

Degradation at each electrode often involves reactions with the electrolyte; SEI growth at the negative electrode involves reaction of solvent and pSEI growth involves reaction with fluorine in the electrolyte. Both of these mechanisms, as well as others, cause a reduction in the amount of electrolyte in the cell. The consumption of electrolyte is not a primary mechanism, it does not happen without the occurrence of one of the other primary mechanisms discussed above. However, it gets a special mention because electrolyte

consumption and depletion may be responsible for battery failure. When the amount of electrolyte is too low, large areas of electrode material can become 'dry' where the electrolyte no longer wets the surface of the electrode meaning the reaction cannot occur. This has the effect of significantly reducing the capacity of the electrode as large areas become dry and hence unreachable by lithium ions. The resistance of the cell can also increase significantly if the conductivity of the electrolyte reduces. Therefore, while the mechanisms described at each electrode initiate degradation, it is the decomposition of electrolyte which can cause cell failure.

Porosity change

During ageing, cell porosity can change due to blocking of the pores after SEI growth. Such growth can cause rapid loss in accessible capacity under rate due to ions not being able to reach large parts of the active material. Sikha et al. show that a worsening porosity can lead to the rapid capacity fade typically seen at the end of life [51]. This mechanism gets special mention as it can quickly lead to large portions of active material being lost and triggering the end of cell life.

2.2.4 Degradation Modes

Degradation modes are a middle ground between degradation mechanisms and observable consequences of degradation. They describe different ways in which each degradation mechanism affects the operation of the cell; they are useful to group together similar effects from different degradation mechanisms. There are 4 main degradation modes, 3 of which affect the thermodynamic properties of the cell and will be discussed first. The first of

these thermodynamic degradation modes is loss of lithium inventory (LLI); this involves the consumption of cyclable lithium from the cell. Secondly and thirdly are loss of active material in the positive electrode (LAM_{PE}) and negative electrode (LAM_{NE}), hence the two additional modes. This involves an amount of electrode capacity being unavailable for electrochemical activity and therefore a loss in capacity of the individual electrode. The effects that these modes have on the thermodynamic properties of the cell will be the subject of a subsequent chapter.

Loss of lithium inventory is the result of any side reaction which involves the consumption of lithium or through the act of trapping lithium inside material which becomes electrochemically inactive. This means prominent mechanisms which lead to loss of lithium are things such as SEI growth and formation which almost always contains lithium. Positive electrode structural decomposition into the rock salt phases often traps lithium as discussed in the positive electrode degradation. Similarly, permanently plated lithium is a loss of lithium in the system. Loss of cyclable lithium does not directly cause a loss of electrode capacity; the electrodes are still able to hold as much lithium as before. However, it does mean that the relative lithiations of each electrode change; the lithiation fraction of one electrode compared to the other changes. This effect is called stoichiometric drift and it describes the relative shifting of one electrode's lithiation compared to the other. This is best depicted in Figure 14 which is adapted from the work of Birkl et al. [52]. In this figure the relative shifting of the electrode stoichiometry causes a reduction in the usable window of lithiation between the two electrodes and hence reduces the electrode capacity. It should be noted that LLI always causes a reduction in this window, never an increase.

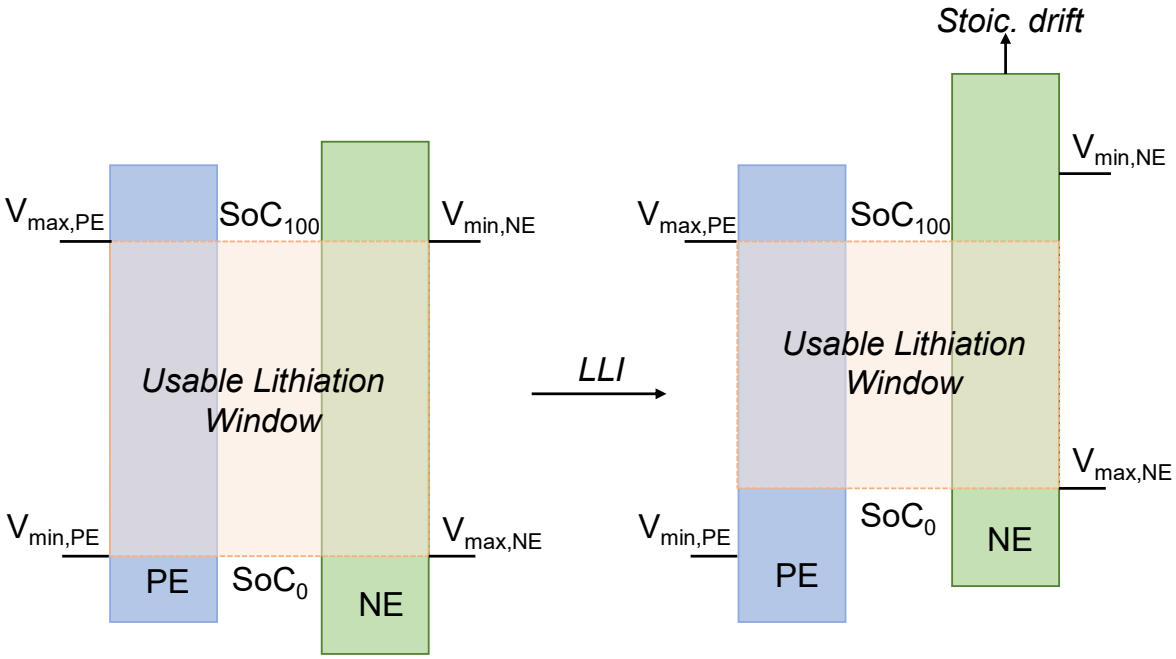

Figure 14: Depiction of how LLI causes stoichiometric drift between electrodes which in turn causes a loss of usable lithiation window; capacity. The usable lithiation window is given by the orange box and is bounded by the maximum and minimum voltage of the limiting electrode (simplification). In this diagram the stoichiometric drift causes the negative electrode (green) to move 'up' compared to the positive electrode (blue). This then causes the lithiation window, and hence capacity, to shrink as the voltage limits move closer together. Adapted from Birkl et al. [52].

Loss of active material occurs in both electrodes and arises from any degradation mechanism which causes a portion of the electrode material to become unavailable for electrochemical activity. A common degradation mechanism which can contribute to loss of active material is island formation, a consequence of advanced stages of particle cracking. Another mechanism is the material decomposition of positive electrode material into a rock salt phase which does not participate in electrochemical reactions and forms pSEI layer. Loss of active material results in a reduction in the amount of capacity that an electrode can store. According to literature, material can be lost in either a lithiated or a delithiated state, LAM_{Li} & LAM_{De}. For lithiated loss of active material, the lithium in the active material is also lost from the system. It will be shown later that it is not possible to distinguish between lithiated and delithiated loss using measurements of the cell's thermodynamics only. Figure

15 is adapted from the work of Birkl et al. [52] and shows how lithiated and delithiated material loss contribute to cell capacity loss. In both cases the loss of active material is seen as a shrinking of the relevant electrode's bar. This shrinkage is seen at the upper end of lithiation for the delithiated case and at the lower lithiation for the lithiated case.

The final degradation mode to be discussed is impedance change. So far, the degradation modes discussed have described ways in which the theoretically available capacity of the cell is reduced. Impedance change joins together any degradation which affects the dynamic behaviour of the cell. Impedance change is referred to in the literature under several names, Vetter et al. [53] use the term impedance rise while Han et al. [54] use the term resistance increase. Regardless of the name, impedance rise groups together the same degradation mechanisms. Dubarry et al. [55] split impedance change further into Ohmic resistance increase and Faradaic rate degradation. The former describes any mechanism which leads to the Ohmic resistance of the cell increasing; current collector corrosion or electrolyte decomposition affecting conductivity. Faradaic rate degradation relates to any mechanism which affect rates of chemical reactions at the electrode electrolyte interface. Examples of degradation mechanisms which cause the slower rates of reaction are SEI layer growth, pore blockage and particle fracture.

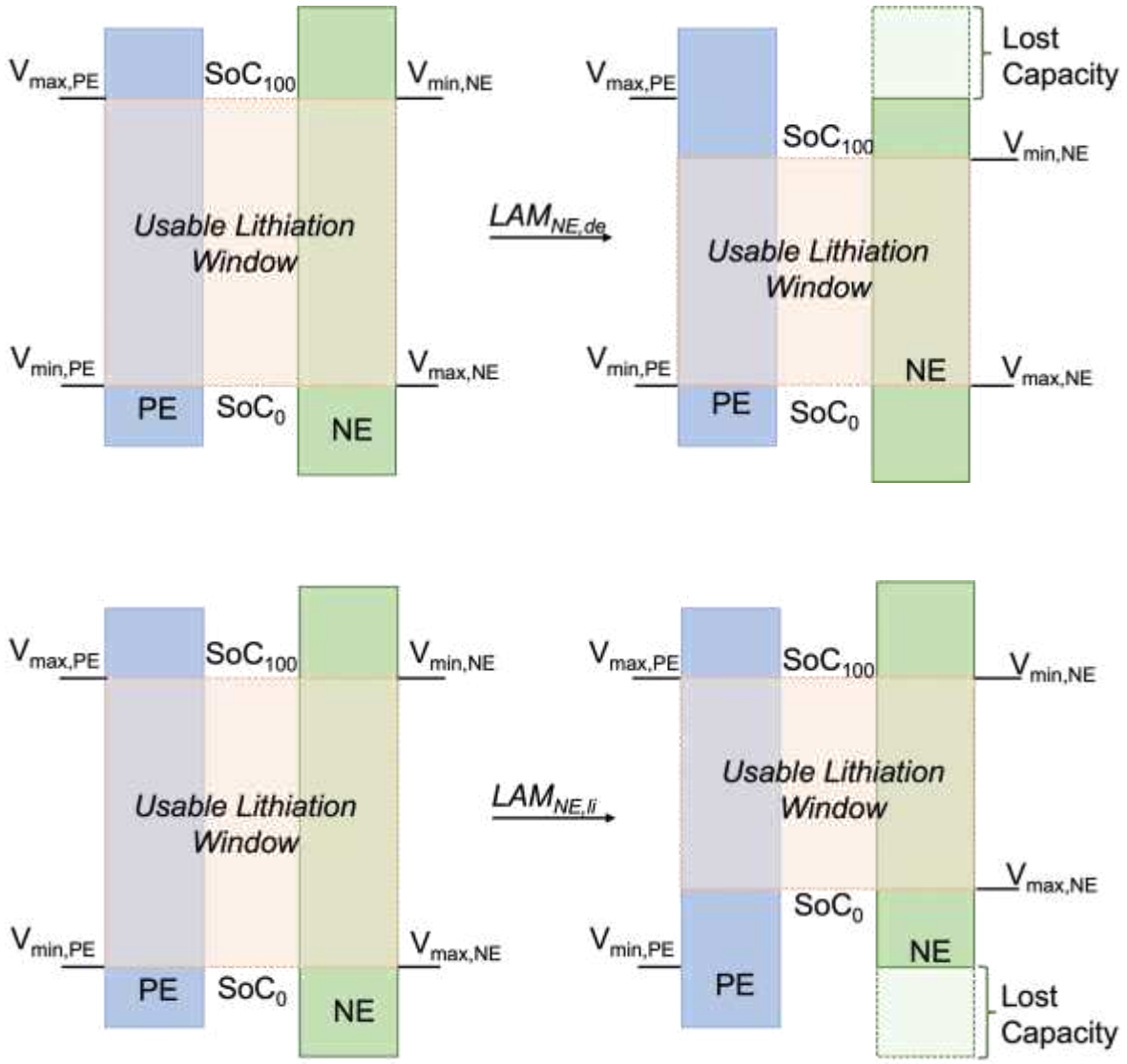

Figure 15: Schematic of lithiated and delithiated material loss and how it leads to a reduction in the capacity of a cell. Material loss is shown for the case of the negative electrode. In each case the loss of material is seen as a shrinkage of the relevant electrode's bar. In the delithiated case, this shrinkage appears at the upper lithiation of the electrode as there is less lithium required to enter the electrode before it reaches its minimum voltage for the cell. Conversely, in the case of lithiated material loss, the reduction appears at the lower lithiation of the electrode. This is due to less lithium needing to leave the electrode before the maximum voltage of the cell is reached.

2.2.5 Degradation Summary and interaction

In this section lithium-ion degradation has been outlined. The concept of the engineering consequences was introduced as the performance changes that a battery sees throughout its lifetime. These are manifested as a reduction in capacity, the amount of charge a battery can store between 0 – 100% SoC, known as capacity fade. Secondly, power fade is the

reduction in the amount of power deliverable at a certain SoC for a given current and arises due to increases in cell resistance. Then degradation mechanisms were explored which are the physical and chemical changes that occur inside the cell which ultimately cause the engineering consequences introduced above. Of the degradation mechanisms, only those that occur first, rather than those that are consequences of other mechanisms were explored. Mechanisms which cause a cell to fail were also outlined. These mechanisms ultimately are the most important to consider in the literature and hence is why only a few other mechanisms were addressed. Finally, degradation modes were introduced, a useful way of grouping together degradation mechanisms which have common effects on the cell. These effects are loss of lithium inventory (LLI), loss of active material (LAM) and impedance change.

Attention has been given to the pathways between degradation and the interlinks between them. Figure 16 is taken from [23], of which I was a co-author, and shows how different degradation mechanisms are related and ultimately which modes and observable consequences they lead to. The primary mechanisms, shown at the leftmost edge of the diagram are those which have been addressed in this section. Of the mechanisms in red, only electrolyte loss and decomposition have been addressed as these could be instrumental in the failure of cells. Those mechanisms which occur in the positive and negative electrodes are given by the top and bottom half split of the diagram. The degradation modes are given in the purple section and show which degradation mechanisms can be grouped into similar effects.

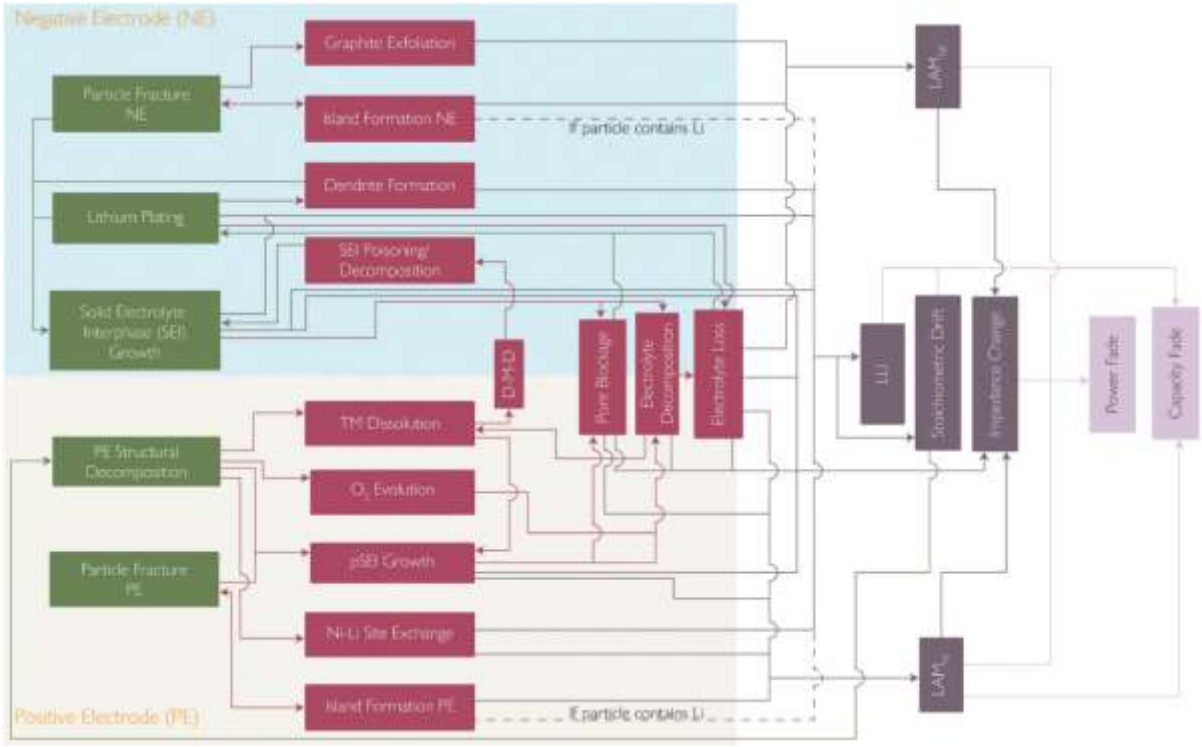

Figure 16: Flowchart of degradation mechanisms, modes and observable consequences for cell performance. The leftmost column represents the primary mechanisms, those which occur first in the mechanism chain. Red indicates secondary and tertiary mechanisms, those which require a primary mechanism to occur. These can be thought of consequences of the primary mechanisms. In dark purple are the degradation modes and pink are the observable consequences on performance. The arrows represent the direction of the mechanism chain.

In this section it has been discussed what each degradation mechanism is, what conditions increase the likelihood of the mechanism occurring and how each mechanism is related. While this information is useful, in order to be able to make assessments of a battery's health and in turn its future performance, the measurement of degradation is imperative. This is known as diagnostics and will be the subject of the next section.

2.3 Degradation and diagnostic techniques; a trade-off

So far, lithium-ion degradation has been introduced and now attention is turned to the detection and measuring of degradation. As previously introduced, degradation can be broadly split into 3 different levels; engineering consequences, degradation modes and

degradation mechanisms. As degradation mechanisms are descriptions of the actual physical and chemical changes that occur within a cell, quantifying each gives the most insight into cell behaviour. Conversely, engineering consequences can result from many combinations of degradation mechanisms and so measurements of capacity fade and power fade give little insight or prediction of how a cell will behave in the future without large amounts of data. A useful insight into using resistance increase data was shown by Aitio et al. [56] where Gaussian process regression was used to find good predictability between the cell resistance increase and the onset of battery failure. However, in lieu of large amounts of data to train models on, the usefulness of these metrics are limited. Between these two extremes lie degradation modes. From the previous section it is shown that degradation modes group degradation mechanisms, but into more distinct groups than engineering consequences. The fact that there are more distinct groups in degradation modes than engineering consequences mean that the information gained from quantifying degradation modes is more useful than quantifying engineering consequences but is still not as powerful as quantifying mechanisms.

If degradation mechanisms give most predictive power in understanding cell behaviour, why wouldn't one just measure these degradation mechanisms and forget completely about other measures of degradation? The answer is that it is very difficult to measure degradation mechanisms. Degradation mechanisms usually require tests which either require taking the cell apart or placing it in some apparatus that is not its normal working environment. This usually involves imaging or spectroscopy of the electrodes after their end of life to detect the presence of certain degradation mechanisms. Conversely to this, measurement of engineering consequences is relatively simple to do while the cell is in its

normal working environment. The common terminology for the different conditions required for measurement are given in Table 3. For practical measurements that are useful throughout cell lifetime, the closer the cell is to in-operando the better.

Table 3: Description of common nomenclature for describing the conditions required for battery degradation measurement techniques

Condition	**Description**
Destructive	Cell needs to be dismantled into component parts
Ex-situ	Cell remains in-tact but is removed from its normal working environment
In-situ	Cell left in working environment but requiring non-normal conditions
In-operando	Measurement performed during normal cell operation

There is clearly a trade-off between a measurement technique's usefulness of output, what level of degradation it measures, and its usefulness in application, which word from Table 3 describes its implementation. The term given to a technique used to measure degradation is a diagnostic technique and will be the nomenclature that is used from now. A diagnostic technique refers to the entire process of obtaining information about cell degradation, including the measurements, data pre-processing and any models used. The literature on diagnostic techniques is vast, much like the literature for degradation. Therefore, only a subset of this literature will be addressed. The literature can be broadly split into the sections given in Figure 17. The horizontal axis here gives the level of detail the technique can provide, and the vertical axis gives the technique's ease of implementation. Finally, a technique can be either quantitative or qualitative. Quantitative techniques can measure

absolute amounts of degradation, whereas qualitative techniques are descriptive, detecting the presence and relative amounts of degradation.

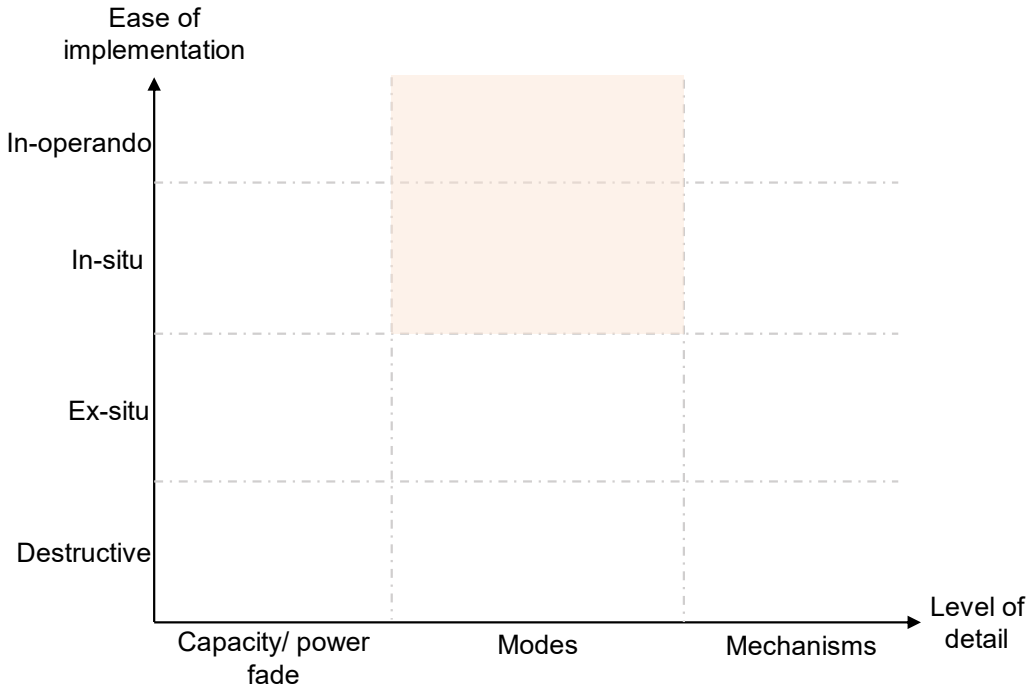

Figure 17: Set of axes which can be used to represent the diagnostic technique literature. Horizontal axis is the level of detail the diagnostic technique achieves, and the vertical axis is the ease of implementation. The highlighted region represents the focus of this literature review.

A review covering all boxes in Figure 17 would be impossible and so choosing the niche to address is important. As degradation mechanisms are very difficult to measure, and measuring capacity and power fade is relatively solved, attention will be given primarily to degradation modes. Further, as this thesis is concerned with diagnostic techniques which are useful throughout the lifetime of a cell, ex-situ and destructive tests will be omitted entirely except for context as described below. Finally, focus will be given primarily to those techniques which are quantitative. In summary, works reviewed here will primarily be diagnostic techniques which:

- Identify degradation modes

- Use in-situ or in-operando conditions
- Are quantitative

The goal of this section is to populate the boxes given in Figure 17 and from this to find any knowledge gaps which exist. There will first be a general discussion around the most common diagnostic techniques which exists outside of the above criteria. This will be more for background information and is not intended to be an in-depth review of this literature. This will allow some relevant techniques to be placed on the figure. Following this, an in-depth review will be conducted on the literature which satisfy the criteria outlined in the previous bullet points.

2.4 Background on diagnostic techniques for mechanisms and consequences

In this section a brief listing and explanation of the most common diagnostic techniques which exist for engineering consequences of capacity and power fade, as well as for identifying mechanisms. For each case, the technique will be assessed for its level of detail and its ease of implementation.

2.4.1 Engineering consequence diagnostic techniques

For capacity fade of engineering consequences, diagnostic techniques produce a direct measure of cell capacity or a measure which is correlated to cell capacity. The most common of these methods is to do a capacity test of the cell, a slow discharge of the cell from its upper voltage limit to its lower. Coulomb counting is used to measure the capacity between these two points. This is by far the most common method of determining the

capacity fade for a cell. Generally, the conditions necessary for this test are a slow discharge of the order C/10, which is typically not seen in cell operation. This would therefore be classed as a quantitative, in-situ technique.

To remove the need for slow discharge, some works have used a technique named incremental capacity analysis (ICA) under higher C-rates to estimate capacity [57]. ICA will be revisited in more detail later, but briefly ICA produces a set of peaks. The plot is produced by plotting the derivative of the charge passed with respect to the cell voltage, dQ/dV. Works then use some form of correlation between the peaks / features in the ICA curves and the capacity of the cell to be able to predict cell capacity from the ICA plot performed under nominal loads. This is a common area of research with most works slightly adjusting a learning model, using a different training data set as the input into the model, or using different features of the ICA curve as predictors. Ultimately though, the works use a similar method and predict similar outcomes just with slightly varying degrees of accuracy. A selection of papers which use these methods are given in [58]–[62].

The power fade is most commonly measured by performing a short current pulse at a predefined SoC or set of SoCs. The voltage response is measured during this current pulse and the change in voltage and the applied current gives an estimate of the resistance of the cell. The resistance of the cell can then be used as a measure of the power fade of the cell, a higher resistance meaning a higher power fade. This technique is often referred to as direct current internal resistance (DCIR) measurement or current pulsing. This technique can be performed in-operando as it has minimal time and equipment requirements. DCIR measurement is one of the more common measures implemented in applications by

industry due to its simplicity. There are common techniques which build a more quantitative picture of cell impedance; however, these will be reserved for the discussions around degradation mechanisms and their diagnostic techniques.

2.4.2 Degradation mechanism diagnostic techniques

Degradation mechanism detection often requires destructive methods whereby the cell is taken apart and the individual components are analysed. The techniques to detect degradation mechanisms are often imaging or spectroscopy based. These include scanning electron microscope (SEM) measurements, computed tomography (CT) and other imaging techniques. The forms of the outputs of these measurements are different but their objective is the same, to detect different forms of degradation mechanisms. These techniques are mostly qualitative in the sense that they detect the presence of a degradation mechanism rather than the absolute amount of a degradation mechanism. By being able to detect the presence of degradation mechanisms, by extension they are also useful to detect the absence of a particular mechanism. For this reason, they can be useful for end-of-life comparisons to see what different mechanisms have been prominent in cells which have been subject to different ageing conditions. As these techniques fall outside of the scope of this review, interested readers can find a recent review article by Jing-Yu et al. [63] which details some ex-situ versions of these imaging techniques.

Another common method of detecting the presence of degradation mechanisms and how they affect a cell's dynamic response is through electrochemical impedance spectroscopy (EIS). The goal of EIS is to obtain the frequency response of a cell by applying a sinusoidal current (galvanostatic) or voltage (potentiostatic) of varying frequency to the cell and

measuring the cell response. Analysis of the resulting Nyquist plot can provide insights into what components make up the cell impedance and how it is changing over time. From this, and with the help of a battery model, it is possible to make some inferences about which degradation mechanisms are contributing to the changing impedance of the cell. This technique does not require the destruction of the cell but does require specialist hardware and careful control over the cell SoC, temperature and connections to obtain accurate measurements. For this reason, EIS is deemed to be an ex-situ technique. EIS can be a quantitative measure of degradation mechanisms in the lab by attributing certain impedance characteristics to degradation mechanisms. However, it is difficult to obtain repeatable measurements from EIS and the interpretation of results is sensitive to the form of the model used in the technique. EIS is probably the most common diagnostic / electrochemical technique applied in the lab and as a result there are many review papers available on the subject. Interested readers can see a recent review at [64].

2.5 Review of diagnostic techniques for quantification of degradation modes

Diagnostic techniques which quantify degradation modes almost exclusively use measurements which use open circuit voltage (OCV) measurements. This makes them in-situ diagnostic techniques. The diagnostic techniques either use the OCV itself as the measurement to determine the degradation modes, or a derivative of the OCV such as IC or differential voltage (DV). The most impactful works will be reviewed here along with a brief description of how each technique works. More detail will be given on exactly how the techniques work in a subsequent theory section. Works will be split according to the technique they use.

2.5.1 Incremental capacity analysis

Incremental capacity analysis (ICA) has already been briefly introduced. It is one of the earliest and most common methods of determining degradation modes. ICA plots the rate of change of cell capacity with respect to the rate of change of cell OCV as is given in Eq. (6) versus the cell OCV to give a plot like that given in Figure 18. IC values give the amount of differential capacity that is stored at a given voltage. The peaks represent areas where the voltage doesn't change much for a significant amount of transferred capacity, known as a stable phase region. The troughs between these peaks represent voltages whereby the cell moves from one stable phase to another known as a phase transition. Areas of stable phases and phase transitions come from the combinations of phases and phase transitions of the individual electrodes. This is given in Figure 18 which is taken from Dubarry et al. [65]. The bars in section b) of the figure represent the positive and negative electrodes and the coloured sections represent the different phases of the electrodes. Section a) of the figure then shows how these combinations of phases lead to the different peaks and troughs in the IC curve. The numbers above each peak in the curve correspond to the combination of individual electrode phases. The areas under the peaks and troughs in the IC curve can give information of how much capacity each electrode has at any given time. Similarly, the shape and position of the peaks can give information about the relative offset between the peaks.

$$IC = \frac{dQ}{dU_{cell}} \tag{6}$$

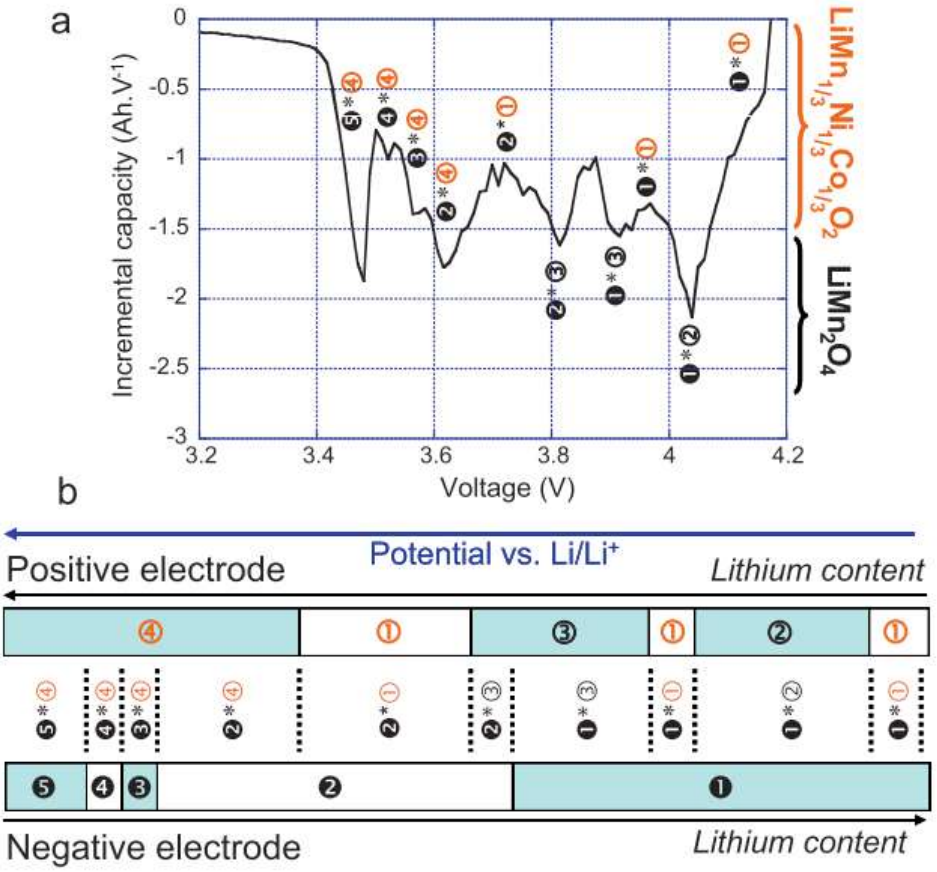

Figure 18: Incremental capacity curves showing how peaks and troughs in the IC spectra correspond to phase combinations from the positive and negative electrodes. Reproduced from [65] *with permission requested.*

Some of the earliest works in degradation mode diagnostics were conducted by Matthieu Dubarry [66] using ICA. ICA had been used previously to this, for example by Dahn & McKinnon [67] who used a form of ICA to quantitatively examine phase transitions in lithium ion cells. However, the works by Dubarry were some of the first to diagnose degradation modes with this technique. Dubarry et al. [66] showed that ICA was capable of identifying degradation modes by being able to identify how reductions of capacities in different phase combinations could lead to conclusions about which degradation mode is present in the cell. Following works showed that ICA could be applied and show different results for cells which underwent different degradation scenarios, different cell chemistries and different cell formats [68]–[70]. While it was shown that ICA could be applied in a

multitude of scenarios, the work was mostly qualitative. In [71], [72] Dubarry et al. introduced a model which could quantify the extent of each degradation mode through a mechanistic model. The model consisted of electrode OCV curves whose capacities and offset to each other could be adjusted and from these adjustments, degradation modes could be quantified. The work then showed how the different degradation modes affect the ICA full cell curves. Further work was done by Dubarry et al. [73] in relating the impact of degradation modes on a cell's ICA curve. Results show that a small number of features from the ICA curve such as peak position, width and height could be used to estimate degradation modes, instead of needing to fit an entire ICA curve model to experimental data.

2.5.2 Differential voltage analysis

Differential voltage (DV) analysis operates on similar principles to ICA; both use a derivative of the OCV curve to obtain their signals. Instead of using the rate of change of capacity with respect to cell voltage, DV uses the reciprocal of this, the rate of change of voltage with respect to the cell capacity. This is then plotted against cell SoC or capacity to obtain the DV curve, an example of which is given in Figure 19 which is taken from Bloom et al. [74]. DV has peaks at the SoCs where the voltage of the cell changes quickly - phase transition regions. Each peak in the DV spectra corresponds to a phase transition from a particular electrode - the electrode which the peaks belong to can be identified by examining the DV spectra for the individual electrodes and fitting this to the full cell DV curve. By tracking how each peak moves relative to others, capacities of each electrode can be estimated and the offset between them can also be calculated.

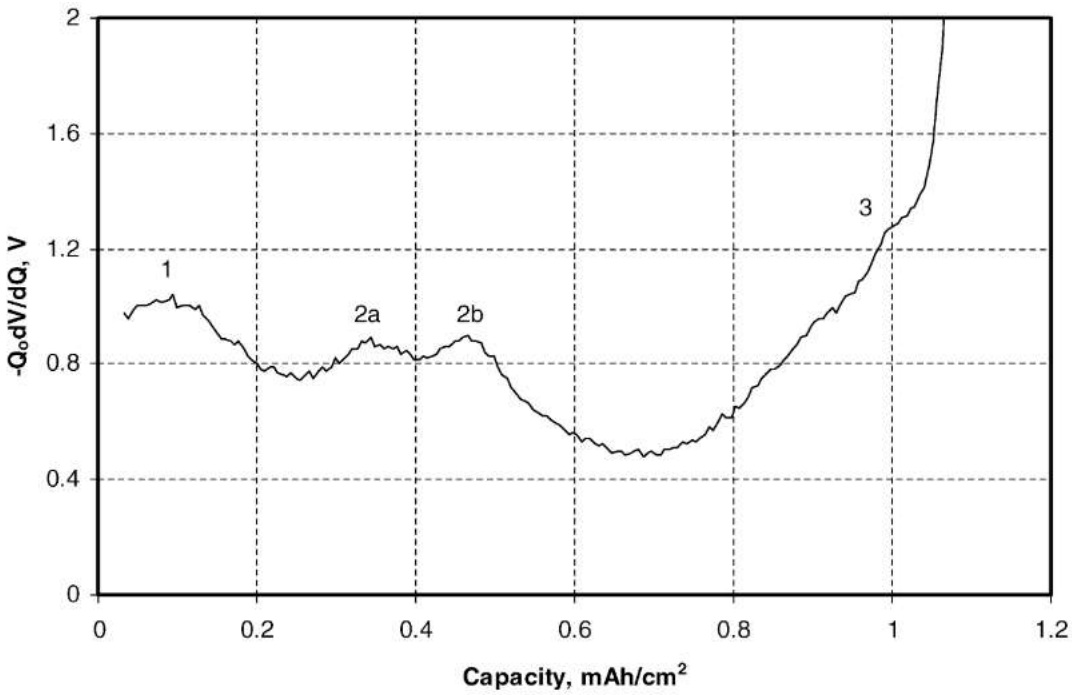

Figure 19: Differential voltage curve showing 4 different peaks. The peaks correspond to phase transitions from individual electrodes. Reproduced from [74] *with permission requested.*

At a similar time as the early ICA work to detect degradation modes, Ira Bloom [74]–[76] used differential voltage (DV) analysis to quantify amounts of electrode capacities and offsets between them. The work by Bloom et al. [76] gives details on how DV can be used to detect the presence of LAM and LLI and establish which is dominant. The work was more qualitative than quantitative but showed that it was possible to predict LAM and LLI through a simple OCV measurement of the cell providing the half-cell OCVs were also known before diagnosis. Bloom produced several follow up papers on the DV technique [74], [75], [77] where it was shown that DV is a method capable of being applied to several cell chemistries and can successfully detect which mode, if any, is dominant at various stages of a cell's life.

2.5.3 Open circuit voltage fitting

The final voltage-based method to be addressed in this section is using the OCV curves from the individual electrodes to fit to the measured full cell OCV curve. This involves scaling and

translating the electrode OCVs to best fit the full cell OCV. In doing this, the capacity of each electrode is determined, as well as the relative offset between the electrode OCV curves. Birkl et al. [78] developed an OCV model which has the capability of reflecting changes in cell electrode capacities and offsets, similar to the way that Dubarry showed in [71]. The model by Birkl et al. in [78] is designed to be a more general OCV model with the ability to model a broad range of possible chemistries. However, from a diagnostics perspective it offers the same functionality as the model developed by Dubarry et al. in [71], [72]. Until this point, the OCV models produced had not been experimentally validated. Birkl et al. [79] validated their OCV model in [78] by constructing coin cells from the electrodes of a full cell but with different amounts of electrode material in each. This artificially created LAM and LLI in the cells. The results showed that the model could accurately predict the amounts of LAM and LLI in the coin cells making the model in [78], [79] a good benchmark for new diagnostic techniques to be evaluated against.

2.5.4 Differential Thermal Voltammetry

Differential thermal voltammetry (DTV) is a novel approach to performing diagnostics introduced by Wu et al. [80]. DTV uses the derivative of temperature with respect to voltage and plots this against the voltage of the cell. This produces a spectra similar to that produced by ICA. However, the key difference between DTV and the OCV based methods is that DTV must be done under load so that a measurable temperature difference is obtained. This means DTV is the only in-operando technique in this review as well as [57] where ICA is performed under appreciable C-rates. Additionally, it uses the entropic information, a component of cell heat generation, as well as the voltage in its spectra. These two characteristics mean firstly that DTV can be performed more frequently than the OCV

related techniques. It also means that the signal obtained with DTV is not only related to the voltage of the cell, meaning it can be used in conjunction with other OCV methods to give a prediction with higher confidence, much like removing bias by using multiple types of sensors.

The initial work by Wu et al. [80] implies that incorporating entropic heat generation information into the measurement would highlight phase change regions in the cell much as is seen in voltage with ICA. Wu et al. [80] showed that DTV can provide the same degradation information as the early ICA and DV works. The findings were qualitative; DTV can detect the presence of degradation but cannot predict the amount of degradation present. The DTV work was further investigated by Merla et al. [81] where it was shown that cells exposed to different degradation scenarios had differing DTV curves, implying that DTV contained information on different degradation modes. However, this work was still not able to quantify the amounts of degradation modes. Merla et al. also applied DTV at the pack level [82] but still no attempt to quantify degradation modes was made. This is the unfortunate shortcoming of DTV, that it was not able to produce quantitative estimates of degradation modes.

2.5.5 Summary of state of the art and proposed work

Figure 20 shows how each of the discussed diagnostic techniques would fit onto the axes first presented in Figure 17. There was not a diagnostic technique in the literature that can be used in-operando to quantify degradation modes. Most techniques in literature use OCV conditions, which is not an in-operando condition. These techniques do however provide the benchmark for any new techniques to be evaluated against, such as the validated OCV

model by Birkl et al. in [79]. DTV is usable in-operando however it's incapable of quantifying degradation modes and can only be used to detect relative differences between cells. DTV did show that a single temperature measurement can be used as a signal that contain information that can be used to diagnose degradation modes. It should also be noted that the works in this review only focus on the degradation modes of LLI and LAM, impedance change is not considered in most of these works.

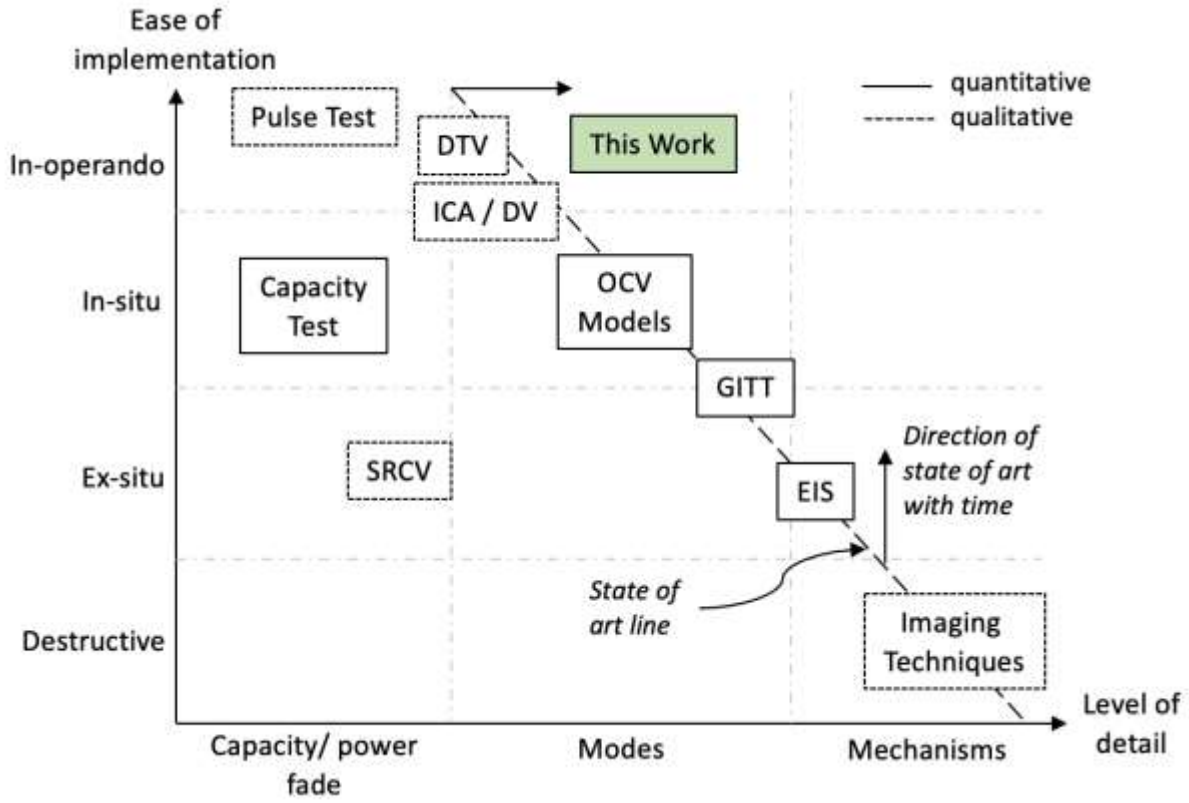

Figure 20: Populated diagram of diagnostic techniques showing the trade-off between level of detail and ease of implementation. The state-of-the-art line gives an idea of where the techniques are as of today and the expected direction of travel in the next years of research. The proposed work in this thesis is shown and is expected to be a quantitative in-operando technique which can diagnose degradation modes.

The knowledge gap that has been highlighted by this literature review is a lack of diagnostic technique that can quantify LLI and LAM in-operando. This thesis aims to address this knowledge gap by proposing a diagnostic technique which can generate quantitative measures of degradation modes under in-operando conditions. The technique will be

evaluated against the validated OCV diagnostic technique as demonstrated and validated by Birkl et al. [79] and will aim to give diagnostic predictions to similar levels of accuracy. The technique will use ideas presented in the DTV literature of using the cell temperature response under dynamic conditions as a signal containing information on cell degradation. The technique is not designed to replace OCV based methods of degradation mode diagnostic but is an option to be used when OCV conditions are not frequently observed. This is made possible by the fact that, much like DTV, the technique will contain information other than the voltage of the cell. In summary the aims for the new technique are to:

- Be applicable in-operando
- Be able to quantify LLI and LAM to a similar accuracy as OCV based techniques popular in literature
- Use temperature-based information to perform its predictions

The following section will begin outlining the theory for how a technique would operate. This includes analysis of the components of lithium-ion battery heat generation and how to parameterise heat generation in terms of degradation modes. This will include how the thermodynamic properties of the cell change for different amounts of degradation modes.

3 Diagnostics Using Heat Generation: Theory

In the previous chapter, a literature review found that there is a gap in current state of the art for an in-operando diagnostic technique which can quantify amounts of degradation modes. Most current methods use open circuit voltage (OCV) based measurements which require in-situ conditions. One technique, differential thermal voltammetry (DTV), is applicable in-operando but is not a quantitative technique. Instead of voltage, DTV uses temperature of the cell. Instead of temperature, the technique in this thesis will rely on cell heat generation as its diagnostic signal. With these points in mind, a new technique is described in the remainder of this thesis which uses heat generation to predict degradation modes.

The purpose of this chapter is to outline the theory that related heat generation and degradation modes. First the origins of heat generation in lithium-ion cells are explored and each component formulated. The order of magnitudes of these components are examined to determine which are the most prominent during normal battery operation for typical commercial cells and from this, the master heat generation equation is formulated. Secondly, this heat generation equation is parameterised in terms of degradation modes and the theory for doing so is outlined. Finally, the theory is extended to electrodes made of arbitrary numbers of component active materials, termed compound electrodes in this thesis.

3.1 Lithium-Ion Cell Heat Generation

The theory for lithium-ion heat generation has been well established in academic literature and many textbooks. As such, the purpose of this section is not to re-derive the origins of heat generation in lithium-ion cells but rather to give the reader an intuition for why each component arises and its relative size compared to other components and how the size of each change for different cell operation and cell parameters. The information developed can then be used to examine what the dominant components are for typical commercial cells under loads seen in application. This allows for a master heat generation equation to be formulated which is a good approximation for the cells and use cases seen in operation.

The total heat generation for an electrochemical cell, q_{cell}, is given in Eq. (7). There are 4 commonly reported components that make up the total heat generation. The irreversible heating, q_{irr}, is the heat that is generated by moving charged particles through a potential difference. The reversible, or entropic heat, q_{rev}, is the heat generated by the reaction entropy of the redox reaction occurring at the surface of the electrode. The heat of mixing, q_{mix}, is the heat generated by molecular movement such as solid diffusion of lithium in the electrode particles, and ion diffusion in the electrolyte. Finally, the side reaction heat, $q_{S.R.}$, is the heat generated by any side reactions that occur. Each of the four terms will now be discussed; their origins, calculation and how the magnitude of each varies with different cell and operating parameters.

$$q_{cell} = q_{irr} + q_{rev} + q_{mix} + q_{S.R} \tag{7}$$

3.1.1 Irreversible heat

Irreversible heat, sometimes called Joule heating, is the heat produced when charged particles are moved through a potential difference. The heat rate is therefore determined by the rate at which charged particles are moved through the potential difference. In a cell, current is the rate of charged particles moving and the overpotentials are generated due to Ohmic resistances due to electronic currents in the solid electrodes and ionic currents in the electrolyte, and the overpotential between the surface of an electrode particle and the electrolyte generated during the redox reaction according to the Butler-Volmer equation. For convenience the terminal voltage can be expressed as the open circuit cell voltage minus the sum of overpotentials in the cell, given in Eq. (8). The irreversible heat is the current multiplied by each of these overpotentials and summed, given by Eq. (9). By combining eqs. (8) & (9), an expression for the irreversible heat is obtained in terms of the cell terminal voltage, V, and the cell OCV, U, which is given in Eq. (10) where I is positive for cell charging. Eq. (10) states that the irreversible heat being the difference between the actual electrical work obtained from the cell, $V\ I$, and the maximum theoretical work obtainable from the cell, $U\ I$. Therefore, the irreversible heat can be thought of as the heat generated by the various resistances in the cell which lead to a difference between the maximum theoretical work that can be delivered and the actual work delivered and the difference being released as heat.

$$V = U_{surface} - \eta_{solid} - \eta_{C.T.} - \cdots \tag{8}$$

$$q_{irr} = I \sum_{i=1}^{N} \eta_i \tag{9}$$

$$q_{irr} = I\left(V - U_{avg}\right) \quad (10)$$

The irreversible heat generated is equal to the applied current multiplied by the difference between the cell voltage and OCV at the surface of the electrode particles. In the absence of diffusion effects, the surface potential can be assumed to be equal to the bulk OCV of each particle which gives the relationship in Eq. (10). The difference between cell OCV and terminal voltage is itself a function of current with higher currents leading to a larger difference. This relationship is non-linear; however, it is often accepted that the irreversible heat scales with the square of current for a cell of given rate capability. When cells of different size are considered, typically larger cells are proportionally more rate capable, and the C-rate becomes a convenient metric to normalise the difference between cell voltage and OCV. It can be said that for equally power dense cells, the difference between cell OCV and voltage is the same for a given C-rate. This means, all other things being equal, that the irreversible heat should scale linearly with cell capacity.

Approximate values for cell irreversible heat generation in commercially available cells can be calculated from cell datasheets if the OCV and the terminal voltage are given for various C-rates. Table 4 lists a set of discharge voltages at 50% SoC obtained from a cell datasheet[1]. For this cell the irreversible heat is approximated by multiplying the difference between the discharge voltage at the lowest rate and each other rate. The resulting heat rate each discharge rate at 50% SoC is also given in Table 4. When this heat rate is divided by the C-rate, the heat generation grows approximately linearly, reinforcing the squared dependence on C-rate.

[1] No reference to cell is given here for confidentiality reasons.

Table 4: Irreversible heating rates for a cell at 50% SoC

Current	C-rate	Voltage @ 50% SoC	Heat rate	Heat rate - C-rate normalised
0.96 A	0.2	3.665 V	-	-
2.40 A	0.5	3.614 V	122 mW	0.245
4.80 A	1.0	3.538 V	610 mW	0.610
9.60 A	2.0	3.433 V	2.23 W	1.11

3.1.2 Reversible heat

Reversible heat, sometimes known as entropic heat, is heat released due to the change in entropy of the species involved in the reaction at the electrode site. The change in Gibbs free energy of a reaction is given by Eq. (11) where G is the Gibbs free energy, H is the enthalpy of the system, T is the temperature of the system and S is the entropy of the system. The magnitude of the Gibbs free energy from the point of view of batteries is the maximum amount of work available to do electrical work and can be related to the equilibrium voltage of the system by Eq. (12) which states the maximum amount of work that can be done by an electrochemical system is equal to the number of Coulombs, $N\ F$, of charge transferred at the systems equilibrium potential, U. The change in energy of the system is negative for a discharging current at a positive equilibrium potential, U.

$$\Delta G = \Delta H - T\Delta S \tag{11}$$

$$\Delta G = -NFU \tag{12}$$

The differential form of Eq. (11) is given in Eq. (13). The change in enthalpy, dH, can be substituted using Eq. (14) where V is volume and P is pressure to yield Eq. (15). It is seen that this equation is a total differential and the entropy, S can be related to the Gibbs free

energy by Eq. (16). where Eq. (12) has been used to relate Gibbs free energy to the equilibrium potential, U.

$$dG = dH - TdS - SdT \tag{13}$$

$$dH = VdP + Tds \tag{14}$$

$$dG = VdP - SdT \tag{15}$$

$$S = -\left(\frac{\partial G}{\partial T}\right)_P = NF\left(\frac{\partial U}{\partial T}\right)_P \tag{16}$$

Eq. (16) has units of Joules / Kelvin, the total entropy of a system with N moles of electrons available for reaction. The quantity of interest for heat generation is the heat rate and so the time derivative of Eq. (16) is taken and given in (17). This uses the fact that the rate of change of charge in a system is equal to the current into that system, and the number of electrons used in the half cell reactions in lithium-ion batteries is equal to 1.

$$\frac{dS}{dt} = I\left(\frac{\partial U}{\partial T}\right)_P \tag{17}$$

The first law of thermodynamics can be used to relate Eq. (17) to the heat generated by the system and was done by Hallaj et al. [83]. Assuming constant pressure and volume, the first law of thermodynamics can be described by (18) where w_{elec} is the electrical work done on the system by an external circuit. The electrical work done to the system is equal to the current multiplied by the voltage at which that current is delivered – the terminal voltage of the cell. Substituting Eqs. (12) & (17) and the relationship between number of Coulombs and current into Eq. yields Eq. (19). By inspecting this equation, it can be seen that the

irreversible heat can be formed and the reversible heat must be given by Eq. (20). The heats of mixing and side reactions do not appear here as the system only considers the electrochemically active species and does not include the losses incurred from the frictions of molecules moving past each other.

$$q = \frac{dG}{dt} + T\frac{dS}{dt} + w_{elec} \tag{18}$$

$$q = -I\,U + T\,I\left(\frac{\partial U}{\partial T}\right)_P + V\,I \tag{19}$$

$$q_{rev} = T\,I\left(\frac{\partial U}{\partial T}\right)_P \tag{20}$$

The partial derivative quantity in Eq. 20 is termed the entropic coefficient. Much like OCV, the entropic coefficient varies with state of charge as the thermodynamic state of the electrode material is a function of its state of charge. The relationship between state of charge and the entropic coefficient is named the entropic profile for the rest of this thesis.

From Eq. (20) the reversible heat scales linearly with current. The entropic coefficient, and hence profile, is a function of the electrode materials and stoichiometry of the cell only and does not change for a cell with a higher capacity. While the reversible heat scales linearly with temperature, the typical temperature ranges that a cell sees in operation of 273 K – 323 K is only a change of around 15% over the full range. Therefore, the temperature that the cell operates at has a much smaller effect on the rate of reversible heating than the current does. For a typical cell with an NMC – graphite chemistry the maximum magnitude

of entropic coefficient is around 0.5mV/K. For a cell at a temperature of 300K, this gives a reversible heat of 0.15W/A for a cell with the entropic profile given. It is seen from Table 4 that as current increases, the irreversible heating term becomes more dominant than the reversible, owing to the squared relationship between current and irreversible heat generation.

3.1.3 Mixing heat

The heat of mixing arises as a consequence of molecules moving in the system which generates heat[2]. This can be due to molecular diffusion in the electrolyte or by solid diffusion of lithium in the electrode particles. The general energy balance for a battery system was derived by Bernardi et al. in [84], one of the earliest works considering the origins of heat generation in batteries. Another work was published by Thomas & Newman in [85]. Importantly, this paper gives a simple equation to estimate the total amount of heat released from mixing. The analysis in the work finds that the heat of mixing within the particle can be given by Eq. (21). The approximation derived by Thomas & Newman is given in [85]. The quantity $d\bar{H}/dt$ is the average rate of mixing heat generation. Descriptions of each quantity and their order of magnitudes are given in Table 5. The quantities $c_{elec} * \bar{V}_{elec}$ is generally considered of the order 1 according to Thomas & Newman [85] which is the reason for the equal orders of magnitudes given in Table 5.

$$\frac{\overline{dH}}{dt} = \frac{1}{c_{elec}\,\bar{V}_{elec}} \frac{\partial \bar{H}_s}{\partial c_s} \left(\frac{I}{F\,D_s}\right)^2 \frac{R^4}{\epsilon\,L} \frac{1}{1050} \frac{A}{t} \tag{21}$$

[2] This molecular motion is strictly the particle motion of molecules past one another and into different locations than they would be at equilibrium. It does not refer to the movement of charge through an electric field which generates an Ohmic heating effect.

Table 5: Descriptions and orders of magnitudes for quantities in Eq. (21). References for values given.

Quantity	Description	Order of magnitude
c_{elec}	Concentration of electrode, mol/m^3	10^5 [85]
$\bar{V}_{elec}$	Molar partial volume of electrode, m^3/mol	10^{-5} [85]
$\frac{\partial \bar{H}_s}{\partial c_s}$	Volume averaged partial molar enthalpy of lithium in electrode, J m^3 / mol^2	10^1 [85]
F	Faraday constant, A s / mol	10^5
D_s	Solid diffusion coefficient,	10^{-14} [86]
R	Particle radius, m	10^{-5} [85]
ϵ	Porosity	10^{-1}
L	Electrode thickness, m	10^{-4} *meas.*
A	Area of planar electrode (2* separator area), m^2	10^{-1} *meas.*
t	Time of cycle, s	various

The values in Table 5 can be applied to Eq. (21) and the result in Eq. (22) is found. This is given for various values of C-rate and corresponding currents and times in Table 6. The percentage of the reversible heat generation is also given. From this very rough calculation that the heat of mixing is relatively negligible below 2C, less than 5% of the reversible contribution. However, based on this analysis at 3C and above the mixing heat is significant, reaching 23% for 5C rates. A paper produced by Chalise et al. [87] gives results which are comparable to those given in Table 6. The work found that mixing heat accounted for ~10% of the total heat generation for a cell at 1C and found that at higher C-rates mixing can account for 22% of the total heat generation as is shown in Figure 21. The numbers in the figure are higher than those in Table 6 but given the approximations present in the analysis it is assumed that Eq. (22) can reasonably predict the heat of mixing for different C-rates.

$$\frac{d\bar{H}}{dt} = 1 * \frac{I^2}{t} \tag{22}$$

Table 6: Mixing heat, reversible heat and mixing heat as a percentage of reversible heat for various C-rates of a 5Ah cell

C-rate	C/2	1C	2C	3C	5C
Current, I, (A)	2.5	5	10	15	25
Time, t, (s)	7200	3600	1800	1200	720
$d\bar{H}/dt$	$8.7\text{x}10^{-4}$	$6.9\text{x}10^{-3}$	$5.6\text{x}10^{-2}$	0.19	0.87
q_{rev} , (W)	0.38	0.75	1.5	2.3	3.8
% q_{rev}	**0.23**	**0.92**	**3.7**	**8.3**	**23**

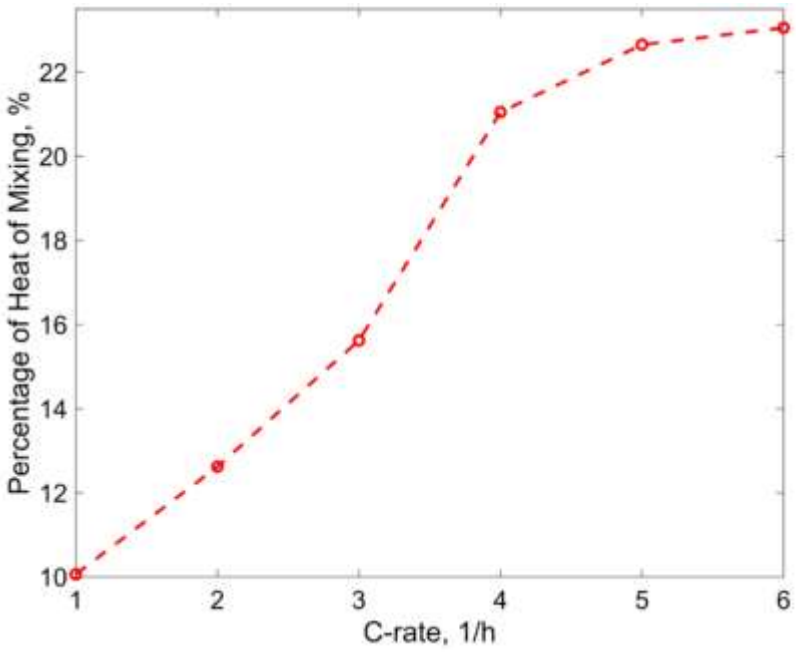

Figure 21: Results from Chalise et al. [87] *which show the percentage of mixing heat which is of similar size to those values found in Table 6. Reproduced with permission from* [87]

Using the analysis developed by Thomas & Newman is has been shown that for high C-rates, the heat of mixing can be significant, as high as 23% of the reversible heat at higher C-rates. This is supported by findings from Chalise et al. [87] who showed that the mixing can nearly

contribute to a fifth of total heat generation at higher C-rates. However, there are studies which support the opposite of this finding. Yan et al. [88] find that mixing contributes to much less than that found by the above analysis and Chalise et al. [87]. In these works, the mixing is found to contribute to a vanishingly small fraction of the total heat generation at C-rates of up to 10C.

Mixing is by no means a trivial effect to calculate and large variations in the literature attest to this. The results displayed in this section are however in line with findings from Chalise et al. [87] and so are assumed to at least be in a sensible ball park. It is shown that for smaller currents of 2C and below the mixing heat has a negligible impact on the heat generation. However, if higher C-rates are used, the heat of mixing may become as important as the reversible heating.

3.1.4 Side reaction heat

Heating from side reactions is the heat of formation of compounds which form inside the battery that aren't the desired intercalation reaction. These reactions could be SEI layer growth, positive electrode reaction with electrolyte, and many more. In all papers read by the author of this thesis, the heat generation from side reactions is ignored.

Consider a cell with a relatively low faradaic efficiency for a commercial cell of 99.9% at 1C. Assume the worst case that 100% of the lost charge is formed as SEI layer, exclusively lithium carbonate Li_2CO_3. This would equate to the entire cell's capacity being consumed in 1000 cycles by SEI growth a wild overestimation for a commercial cell. Per 1 amp-hour of capacity, there are 3600 Coulombs of lithium ions exchanged, this means that 3.6 Coulombs

of lithium are consumed in the SEI side reaction. This is a total of 3.73×10^{-5} mol of lithium atoms. Per mole of lithium carbonate there are 2 moles of lithium atoms, meaning that a total of 1.87×10^{-5} mol of lithium carbonate form per cycle per Ah of capacity. The heat of formation of 1 mol of lithium carbonate is 1216kJ [89]. This means that the maximum total energy released during the cycle from the formation of SEI is 22J. Over 1 hour this equates to a heating rate of 6mW /Ah. Compared to the 150mW / Ah for the reversible component, it can be seen that even in this vastly over exaggerated case, the heat rate from side reactions is negligible.

With this said, the heat of side reaction becomes very important during thermal runaway. Here, rapid exothermic degradation of SEI and positive electrode can cause a cell to begin self-heating and eventually enter thermal runaway. However, it is unlikely that a diagnostic technique to quantify LAM and LLI would be much use during thermal runaway and so this scenario will not be considered in this work.

3.1.5 Summary of heat generation and assumptions

In this section the 4 most reported terms in cell heat generation are examined these terms are repeated in Eq. (10) for convenience. Their origins are explained and then their rough magnitudes are stated with some example cell data. From the analysis performed it is now possible to decide which terms will be included in the master heat generation equation used in the diagnostic technique along with any assumptions required for this equation

$$q_{cell} = q_{irr} + q_{rev} + q_{mix} + q_{S.R.} \tag{23}$$

From the analysis on the heat of side reactions, it is clear that the heat due to side reactions, $q_{S.R.}$, is negligible compared to the other rates of heat generation and so is not considered in the final equation. However, under some conditions, all 3 other terms can be of comparable magnitudes. It was shown for low to medium C-rates (up to 2C) the heat of mixing is acceptably small compared to the reversible heat generation. However, for higher rates, 5C in the example case, the mixing heat becomes significant, as big as 23% of the reversible heat. In order to neglect the heat of mixing, it must be accepted that the rates cannot be too large. It is accepted that this is a 'soft' limit of maximum applicable C-rate but the maximum C-rate cannot be estimated until the size of the cell is known. Therefore, the heat of mixing is neglected for currents which give a mixing heat of less than 5% of the reversible heating. This leaves the reversible and irreversible heating terms which are both of similar magnitudes for nominal C-rates seen in commercial cells. Rewriting the heat equation from Eq. (23) including the terms for the irreversible and reversible heat generations yields Eq. (24). The following assumptions apply for Eq. (24):

- The currents are low enough so that the heat of mixing is < 5% of the reversible heat generation
- The cell is at a uniform temperature, T
- Concentration gradients in the active material particles are negligible, 0-D model. I.e. $U = U(t)$ only and not of concentration, similar for $\partial U/\partial T$.

$$q_{cell} = I\left(V - U + T\frac{\partial U}{\partial T}\right) \tag{24}$$

With the heat generation equation has been established, the next section will be dedicated to developing the theory for how this equation can be parameterised in terms of degradation modes and how the degradation estimation algorithm works in practice.

3.2 Parameterising heat generation with degradation modes

The master heat generation equation to be used in the diagnostic technique is given in Eq. (24) and contains terms for the reversible and irreversible heat. Attention is now turned to how this equation may be parameterised in terms of degradation modes. To do this, it is necessary to decide which terms will be parameterised and hence will be the fitting terms, and which will be measured. In Eq. (24), the current, I, voltage, V and temperature T are all readily measured quantities. The heat generation of the cell, q_{cell}, whilst not as trivial to measure as the previous 3 quantities, can be measured through calorimetry or through energy balances of the heat leaving & entering the cell. This leaves the OCV, U, and the entropic coefficient of the cell, $\partial U/\partial T$. The goal of this section is to outline the theory to parameterise these terms by the degradation modes so they can be used as fitting parameters in the diagnostic algorithm.

3.2.1 Stoichiometric parameterisation

Before addressing degradation modes, it is necessary to make a detour and define what will be known from this point as stoichiometric parameters and the parameterisation of the OCV and entropic profiles of the cell. Much of the discussion in this section will be built from works by Dubarry et al. in [55] and Birkl et al. in [79] but its presentation and explanation is necessary here to facilitate further sections.

Both cell OCV and entropic coefficient can be expressed as the difference between each electrode's contribution. This is very clear for OCV maybe less so for entropic coefficient. The entropic coefficient is the change in the cell's voltage when the temperature of the cell is changed. The total change in the cell voltage is the change in the positive electrode's voltage minus the change in the negative electrode's voltage. Hence, the entropic coefficient of cell is the difference in the entropic coefficient of both electrodes. The value of these two quantities for the cell at a given amount of charge throughput, Q_{cell}, is equal to the difference between the electrode quantities at their charge throughput, Q_{PE} & Q_{NE}. Q_{cell} is 0 at cell SoC = 0 and Q_{PE} & Q_{NE} are 0 when their lithiation fractions equal 0. Expressions for OCV and entropic coefficient are given in eqs. (25) & (26). From these expressions, it is seen that the full cell OCV and entropy are a function of the half cell OCVs and entropies. The electrode OCV and entropy is a function of the amount of lithium in the electrode.

$$U(Q_{cell}) = U_{PE}(Q_{PE}) - U_{NE}(Q_{NE}) \tag{25}$$

$$\left(\frac{\partial U}{\partial T}\right)_{Q_{cell}} = \left(\frac{\partial U_{PE}}{\partial T}\right)_{Q_{PE}} - \left(\frac{\partial U_{NE}}{\partial T}\right)_{Q_{NE}} \tag{26}$$

For each individual electrode, the shape of the OCV or entropic coefficient across its full range of charge should not be dependent on the capacity of the electrode. Put differently, two electrodes of identical material should have identical OCV and entropy profile plots when capacity is normalised. Much like SoC, the term for electrode state of charge is lithiation fraction, a measure of how full the electrode is of lithium with 1 indicating completely full and 0 indicating completely empty. The lithiation fraction is defined in Eq. (27). Any of the electrode-based quantities eqs. (25) & (26) can be written in terms of the

lithiation fractions. Using U_{PE} as an example this is shown in Eq. (30). Here, $\overline{U}_{PE}$ is the OCV of the positive electrode as a function of lithiation fraction and is a constant relationship regardless of the capacity of the electrode. The same relationship applies to the entropy coefficient and for the negative electrode quantities. The relationship between the thermodynamic quantities and Q have been established. Now the task of relating Q_{elec} to Q_{cell} remains.

$$x_{elec} = \frac{Q_{elec}}{C_{elec}} \tag{27}$$

$$U_{PE}(Q_{PE}) = \overline{U}_{PE}(x_{PE}) = \overline{U}_{PE}\left(\frac{Q_{PE}}{C_{PE}}\right) \tag{28}$$

During cell operation, lithium is shuttled between the positive and negative electrodes. This is shown in Figure 22 which shows how lithium is shuttled from positive electrode to negative electrode during charge and vice versa during discharge. In Figure 22, Q_{ref} is a reference axis that allows a relationship between Q_{cell}, Q_{PE} & Q_{NE}. The equations relating these quantities are given in eqs. (29) - (31). By addition of eqs. (29) & (30), it is seen that the sum of Q_{PE} & Q_{NE} is equal to the constant b, which is true for any value of Q_{ref}. It should be clear from the diagram that the addition of Q_{NE} and Q_{PE} and hence the constant b, is the total amount of lithium in the system. The length of each axis in Figure 22 represents the capacity of the electrode / cell. Any point on the axis can be represented by Eq. (32) where x is a fractional amount of the way along the axis and C is the capacity electrode/ cell. For the cell, x is the SoC and for the electrodes it's the lithiation fraction.

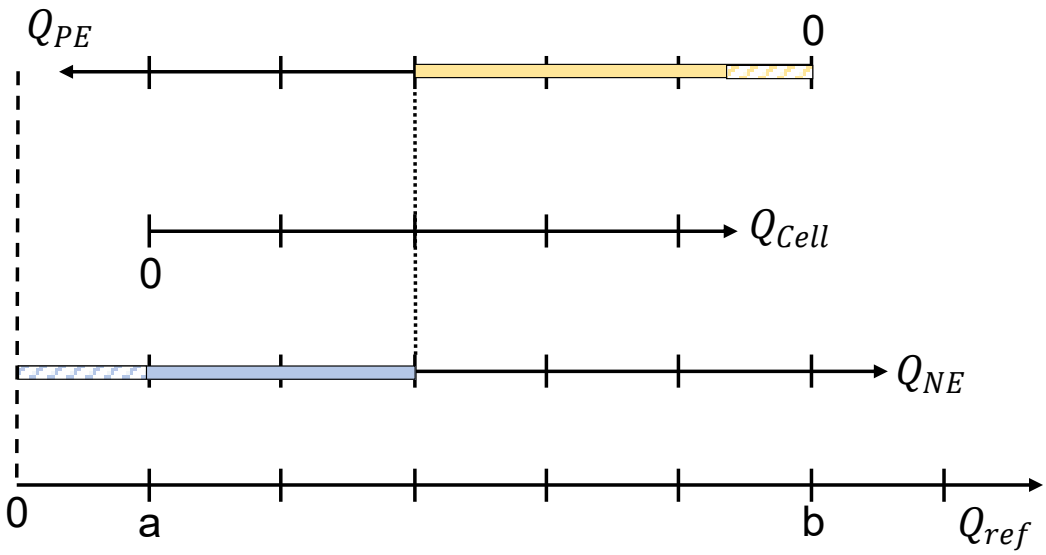

Figure 22: Depiction of how Q_{cell} , Q_{PE} & Q_{NE} are related during cell operation. Bars represent the lithium in the system. As the cell charges, the dotted line moves to the right. This means the blue bar of Q_{NE} grows to the right and the yellow Q_{PE} bar shrinks to the right as lithium moves from positive electrode to negative. The hatched regions of Q_{NE} & Q_{PE} are capacity of lithium that is outside the operating limits of the cell.

$$Q_{NE} = Q_{ref} \tag{29}$$

$$Q_{PE} = b - Q_{ref} \tag{30}$$

$$Q_{cell} = Q_{ref} - a \tag{31}$$

$$Q = x\ C \tag{32}$$

Figure 23 shows a case where the cell starts at a charge throughput of $Q_{cell,0}$ and the electrodes start at their corresponding charge throughputs of $Q_{elec,0}$. An amount of capacity is charged into the cell of ΔQ. For both electrodes and cell, the size of ΔQ is equal. The relationship between the start and end charges for Q_{PE}, Q_{NE} and Q_{cell} is given in eqs. (33) - (35). Without loss of generality, $Q_{cell,0}$ can be given the value of 0 and treated as a datum. This yields an expression for Q_{PE} and Q_{NE} in terms of Q_{cell}. This expression implies that if

the starting values, $Q_{PE,0}$ & $Q_{NE,0}$ are known, then the electrode charge throughputs can be known for any cell charge throughput.

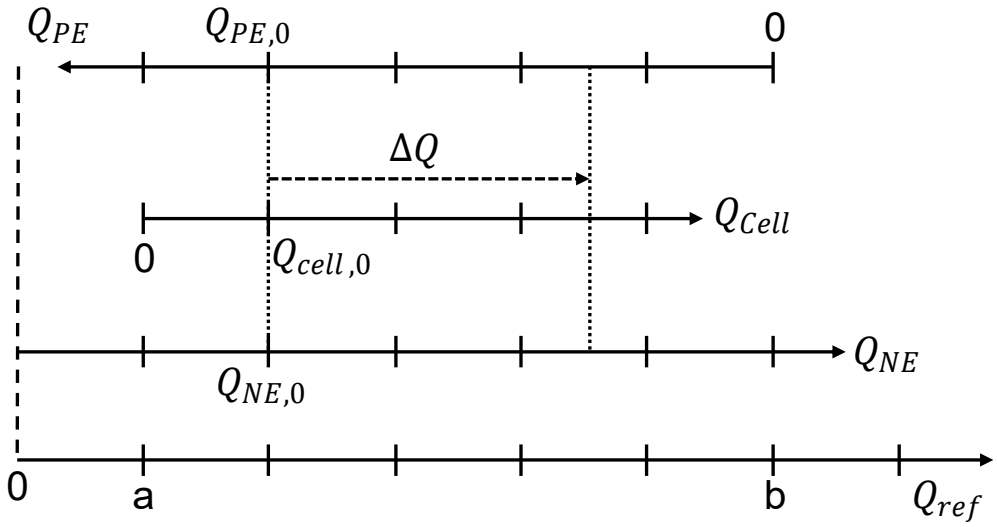

Figure 23: Schematic Depicting the relationship between the Q_{cell}, Q_{NE} and Q_{PE}.

$$Q_{PE} = Q_{PE,0} - \Delta Q \tag{33}$$

$$Q_{NE} = Q_{NE,0} + \Delta Q \tag{34}$$

$$Q_{Cell} = Q_{cell,0} + \Delta Q \tag{35}$$

$$Q_{PE} = Q_{PE,0} - Q_{cell} \tag{36}$$

$$Q_{NE} = Q_{NE,0} + Q_{cell} \tag{37}$$

Substitution of Eq. (36) into Eq. (28) yields an expression for U_{PE} in terms of the initial electrode lithiation fraction, the charge throughput into the cell at any time and the capacity of the electrode - this is given in Eq. (38). Electrode capacity can be calculated given two points of lithiation fractions and the amount of capacity between them, given in Eq. (39) for the positive electrode, where subscript 1 indicates the second point on the axis after moving

ΔQ. Again, without loss of generality, ΔQ can become the signed cell capacity, C_{cell}, which is positive on charging and negative on discharging. This is regardless of the actual measure of the cell capacity, and is a quantity of charge throughput over a given window of interest such as a charge or discharge. Applying this and substitution of Eq. (39) into Eq. (38) yields the result in Eq. (40). As a sanity check, when Q_{cell} is at its largest magnitude, it is the same as C_{cell} and so the expression inside the bracket cancels to $x_{PE,1}$ which was defined as the lithiation fraction when $Q_{cell} = C_{cell}$. Therefore, the expression does not cause a contradiction and behaves as expected.

$$U_{PE}(Q_{PE}) = \overline{U}_{PE}\left(x_{PE,0} - \frac{Q_{cell}}{C_{PE}}\right) \tag{38}$$

$$C_{PE} = \frac{\Delta Q}{x_{PE,0} - x_{PE,1}} \tag{39}$$

$$U_{PE}(Q_{PE}) = \overline{U}_{PE}\left(x_{PE,0} - \frac{Q_{cell}}{C_{cell}}\left(x_{PE,0} - x_{PE,1}\right)\right) \tag{40}$$

An equivalent relationship to Eq. (40) for negative electrode quantities can be derived and is given in Eq. (41). In this section, it has been shown that the full cell OCV and entropy coefficient can be parameterised in terms of the start and end lithiation fractions for each electrode, a total of 4 parameters. This relies on the individual electrode OCVs, and entropic profiles also being known. In the next section the degradation modes are related to the lithiation fractions.

$$U_{NE}(Q_{NE}) = \overline{U}_{NE}\left(x_{NE,0} + \frac{Q_{Cell}}{C_{cell}}\left(x_{NE,1} - x_{NE,0}\right)\right) \tag{41}$$

3.2.2 Degradation modes from lithiation fractions

With the capacity of electrodes and total amount of lithium in the system defined from Figure 22 and Figure 23 in the previous section, these and hence the degradation modes, can be related to the lithiation fractions. Loss of lithium inventory (LLI) would mean a decrease in the total amount of lithium in the system. This loss occurs without changing the capacity of either electrode, i.e. the length of the axes in Figure 22 do not change for LLI. A loss of lithium would imply that the blue and yellow bars would decrease in size. This would have the effect of pulling the point b closer to zero. Schematically it is seen that LLI manifests as the positive electrode axis moving left relative to the negative electrode axis. Therefor loss of lithium is given by Eq. (42) where Q_{Li} replaces b as the total amount of lithium in the system at a given time, and $Q_{Li,0}$ is the value of Q_{Li} at beginning of life.

$$LLI = Q_{Li_0} - Q_{Li} \tag{42}$$

The amount of lithium in the system, Q_{Li}, can be related to the lithiation fractions of the electrodes. Any two corresponding points of lithiation on the positive and negative electrode axes can be used to get Q_{Li}. To be consistent with the previous section, the initial or final lithiation points should be chosen. Substitution of the previously defined relationships for C_{NE} & C_{PE} into Eq. (43) yields Eq. (44). This can be calculated at beginning of life to calculate $Q_{Li,0}$ and then each subsequent diagnosis can calculate the new Q_{Li} and apply Eq. (42) to find the amount of LLI.

$$Q_{Li} = x_{NE,0}\, C_{NE} + x_{PE,0}\, C_{PE} \tag{43}$$

$$Q_{Li} = C_{Cell}\left(\frac{x_{NE,0}}{x_{NE,1} - x_{NE,0}} + \frac{x_{PE,0}}{x_{PE,0} - x_{PE,1}}\right) \quad (44)$$

Loss of active material (LAM) implies the shrinking of the length of the electrode axis. From Eq. (32) it is seen that if the capacity of the electrode decreases, the axis will scale linearly around Q_{elec} = 0. Schematically, this means the axis shrinks about the 0 point for the electrode which undergoes LAM. When the electrode axis is linearly scaled, the total amount of lithium in the system is constrained to be constant. Mathematically, this allows the variables of electrode capacities and amount of lithium in the system to be orthogonal. This means that a change in any one of the three terms does not cause a change in the other two, the variables are independent. LAM is simply calculated as the difference in electrode capacity from beginning of life as a percentage of the original capacity as is given in Eq. (45).

$$LAM_{elec} = 1 - \frac{C_{elec}}{C_{elec,0}} \quad (45)$$

3.2.3 Overall diagnostic algorithm and optimisation

In the previous sections the heat generation equation to be used in the diagnostic algorithm has been formed as well as parameterising this equation in terms of stoichiometric parameters which can be related to the amounts of LAM and LLI. In this section, the optimisation algorithm is created, and boundaries and constraints are assigned to the problem. After this section, the basic form of the diagnostic model and algorithm is complete.

The system of equations to parameterise heat generation in terms of stoichiometric parameters is given in Eqs. (46) - (50) where the terms in the equations have the meanings given in the previous sections. These equations show that given voltage, current and temperature readings, the instantaneous heat generation can be calculated for any set of lithiation fractions. This analysis does however rely on knowledge of the electrode OCV and entropic profiles versus lithiation fraction[3]. However, this information can be collected a-priori and is valid throughout the entire cell's lifetime.

$$q_{cell} = I\left(V - U_{cell} + T\frac{\partial U_{cell}}{\partial T}\right) \tag{46}$$

$$U_{cell}(Q_{cell}) = U_{PE}(Q_{PE}) - U_{NE}(Q_{NE}) \tag{47}$$

$$\frac{\partial U_{cell}(Q_{cell})}{\partial T} = \frac{\partial U_{PE}(Q_{PE})}{\partial T} - \frac{\partial U_{NE}(Q_{NE})}{\partial T} \tag{48}$$

$$\mathrm{X}_{PE}(Q_{PE}) = \bar{\mathrm{X}}_{PE}\left(x_{PE,0} - \frac{Q_{cell}}{C_{cell}}\left(x_{PE,0} - x_{PE,1}\right)\right) \tag{49}$$

$$\mathrm{X}_{NE}(Q_{NE}) = \bar{\mathrm{X}}_{NE}\left(x_{NE,0} + \frac{Q_{Cell}}{C_{cell}}\left(x_{NE,1} - x_{NE,0}\right)\right) \tag{50}$$

From the above set of equations, it is seen that the heat generation can be modelled if the lithiation fractions are known. However, the goal of the technique is to estimate the correct lithiation fractions so that the degradation modes can be estimated. The heat generation of the cell can be calculated from temperature measurements and compared to the predicted heat generation for the given set of lithiation fractions. By doing this, new sets of lithiation

[3] This work does not account for the effects of hysteresis. In this work the charging OCV is used for charging datasets and discharging OCV for discharging datasets.

fractions can be input into the right-hand side of the equation and the set that match the measured left-hand side of the equation can be assumed to be the true lithiation fractions.

This forms the basis of an optimisation problem, the heat generation is measured for a length of time throughout some cycle, this gives a measured heat generation curve for the left-hand side of the equation. The right-hand side of the equation is parameterised by the lithiation fractions at the beginning and end points of the period that the heat generation is measured for. The optimisation would then aim to find the set of start and ending lithiation fractions, $\vec{x}_{Li}$, that minimises the error between the measured left-hand side and modelled right hand side of Eq. (46). The formal definition of the optimisation problem requires an objective function, parameter set, search space and a set of constraints. Beginning with the objective function, this should be the sum of the squared difference between the measured and modelled heat generation at every instance over the heat generation period. This is given in Eq. (51) where the subscript k represents the value of each term at a given instant in the heat generation period. In Eq. (51), the cell OCV, U_{cell}, and entropic coefficient, $\partial U_{cell}/\partial T$ are parameterised by $\vec{x}_{Li}$ whereas all other quantities are experimentally measured at discrete time intervals.

$$f(\vec{x}_{Li}) = \sum_{k} \left(q_{cell_k} - I_k \left(V_k - U_{cell}(\vec{x}_{Li})_{\,k} - T_k \frac{\partial U_{cell}(\vec{x}_{Li})}{\partial T}_{k} \right) \right)^2 \tag{51}$$

The objective function is a score of how close the measured and modelled heat generation match. This value will be different for each set of lithiation fractions, $\vec{x}_{Li}$, passed to the objective function. Therefore, the *parameter set* of the problem is the set of beginning and ending lithiation fractions for each electrode. The optimisation problem aims to minimise

value of the objective function over the entire possible range of the parameter set. The range of the parameter set is the *search space* of the problem and is defined by the *bounds* of the problem. The bounds are the possible values that the beginning and end lithiation fractions can take. The possible values of lithiation fractions can take are anywhere between zero and one. This is represented mathematically by the expression given in (52). Here, the superscript 4 is used to denote that there are 4 parameters in the vector of $\vec{x}_{Li}$. With this, the optimisation problem can be defined by the statement given in (53).

$$\vec{x}_{Li} \in [0,1]^4 \tag{52}$$

$$\begin{aligned} &\min f(\vec{x}_{Li}) \\ &\text{s.t.} \quad \vec{x}_{Li} \in [0,1]^4 \end{aligned} \tag{53}$$

The optimisation objective function, parameter set, and the search space have been defined. However, although values of lithiation fraction can take any value between zero and one, there are combinations of values of lithiation fractions which would yield physically impossible results. Therefore, a set of constraints need to be applied to the problem. Firstly, the capacities of the positive and negative electrodes must be strictly positive. The calculations of these capacities are repeated in eqs. (54) & (55). This is true for a negative ΔQ_{cell} on discharge, or a positive ΔQ_{cell} on charge. If the quantities in eqs. (54) & (55) are positive, their reciprocals must also be positive. Applying this transform and rearranging yields the set of linear constraints given by the set of equations in (56). These constraints are valid at all times when the diagnostic algorithm is applied.

$$C_{PE} = \frac{\Delta Q_{cell}}{x_{PE,0} - x_{PE,1}} > 0 \tag{54}$$

$$C_{NE} = \frac{\Delta Q_{cell}}{x_{NE,1} - x_{NE,0}} > 0 \tag{55}$$

$$\begin{bmatrix} -\frac{1}{\Delta Q} & \frac{1}{\Delta Q} & 0 & 0 \\ 0 & 0 & \frac{1}{\Delta Q} & -\frac{1}{\Delta Q} \end{bmatrix} \begin{bmatrix} x_{PE,0} \\ x_{PE,1} \\ x_{NE,0} \\ x_{NE,1} \end{bmatrix} < \vec{0} \tag{56}$$

The constraints in (56) are true at every iteration of the diagnostic technique and is independent of any iteration before it. However, there are also constraints which depend on the results of the diagnostic technique from the iteration before. These constraints are that the amounts of LAM and LLI must monotonically increase from the first iteration of the diagnostic technique. Using the subscript k to denote iteration step of the diagnostic technique, these relationships can be written in terms of the lithiation fractions and are given in eqs. (57) - (59).

$$x_{PE,1} - x_{PE,0} < -\frac{\Delta Q_k}{C_{PE_{k-1}}} \tag{57}$$

$$x_{NE,0} - x_{NE,1} < -\frac{\Delta Q_k}{C_{NE_{k-1}}} \tag{58}$$

$$\frac{x_{NE,0}}{x_{NE,1} - x_{NE,0}} - \frac{x_{PE,0}}{x_{PE,0} - x_{PE,1}} < \frac{Q_{Li_{k-1}}}{\Delta Q_k} \tag{59}$$

It is prudent to assume that there is an error associated with each iteration of the diagnostic technique. In cases where diagnostic modes are overestimated, this may cause difficulties in applying the constraints given in Eqs. (57) - (59). To account for this, an error can be allowed

in each constraint. In this case the value of the error is a percentage of each of the previous iterations value of capacity. The objective function is modified to minimise these errors values as well and the result is given in Eqs. (60) - (62).

$$x_{PE,1} - x_{PE,0} + \frac{\Delta Q_k}{(1+\varepsilon_{PE})C_{PE_{k-1}}} = 0 \tag{60}$$

$$x_{NE,0} - x_{NE,1} + \frac{\Delta Q_k}{(1+\varepsilon_{NE})C_{NE_{k-1}}} = 0 \tag{61}$$

$$\frac{x_{NE,0}}{x_{NE,1} - x_{NE,0}} - \frac{x_{PE,0}}{x_{PE,0} - x_{PE,1}} - \frac{Q_{Li_{k-1}}(1+\varepsilon_{Li})}{\Delta Q_k} = 0 \tag{62}$$

The inclusion of the error term is twofold; it allows the present iteration of the diagnostic technique to have degradation mode amounts which exceed the previous iterations as discussed, but it also allows the constraints to be transformed into equality constraints. To accept this fact, consider the case where the error is positive; there is a smaller amount of one of the degradation modes than the previous iteration. The error should be the minimum value that satisfies the inequality constraint; the value which makes the constraint equal to 0, in this case a positive value for the error. Similarly consider the case where there is a negative error; the degradation modes calculated for the present iteration are greater than the previous iterations. In this case the error term can be negative to make the equality constraints hold true. Therefore, including the error term allows a freedom which would not be possible if they were omitted. However, the optimisation routine should be discouraged from having large positive errors and is required to be indifferent to negative errors regardless of their size. To achieve this, the objective function must be modified to account for this.

The objective function must be modified to account for the amount of error in the constraints. There are several considerations here; firstly the error defined in the already established objective function and the errors in the constraints above are not of comparable magnitudes and so simply adding the error terms onto the objective function would not work. Instead, the error terms can multiply the objective so that an increase in error gives a relative increase in the objective function. The second consideration is that only positive values of the error terms should be penalised. This avoids the case where the objective function is made smaller artificially by having negative errors. To allow this, the error needs to be switched on when positive and off when negative. Ideally the function that does this would be continuous and differentiable. To achieve this a sigmoid function is used, the form of which is given in Eq. (63). The a term can be used to control rate that the function rises from 0 to 1. The modified objective function is given in Eq. (64) where $f(x)$ is the original objective function and the definition of s_x is given in Eq. (65).

$$y = \frac{1}{1 + e^{-ax}} \tag{63}$$

$$f_\varepsilon(x) = (1 + s_{Li} + s_{PE} + s_{NE}) f(x) \tag{64}$$

$$s_x = \frac{\varepsilon_x}{1 + e^{-a\varepsilon_x}} \tag{65}$$

The complete optimisation problem with parameters, objective function, bounds, and constraints is given by the set of equations in (66). This is the optimisation that will be solved at every iteration of the diagnostic technique. Initially, the three final constraints do not apply as the point $k - 1$ does not exist. The complete parameter list is the 4 lithiation fractions plus the 3 error terms associated with each degradation mode. The three error

terms are not used in the first optimisation iteration. In the next section, the theory and optimisation procedure will be extended to cells with compound electrodes, those that are comprised of more than one active material.

$$\min f_{\varepsilon}(\vec{x})$$

$$f_{\varepsilon}(\vec{x}) = (1 + s_{Li} + s_{PE} + s_{NE}) f(\vec{x})$$

$$\begin{bmatrix} -\frac{1}{\Delta Q} & \frac{1}{\Delta Q} & 0 & 0 & 0 & 0 & 0 \\ 0 & 0 & \frac{1}{\Delta Q} & -\frac{1}{\Delta Q} & 0 & 0 & 0 \end{bmatrix} \begin{bmatrix} x_{PE,0} \\ x_{PE,1} \\ x_{NE,0} \\ x_{NE,1} \\ \varepsilon_{PE} \\ \varepsilon_{NE} \\ \varepsilon_{Li} \end{bmatrix} < \vec{0} \tag{66}$$

$$x_{PE,1} - x_{PE,0} + \frac{\Delta Q_k}{(1 + \varepsilon_{PE}) C_{PE_{k-1}}} < 0$$

$$x_{NE,0} - x_{NE,1} + \frac{\Delta Q_k}{(1 + \varepsilon_{NE}) C_{NE_{k-1}}} < 0$$

$$\frac{x_{NE,0}}{x_{NE,1} - x_{NE,0}} - \frac{x_{PE,0}}{x_{PE,0} - x_{PE,1}} - \frac{Q_{Li_{k-1}}(1 + \varepsilon_{Li})}{\Delta Q_k} < 0$$

3.3 Application to compound electrodes

It is common for an electrode to contain more than one active material which is electrochemically active over its own voltage range. A common example of this is the combining of silicon with graphite in anodes to boost the energy density of the cell. The amount of silicon in the graphite will alter the thermodynamic properties of the overall electrode. This idea extends to degradation, if the amount of each component of an electrode changes at a different rate to the others, the relative amounts of each will change

hence changing the thermodynamic properties of the electrode. This section is dedicated to developing the mathematical relations between OCV and entropic coefficients for electrodes with more than one electrochemically active component.

3.3.1 Open circuit voltage

The amount of capacity that can be stored by an electrode from empty up to a given voltage is obtained by integrating dQ/dV between lower cell voltage to the voltage of interest. The differentiated form of this plot is the incremental capacity (IC) curve which states the differential amount of capacity that can be stored at each OCV. For the case where there are multiple components to the electrode, the total amount of charge transferred to a given voltage is the contribution of stored charge from each electrode component up to that voltage. This is given in Eq. (67) for the case of N electrode components. This equation assumes that at equilibrium the voltage of each component is the same, hence the common OCV term used in the equation. This assumption can be reasoned by assuming that if there were any appreciable differences in voltage between the components, charge would be transferred until the voltages are equal.

$$Q_{elec}(U) = \sum_{i=1}^{N} Q_i(U) \tag{67}$$

The lithiation fractions can be obtained from Eq. (67) and are given in Eq. (68) where C_i is the capacity of electrode component i. Division by the electrode capacity yields the final expression for determining the OCV versus lithiation fraction for a compound electrode with a general number of components. This is given in Eq. (69) where w_i is the capacity weight of component i which is the fraction of capacity of component i divided by the total cell

capacity. The values of w for each component must be between 0 and 1 for all times in the cell's existence. The differentiated form of Eq. (69) yields the capacity normalised IC for the electrode in terms of its component ICs and their capacity weights. If the individual component's OCV versus SoC is known, Eq. (69) gives the full electrode's OCV or IC for any combination of capacity weights for each component.

$$C_{elec}\, x_{elec}(U) = \sum_{i=1}^{N} C_i\, x_i(U) \tag{68}$$

$$x_{elec}(U) = \sum_{i=1}^{N} w_i x_i(U) \tag{69}$$

3.3.2 Entropy

Knowledge of the entropic coefficient of the full electrode is required to apply the optimisation technique developed in the previous sections. This means knowledge of how the entropic coefficient versus lithiation fraction changes for different amounts of constituent parts of the electrode. The starting point for this analysis is from the reversible heat generation of a given electrode. The total amount of heat generated by the electrode is the sum of the heat generated by each individual component of the electrode. This is given in Eq. (70) where the temperature and capacity terms have been cancelled. The unknown terms in Eq. (70) are the electrode entropy coefficient, $(\partial U/\partial T)_{elec}$, and the rate of change of lithiation fraction for component i, dx_i/dt. We aim to express the rate of change of lithiation fraction for each component in terms of known quantities.

$$\frac{dx_{elec}}{dt}.\left(\frac{\partial U}{\partial T}\right)_{elec} = \sum_{i=1}^{N} w_i \frac{dx_i}{dt}\left(\frac{\partial U}{\partial T}\right)_i \tag{70}$$

The chain rule can be applied to the rate of change of lithiation fraction of component i. This is performed in Eq. (71). As the rate of change of OCV is the same for all components in the electrode, and hence the entire electrode, the further substitution is made in Eq. (71). The chain rule can be applied to the last term in Eq. (71), doing so yields Eq. (72). This can be further simplified by realising that the rate of change of electrode lithiation is simply the cell current divided by the capacity of the electrode. Substitution of Eq. (72) into Eq. (71) yields Eq. (73) which is the final expression for the rate of change of lithiation fraction of component i.

$$\frac{dx_i}{dt} = \frac{dx_i}{dU}\frac{dU_i}{dt} = \frac{dx_i}{dU}\frac{dU_{elec}}{dt} \tag{71}$$

$$\frac{dU_{elec}}{dt} = \frac{dU_{elec}}{dx}\frac{dx_{elec}}{dt} = \frac{dU_{elec}}{dx}\frac{I}{C_{elec}} \tag{72}$$

$$\frac{dx_i}{dt} = \frac{I}{C_{elec}}\left(\frac{dx_i/dU}{dx_{elec}/dU}\right) \tag{73}$$

The expression for the rate of change of lithiation of component i can be substituted into Eq. (70) to yield Eq. (74) where the cell current and electrode capacity term cancels with the first term on the left-hand side of the equation. Finally, substitution of the expression for the full electrode IC from Eq. (69) into the denominator of the right-hand side yields Eq. (75) which is an expression for the full electrode entropic coefficient in terms of the individual components entropic coefficient and IC for any set of capacity weights. As a sanity check, it is seen that the for the case of $N = 1$, the electrode entropic coefficient is the same as the

component entopic coefficient which is as expected. A more interesting question is why the IC of the individual components as a fraction of the total IC multiplies the components entropic coefficient. This is likely because the IC gives an indication on the incremental state of charge change for a given voltage change which occurs due to the change in temperature. This then causes a change in SoC of the components of the electrode which contributes to the change in voltage seen when temperature changes.

$$\left(\frac{\partial U}{\partial T}\right)_{elec} = \frac{\sum_{i=1}^{N} w_i \frac{dx_i}{dU} \left(\frac{\partial U}{\partial T}\right)_i}{\frac{dx_{elec}}{dU}} \tag{74}$$

$$\left(\frac{\partial U}{\partial T}\right)_{elec} = \frac{\sum_{i=1}^{N} w_i \frac{dx_i}{dU} \left(\frac{\partial U}{\partial T}\right)_i}{\sum_{i=1}^{N} w_i \frac{dx_i}{dU}} \tag{75}$$

The previous two sections have provided the theory to extend the optimisation framework to include electrodes with components which may degrade at different rates. However, this comes at a cost of requiring extra additional optimisation variables in the weights of each component, w_i. For N electrode components, there are $N - 1$ additional optimisation variables in the problem.

3.4 Overall diagnostic model and algorithm

So far, this chapter has developed the theory to:

- Write the cell heat generation in terms of the most dominant terms
- Parameterise the thermodynamic quantities in terms of their lithiation fractions
- Relate lithiation fractions to the degradation modes

- Define the optimisation problem surrounding these lithiation fractions and measured versus modelled heat generation
- Define the constraints of the optimisation problem
- Extend the theory to compound electrodes.

The goal of this chapter is to represent this theory and optimisation problem as an algorithm which can be implemented in code. By the end of this section, the diagnostic algorithm will be completed from a model and optimisation perspective and the only remaining task will be to define how to experimentally measure heat generation, which will be a question of experimental set up.

The objective function is non-linear in the optimisation variables and so the optimisation problem is likely non-convex meaning that the optimisation problem likely has many local minima which mean that finding a global minimum will be very difficult. As a result much effort will be spent in the next chapter to assess the robustness of the optimisation technique and how the identifiability of the parameters impacts the optimisation results.

The flowchart in Figure 24 shows the order in which operations in the algorithm happen. Each of the parameters is shown in the box and the arrows represent which parameters enter which functional blocks. The numbers in the functional blocks correspond to the equation or system of equations given in Table 7. The first step is to pass the parameters through the constraint equations to ensure that none of the constraints are violated in the

choice of parameters[4]. The OCV and entropic coefficient are then calculated for each electrode from their component parts and the full cell of each are then calculated for all lithiation fractions. Once these quantities are established, the heat generation is calculated for each timestep. The objective function is then evaluated, and the optimisation repeats until the termination criteria are met. The final set of parameters after the optimisation has completed are then used to calculate the cell capacity and amount of lithium in the system. These values can then be used to finally calculate the amounts of each degradation mode.

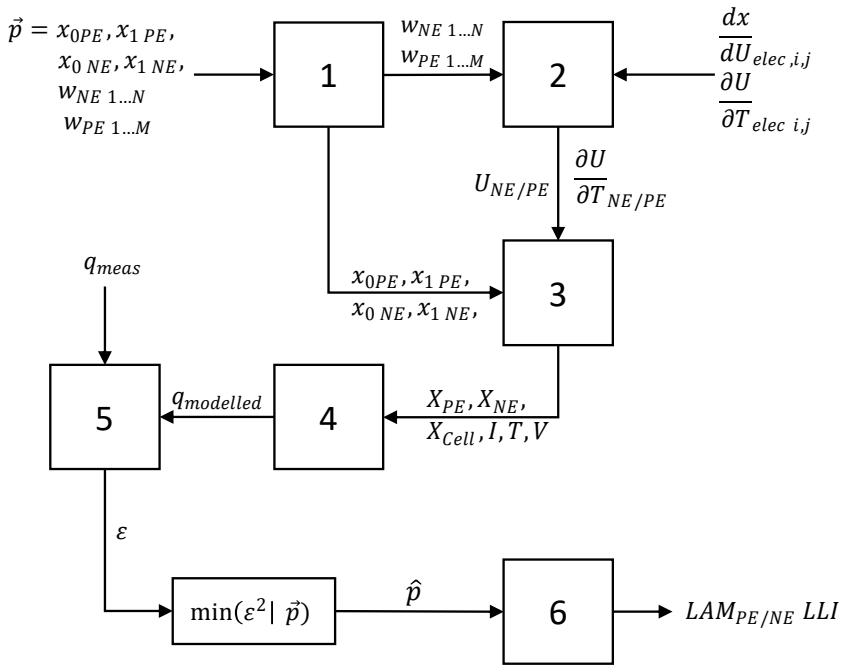

Figure 24: Flow chart representing the flow of information in the diagnostic technique and optimisation routine. The numbered blocks represent sets of functions which are given in Table 7.

[4] In most capable optimisation solvers, a 'pre-solve' step is taken before any optimisation of parameters takes place. This process involves using the constraint equations to eliminate any of the optimisation variables by algebraic manipulation. This is functionally not different to ensuring that all constraints are met when selecting a set of parameters

Table 7: Corresponding function block numbers from fig and the system of equations each represents

Block no.	Description	Equation system
		See system of equations in (66)
1	Do parameter values obey constraints	$\sum_{i=1}^{N} w_{NE_i} = 1$ $\sum_{j=1}^{M} w_{PE_j} = 1$
2	Full electrode OCV and entropy from electrode components	$\left(\frac{\partial U}{\partial T}\right)_{elec} = \frac{\sum_{i=1}^{N} w_i \frac{dx_i}{dU} \left(\frac{\partial U}{\partial T}\right)_i}{\sum_{i=1}^{N} w_i \frac{dx_i}{dU}}$ $x_{elec}(U) = \sum_{i=1}^{N} w_i x_i(U)$
3	Full cell thermodynamic quantity from electrode contribution at given lithiation fraction	$\mathrm{X}_{PE}(Q_{PE}) = \bar{\mathrm{X}}_{PE}\left(x_{PE,0} - \frac{Q_{cell}}{C_{cell}}\left(x_{PE,0} - x_{PE,1}\right)\right)$ $\mathrm{X}_{NE}(Q_{NE}) = \bar{\mathrm{X}}_{NE}\left(x_{NE,0} + \frac{Q_{Cell}}{C_{cell}}\left(x_{NE,1} - x_{NE,0}\right)\right)$ $X_{cell}(Q_{cell}) = X_{PE}(Q_{PE}) - X_{NE}(Q_{NE})$
4	Calculate Modelled cell heat generation for parameter set at every timestep, k	$q_{cell_k} = I_k\left(V_k - U_{cell}\left(Q_{cell_k}\right) + T_k \frac{\partial U_{cell}\left(Q_{cell_k}\right)}{\partial T}\right)$
5	Calculate value of objective function	$f_\varepsilon(\vec{x}) = (1 + s_{Li} + s_{PE} + s_{NE}) f(\vec{x})$ $f(\vec{x}_{Li}) = \sum_k \left(q_{meas_k} - q_{cell_k}\right)^2$

6	Calculate degradation mode amounts	$LAM_{elec} = 1 - \frac{C_{elec}}{C_{elec,0}}$ $LLI = Q_{Li_0} - Q_{Li}$

This chapter has provided the theoretical foundation to develop a diagnostic algorithm which allows the modelling of heat generation in terms of starting and final lithiation fractions over a period. This in turn is used to quantify amounts of degradation modes by comparing measured heat generation to the modelled heat generation and applying an optimisation algorithm. The optimisation algorithm is defined with a set of hard constraints - constraints which cannot be broken - in the form of the capacity being non-negative. There are also a set of soft constraints – constraints which can be 'broken' but are penalised for their amount above 0 - n the form of the amount of degradation modes being monotonically increasing. Finally, the entire algorithm is presented such that it can be written into code and applied.

The next chapter will focus on the application of the algorithm and importantly will define the final part of the technique which has not yet been addressed; the measurement of heat generation and experimental methods for doing so. The evaluation of the performance of the diagnostic technique is then carried out and the results compared to those given by the state of the art OCV technique.

4 Experimental Implementation of Diagnostic Technique and Evaluation of Performance

In the last chapter the theory for modelling heat generation and parameterising the model by lithiation fractions was developed. The lithiation fractions can then be used to calculate the amounts of each degradation mode. The values of the lithiation fractions are obtained by performing an optimisation which seeks to minimise an objective function; the difference between the measured heat generation and the modelled heat generation for a given parameter set. The previous chapter dissected how the modelled part of the objective function is formed, this chapter will address the measured part of the heat generation. The heat generation model will be developed and then the experimental set up and method to measure the heat generation will be detailed. With this experimental set up, the diagnostic technique can be performed and evaluated.

The performance of the diagnostic technique will be evaluated by comparing its results to a diagnostic technique which is the state of the art. The diagnostic technique chosen for this is the OCV methods which have been introduced in the literature review chapter. The degradation mode amounts calculated by each diagnostic techniques will be compared which will give an indication of the relative accuracy of the heat generation technique. Analysis on the identifiability of each degradation mode will also be performed for each technique to give an indication of how robust the optimisation procedure is for each technique.

4.1 Measuring cell heat generation

In this section the heat generation measurement model will be defined. This will include the rationale for the selection of model and the experimental set up used to physically replicate the model.

4.1.1 Measuring heat generation

To predict cell degradation, the total cell heat generation predicted by the theory laid out in the previous section must be compared to the experimentally measured cell heat generation. This can be done via thermal pathway model which defines the equations of heat transfer along each potential route that heat can flow from the cell and accumulate in the cell which is the chosen method for this work. The theory developed in the previous section is valid for a 0-dimensional cell, meaning the state of the cell is uniform throughout the volume of the cell. Therefore, it is important for the cell to be as uniform as possible when conducting any heat generation tests. Zhao et al. [90] show under tab cooling conditions - when the primary heat rejection pathway from the cell is the tabs – the cell is at its most uniform and closest to 0-dimensional. Because of this consideration, tab cooling is chosen as the method of cooling the cell for this chapter.

The rate of heat conduction away from the cell is given in Eq. (76). It is seen that the heat rate can be estimated by measuring the temperature difference between two points assuming that the temperature profile between the points is linear. However, for transient conduction, the temperature profile is non-linear. The rate at which a material's temperature profile approaches linear is related to the thermal diffusivity of the material, α which is calculated by Eq. (77). Figure 25 shows the transient behaviour for a material with

high thermal diffusivity and a material with a low thermal diffusivity. Cell tab materials have high thermal diffusivities which therefore makes them a good candidate for being part of the measurement path for conduction.

The final consideration is whether the thermal gradient across the tab will be large enough to be measurable with reasonably small error for the expected heat flux magnitude. This is defined as the thermal conductance of the body. The thermal conductance determines the rate of heat transfer through a body for a given temperature gradient. This means that a lower thermal conductance is beneficial to reduced measurement error as a larger temperature gradient is needed to remove a given amount of heat. Zhao et al. [91] show that the cell tabs are an area of relatively low thermal conductance. Determining the thermal conductance of cell tabs is not trivial. However, Hales et al. have already done this in their works in determining the cell cooling coefficient (CCC) for the tabs of the cell used in this study [92], [93]. Here, the CCC for positive and negative tabs will be used as the cell tab thermal conductances and their values are given in Table 8. Now the thermal gradient between cell and tab can be measured and the CCC values used to estimate the amount of heat flowing from the cell.

$$\dot{Q}_{cond} = -\frac{k\,A}{L}\frac{\partial T}{\partial x} \tag{76}$$

$$\alpha = \frac{k}{\rho\,C_p} \tag{77}$$

$$S = \frac{kA}{L} \tag{78}$$

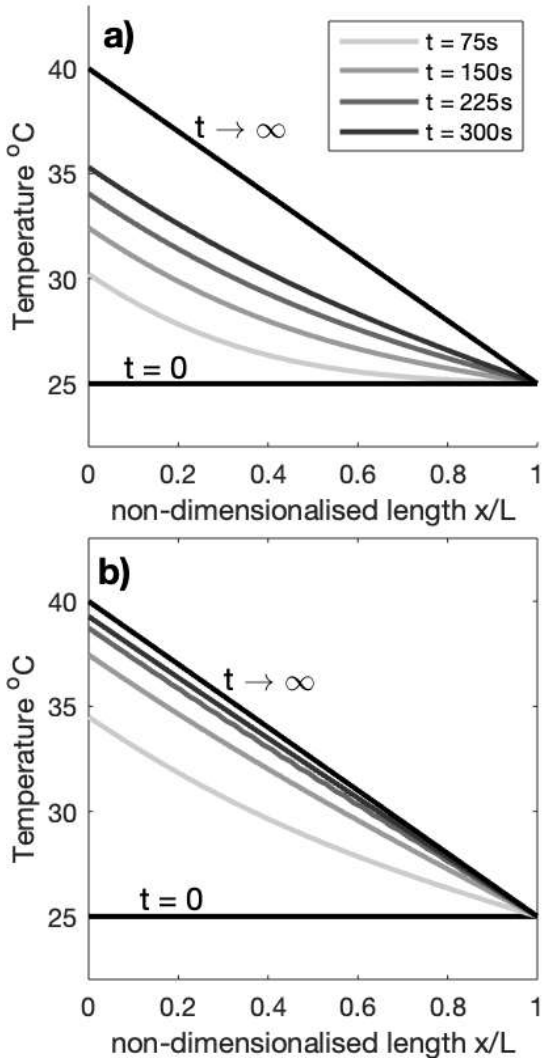

Figure 25: Transient temperature profiles for a material with a) low thermal diffusivity b) high thermal diffusivity for a constant thermal conductivity, constant heat flux at x=0 and constant temperature at x=1.

Table 8: Cell cooling coefficient (CCC) values giving heat conductance for each cell tab.

CCC_{Pos} (W/K)	0.1471

CCC_{neg} (W/K)	0.1849

With the primary heat pathway and measurement location established as the cell tabs, the heat transfer model can be defined. The thermal circuit for the system is given in Figure 26 and the equations which describe the heat flows are given in Eqs. (79) - (83). The thermal resistance of the cell tabs is equal to the reciprocal of the thermal conductance. As the cell is assumed to be at a uniform temperature, the cell acts as a simple thermal capacitor and is not discretised. The heat flowing through all other thermal pathways is grouped through a thermal resistance R_{loss} which represents the total resistance to heat travelling through the surfaces of the cell that aren't the tabs. R_{loss} is measured by setting the cell tabs to a temperature different to ambient temperature and measuring the heat transfer through the tabs. This heat transfer must be equal to the heat that is entering through R_{loss} and the temperature difference between cell and ambient can be used to calculate R_{loss}. Characterisation of R_{loss} is dependent on the experimental set up and details of how to do this are given in a later section.

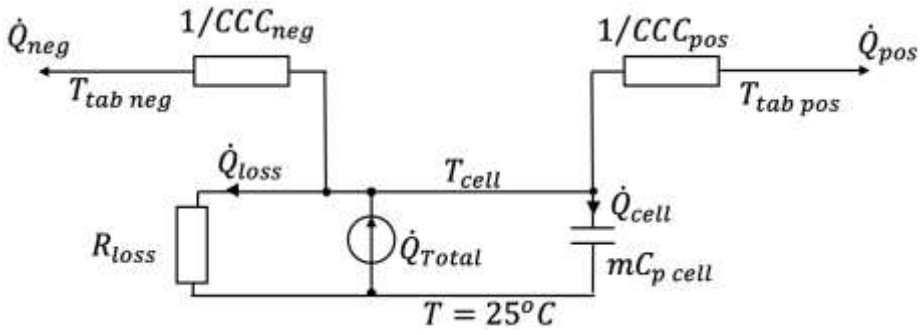

Figure 26: Thermal equivalent circuit of heat generation measurement set up

$$q_{Total} = q_{neg} + q_{pos} + q_{loss} + q_{cell} \quad (79)$$

$$q_{neg} = CCC_{neg} * (T_{cell} - T_{tab}) \quad (80)$$

$$q_{pos} = CCC_{pos} * (T_{cell} - T_{tab}) \quad (81)$$

$$q_{loss} = \frac{T_{cell} - T_{amb}}{R_{loss}} \quad (82)$$

$$q_{cell} = mC_{p\,cell} \frac{dT_{cell}}{dt} \quad (83)$$

All temperatures from Eqs. (79) - (83) are easily measured and so the heat fluxes through the heat paths are easily calculated. The heat capacitance of the cell is the product of its mass and heat capacity, the latter was measured previously by calorimetry. In this model, it is assumed that R_{loss} is a constant value. In reality R_{loss} is related to the convective heat transfer coefficient which is a function of surface temperature and fluid temperature. Therefore, R_{loss} is not constant in reality, however, steps are taken to ensure R_{loss} is maximised so that the constant R_{loss} assumption is sufficient to still give accurate results.

4.1.2 Physical set up to replicate model

The measurement of heat generation requires a thermal gradient between cell and tabs. To do this, the cell tabs are clamped to brass busbars whose temperature at the ends away from the cell are controlled by Peltier elements and maintained at ambient temperature. To maximise the value of R_{loss}, the top and bottom surfaces of the cell are insulated. A schematic of the setup is given in Figure 27. The temperature of the cell is measured at 3

points along the top surface of the cell and the average of these temperatures is taken as the cell temperature for use in Eqs. (80) - (82). All surfaces are insulated from the surroundings using insulating foam material. When calculating the heat transfer from the cell, the centre temperature of the cell and tab temperature is used as this is how Hales et al. define the CCC in [93]. Tab temperature is measured as close to the cell side of the tab as possible to allow maximum contact area between the clamps and cell tab so that heating due to the contact resistance between tab and clamp can be neglected. All temperatures are measured using K-type thermocouples and logged using a Pico Technology TC-08 unit.

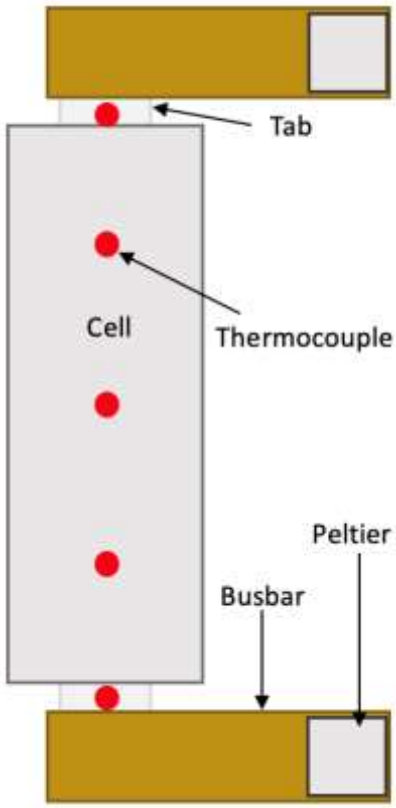

Figure 27: Heat generation measurement experimental set up

At the beginning of the test, the rig is allowed to thermally soak at the ambient temperature of 25^{o}C for 8 hours, after which it is assumed that the system is in thermal equilibrium. With the system at the same temperature, offsets between thermocouples are calculated by

averaging each thermocouple's readings and subtracting from the average temperature read by all thermocouples. After the thermal soak period, a characterisation period begins where the Peltier elements cool the ends of the busbars to 15°C and the system is allowed to reach steady-state over 8 hours. This steady-state characterisation period is then used to calculate R_{loss} from the thermal equivalent circuit in Figure 26. R_{loss} is calculated by measuring the thermal gradient between cell and ambient and dividing by the total heat flow out of the cell through the tabs as given in Eq. (84). The Peltier elements then heat the busbars to ambient temperature and the rig thermally soaks for a further 8 hours before testing begins.

$$R_{loss} = \frac{T_{cell\ avg} - T_{amb}}{q_{pos} + q_{neg}} \tag{84}$$

4.1.3 Cell selection

The cell used for this study is the Kokam 5Ah cell, a summary of the key data is given in Table 9. The chemistry of the cell is an NMC positive electrode and a graphite negative electrode. The reasons for the selection of this cell are as follows:

- A large tab area allows for ease of thermocouple placement and busbar clamping, minimising the heat generation by contact resistance at the tabs.
- Rate capable; minimises the effects of concentration and thermal gradients meaning the cell is as close to 0-dimensional as possible
- Operating currents; allows a wide range of C-rates to be tested

Table 9: Key data values for Kokam 5Ah cell

Description	Value
Nominal capacity	5Ah
Voltage range	2.7V – 4.2V
Maximum continuous discharge rate	30C – 150A
Maximum continuous charge rate	2C – 10A

The positive electrode of the cell is a compound electrode of NMC and LCO particles. However, the individual components of these electrodes are not generally available; the NMC stoichiometry is unknown. Therefore, despite the electrode having a compound chemistry, the electrode will be treated as a single component.

4.1.4 Quantifying measurement uncertainty

The heat generation is measured using thermocouples which have errors in their measurements. In this section an error analysis to understand the propagation of the thermocouple measurement error to the total measured heat generation is performed. The immediate goal of this section is to assess the relative magnitude of the errors in heat generation to the measured value of the heat generation and with this information a decision is to be made on whether these errors are to be accounted for in the model and diagnostic algorithm as a whole.

The measured temperature reading from sensor j at timestep i can be described by Eq. (85). Here, T_{true} is the true temperature at the measurement location, β is the bias in the measurement which is assumed to be constant for a given sensor, and w is the random

noise in the sensor which is sampled from random variable W which is assumed to follow a normal distribution with zero mean and standard deviation σ_w as described in Eq. (86). The bias, β, is also assumed to be sampled from a random variable B which has zero mean and standard deviation σ_β as described in Eq. (87).

$$T_{meas,i,j} = T_{true,i} + \beta_j + w_i \tag{85}$$

$$W \sim N(0, \sigma_w^2) \tag{86}$$

$$\mathrm{B} \sim N\left(0, \sigma_\beta^2\right) \tag{87}$$

It is assumed that the biases can be neglected if the thermocouples are calibrated against each other at the beginning of the test. The method to do this is outlined in section 4.1.2. This only leaves the noise component in the measurement to be estimated. To calculate σ_w the measured temperature is sampled at a constant true temperature for a large number of samples. If the true temperature is constant, and the bias is constant then any variation in the measured temperature must be a result of the random sensor noise. This means the sample variance for the measured temperature in this case is equal to the sample variance of the random noise term. For a large number of samples, the law of large numbers dictates that the sample variance will approach the population variance. These two facts are described in Eq. (88) & Eq. (89).

$$\sigma_w^2 = \sigma_T^2|_{T_{true}=const} \approx s_T^2 = \frac{1}{N-1}\sum_{i=1}^{N}\left(T_i - \mu_T|_{T_{true}=const}\right)^2 \tag{88}$$

$$\mu_T|_{T_{true}=const} \approx \bar{T} = \frac{1}{N}\sum_{i=1}^{N} T_i \tag{89}$$

To obtain the variance of the random noise, σ_w, the readings from a thermocouple are taken for the system in a thermal chamber at 25°C. There is an oscillation in the thermal

chamber over a long period of time due to the controller of the thermal chamber not holding temperature steady. This can be seen in Figure 28. To remove this oscillation a high pass filter is applied to the signal with gain of 1 and a corner frequency of 0.01 Hz which is 2 decades below the sample period of 1 Hz. This achieves the filtered signal shown in Figure 29. From this data, the sample variance and hence σ_w is equal to 0.0059°C.

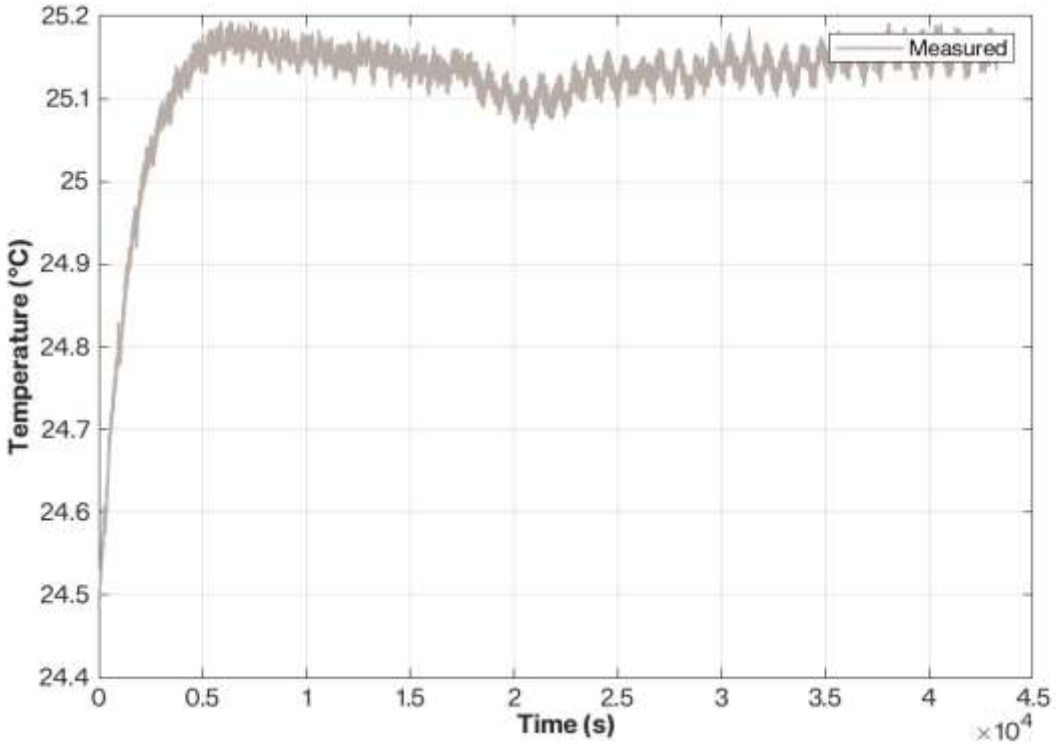

Figure 28: Original signal showing the oscillations in the measured temperature as well as a period of original temperature adjustment and thermal soak.

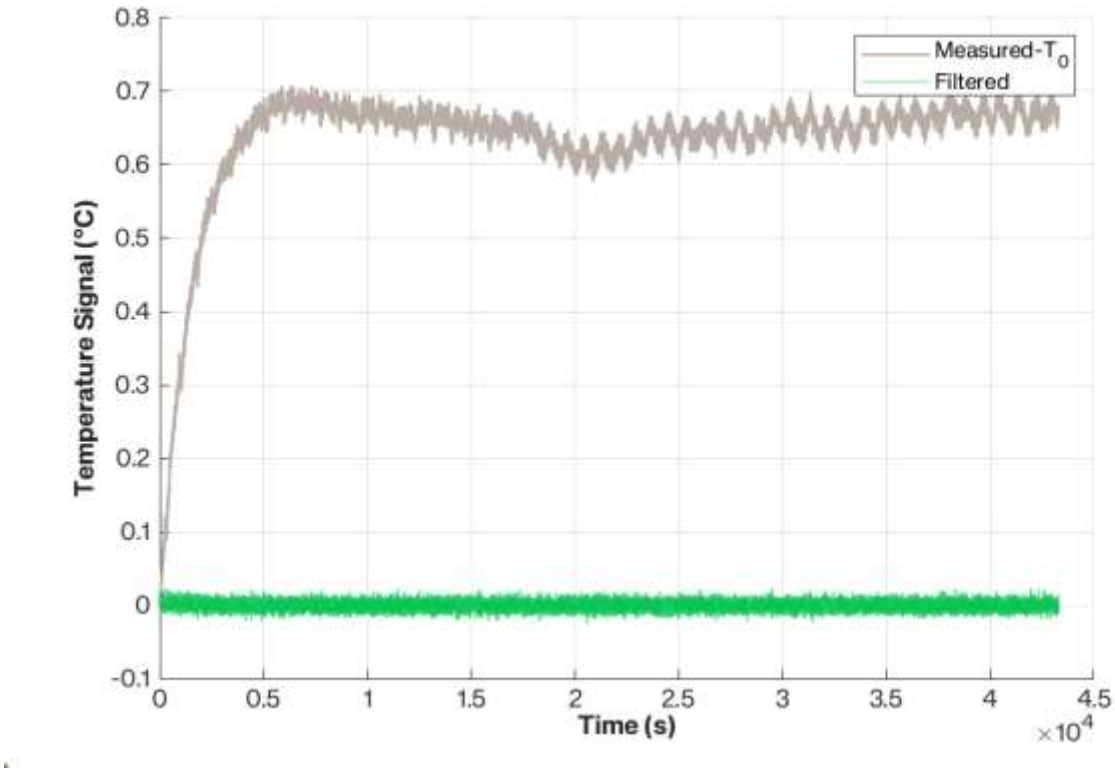

Figure 29: The normalised measured signal and the filtered signal with only the noise component remaining.

With a value for the standard deviation of the thermocouple noise calculated, values for corresponding standard deviation for the measurement of heat generation can be calculated. The overall heat generation can be calculated by Eqs. (79)-(83). The value for T_{cell} is taken as the average of three thermocouples and so the variance of the value for T_{cell} is given by Eq. (90). The variance operator is then be applied to Eqs. (79)-(83). to obtain the expressions for the variance of each of the heat generation components which are given in Eqs. (80) - (83). The derivative term is approximated as the difference between subsequent temperature measurements and then divided by the time step and its variance is expressed. This can then be summed to obtain the total heat generation variance which is given in Eq. (95).

$$Var(T_{cell}) = \frac{\sigma_w^2}{3} \tag{90}$$

$$Var(q_{neg}) = \frac{4}{3} CCC_{neg}^2 \ \sigma_w^2 \tag{91}$$

$$Var(q_{pos}) = \frac{4}{3} CCC_{pos}^2 \ \sigma_w^2 \tag{92}$$

$$Var(q_{loss}) = \frac{1}{3} \frac{\sigma_w^2}{R_{loss}^2} \tag{93}$$

$$Var(q_{cell}) = \frac{2}{3} \left(\frac{mC_p}{\Delta t}\right)^2 \sigma_w^2 \tag{94}$$

$$Var(q_{Total}) = \frac{4}{3} \sigma_w^2 \left(CCC_{neg}^2 + CCC_{pos}^2 + \frac{1}{2} \left(\frac{mC_p}{\Delta t}\right)^2 + \frac{1}{4 R_{loss}^2} \right) \tag{95}$$

The values for the constants given in Eq. (95) and hence the value for the variance and standard deviation of the heat generation measurements are given in Table 10. The value of the standard deviation is significant in the case, it is bigger than 1 order of magnitude smaller than the signal meaning there is a significant signal to noise ratio. To alleviate some of this, the signal is filtered using a Savitzky-Golay filter is used to smooth the signal [94].

Table 10: Values for the constants used to calculate the standard deviation of the heat generation as well as the calculated values for the heat generation.

Description	Value
σ_w	0.00590 °C

CCC_{neg}	0.185 W/K
CCC_{pos}	0.147 W/K
mCp	127 J/kg
Δt	1.00 s
R_{loss}	33.0 K/W
$Var(q_{total}) = \sigma_Q^2$	0.374 W^2
σ_Q	0.612 W

The Savitzky-Golay filter also has the benefit of being able to calculate the derivative of the signal it is smoothing and so the numerical difference derivative outlined here does not need to be used. While filtering the signal does not add any information content to the heat generation, it may make it easier for the optimisation to find a global minimum. As pointed out by Shmid et al. [95] an advantage of the Savitzky-Golay filter is that it can conserve peaks in spectra better than other filters whilst having similar noise suppression to other filters. This is beneficial for this work as the features in the spectra will be key for ensuring robust optimisation.

While the noise of the measurements are not used to calculate any error in the estimated parameters for the signal in this work, it would be an interesting and important piece of future work to see how the measurement error impacts the uncertainty of the estimated degradation mode amounts. By incorporating the noise into measurements, Bayesian optimisation techniques can be used which automatically give an uncertainty to the states or parameters that are being estimated. This is a common approach throughout the

literature and details of implementing such techniques can be found in a widely adopted textbook by Sarkka [96].

4.2 Benchmark technique – OCV model

To evaluate the performance of the diagnostic method, it must be compared to an already established benchmark. An established and reliable benchmark is the OCV based technique which predicts stoichiometric parameters - cell capacity and offset – from the OCV of the cell at different points in its life as shown in [73], [79]. To measure the OCV, the cell undergoes a C/25 constant current discharge which is considered a pseudo OCV test in [79]. The ambient temperature for the OCV tests are 25°C. The technique aims to generate a modelled OCV curve from stoichiometric parameters, as described earlier in this thesis. The optimisation minimises the objective function which is the sum of the squared differences between the measured and modelled OCV. In this work, the OCV model is implemented with the same optimisation framework as the heat generation model but for an objective function which only considers cell OCV. This objective function, $f(\vec{x})_{OCV}$, is given in Eq. (*96*). The lithiation fractions produced by this optimisation are then used to calculate the stoichiometric parameters of the cell. The stoichiometric parameters yielded from the OCV diagnostic technique, and the heat generation diagnostic technique can then be compared.

$$f_{OCV}(\vec{x}) = \sum_i (U_{meas_i} - U_{mod}(\vec{x}, SOC_i) \tag{96}$$

4.3 Obtaining half-cell measurements

4.3.1 Creating Half-cells

To apply the heat generation and OCV models described in this thesis, OCV and entropic coefficients of the individual electrodes must be known. To achieve this, coin cells of the electrodes are made so the OCV and entropic coefficients versus lithiation fraction can be measured. The cells used in the test are 5Ah Kokam pouch cells with an NMC-LCO blend cathode and a graphite anode. Electrodes were harvested from the pouch cells by removing the pouch bag from the commercial cell and removing the layers of electrodes in an argon-filled glovebox, the electrode layer configuration is shown in Figure 30. As the electrode layers are double-sided, one side of the electrode was removed using NMP solvent. Top and bottom electrodes in the electrode stack are single-sided cathodes which already have exposed current collectors on one side and so do not require cleaning with NMP. Electrodes are then cut into discs and washed in DMC solvent to remove any excess NMP and are then dried in an antechamber vacuum oven at 50^{o}C for 1 hour.

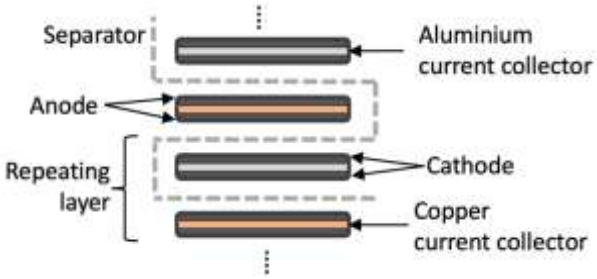

Figure 30: Schematic of Kokam pouch cell electrode stack configuration

Coin cells half-cells are made from the cut, washed and dried electrodes; a schematic of the coin cell construction is shown in Figure 31. A spring and spacer are placed in the negative can and then a disc of lithium placed on top. The lithium disc is scraped with a metal spatula

before being put into the coin cell to ensure the disc is clean and 3 drops of electrolyte are pipetted onto the lithium disc. The electrolyte used in the coin cells is 50:50 EC: DMC solvent with $LiPF_6$ salt. A glass fibre separator is then placed on top of the lithium disc and excess electrolyte is added to completely saturate the separator. The electrodes discs harvested from the commercial cell are then placed on the separator and the positive coin casing placed on top of the assembly. The assembly is then crimped, and excess electrolyte cleaned from the crimped cell.

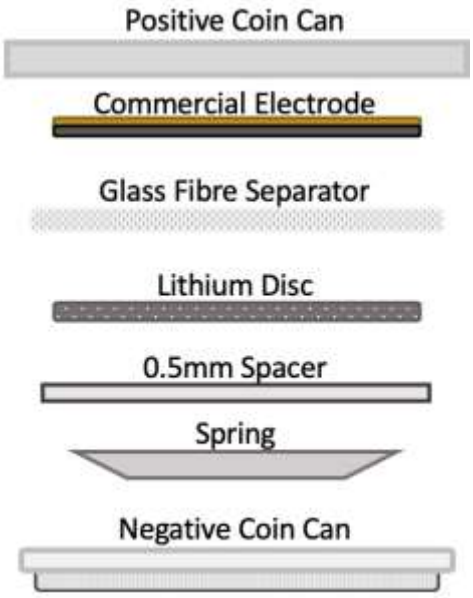

Figure 31: Schematic of the coin cell component layout

4.3.2 Coin cell Testing for OCV and Entropy vs SOC

The coin cells undergo a testing regime which consists of 5 formation cycles, slow rate cyclic voltammetry (SRCV) sweeps for positive and negative scan rates to obtain OCVs and finally a potentiometric entropy test. The exact protocols for each test are detailed in Table 11. The formation cycles were performed with a 200 μA constant current charge and discharge corresponding to a C-rate of approximately C/10. After 5 formation cycles, the half-cells were all stable with repeatable voltage curves and similar capacities between charges and

discharges. The scan rates chosen for the SRCV measurements correspond to a sweep time of approximately 40 hours and is deemed slow enough to collect OCV data from.

The potentiometric entropy test was performed by measuring the voltage response to a step temperature change over 5 temperature levels as is common in literature [97], [98]. The applied temperature profile is shown in Figure 32. Each temperature has a soak period of 30 minutes with a 3-hour OCV relaxation phase before the temperature steps are applied. The cell is discharged by 5% SOC and the process is repeated. The cells are tested using a Biologic VMP-300 potentiostat and cell ambient temperature was controlled using a Binder KB23 environmental chamber.

Table 11: Coin cell test protocols

Electrode	Formation Protocol	SRCV Protocol	Potentiometric Entropy Protocol
Cathode	**1.** CC Charge @ 0.2 mA (C/10) to 4.3V **2.** CC Discharge @ 0.2 mA to 3V **3.** Repeat 4 times	**1.** CC charge to 4.3V **2.** CV hold at 4.3V until current < 40 μA **3.** SRCV scan from 4.3V to 3V at -33 mV/h **4.** SRCV scan from 3V to 4.3V at +33mV/h	**1.** CC charge to 4.3V **2.** CV hold at 4.3V until current < 40 μA **3.** 3h rest for OCV relax **4.** Adjust temperature to 15^{o}C and rest for 30m **5.** Increase temperature by 5^{o}C and rest 30m **6.** repeat step 5 three more times **7.** CC discharge at 0.1mA (C/20) for 1h (5% SOC) **8.** Repeat steps 3 – 7 until cell voltage reaches 3V

Anode	**1.** CC Charge @ 0.2 mA (C/10) to 1.5V **2.** CC Discharge @ 0.2 mA to 10 mV **3.** Repeat 4 times	**1.** CC charge to 1.5V **2.** CV hold at 1.5V until current < 40 μA **3.** SRCV scan from 1.5V to 10 mV at -38 mV/h **4.** SRCV scan from 10 mV to 1.5V at +38mV/h	**1.** CC charge to 1.5V **2.** CV hold at 1.5V until current < 40 μA **3.** 3h rest for OCV relax **4.** Adjust temperature to 15°C and rest for 30m **5.** Increase temperature by 5°C and rest 30m **6.** repeat step 5 three more times **7.** CC discharge at 0.1 mA (C/20) for 1h (5% SOC) **8.** Repeat steps 3 – 7 until the cell voltage reaches 10 mV

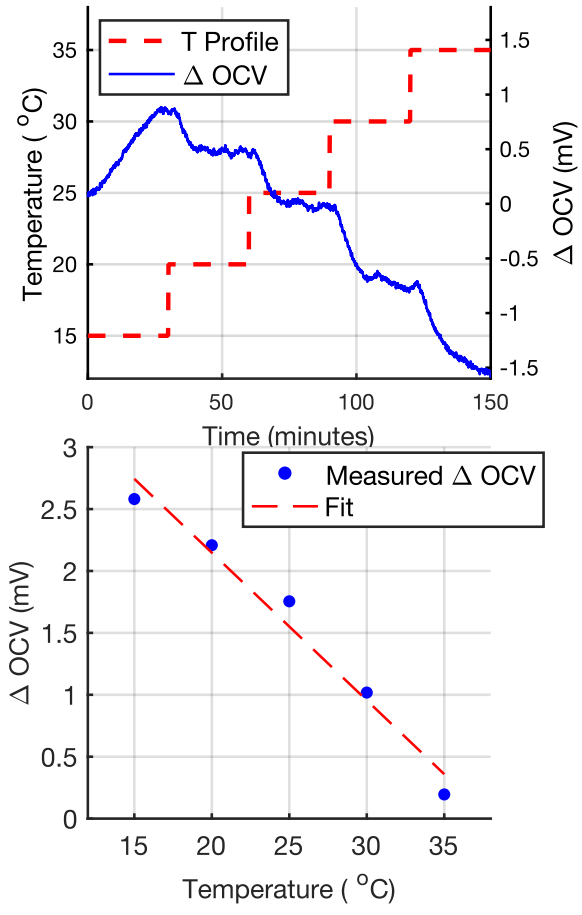

Figure 32: Temperature profile and recorded ΔOCV (top) and fitted steady ΔOCV vs Temperature fit (bottom)

The OCV and entropic profile are collected from the SRCV and potentiometric entropy tests respectively. The OCV curve is obtained by integrating the SRCV profile, charge for the positive scan rate and discharge for the negative scan rate. The integrated profile gives the charge versus voltage profile which can then be normalised by the cell's capacity to give lithiation fraction. The voltage limits and corresponding assumed lithiation fractions are given in Table 12. The entropic coefficients are obtained by plotting the measured OCV versus temperature for the temperature steps at a given SOC point. The gradient of the line of best fit through these points is taken to be the entropic coefficient at that lithiation fraction. This process is repeated for each SOC point that the temperature profile was applied at. An example voltage response versus applied temperature is given in Figure 32 to demonstrate how the entropic coefficient is calculated.

Table 12: Corresponding voltages to upper and lower voltages to electrode lithiation fractions

Electrode	Upper Voltage (x = 0)	Lower Voltage (x = 1)
NMC - LCO	4.3 V	3 V
Graphite	1.5 V	10 mV

4.4 Experiment to compare diagnostic technique performance

4.4.1 Overall Experimental Procedure

The overall experimental procedure is given in Table 13. First the pseudo OCV test is performed with a C/20 discharge. Following this, the heat generation experiments are performed for both charging and discharging. The C-rates for heat generation are 0.5C, 1C and 2C. The profile is a constant current charge across the entire SoC range of the cell until the voltage limit is reached, 4.2V on charge, 2.7V on discharge. A CV hold is applied at these voltages to ensure the cell is always starting from the same SoC. Following each charge / discharge, the cell is allowed to thermally equilibrate for 3 hours before the next C-rate test is performed. Throughout the entire test, the Peltier elements maintain busbar end temperatures at ambient. The cell is cycled using a Maccor battery cycler and the rig is placed in a Binder KB-400 environmental chamber to maintain an ambient temperature of 25°C.

Table 13: Overall test procedure

Step Description	**Control**	**End Criteria**
1. Initial charge to 100% SOC	CC Charge 5A CV Hold 4.2V	E_{Cell} > 4.2V $\|I\| < 100$ mA
2. Thermal Soak	Rest	Time > 3h
3. pseudo-OCV	CC Discharge 250mA	E_{Cell} < 2.7V
4. charge to 100% SoC	CC Charge 5A CV Hold 4.2V	E_{Cell} > 4.2V $\|I\| < 100$ mA
5. Thermal Soak	Rest	Time > 3h
6. Heat Generation Discharge	CC Discharge xA CV Hold 2.7V	E_{Cell} < 2.7V $\|I\| < 100$ mA
7. Thermal Soak	Rest	Time > 3h
8. Heat Generation Charge	CC Charge xA CV Hold 4.2V	E_{Cell} > 4.2V $\|I\| < 100$ mA

9. Repeat steps 5 - 8 for x = 2.5, 5, 10	-	-

4.5 Performance of techniques on a fresh cell

4.5.1 OCV & Heat Generation Fits

Both techniques are first evaluated for their quality of fits. The techniques use the same optimisation procedure with the same constraints. The constraints applied in this round of optimisations are that the capacity of each electrode must be positive. The optimisation algorithm used to estimate the beginning and end lithiation fractions for each of the datasets is a genetic algorithm. A genetic algorithm is used as it can find the global minimum of an objective function. Finding the global minimum would be difficult for traditional gradient based methods as it is expected that the optimisation space is highly non-convex. This means the methods could be easily trapped in the local minima and so would be highly dependent on the initial point used in the optimisation routine. However, while a genetic algorithm can find the global minimum of a function, this doesn't mean it will every time the algorithm is run; they can often give non-repeatable results due to their random nature. Despite this, the genetic algorithm is chosen as the optimisation algorithm to produce the fits in this section.

OCV model fit and stoichiometric parameters

The first fit to be examined is the OCV method. The optimisation routine follows the same as is laid out in the theory section for the heat generation technique. The only constraints relevant at beginning of life are that the electrode capacities must be greater than 0 and

lithiation fractions are bounded between 0 & 1. A resulting fit from the genetic algorithm is given in Figure 33. The figure shows that the modelled OCV fits the measured very well – the objective function score is very low and so it is safe to assume this fit is at least close to the global minimum of the parameter search space. From this fit alone, it would appear that the optimisation procedure has found the correct parameters. This can be said because the fit seems to capture the detailed features of the OCV curve. The calculated stoichiometric parameters are given in Table 14. All of these parameters seem reasonable; the positive and negative capacities are in the expected region and lithium inventory seems feasible. Overall, this fit and the parameters seem to be to a good standard.

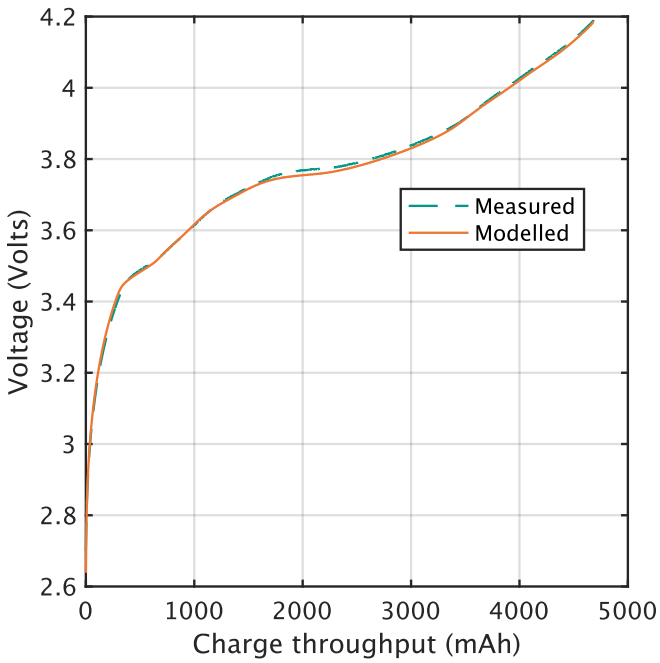

Figure 33: Fitting of modelled OCV against measured OCV. A very good fit is achieved using the genetic algorithm optimisation of the start and end lithiations for each half cell OCV

Table 14: Stoichiometric parameter values calculated from the OCV model's fit to measured data

Parameter	Value (mAh)
Negative electrode capacity, C_{NE}	5,917
Positive electrode capacity, C_{PE}	5,347
Lithium inventory, Q_{Li}	4,694
Measured charge transfer, dQ	4,682

So far, the OCV method seems to give good predictability for the stoichiometric parameters. However, the above is a cherry-picked example of the OCV fit which gives a good fit and good stoichiometric parameters. Figure 34 shows another common output of the optimisation routine where the fit is not as good – but is still an acceptable fit – and the resulting stoichiometric parameters are given in Table 15. The objective function scores in both cases are similar, but there are huge differences in the calculated stoichiometric parameters. The stoichiometric parameters in this case are less plausible than those given in the previous iteration. The positive electrode capacity seems too low, and the negative electrode capacity seems too high. However, the optimisation routine doesn't know this and will return any values which give low objective function scores.

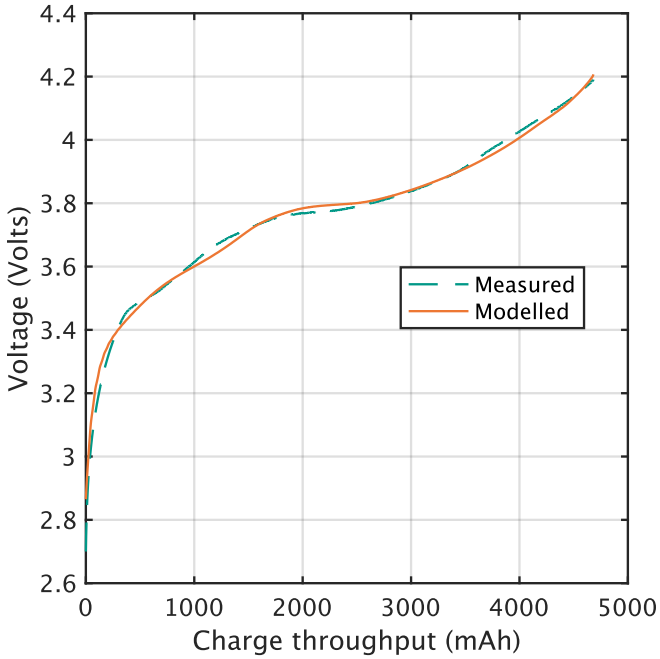

Figure 34: Fitting of modelled OCV against measured OCV after a more typical optimisation run. The fit is still good and would not be deemed as unacceptable but is not quite as good as Figure 33.

Table 15: Stoichiometric parameter values calculated from the OCV model's fit to measured data for the more typical OCV fit case.

Parameter	Value (mAh)
Negative electrode capacity, C_{NE}	4,682
Positive electrode capacity, C_{PE}	10,495
Lithium inventory, Q_{Li}	10,332
Measured charge transfer, dQ	4,682

The goal of the above analysis is not to mislead the reader and nor is it to find flaws with the OCV technique so that the heat generation technique's results look more appealing. This simple observation serves as a reminder that non-convex optimisation is difficult and the results from the optimisation should not be judged on fitness alone. A good fit certainly helps – as is seen in the first fitting – but it is not the complete picture, and a more thorough analysis of technique must be done. These initial results may suggest that the parameter identifiability and robustness of this technique is not as good as the fit in Figure 33 might suggest. In fact, these results would suggest that knowing the 'correct' stoichiometric parameters for these techniques is not as simple as applying an OCV model. A similar analysis will now be performed for the heat generation technique's different cases to see what sort of variations are present in its optimisation procedure.

Heat generation model fit and stoichiometric parameters

The heat generation cases have a total of 6 different test instances; 3 charge and 3 discharge, each at different C-rates. Firstly, the fits of each will be assessed without regard to the stoichiometric parameters output. This is to discern whether the technique would stand any chance at all in providing parameters which are meaningful. If the shape is captured reasonably well, then the technique is at least capable of potentially yielding some useful information. Figure 35 shows the 3 charge cases. From top to bottom they are C/2, 1C and 2C. It can be seen in all cases, the modelled heat generation matches the measured heat generation well. There is a trough that is well captured by the model in all cases and the rest of the shape is also in agreement between measured and modelled values. The trough occurs due to the shape of the positive electrode's entropic coefficient versus state-

of-charge. The magnitudes of measured and modelled heat generation are also in good agreement for all datasets. Overall, the fits of modelled to measured heat generation for all charging datasets are close.

Figure 36 shows the 3 discharging cases. The outcome of these fits is very much the same as in the charging cases. There is a peak toward the end of the discharge that is captured well in all instances. As in the charging cases the peak is due to the entropic coefficient vs SoC in the positive electrode but flipped this time because of the opposite direction of current. Again, the magnitudes of the heat generation are captured well in all cases and overall, it can be said that the discharging heat generation model matches well with the measured heat generation. From these two figures, the heat generation model can replicate the measured heat generation with a good degree of accuracy. This means there is a chance that the stoichiometric parameters found in this analysis could be accurate and the technique may have some predictive power.

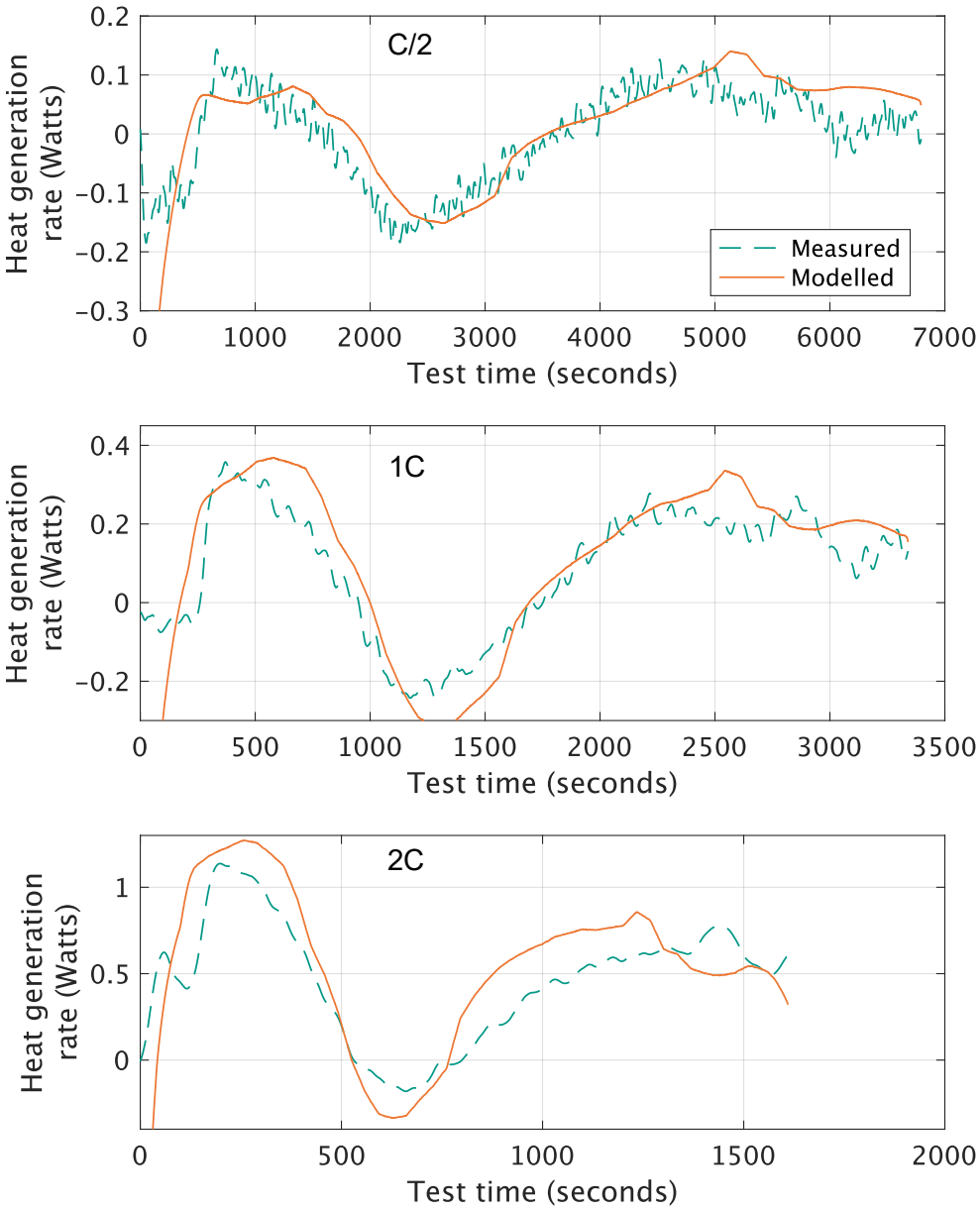

Figure 35: Modelled heat generation fits with measured heat generation for charge datasets. The shapes and magnitudes are captured well by the parameters extracted in the optimisation.

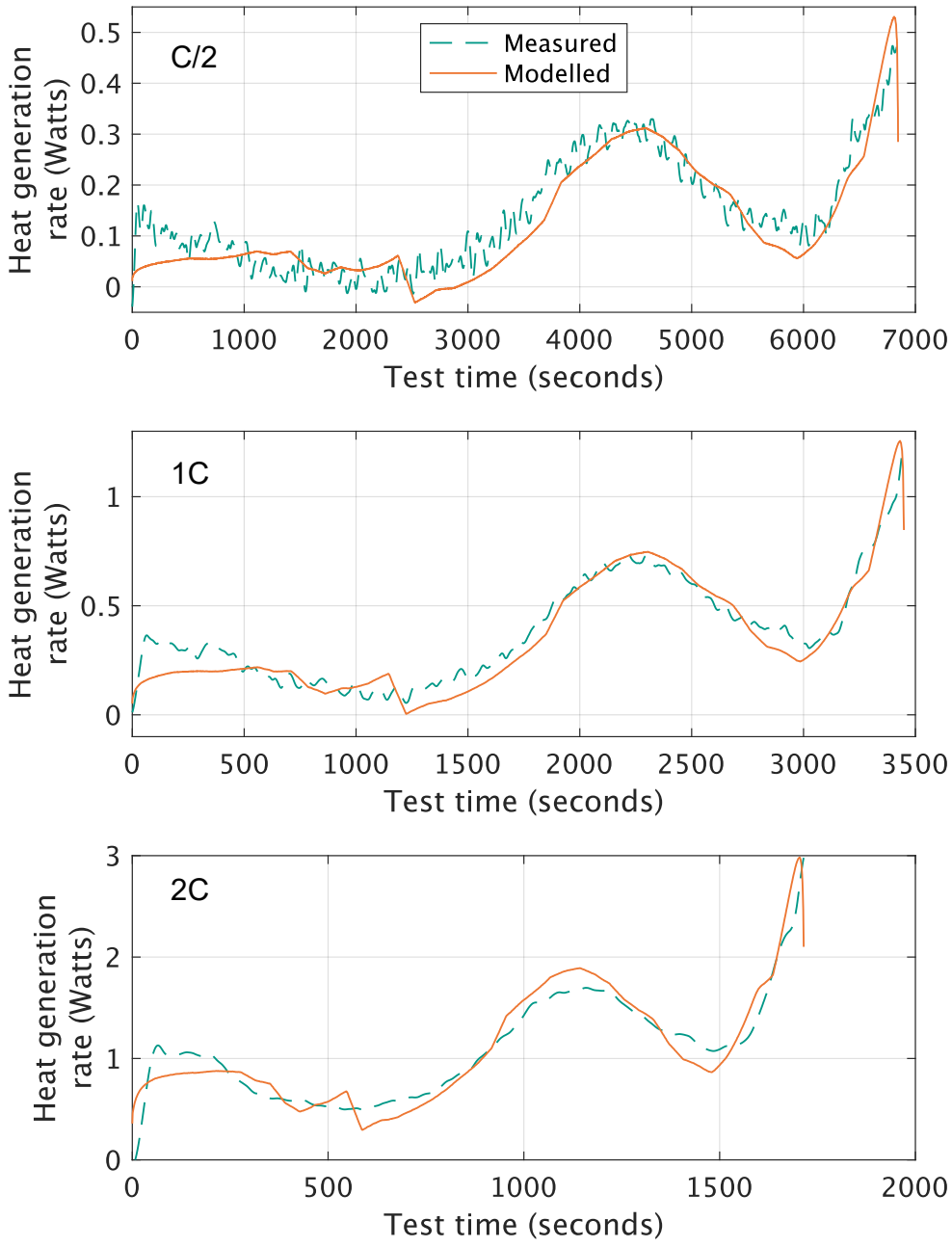

Figure 36: Modelled heat generation fits with measured heat generation for discharge datasets. The shapes and magnitudes are captured well by the parameters extracted in the optimisation.

With the fits established for the heat generation datasets, attention is now turned to the predicted stoichiometric parameters for each dataset. Figure 37 shows the stoichiometric parameters predicted by each dataset. Firstly, the positive electrode capacities are relatively

repeatable with a variation of approximately 500mAh across all datasets. The magnitudes of positive electrode capacities also look reasonable in all cases. The negative electrode capacities and lithium inventories however are much more variable, the 1C charge case in particular with wildly different predictions to the other datasets. There are however some datasets which do yield sensible results; both C/2 cases and the 2C discharge all give values which are plausible for both negative electrode capacities and lithium inventories. Overall, it seems the heat generation technique is capable of outputting stoichiometric parameters which are plausible. However, as is the case with the OCV technique, there are clearly times when the optimisation procedure finds a different set of parameters which are less feasible.

For both techniques reasonable stoichiometric parameters can be found. However, there are also clear cases when both techniques struggle to output reasonable parameters due to the non-convex optimisation space. It would be simple to now say that the heat generation technique works predominantly for low-rate cases of C/2 and for higher rate discharges 2C. This could be qualified with some hazy scientific reason and then the technique deemed as useful. However, this is probably not the case and further investigation into the optimisation process and its robustness should be done. In the next section the robustness and the parameter identifiability are explored for both the OCV and heat generation techniques. The aim of this analysis will be to qualify why the parameters are as variable as they are and to quantify some metrics relating to this.

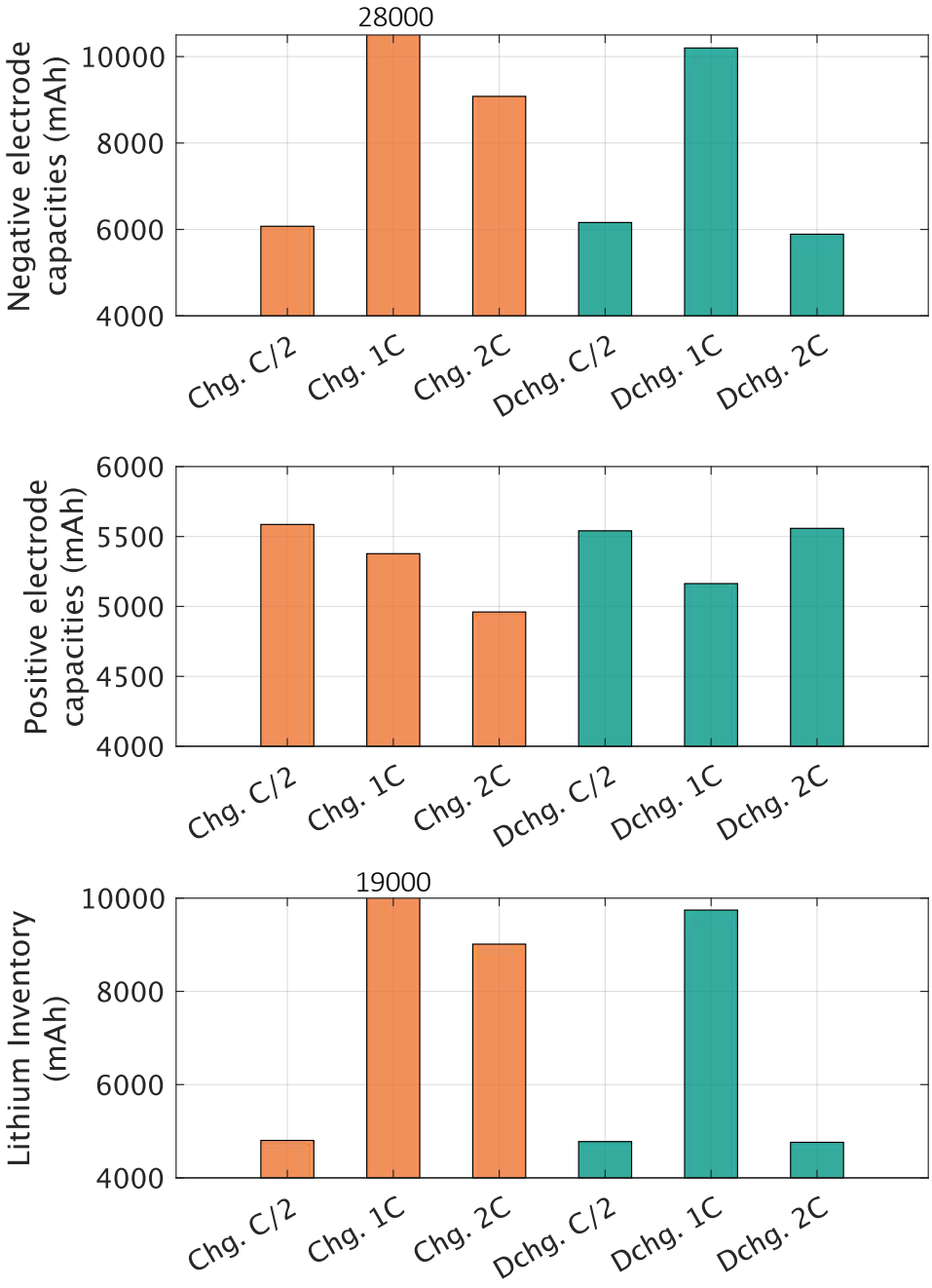

Figure 37: Stoichiometric parameters predicted by each heat generation fit. Charge in orange and discharge in teal. The positive electrode capacities are repeatable with all cases around the 5000mAh region. The negative electrode capacities and the lithium inventories contain results which vary much more, some wildly so. Despite this there are values of both which seem plausible such as both C/2 cases and the 2C discharge case.

4.6 Technique robustness and parameter identifiability

From the above analysis, there is a need to perform more in-depth analyses on the two diagnostic techniques. It is seen that both techniques are susceptible to converging on different solutions due to the likely non-convexity of the optimisation space. It is also seen

that the output for the positive electrode capacity is more stable than the negative electrode capacity and the lithium inventory. This suggests that an investigation into the parameter identifiability should be conducted to see if one parameter's value dominates the optimisation function over the others. Once both of these analyses are performed a more concrete evaluation of the diagnostic techniques' effectiveness can be made – beyond just the goodness of the fit between the measured and modelled data.

The robustness will be evaluated by performing the optimisation routine with a local optimisation method – not the genetic algorithm – and starting at many different initial conditions. The resulting stoichiometric parameters will be then plotted on a scattered bar chart to evaluate how many parameter sets can be found. The initial conditions explored will be the highest and lowest 30% of the lithiation fractions for each electrode, this is given in Eq. *(97)* for charging cases and Eq. *(98)* for discharging cases. Sample points are generated using the Latin hypercube sampling technique to give more evenly spread sample points than standard random sampling. The optimisation routine used is MATLAB's 'fmincon' function with the default algorithm and settings. The number of initial points chosen is 400. Optimisation is performed on all of these points and the objective function score is noted for each converged optimisation point.

$$x_{NE,0}, x_{PE,1} \in [0, 0.3] \quad x_{NE,1}, x_{PE,0} \in [0.7, 1] \tag{97}$$

$$x_{NE,1}, x_{PE,0} \in [0, 0.3] \quad x_{NE,0}, x_{PE,1} \in [0.7, 1] \tag{98}$$

Parameter identifiability is found by performing a sensitivity analysis on each diagnostic technique's objective function with respect to the model inputs – the lithiation fractions.

The sensitivity analysis method chosen is that of Sobol [99] with an implementation described by Saltelli [100]. Sobol's method is a method of performing a global sensitivity analyses; the sensitivity of the output for different parameters across the entire spectrum of the parameter input space. This is different to most sensitivity analyses which perform local sensitivity analyses – finding the derivative of the model with respect to each parameter at a fixed set of input parameters. The global sensitivity analysis is more applicable in this case as there is no obvious true set of parameters extractable from the techniques and so choosing a local point to perform local sensitivity analysis at is not possible.

The Sobol method find the fraction of model output variance that can be attributed to each parameter. This is achieved through a set of sensitivity indices termed the first order and total effect indices. The first order indices represent the fraction of total variance of the model accounted for by changing that variable in isolation. The total effect indices represent the variance attributed to a parameter including its interactions with changes in other parameters, not just changed in isolation. Here, the total effect indices will be used to determine which parameters are the most important in the model output and hence are the most identifiable. A full description of the Sobol method and its implementation in this work can be found in Appendix A.

Robustness of the OCV and heat generation diagnostic techniques

With the method to measure robustness established above, the analysis is applied to the OCV and heat generation techniques. Figure 38 shows a 'scatter-bar' chart for the OCV technique. In this plot a point is given to each value that the optimisation outputs for a

given set of initial parameters. The transparency of the points is calculated from the objective function score obtained for the output parameters given with a more transparent point giving a higher objective function score – the optimisation routine aims to minimise the objective function. The number of point clusters represents the number of local minima that the optimiser could find. The opacity of the points represents the likelihood that the optimisation will stay in that minimum. For example, one cluster for each parameter with very dark points means the optimisation space is likely convex, and the optimiser is likely to converge to the same parameter set every time. Conversely, many dark clusters mean the optimiser is likely to converge on any of these points which means the technique is not robust.

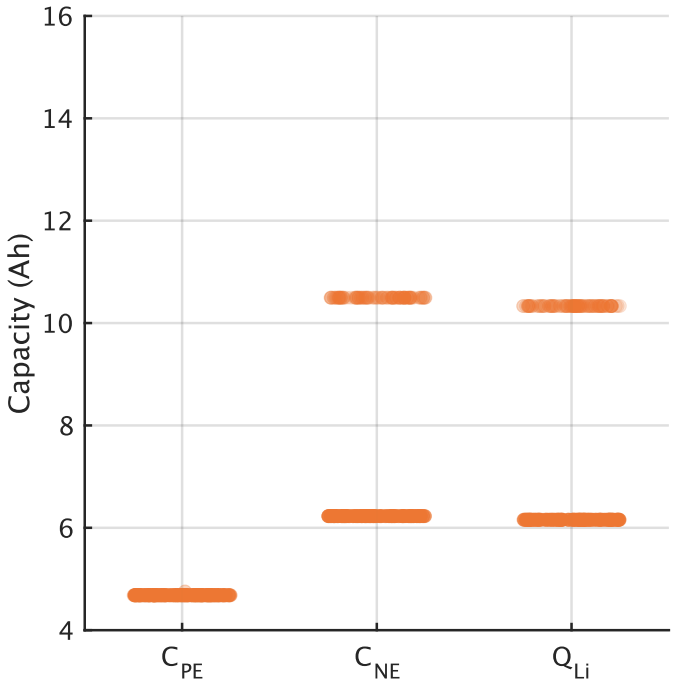

Figure 38: Scatter-bar plot of the stoichiometric parameters predicted by the OCV technique for 400 sampled optimisation starting parameters. The opacity of each point is related to the objective function score, a more opaque point is a better fit. The number of clusters is related to the potential convergence parameters for the optimisation routine.

The results in Figure 38 show that the positive electrode capacity prediction is robust, the value of the cluster is 4.7Ah. This agrees with one of the earlier results but does not include the 5.3Ah value found in the first 'best fit' case. This shows that the convergence point is difficult to find for the optimisation routine used here. Generally, though, the positive electrode capacity parameter seems to be robust. The negative electrode capacity and the lithium inventory however are different stories – both have 2 opaque clusters at differing values. This means that the optimisation routine is likely to converge on either of these points during the technique's use. Therefore, it can be said that the technique is robust to the positive electrode capacity prediction but is less robust for the negative electrode capacity. It is important to be aware that this analysis doesn't provide any information on the accuracy of the outputs of the technique, just the robustness of its output.

Attention is now turned to the heat generation cases. Figure 39 is the scatter-bar plot for the heat generation charging cases at the C-rates indicated. Immediately it is seen that the C/2 case has one very strong minimum at around 11 Ah for positive electrode capacity and lithium inventory. The y-axis of this plot has been truncated but the corresponding point for negative electrode capacity is >20 Ah. While this is a strong minimum point, there are a large number of convergence points around 5 Ah for the positive electrode. This means that the global optimisation routine could feasibly converge at this point but it could also get stuck at the stronger minimum at 11 Ah. There are very weak points for the negative electrode capacity and the lithium inventory which show that the parameter outputs for this dataset are not robust. There is a very similar story at the 1C charging case with slightly stronger optimums around 5Ah for the positive electrode capacity and still weak optimums for the negative electrode capacity. Overall, for C/2 and 1C the negative electrode capacity

and lithium inventory are not robust and the positive electrode capacity is semi robust at best.

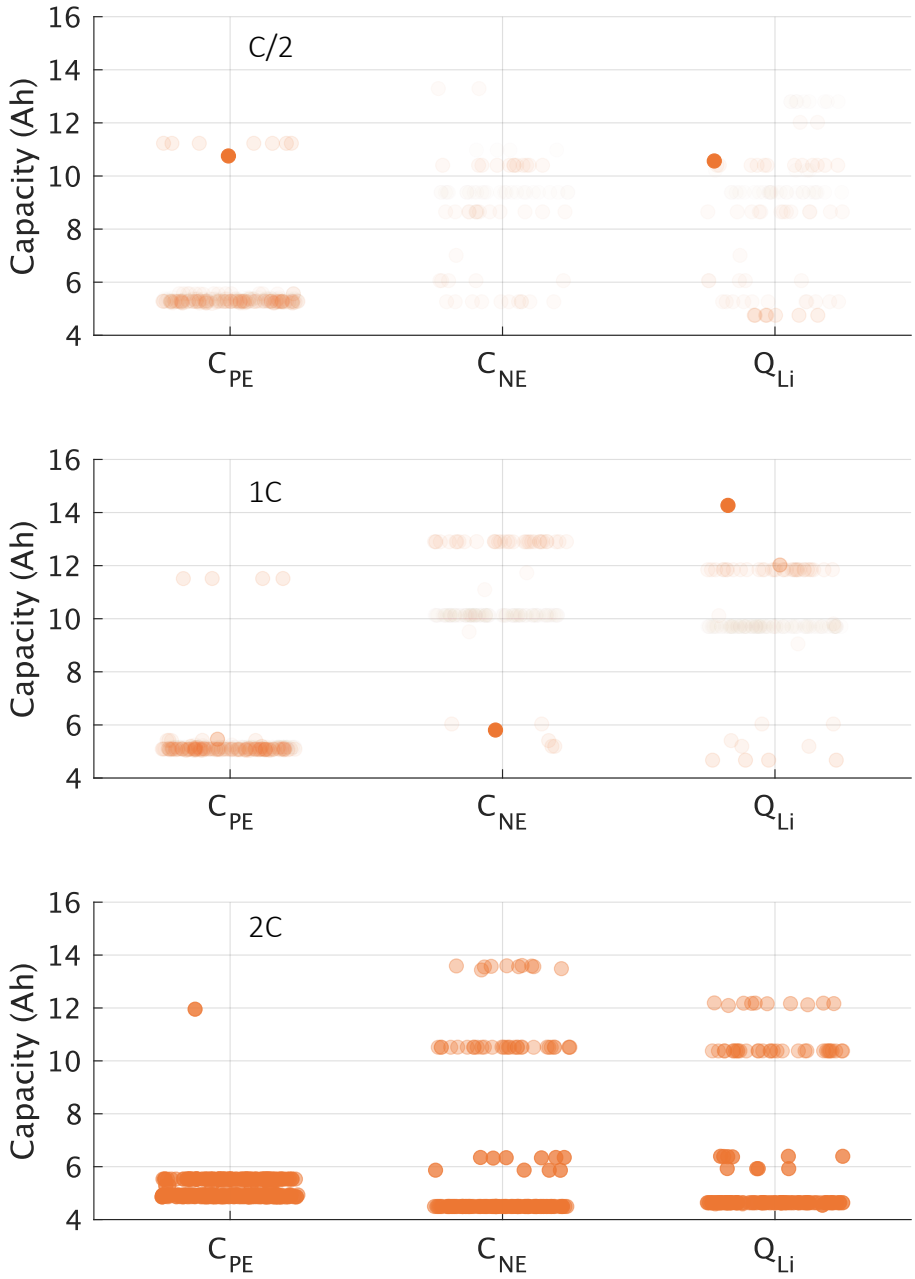

Figure 39: Scatter bar plot of the stoichiometric parameters predicted by the heat generation technique under charging at different C-rates (indicated) for 400 different optimisation starting points. The opacity of each point is related to the objective function score, a more opaque point is a better fit. The number of clusters is related to the potential convergence parameters for the optimisation routine.

The 2C charging case given in Figure 39 is more promising than the C/2 and 1C case as there are stronger minimums at reasonable values. The positive electrode capacity has most of the minimums around 5 Ah with one outlier at 12 Ah. It is reasonable to assume the optimisation will give a positive electrode capacity of 5 Ah in most cases and so is robust. The negative electrode capacity and lithium inventory are still not robust with 4 possible clusters of points. Overall, at 2C charging, the robustness of the positive electrode capacity is strong.

The scatter-bar plots for the heat generation discharge cases are given in Figure 40. The positive electrode capacity for all rate cases seems to be quite robust with strong minimums occurring around the 5Ah level. The positive electrode capacity estimate seem to be robust across all three C-rate cases giving the same region of estimate both within each dataset – dark clusters at one value – and also between datasets – the same value for all dark clusters in the datasets. The negative electrode capacity and lithium inventory have results which are not robust. The C/2 and 1C cases are very weak and the optimisation process would not consistently find the same minimum point. The 2C case, whilst still not particularly robust is much better than the C/2 and 1C cases with most of the points at the 7 Ah and 5.5 Ah levels for negative electrode capacity and lithium inventory. There are a few outlier points which lie at higher capacities, but it is more likely that the optimiser would converge on the values around 7 Ah. Again, it is important to note that this analysis does not give an indication of accuracy of technique, only an indication of how likely the optimiser is to converge on a consistent result.

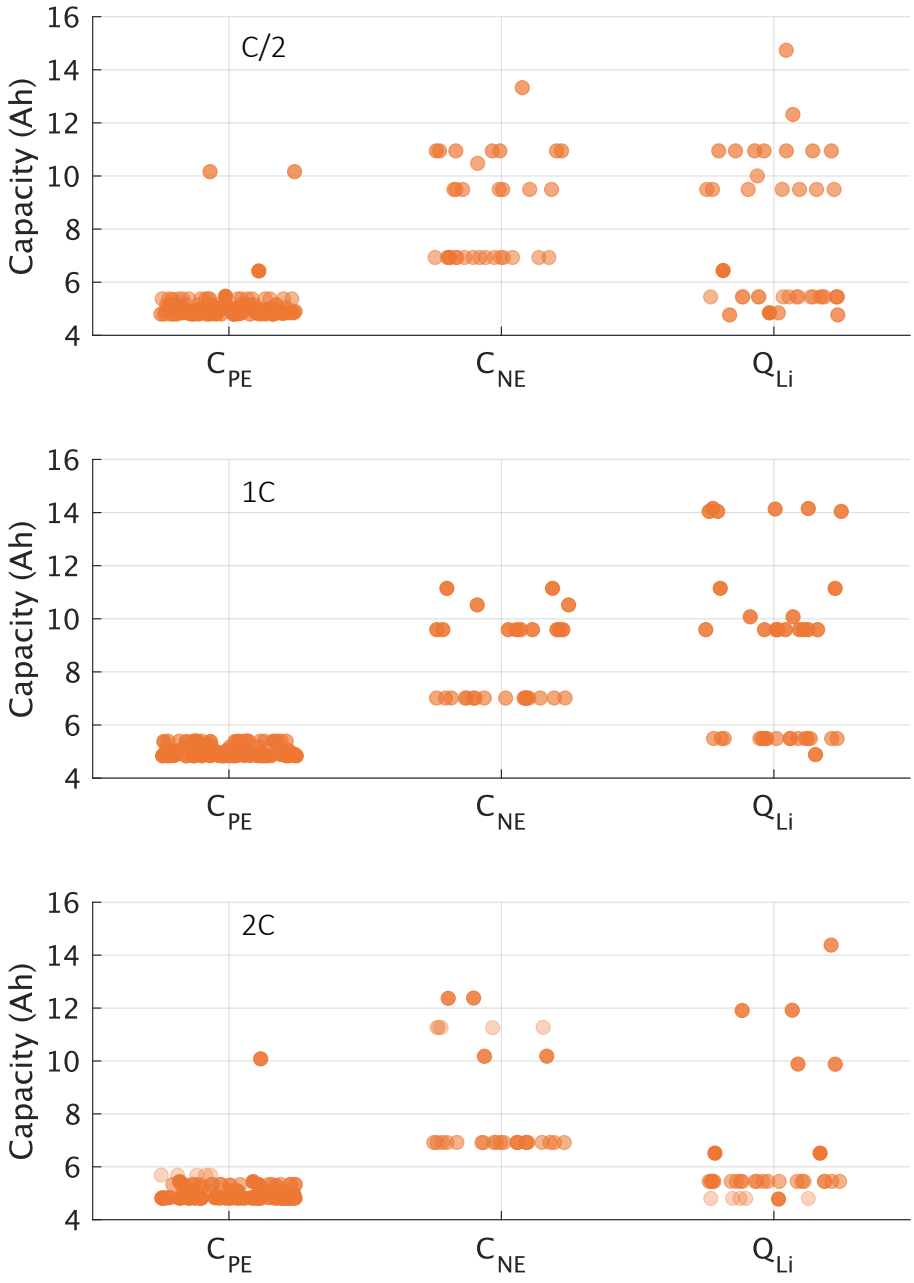

Figure 40: Scatter bar plot of the stoichiometric parameters predicted by the heat generation technique under discharging at different C-rates (indicated) for 400 different optimisation starting points. The opacity of each point is related to the objective function score, a more opaque point is a better fit. The number of clusters is related to the potential convergence parameters for the optimisation routine.

Comparing the results across both techniques; both seem to be able to robustly identify positive electrode capacity and both are less robust in identifying negative electrode capacity. The reason for this may be that the positive electrode capacity may be a more identifiable parameter than the negative electrode capacity and the lithium inventory. This

means changes in the negative electrode related parameters does not impact the objective function score by much as it does not affect the overall signal by much. In the heat generation cases, discharge profiles are generally more robust than charge profiles. The reason for this improved robustness may be that discharging causes the entropic heat to be positive – to heat the cell up – and in turn makes the heat generation more easily measurable with less measurement noise and error. This reason would also explain the better robustness for the 2C charging case over the 1C and C/2 cases.

In summary, the heat generation diagnostic technique gives a similar robustness to the OCV technique for positive electrode capacity, especially under discharging and higher rates possibly owing to the larger magnitude of heat generated. The negative electrode capacity and lithium inventories are less robust for the heat generation technique than the OCV technique, however the same pattern applies with higher rates and discharging outperforming the low-rate charge datasets. The OCV method does also have weaker robustness for negative electrode capacity and lithium inventory. In the next section, the Sobol method is used to explore why both techniques are more robust to the positive electrode capacity and less robust to the negative electrode capacity and lithium inventory.

Parameter identifiability for OCV and heat generation techniques

In this section, the Sobol method of global sensitivity analysis is applied which allows a quantitative measure of how much of the total variance of the output objective function can be attributed to each parameter. This gives a direct measure to how identifiable a parameter is. A low Sobol total effect index means that varying a given parameter and

including the effects of varying other parameters along with it, does not influence the output of the objective function very much. This would mean the parameter has a low identifiability and would indicate the optimisation routine would have difficulty finding an optimum and consistent value. The converse is true for a high Sobol total effect index, the optimiser would be able to successfully converge on an optimum and consistent value for the parameter.

Sobol analysis requires that the input parameters be randomly sampled a large number of times and the value of the objective function computed for each of these sample input parameters. The input parameters in this case are the start and end lithiation fraction for the positive and negative electrodes. The parameters are sampled using a uniform distribution at the top and bottom 0.3 of the lithiation ranges as is given in Eq. for charge and discharge respectively. In this analysis, the number of input parameter points chosen is 10,000. Latin hypercube sampling is used again for this sampling procedure to ensure an even distribution of parameters is chosen. With these samples, the objective function is evaluated for each and from these evaluations the total effect indices for each input parameter are calculated. For in depth information on how the total effect indices are calculated, see appendix A.

$$x_{NE,0}, x_{PE,1} \in [0, 0.3] \quad x_{NE,1}, x_{PE,0} \in [0.7, 1] \tag{99}$$

$$x_{NE,1}, x_{PE,0} \in [0, 0.3] \quad x_{NE,0}, x_{PE,1} \in [0.7, 1] \tag{100}$$

The total effect indices for each lithiation fraction limit for all technique datasets is given in Figure 41. In this analysis, the main comparison will be between different parameters for the same dataset. Because the total effect index is a function of the total variance for the

given dataset and the optimisation is generally not normalised to total variance, a direct comparison between techniques and datasets is not straightforward. Across all datasets, the total effect index is much higher for the positive electrode lithiation fractions than the negative electrode fractions. This is true for the OCV technique and all datasets in the heat generation technique also. The higher total effect index means the positive electrode lithiation limits are more identifiable than the negative.

The difference in identifiability between the negative lithiation fractions and positive lithiation fractions explains the differences in robustness for the stoichiometric parameters. Because both lithiation limits are identifiable in all techniques, the positive electrode capacity is also identifiable as it is calculated from the lithiation fractions. Because the negative electrode lithiations are not identifiable, the negative electrode capacity is also not easily identifiable, and therefore the optimisation routine has difficulty finding repeatable parameters. Similarly, the lithium inventory is calculated using one of negative electrode lithiation fractions and hence it is also not easily identifiable. Parameters with total indices of less than 0.05 are deemed unimportant. This means their value can be arbitrarily set and there would be very little impact on the model output. This is the case for at least one negative electrode lithiation fraction in every technique case. Therefore, this means that any output of negative electrode capacity from the technique is effectively guesswork.

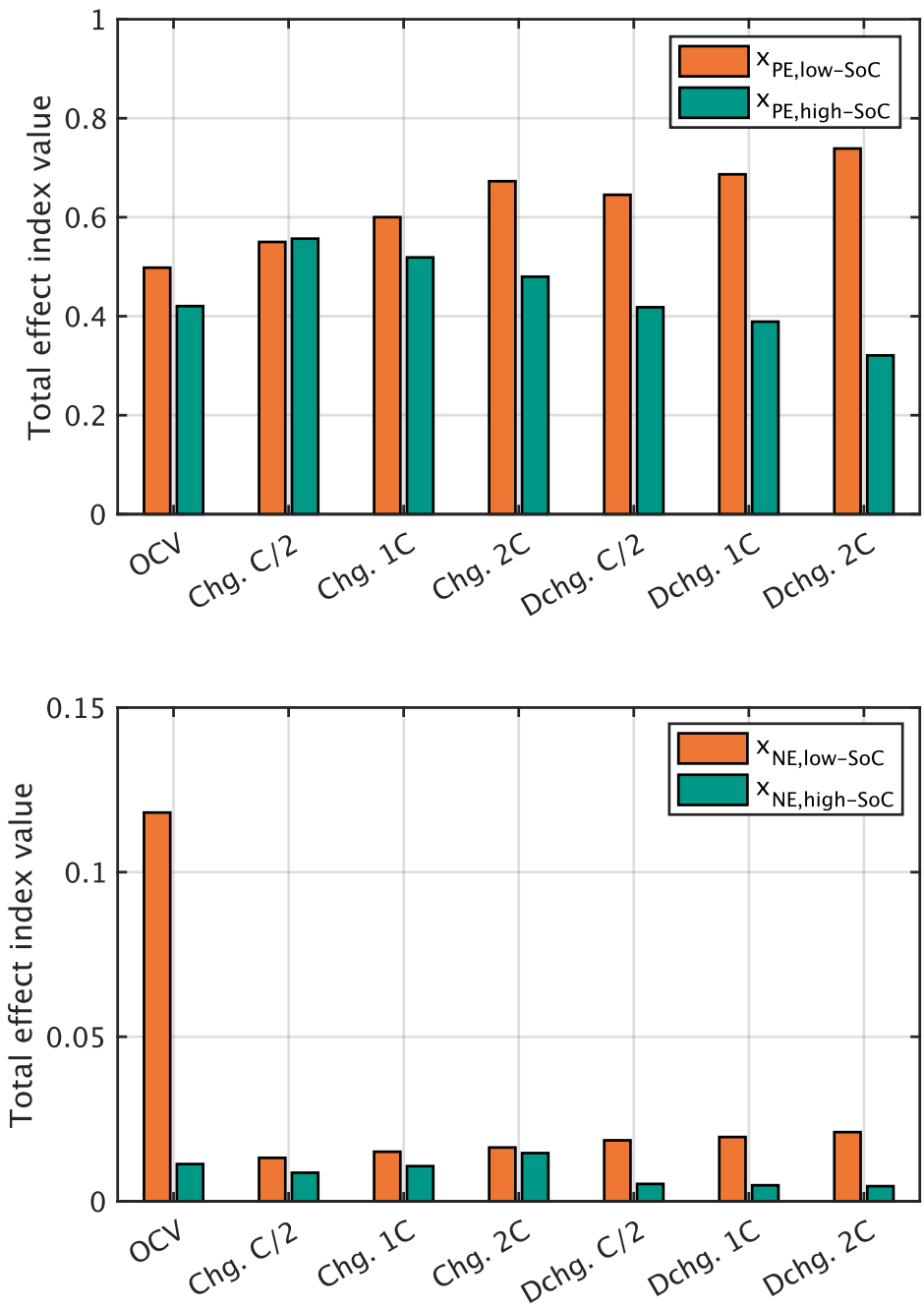

Figure 41: Bar plots showing total effect indices calculated using Sobol's method. A larger total effect index for a parameter means that it causes the objective function to vary more than a parameter with a low total effect index. It is important to note that the main comparison here is to compare the parameters within a dataset, i.e., the negative electrode lithiation limits against the positive electrode lithiation limits for each dataset.

The analysis performed above explains why the negative electrode capacity and lithium inventory are so difficult to identify. This is owed primarily to the flat nature of the negative electrode OCV and entropy curve and objective functions are not sensitive to the subtle features that it adds to the heat generation profile or OCV profile.

There have been several studies which outline the difficulty of identifying quantities relating to the negative electrode. Bizeray et al. [101] show how identifiable several parameters in the single particle model are. The authors in this work analyse the structural identifiability – the theoretical identifiability – of the parameters in the single particle model. For diffusion related quantities, it is found that a gradient of zero in either of the positive or negative electrode OCP versus lithiation curve causes that diffusion time constant – a grouped set of physical parameters – to become unidentifiable. This is due to diffusion changing the surface concentration and hence the surface potential of the single particle model. This change in potential can be detected in the terminal voltage of the cell. However, if changing the surface concentration has no effect on the voltage – a flat OCP versus lithiation curve – then there is no change in voltage to measure.

Another work which shows the difficulty of identifying the negative electrode diffusion coefficient is by Antti Aitio et al. [102] where a Markov Chain Monte Carlo (MCMC) method is used to assess the probability distribution of several parameters of the single particle with electrolyte (SPMe) model. The paper tests several simulated cases, one set of these being localised zero mean multi-sine excitation at various SoC points. The other case being a 1C biased single sinusoidal signal to cover a wide range of SoC points in one simulation. The work shows that in the cases whereby the negative electrode OCP curve is flat, the negative electrode diffusion coefficient becomes much less identifiable than when the OCP has a steeper slope.

These results are similar to the conclusions in this section. By shifting the negative electrode curve a small amount via LLI or LAM – the same effect as changing the surface concentration

of the negative electrode in the previously mentioned study – there is very little change in the voltage over the majority of the full cell OCV owing to the mostly flat negative electrode OCP. There are only a few localised points over the state of charge window which are impacted by a shift in the electrode curve. This is converse to the positive electrode whose OCP curve is much more sloped and so a small shift in the positive electrode OCP relative to the negative electrode OCP is a larger change in the full cell OCV.

The scatter-bar plots and total effect indices show that neither technique is capable of reliably predicting the two parameters relating to negative electrode lithiation fractions. This is supported by the findings by Bizeray et al. [101] and Aitio et al. [102] that show the negative electrode diffusion cannot easily be identified because of the small gradient of the negative electrode OCP curve. However, both techniques are capable of estimating positive electrode potential which is a useful output by itself. As the techniques should be generally applicable to any state of degradation, the next section investigates both technique's performance on a cell which has undergone a significant amount of degradation. It can then be seen if the ability of either technique to robustly predict positive electrode capacity is diminished.

4.7 Performance of diagnostic techniques on a degraded cell

In this section, the OCV and heat generation diagnostic techniques are performed on a cell with an unknown degradation history. The cell used in this section is of the same make and model as is used in the previous section and so the chemistry is assumed to be identical and the half-cell properties are assumed to be the same, i.e., the electrode OCVs and entropic coefficients vs lithiation fraction remain unchanged. The same experimental procedures are

used for this cell as in the previous section. For heat generation, the same apparatus and measurements are used to calculate heat generation, and the same charge and discharge C-rates are tested. For the OCV test, the same C-rate is used, and the ambient temperature is also the same.

4.7.1 OCV technique – fits, robustness, and parameter identifiability

The OCV technique's performance is assessed using the same 3 criteria that were used in the previous section. In this section less time is spent on explaining why the tests are performed, instead the data is presented and then subsequently discussed. Figure 42 shows the fit between the measured and modelled OCV using a genetic algorithm optimisation routine. In this case, the fit is of a similar quality to the previous fit, it is a satisfactory fit but some of the more nuanced parts of the curve are not captured. As these are definitely present in the half cell OCV curves, it casts doubt on whether the fit is truly correct. The stoichiometric parameters obtained by the optimisation routine are given in Table 16. The negative electrode capacity looks plausible; however, the positive electrode capacity is only 20 mAh more than the measured cell capacity. A larger positive electrode capacity would also mean that the features around 500 mAh charge throughput would be better captured as they are contained in the negative electrode OCV curve.

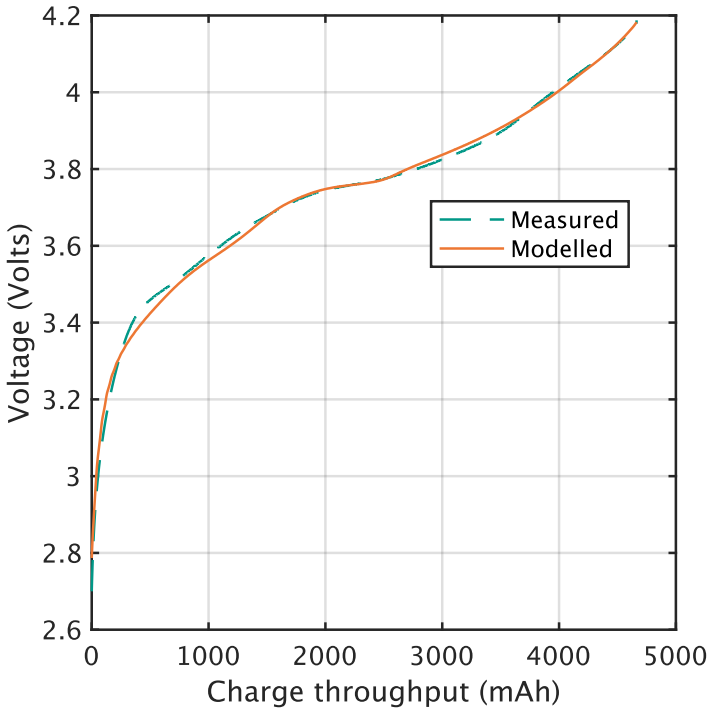

Figure 42: Fit between the modelled and measured OCV for the case of the degraded cell. The fit is obtained through an optimisation routine using a genetic algorithm. The fit – while satisfactory – does not capture some of the more nuanced parts of the curve.

Table 16: Stoichiometric parameters obtained from the genetic algorithm optimisation procedure to produce the fit given in Figure 42.

Parameter	Value (mAh)
Negative electrode capacity, C_{NE}	5,535
Positive electrode capacity, C_{PE}	4,688

Lithium inventory, Q_{Li}	5,368
Measured charge transfer, dQ	4,663

With the representative fit in Figure 42 appearing to give a lower-than-expected positive electrode capacity, the robustness analysis may be able to shed some light on whether this output is common, or if an anomalous output has been found. The scatter-bar plot for the stoichiometric parameters found by the robustness analysis for the OCV data is presented in Figure 43. Here, the positive electrode has two distinct clusters for the positive electrode. These values are 4.7Ah and ~5.0Ah. The negative electrode and lithium inventory have singular clusters at 5.5Ah and ~5.4Ah respectively. The values in the scatter-bar plot are in line with the results from the fit obtained in Figure 42 and indicate that there is indeed a scenario where a larger positive electrode capacity can be found. Arguably, the higher positive electrode capacity cluster is darker than the lower set. This means that a better fit is possible with a larger positive electrode capacity which is possibly a more reasonable value.

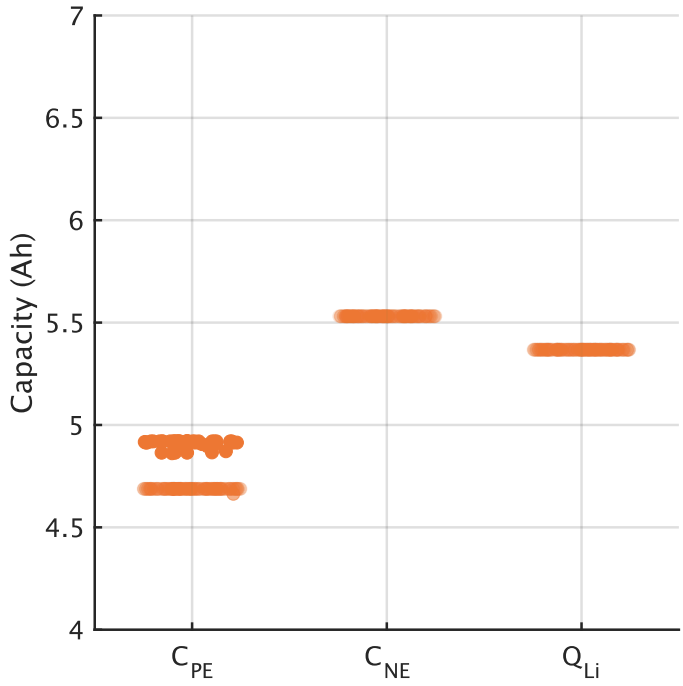

Figure 43: Scatter-bar plot of the stoichiometric parameters predicted by the OCV technique on the degraded cell for 400 sampled optimisation starting parameters. The opacity of each point is related to the objective function score, an opaquer point is a better fit. The points of dark clusters are parameter values which are likely to be converged on in the optimisation routine.

The results of Figure 43 are interesting when compared to the earlier robustness analysis on the fresh cell. In this case the positive electrode capacity has two distinct clusters whereas negative electrode capacity and lithium inventory have a single cluster each[5]. This is the opposite case to what was seen for the fresh cell where one cluster was observed for positive electrode capacity, and multiple clusters seen for the negative electrode capacity and lithium inventory. The analysis for fresh or aged cell should not matter for the OCV technique, because there is no difference between the application of the technique – the different stoichiometric parameters and different resistance of the cell should not matter.

[5] There are also clusters at much higher capacities for both negative electrode capacity and lithium inventory. However, the y axis scale has been adjusted so these points are hidden as they are almost certainly not the true case for parameters in this cell and could easily be filtered out.

The observation in the previous paragraph highlights that the robustness of the OCV technique may need to be conducted over many combinations of stoichiometric parameters to identify a 'true' robustness of the technique. This is possible as a simulated measured OCV curve can be made by choosing a set of stoichiometric parameters and then applying the analysis above to the simulated OCV curve. If this is repeated for many stoichiometric parameters, an idea of the robustness of each parameter across the entire set of possible stoichiometric combinations can be observed. The difficulty in this technique is how to quantitatively interpret and compare the large number of scatter-bar plots that are produced. However, if this difficulty can be overcome this analysis may prove to be quite powerful; offering a methodology to evaluate the OCV technique's robustness for any given chemistry combination.

The identifiability of each of the lithiation fractions - and by extension of the stoichiometric parameters – is measured using the total effect indices produced by Sobol's analysis as was performed on the fresh cell. The values for the total effect indices for the Sobol analysis on the beginning of life cell and the degraded cell are given in Table 17. The main difference between the fresh and aged cell total effect indices is the relatively low index for one of the lithiation limits of the positive electrode in the aged case. This could be the reason for the poorer robustness of the positive electrode seen in the previous analysis. Aside from this result, the other total effect indices are similar; both negative electrode lithiation limits are low. Despite the low identifiability, the robustness analysis showed a single cluster for both negative electrode capacity and lithium inventory. There are however clusters of negative capacity and lithium inventory at much higher values – larger than 20Ah – when the

robustness analysis is performed. The large variation in their clusters is made possible by the low total effect indices for the negative electrode lithiation limits.

Table 17: Total effect indices obtained through Sobol's method for the OCV technique on the degraded cell

Parameter	Total effect index fresh	Total effect index aged
$x_{PE,\ Low-SoC}$	0.50	0.71
$x_{PE,\ High-SoC}$	0.41	0.19
$x_{NE,\ Low-SoC}$	0.12	0.13
$x_{NE,\ High-SoC}$	0.01	5.7E-3

Again, the Sobol method shows that for the OCV technique, the parameter identifiability is dependent on the stoichiometric parameters of the measured cell. Similar to the robustness analysis, the Sobol method can be applied to many simulated OCV curves which are generated using a random set of stoichiometric parameters. However, unlike the case of the robustness analysis the output for each total effect index is a single number. The total effect index for each parameter can be plotted on a histogram to observe the relative distributions of each across all sets of stoichiometric parameters. This analysis would be able to evaluate the identifiability for each stoichiometric parameter for a given chemistry.

The analysis performed here and in the previous section provides a snapshot of the efficacy of the OCV diagnostic technique. It has been seen that the robustness is dependent on the stoichiometric parameters of the measured OCV curve. Despite this, in the two cases analysed here, the positive electrode capacity is more identifiable than the negative

electrode capacity and the lithium inventory. In the aged case, even though there are two clusters for the positive electrode capacity in the robustness plot the identifiability is higher for the positive electrode capacity and there exists a strong cluster at the value of positive electrode capacity which is most likely correct. The negative electrode capacity and lithium inventory both have weak identifiability, and this is shown by the large variations in clusters in both parameters in the aged and fresh case. Overall, from this analysis, the OCV technique can be said to be accurate and robust when predicting positive electrode capacity but has a weak predictive power for negative electrode capacity and lithium inventory.

4.7.2 Heat generation technique – fits, robustness, and parameter identifiability

The heat generation technique will now be evaluated for the same criteria as before, starting with the quality of fits. The fits between modelled heat generation and measured heat generation for the charging dataset are given in Figure 44. It is seen in these fits that the lowest of the C-rates, C/2, is a very good fit with both magnitude and shape captured well. However, as the C-rate increases the quality of fit becomes progressively worse. In the 2C case, the characteristic trough appears stretched in the measured data versus the modelled data. The peak and trough are a feature found in the positive electrode entropic coefficient vs SoC. The stoichiometric parameters given in Figure 45 reflect this fact where the C/2 and 1C cases give positive electrode capacities which are plausible, whereas the 2C case does not. In all cases, the negative electrode and lithium inventory amounts seem unlikely but especially so in the 2C case.

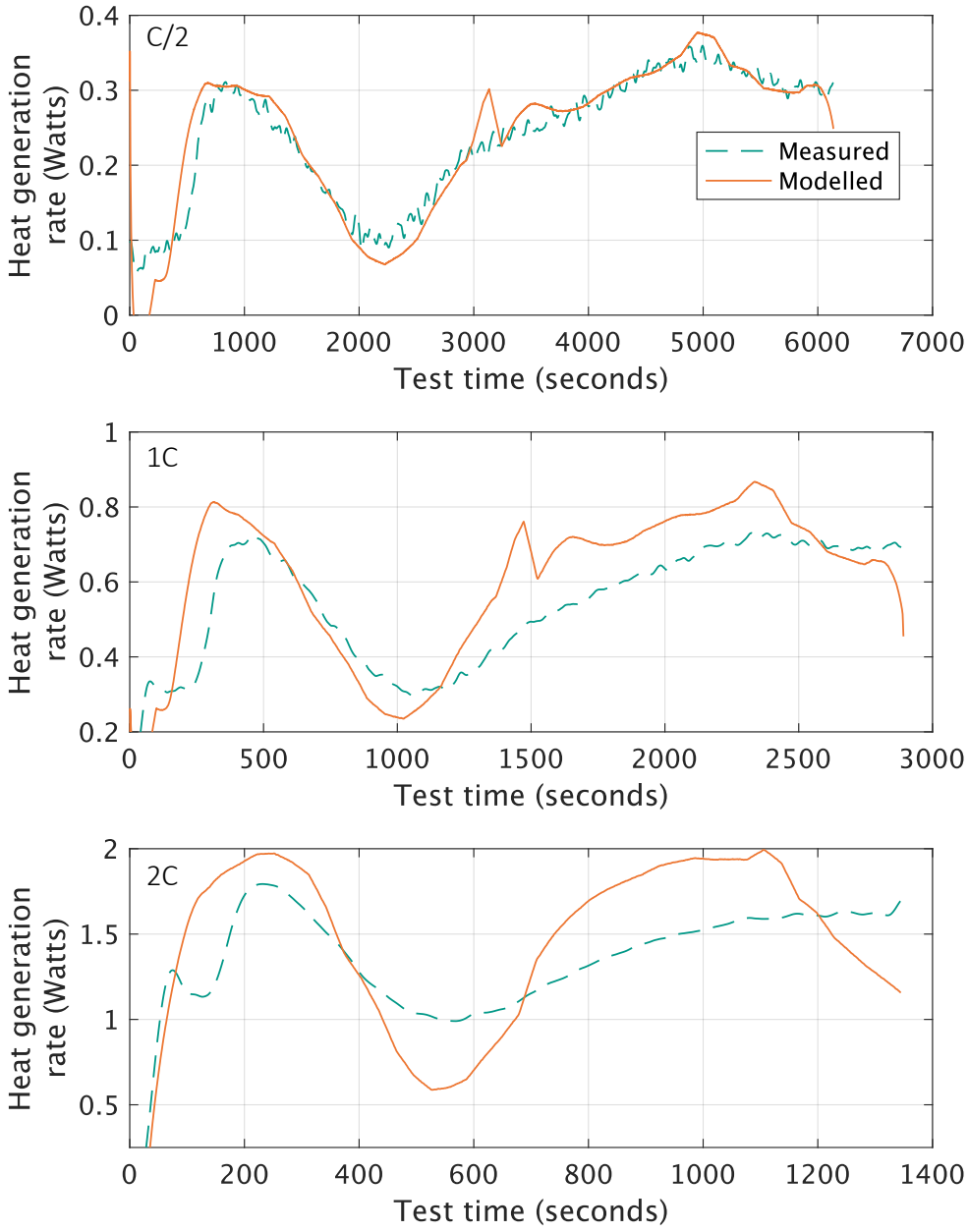

Figure 44: Modelled heat generation fits with measured heat generation for charge datasets on the aged cell. The lower C-rate cases – C/2 & 1C – capture shape and magnitude relatively well. The measured 2C case appears to be a stretched version of the modelled heat generation and the fit is not as strong.

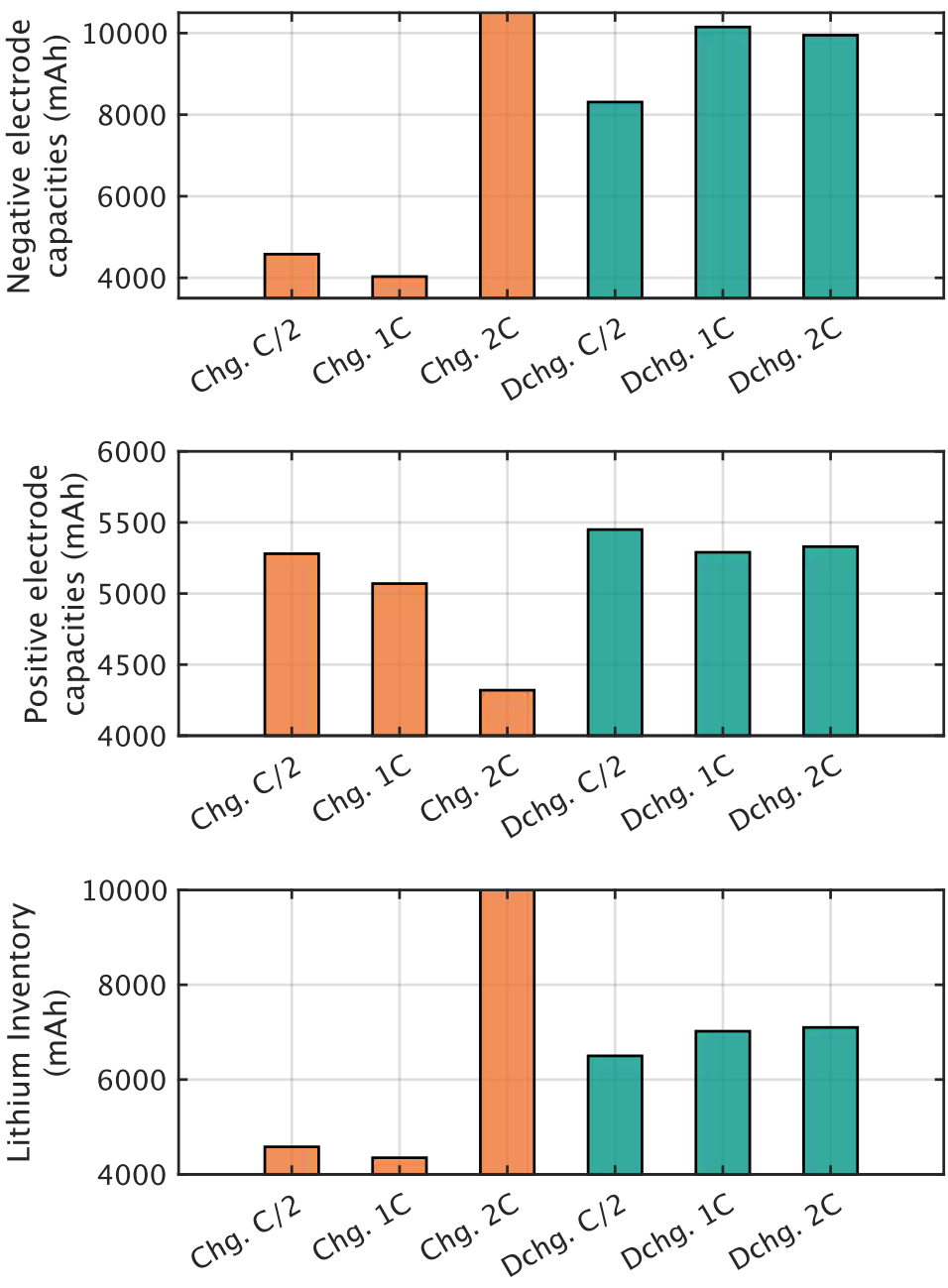

Figure 45: Stoichiometric parameters predicted by each heat generation fit for the aged cell. The charge cases positive electrode capacities reflect the worsening fits for the higher C-rate cases in Figure 44.

The fits for the discharging dataset are given in Figure 46. In this case, none of the modelled heat generations match the measured particularly well; the peak/trough seen in the modelled data seems to be missing from the measured heat generation, especially in the higher C-rate cases. This is a very similar observation to the charging cases given in Figure 44 but is even more pronounced. Despite the poor fits, the positive electrode capacities in

Figure 45 are similar between all datasets. However, this is not an indication of the robustness of the technique. Like the charging cases, the negative electrode capacities and lithium inventories predicted seem to be unlikely. While this was an issue in the fresh cell case, the problem is most likely exacerbated by the loss of the peak and trough in the measured data.

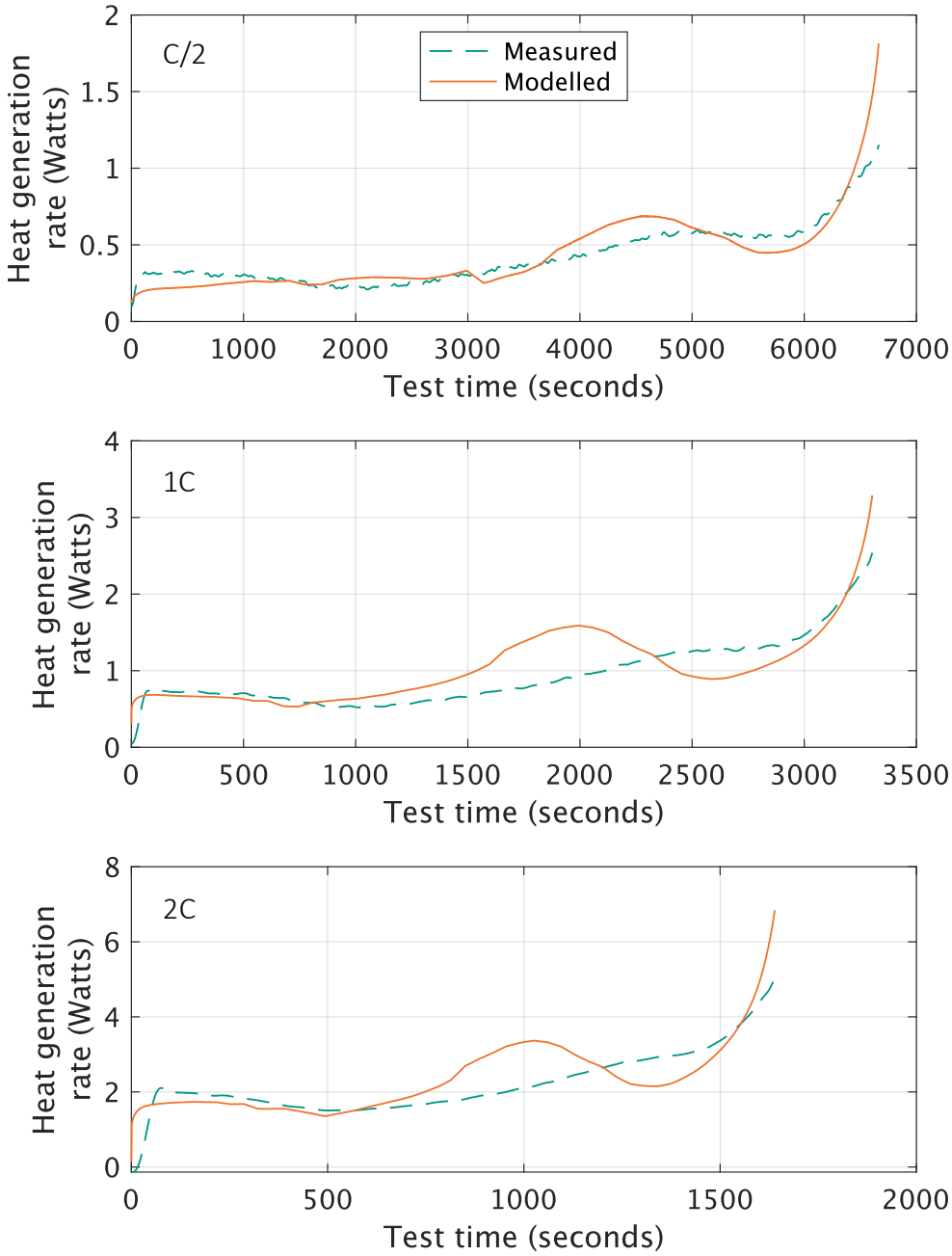

Figure 46: Modelled heat generation fits with measured heat generation for charge datasets on the aged cell. In all cases, the shape of the modelled heat generation does not match the measured. In all measured cases, the characteristic peak and trough appear to have disappeared.

A likely explanation of the loss of peak / trough is that the decrease in active material and possibly porosity of the electrodes means that diffusion related phenomena are now more important. This would manifest as a smoothing effect of the features in the OCV and entropic coefficient vs SoC curves. This arises due to different parts of the electrode being at

different SoCs and hence having different values for their OCV and entropic coefficients. This would also explain why the low C-rate charging case preserves the peak and trough but the low rate discharging cases lose the peak and trough. The peak and trough occur at the beginning of the charge, where diffusion effects are not yet established whereas the discharge case sees the peak and trough at the end when diffusion gradients are fully established. This will most likely have an effect on the robustness and identifiability of the parameters which will be explored next.

The scatter-bar plot for the stoichiometric parameters for each of the charging cases is given in Figure 47. The findings in this plot echo those of the fit for the charging case; as the C-rate increases the positive electrode parameters become less robust and more transparent. The y-axis has been truncated but there are clusters that exist above the 7 Ah for each of the stoichiometric parameters in each of the charging cases. More transparent cases shown mean that the clusters at higher capacities are stronger optimums. Examining positive electrode capacity; for the C/2 case, there is a relatively strong cluster around the 5 Ah region, 4.5 Ah and a few strong points at 5.6 Ah. For the 1C and 2C cases, these clusters are more transparent meaning that they are less likely to be the result of the global optimisation. A similar observation can be made for the negative electrode capacity and lithium inventory where clusters become more transparent for higher C-rates.

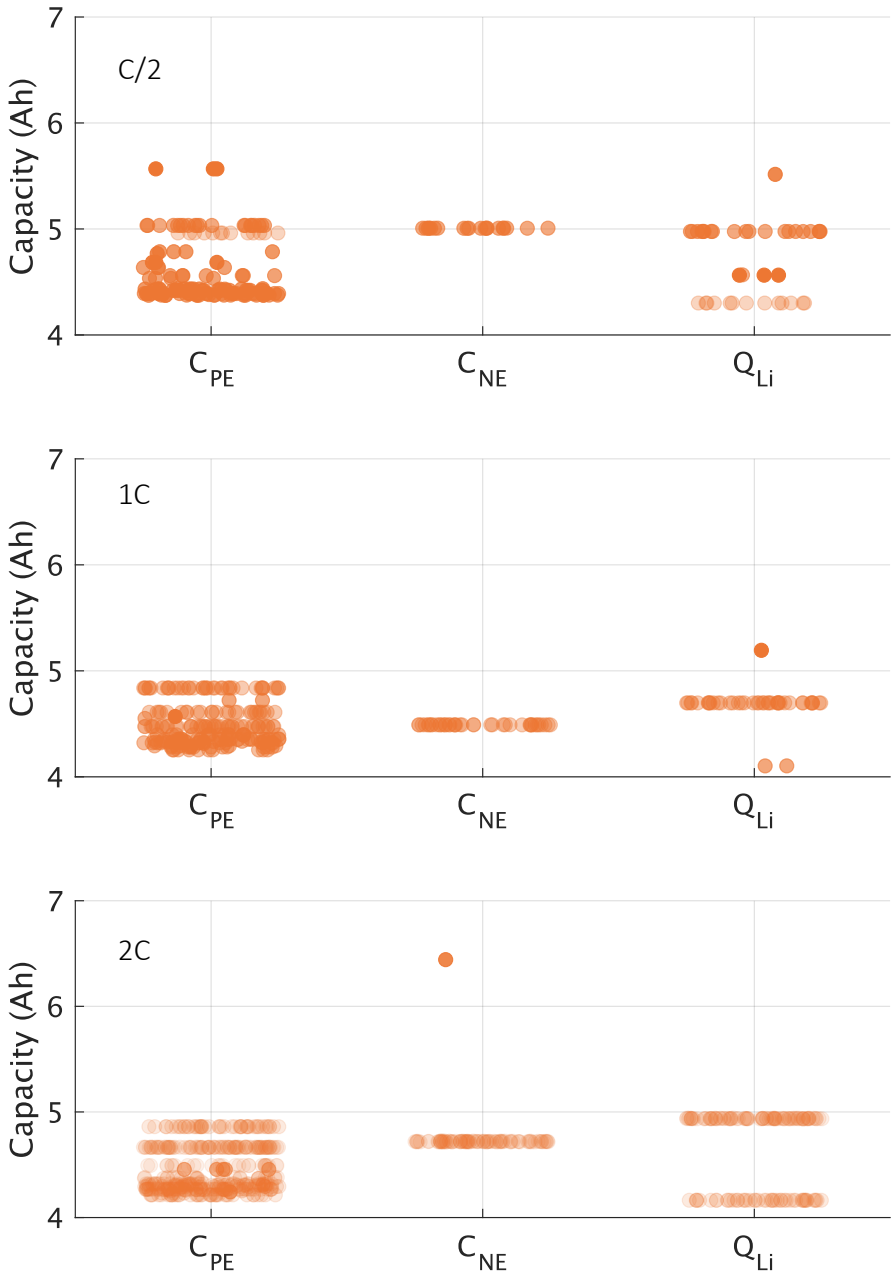

Figure 47: Scatter-bar plot of stoichiometric parameters for each charge dataset after performing robustness analysis. More transparent points have a higher scoring objective function than darker and so are less likely to be observed after the optimisation routine using the genetic algorithm.

The scatter-bar plots for the robustness for the discharge cases are given in Figure 48. Unlike the case with the charging plots, it seems the optimums get stronger with the increasing C-rate for all stoichiometric parameters. The positive electrode capacities however seem to become more spread out at higher C-rate indicating that there are lots of

local optimum around 5.4 Ah which do a good job of minimising the objective function. The lithium inventory and negative electrode capacity also seem to be more robust at the higher C-rates which is unexpected given the seemingly worse fit. It is worthwhile remembering at this point that the results presented here give little insight into whether the robust values are accurate. They only give an idea of how many local optimum exist in the search space, and how strong the optimums are. With this being said, the values for the discharge datasets seem to be plausible.

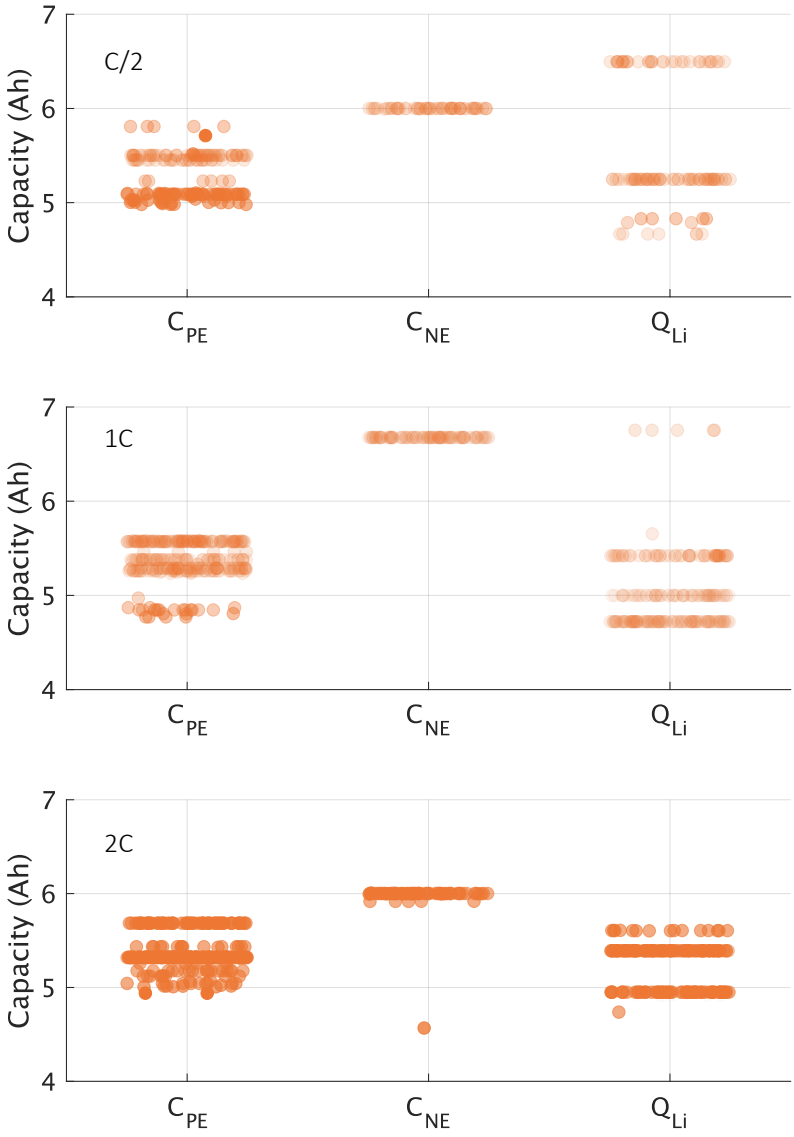

Figure 48: Scatter-bar plot of stoichiometric parameters for each discharge dataset after performing robustness analysis. More transparent points have a higher scoring objective function than darker and so are less likely to be observed after the optimisation routine using the genetic algorithm.

The parameter's robustness for the discharge case seem to – counterintuitively – get better with the increasing C-rate. This is despite the fit getting progressively worse for higher C-rates. The charging case seems to be in line with what is expected from the quality of fits, with robustness getting worse as the C-rate increases. The final tool for analysis of the heat generation results is to generate the total effect indices for each lithiation limit using Sobol's

analysis. The total effect indices allow an understanding on how identifiable each stoichiometric parameter is.

The total effect index for each lithiation limit is given in Figure 49 for all heat generation cases and the OCV case for reference. Beginning with the discharge cases; for the higher charging rates, the identifiability of one of the positive electrode lithiation limits becomes stronger relative to the other. This may mean that the optimisation has a strong optimum around this parameter and then lands in a range for the other positive electrode lithiation limit. This would mean there would be a range of dark scattered points around a value for the robustness plot. This is indeed what is seen for the highest C-rate case in the discharge scatter-bar plot in Figure 48. Conversely for the C/2 discharge case, the total effect index of each positive electrode lithiation limit is lower but both are much closer together. This means the optimum may not be as strong, but for each optimum of one limit, there is an identifiable optimum for the other limit. This would result in more transparent points in the scatter-bar plot, but distinct groups of these points rather than hazy values. This is the case in the C/2 case in Figure 48.

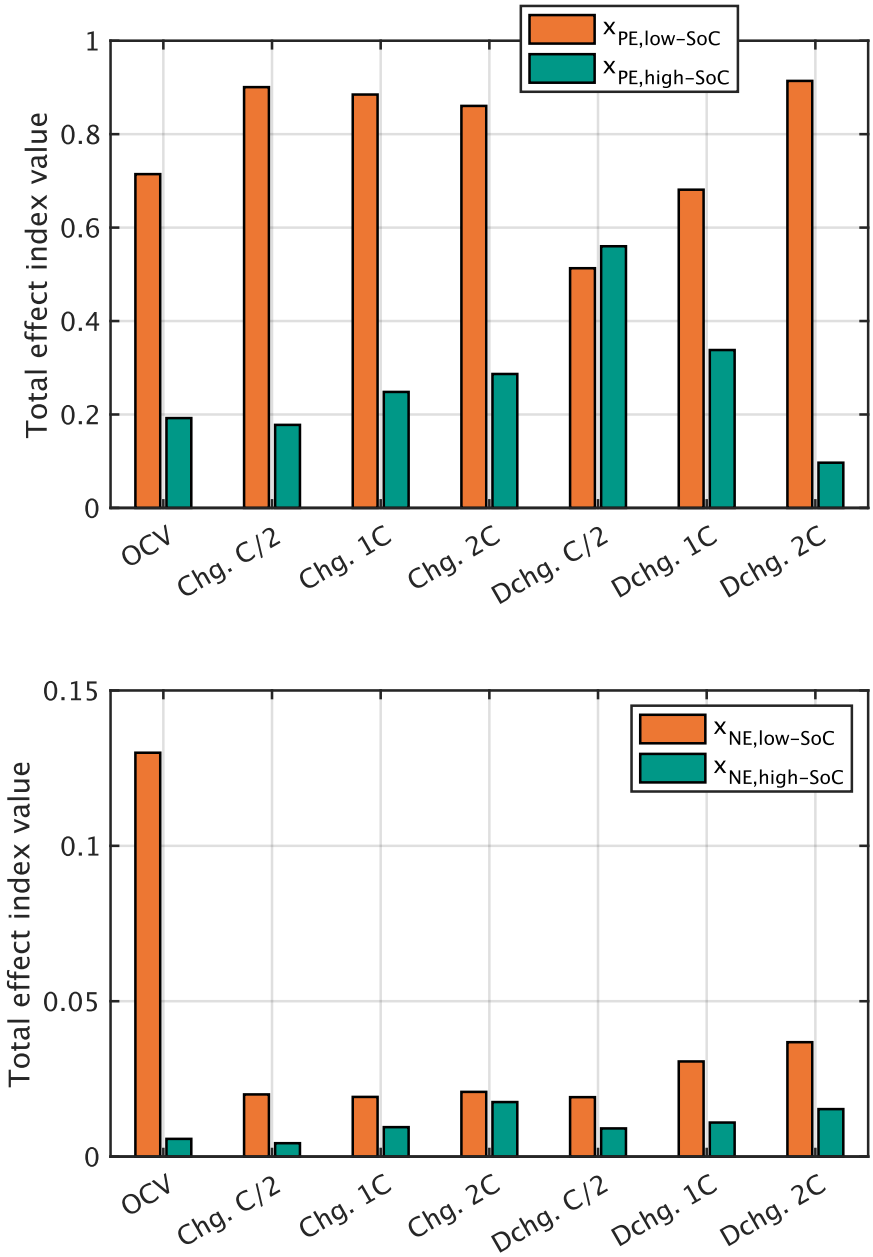

Figure 49: Total effect indices for the aged cell for all datasets; heat generation charge & discharge, and the OCV technique.

The logic in the previous paragraph can also be used to describe some of the phenomenon seen for the positive electrode capacity in the charging datasets. For charging, the reverse is seen, for the higher C-rates the total effect indices of each lithiation limit get closer together with one decreasing and one increasing. Therefore, the positive electrode capacity

in the C/2 case has a strong optimum but a hazy scatter of clusters is seen in the scatter-bar plot given in Figure 47 is seen. For the 2C case, the lithiation limits are relatively close together – either the low SoC limit causes less variation, the high SoC limit causes more variation, or a combination of both. This means that the optimum for one of these points is no longer as strong, but for a given value of one lithiation limit, an optimum for the other is easier to find. The result of this in Figure 47 is a more clearly defined set of clusters, but more transparent.

Finally, the identifiability of the negative electrode lithiation limits is low for all datasets. This means it is unlikely that the output from the heat generation technique is much use for these two parameters. The low identifiability of these parameters means that very extreme values of the parameters are possible. Hence, there are so many points above the 7Ah level for both of these parameters. As lithium inventory is calculated using one positive electrode lithiation limit – with good identifiability – and one negative electrode lithiation limit – with poor identifiability – large variations in results occur. In the case of the negative electrode capacity both parameters have poor identifiability but are both close together and so results can vary wildly but remain in clusters.

4.8 Conclusions on the performances of both techniques

In this chapter, an attempt has been made to perform detailed analysis on the performance of the diagnostic techniques. Whilst the analysis does not give clear cut evidence of how each technique performs, and some analysis is still missing, it does give some useful insights from which concluding remarks can be made for both techniques. The aim of the analysis performed in this chapter is not to provide a methodology for human down-selection of sets

of results from fits or from the scatter-bar plots. Instead, the questions asked are; should the outputs of these diagnostic techniques be taken in complete confidence and how confident can one be in the results of a single optimisation run with some arbitrary initial points. Hopefully, in the subsequent paragraphs these questions can be answered.

Firstly, the identifiability of the negative electrode lithiation limits are much lower than the positive electrode lithiation limits. This means the negative electrode capacity and lithium inventory values output by the techniques are less likely to be accurate and robust. This is also seen in the robustness analysis of both techniques in at least one instance. On the other hand the positive electrode lithiation limits are identifiable which means the results for the positive electrode can be taken with more confidence. The robustness for the positive electrode is generally better for both techniques as well. Overall, both techniques are useful in predicting positive electrode capacities, but are less useful in predicting negative electrode capacities and the lithium inventory.

Generally, the robustness of the OCV technique is better than the heat generation technique, but both techniques have similar parameter identifiability ratios between parameters. The OCV technique is likely to be a better choice when available for the robustness reasons. However, in times when the OCV is not available or is only sporadically available then the heat generation technique is a more than capable technique to acquire positive electrode capacities. In addition to this, the heat generation benefits from being able to take measurements in quick succession meaning every time a cell is cycled, a new datapoint can be acquired. The capturing of multiple datapoints in quick succession can facilitate the use of filtering techniques to obtain a more accurate estimation.

Both techniques were tested on a fresh cell and an aged cell. The OCV technique's results should not be affected by degradation state. However, it is seen that the robustness and identifiability of each parameter is dependent on the true stoichiometric parameters of the measured OCV. As the robustness is dependent on the stoichiometric parameters used, the robustness and identifiability of parameters should be evaluated for all combinations of stoichiometric parameters to find a true representation of the technique's efficacy as a diagnostic technique. A semi-complete methodology is outlined for this in an earlier section and would be valuable to complete for any practitioner of these techniques. However, such an analysis is not performed in this thesis as the aim is to develop the heat generation technique rather than to develop analysis techniques for the OCV technique only.

The heat generation fit results were affected significantly for the aged cell when compared to the fresh cell. The reason for this is anticipated to be diffusion effects being much more impactful in the aged cell when compared to the fresh cell. This will undoubtedly affect the performance of the technique, including its robustness and parameters identifiability. It is thought that by improving the fit with the aged datasets, the identifiability and robustness of the parameters can be improved. Despite this, there did not seem to be an effect on which parameters were more identifiable and which were more robust between the fresh and aged datasets. This could suggest that the heat generation technique's robustness and identifiability is less affected by the actual values of the stoichiometric parameters.

In an attempt to improve the heat generation techniques performance for cases where diffusion is more prominent, the next chapter is dedicated to implementing a low computational cost diffusion model and seeing if its inclusion improves the fit between

model and measured heat generations and by extension improving robustness and identifiability of the output parameters.

5 High-Energy & High C-rate Applications

In the previous chapter, it is seen that the heat generation diagnostic technique's fits between measured and modelled heat generation are impacted when the technique is used on an aged cell. Improving the fits between the measured and modelled technique is expected to improve the identifiability of parameters and the robustness of the parameters. The cause of the poor fit is anticipated to be diffusion effects playing a bigger role in the aged cell's heat generation and causing the loss of some of the features in the heat generation profile. It is thought that this can be overcome by the inclusion of a diffusion model in the diagnostic technique's heat generation model.

The remainder of this chapter will firstly review the different types of lithium-ion battery models with their merits and drawbacks. Following this, a reduced order model is derived with a focus on computational speed and a low number of parameters. The numerical scheme for the diffusion model will then be derived and the stability, accuracy and speed of the scheme will be evaluated. With the diffusion model in place, its integration with the heat generation model is outlined as well as how the optimisation procedure would be performed during the diagnostic technique. The augmented diagnostic technique will then be tested on a high energy cell at high C-rates to generate a large concentration gradient. This version of the technique will be compared to the 0-D model by first examining the quality of fit, and subsequently by evaluating the robustness. The diffusion augmented model will then finally be compared to the OCV based model to evaluate how similar the results given by each are.

5.1 A review of lithium-ion battery models with diffusion dynamics

There are many methods of modelling lithium-ion battery dynamics, each with merits and drawbacks. Generally, models trade-off between spatial dimensionality and accuracy, and speed of execution. In this section, physics based models are briefly outlined and their computational costs and accuracies are discussed. Following this, the rationale for selecting a model is outlined. The goal of this section is to select a model which can add the necessary diffusion dynamics into the model.

The single particle model – SPM – represents each electrode as a single spherical particle which allows for the modelling of intercalation dynamics as a diffusion process. This means the current is assumed to be uniform across the particles in each electrode and a uniform concentration across the electrolyte. Owing to its low number of parameters and only requiring 2 linear spherical diffusion equations, the SPM is computationally inexpensive however, its usefulness is mainly at low to moderate C-rates.

The SPM with electrolyte – SPMe – model adds in the dynamics of the electrolyte by accounting for the concentration of the electrolyte through the thickness of the cell whilst still assuming that the electrodes can be modelled as uniform particles in the electrode with equal current densities [103]. The SPM-e adds 3 more diffusion equations for the the electrolyte in the separator and both electrode regions, meaning the SPMe has a higher computational cost than the SPM. However, the reward for this additional computational is that the SPMe has better accuracies for moderately high to very high C-rates as has been reported in the literature in works such as that by Perez et al. [104].

The pseudo-two-dimensional (P2D) model reported by Doyle et al. [105] does not have the assumptions on uniform current densities across the electrode particles, meaning the P2D model is able to capture the dynamics of the cell even more closely than the SPMe model. However, this model is now a coupled set of partial differential equations meaning each particle must be solved at each timestep given the electrolyte concentration at the surface of that electrode.

Planella et al. [106] give 2 more model types of lithium-ion models commonly found in literature, these are 3D homogenous models and 3D inhomogeneous or microscale models. The 3D homogenous models extend the DFN / P2D model to include the in plane direction of the cell electrodes and assumes that the electrode is made of a homogenous material which has the same material properties and composition throughout each electrode. On the other hand microscale models account for the material and geometrical differences throughout the electrode material such as the porous binder structure and the shape of different particles throughout the electrodes. These models have a higher geometric dimensionality, a higher level of required parameterisation – especially the microscale model which requires imaging of the electrodes to generate the microstructure details – and a much more computationally capable system. These 3 facts combined make them unsuitable for this work as the goal is to achieve a lightweight model which could be used on-line.

The SPM, SPMe and P2D models also have varying parameterisation and computational requirements. Parameterisation of these models is difficult and so selecting a model with the lowest number of parameters gives the technique developed in this thesis the best

chance of being useful in application. In the model types mentioned above, the SPM has the fewest number of parameters and the P2D model has the most parameters. The parameters used in these models are hard to measure meaning that the primary method of extracting the parameters is via fitting the model output to some measured experimental data. However, it has been reported by Andersson et al. [107] that several parameters cannot be identified reliably through fitting to experimental data alone. Therefore, it is advantageous to select a model which provides the accuracy required with the minimum number of parameters for ease of parameterisation which in this case is the SPM.

The computational effort required to run and solve the model is also critical to the success of the diagnostic technique. The computing power of battery management systems is limited and so the choice of model should be that with the minimum computational requirements whilst still meeting the required accuracy. Again, the model with the highest fidelity and hence potential accuracy is the P2D model but it is also the model with the highest computational load. The SPM on the other hand represents the simplest model form meaning it has a lower computational load but a lower accuracy under certain conditions.

The voltage response of the different types of model are given in Figure 50 which is adapted from [108]. It is seen that all three model formats have a similar response up until 2C. At very high C-rates, the SPM has significantly different behaviour than the SPMe and P2D, also known as the Doyle, Fuller, Newman (DFN) model meaning that at higher C-rates, the SPM may not be suitable. Up to 2C however, the SPM has comparable results to the SPMe and the DFN and so it is assumed that if the currents used are moderate, then the SPM is a suitable choice of model.

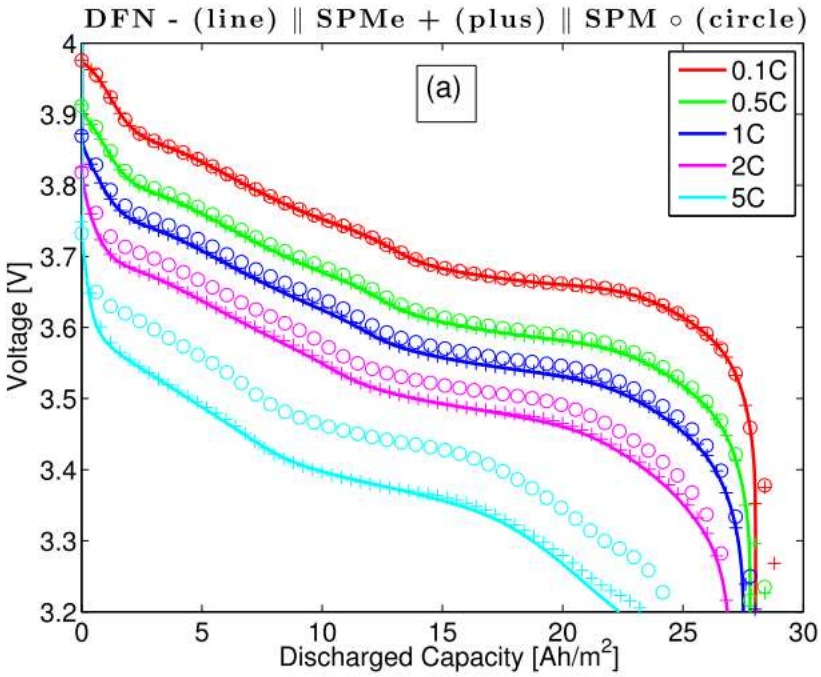

Figure 50: A comparison of the voltage response from the different types of models for different C-rates. Adapted from Mehta et al. [108]

In this short review, different models have been introduced and their merits and drawbacks discussed. The 3 most common models in literature are the SPM, the SPMe and the P2D models which all describe physical phenomenon inside the cell to various levels of fidelity. The P2D model is the highest fidelity model but requires the most computational resource and parameterisation effort. The SPM on the other hand has the lowest fidelity but requires the lowest computational resource and parameterisation effort. Given the goal of this diagnostic technique being applicable to many different systems and being able to run on-line with computational resources typical in battery management systems, a simpler model is preferred. Therefore, for the rest of this chapter the SPM will be used as the model to add the diffusion dynamics. The following sections will discuss how to further simplify the SPM for use in this technique and how the SPM can be used in calculating the heat generation of a battery.

With the selection of the model confirmed as the single particle model, now attention is turned to parameterisation of the single particle model. Specifically, if the number of parameters in the single particle model can be reduced. In a work by Bizeray et al. [101] a methodology for reducing the single particle model to its minimum number of parameters is outlined. In this paper the authors reduce the single particle model to 6 unique parameters by introducing several non-dimensional quantities and then grouping the remaining constants. The reason for doing this is to make the parameters identifiable from curve fitting alone. In this thesis a similar approach is taken to reducing the number of parameters but there will be some key differences compared to the work by Bizeray et al. Similarly to Bizeray et al. the diffusion equations for positive and negative electrodes will be non-dimensionalised. However, this thesis does not contain equations for the electrode – electrolyte overpotentials and time will also be non-dimensionalised in the diffusion equations. In this work, the starting point is the spherical diffusion equation.

5.2 Solid diffusion model

Incorporating solid diffusion dynamics in the model provides the physics to allow the spreading in the peak / trough of the heat generation that are seen in data at higher C-rates and at states of higher degradation. Thus, by incorporating diffusion dynamics for both electrodes, a benchmark is created to which less computationally expensive methods can be compared. In this section, the theory for developing a low computational cost diffusion model is given. Following this, an evaluation of the accuracy and stability of the model under a range of input currents, step sizes and parameters is given. The theory developed in this section is for one single electrode, in the final heat generation model there will be two copies of this model, one for each electrode.

Assumptions for the diffusion model will be introduced and justified as they naturally arise in the subsequent sections, however in summary the full list of assumptions applied in this section are given below.

#1 Axisymmetric spherical diffusion: Particles are considered perfect spheres. Additionally, it is assumed that a uniform current density is seen across the surface of the particle and so the lithium concentration in the particle is one-dimensional in the radial direction.

#2 Constant diffusion coefficient: The diffusion coefficient is modelled as a constant and is not dependent on temperature or state-of-charge.

#3 Uniform current density for all particles: Each particle is assumed to see the same total current and that current is assumed to be uniformly distributed across the surface of each particle to allow #1 to remain true.

5.2.1 Non-dimensional spherical diffusion equation

Reducing the number of parameters in the diffusion model is important for several reasons; the time taken to perform any optimisation is exponentially related to the number of parameters in the system. Secondly, many parameters means the optimisation routine is more likely to find local minima meaning that for different sets of data, the optimisation routine will output different results, destroying the robustness of the technique which has already been established. Therefore, this section outlines the theory for developing a diffusion framework with the minimum number of parameters through nondimensionalization of the standard diffusion equations. The objective of this section is to produce a diffusion equation with the minimum degrees-of-freedom. If the phenomena

observed in the previous heat generation results cannot be accurately accounted for by the minimum degrees-of-freedom, then the degrees-of-freedom can be sequentially increased until satisfactory performance is obtained. The work here is similar to that produced by Bizeray et al. [101] who combine the parameters in the SPM to reduce the order of the model. In this work there are some differences and hence the re-derivation is justified as the Butler-Volmer equation is not included and there is a specific numerical scheme derived for computational efficiency.

The partial differential equation for axisymmetric spherical diffusion with constant diffusion coefficient, D, is given by Eq. (101) and Eq. (102) [22]. The notation used in Eq. (102) will be used throughout the remainder of this chapter. Two assumptions are made, first axisymmetric spherical diffusion is commonly assumed in literature and provides a good baseline approximation of the reality of lithium diffusion. Secondly, constant diffusion coefficient is assumed. In reality it is known that diffusion coefficients dependence on temperature follows an Arrhenius relationship as given in Eq. (103). This introduces an extra parameter, the activation energy E_a, which allows for a more accurate representation of diffusion but adds a parameter to the diffusion model. Suihan et al. find that the diffusion coefficient of NMC 622 varies from ~7E-11 cm^2s^{-1} at 25°C, to ~9E-11 cm^2s^{-1} at 50°C [109]. This is an increase of 28% and although this is a significant difference, the cells in question only rise to around 35°C and so the expected change in diffusion coefficient is expected to be around half of this. Furthermore, portion of the heat generation profile which is most affected by diffusion is only a small portion of the state-of-charge window and so the expected a change in diffusion is expected to be less still. For these reasons, the change in

diffusion coefficient with temperature is not considered in this model but could be easily added for cases where the change in diffusion coefficient is more significant.

The diffusion coefficient also likely varies with state-of-charge [110]. Incorporating this into the model would require either the use of data found by other studies on materials which may be different to those used in this work, or the generation of data for the materials in this study which is not feasible in the timeframe of this work but would be an interesting addition to the model.

$$\frac{\partial c}{\partial \hat{t}} = D\left(\frac{\partial^2 c}{\partial \hat{r}^2} + \frac{2}{\hat{r}}\frac{\partial c}{\partial \hat{r}}\right) \tag{101}$$

$$c_{\hat{t}}(\hat{r},\hat{t}) = D\left(c_{\hat{r}\hat{r}}(\hat{r},\hat{t}) + \frac{2}{\hat{r}}c_{\hat{r}}(\hat{r},\hat{t})\right) \tag{102}$$

$$D = D_0 \exp\left(-\frac{E_a}{T}\right) \tag{103}$$

The terms in Eq. (101) can be normalised to reduce the number of parameters required. First, the concentration, c, can be expressed in terms of the normalised concentration, x, which is commonly known as the lithiation fraction. The expression relating c to x is given in Eq. (104) as well as the bounds on x. c_0 is the minimum concentration and c' is the slope of the line relating x to c. The particle radial position, $\hat{r}$, can be expressed as a normalised radius, r, which is given in Eq. (105) where R is the particle radius. Finally, instead of absolute time, $\hat{t}$, a non-dimensional time, t, can be introduced which is given in Eq. (106). τ in this case is the time constant of the system.

$$c = c'x + c_0 \qquad\qquad x \in [0,1] \tag{104}$$

$$\hat{r} = Rr \qquad r \in [0,1] \tag{105}$$

$$t = \frac{\hat{t}}{\tau} \qquad t > 0 \tag{106}$$

Derivatives of eqs. (104) - (106) can be substituted into Eq. (102) and their derivatives evaluated, the result of which is given in Eq. (107). Note that c' appears in each term and as it is non-zero can be cancelled. If τ is chosen to be the ratio of the diffusion coefficient to particle radius squared (Eq.(108)) then Eq. (107) reduces to the dimensionless diffusion equation given by Eq. (109). This form of the diffusion equation dictates that for a given input and initial / boundary conditions, the diffusion profile evolution is identical for any material properties when time is expressed as a fraction of the time constant given in Eq. (108). Although τ does not appear in Eq. (109), knowledge of its value is required to be able to solve real diffusion problems as the mapping of non-dimensional time to real time is required.

$$\frac{c'}{\tau} x_t(r,t) = D\left(\frac{c'}{R^2} x_{rr}(r,t) + \frac{2c'}{rR^2}\, x_r(r,t)\right) \tag{107}$$

$$\tau = \frac{D}{R^2} \tag{108}$$

$$x_t(r,t) = x_{rr}(r,t) + \frac{2}{r}\, x_r(r,t) \tag{109}$$

The boundary conditions for the particle are given in eqs (110) & (111). Eq. (110) states that the gradient of concentration is 0 about the centre point of the particle due to the symmetry of the problem. Eq. (111) states that the gradient of concentration at the boundary is proportional to the areal flux of ions at the surface of the particle, j_{Li}, which is an expression of Fick's first law of diffusion. By substitution of the normalised /

dimensionless quantities from eqs. (104) & (105), the boundary conditions can be expressed in terms of the same variables as the diffusion equation in Eq. (109) as given in eqs (112) & (113). Note that we again need to know τ to be able to map the ion flux from real time to dimensionless time.

$$c_{\hat{r}}(0,\hat{t}) = 0 \tag{110}$$

$$c_{\hat{r}}(R,\hat{t}) = -\frac{D}{F}\, j_{Li}(\hat{t}) \tag{111}$$

$$x_r(1,t) = -\frac{DR}{c'F}\, j_{Li}(t) \tag{112}$$

$$x_r(0,t) = 0 \tag{113}$$

The ion flux, j_{Li}, is proportional to the total current, I. If the assumption is made that all particles see an equal share of current, j_{Li} is also inversely proportional to the area of a single particle and also the total number of particles in the electrode. If this assumption is not made, a more sophisticated model would need to be implemented such as a P2D model which allows different particles to see different amounts of current. Also, by making this assumption the total number of particles can be expressed in terms of the loss of active material (LAM). Finally, by normalising total current to the capacity of the electrode, the normalised current, $\bar{I}$, is introduced . Combining these proportionality relationships, an expression for j_{Li} is obtained in Eq. (114) where α is the constant of proportionality combined with all other constants. Combining eqs. (112) & (114) gives an expression for the diffusion boundary condition in terms of the total cell current which is given in Eq. (115) where A is the combined constant of proportionality.

$$j_{Li}(t) = \alpha \frac{\bar{I}(t)}{1 - LAM} \tag{114}$$

$$x_r(1, t) = A \frac{\bar{I}(t)}{1 - LAM} \tag{115}$$

So far, the non-dimensional diffusion equation has been shown to be a function of a single parameter, A, which is the constant of proportionality given in the boundary condition at the particle surface. Further to this, in order to apply the non-dimensional diffusion equation to real world problems, knowledge of the system time constant, τ, is required so that non-dimensional time can be mapped to real time. In this section we aim to find an expression for τ in terms of A. The average lithiation of the particle at any real time, $\hat{t}$, for a given input constant C-rate, $\bar{I}$, is given in Eq. (116). Note that this relationship can be extended to non-constant normalised currents, $\bar{I}(\hat{t})$, by integrating over time rather than multiplying. The 3600 appears here as C-rates are usually expressed in terms of hours rather than seconds, but real time is expressed as seconds. Similarly, the volume averaged integral of the lithiation fraction, $x(r, \hat{t})$, is also equal to the average lithiation fraction and is given in Eq. (117).

$$x_{av}(\hat{t}) = \bar{I} \frac{\hat{t}}{3600} \tag{116}$$

$$x_{av}(\hat{t}) = 3 \int_0^1 r^2 x(r, \hat{t}) dr \tag{117}$$

Eqs. (116) & (117) can be equated and by substituting dimensionless time, t, for $\hat{t}$ an expression for τ can be obtained and is given in Eq. (118) which is true for any value of t and $\bar{I}$. It should be noted that Eq. (118) is constant for all t and so can be used to indirectly

evaluate the accuracy of any numerical solution of $x(r,t)$ since the analytical solution is not trivial to calculate. As already established, $x(r,t)$ is completely determined by the parameter A in the boundary condition at the particle surface. Eq. (118) then allows calculation of τ for any choice of A. Therefore, a diffusion model has been established which is parameterised entirely by A. This reduces the search space when optimising as well as retaining the robustness that has already been established in the technique this far. The governing equations for the diffusion model are summarised in Table 1. Now attention must be turned to solving this system for general input of $\bar{I}$.

$$\tau = \frac{10800}{\bar{I}\,t} \int_0^1 r^2 x(r,t) dr \tag{118}$$

Table 18: Summary of diffusion model governing equations and restated equation numbers for reference.

Description	*Equation*	*Eq. #*
Spherical Diffusion Equation	$x_t(r,t) = x_{rr}(r,t) + \frac{2}{r}\, x_r(r,t)$	(109)
Boundary Condition r=0	$x_r(0,t) = 0$	(114)
Boundary Condition r=1	$x_r(1,t) = A\, \frac{\bar{I}(t)}{1 - LAM}$	(113)
Initial condition	$x(r,0) = x_0(r)$	(119)
Conservation of mass	$x_{av}(t) = 3 \int_0^1 r^2 x(r,t) dr$	(117)

5.2.2 Numerical solution of non-dimensional diffusion equation

An analytical solution to the non-dimensional diffusion equation could feasibly be constructed for very simple input $\bar{I}$ such as constant current. However, for an arbitrary load this is much less trivial to do, and the system of equations is better solved numerically. The numerical scheme will employ a grid structure as shown in Figure 51 where radius is represented by equally spaced discretised points from 0 – 1 with a spacing of Δr. Similarly, time is discretised in equally spaced points, starting from 0 and advancing with spacing of Δt. Numerical analysis is prone to instabilities and so a scheme must be chosen which is stable for any choice of Δr & Δt. The Crank-Nicolson (CN) scheme is a widely used and is known for being numerically stable when solving heat / diffusion equations in the cartesian domain. Eq. (107) is in the spherical domain, however by using the substitution given in Eq. (120), Eq. (107) is transformed to the cartesian diffusion equation in $u(r,t)$. The governing equations representing the system are redefined with this substitution in eqs (121) - (125).

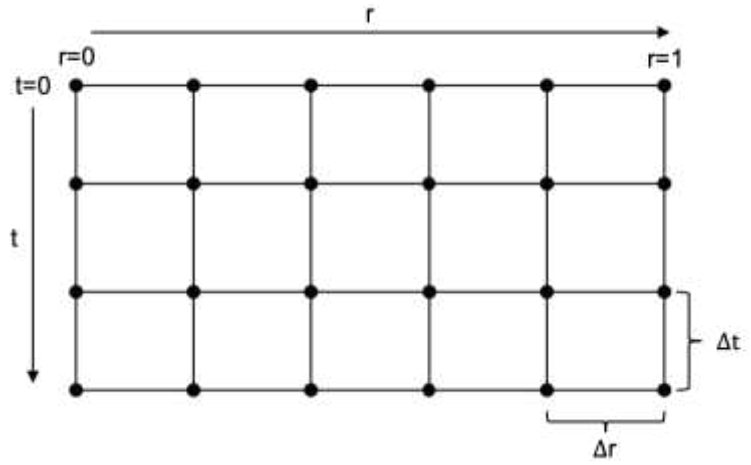

Figure 51: Numerical grid scheme used to solve diffusion equation in space and time

$$u(r,t) = r\,x(r,t) \tag{120}$$

$$u_t(r,t) = u_{rr}(r,t) \tag{121}$$

$$u(0,t) = 0 \tag{122}$$

$$u_r(1,t) - u(1,t) = A\frac{\bar{I}(t)}{1 - LAM} \tag{123}$$

$$u(r,0) = r\, x_0(r,0) \tag{124}$$

$$x_{av}(t) = 3\int_0^1 r\, u(r,t)dr \tag{125}$$

The CN scheme can be defined for eqs. (121) - (124). The CN method is an implicit numerical scheme which means that all points forward in one timestep must be solved simultaneously as opposed to explicit schemes such as forward Euler. This adds computational complexity to the method as the simultaneous solving requires the creation of a set of linear equations and the subsequent inversion of this matrix to solve the system for the next timestep. What the CN scheme adds in its complexity it makes up for in its stability; the scheme is stable for all values of Δr and Δt. This is especially important in the case of the non-dimensional diffusion equation as the real world timestep that is defined during the experiment is not the same as the non-dimensional timestep. A scheme that is stable regardless of choice of timestep is therefore very useful. The CN scheme for the system defined by eqs. (121) - (124) is given in eqs. (126) - (128). The subscript i represents the radius discretisation point, the superscript n represents the time discretisation point and m is the final radius discretisation point. A full derivation of the CN scheme can be found in [111].

$$\begin{aligned} -\lambda\, u_{i-1}^{n+1} + (2+2\lambda)\, u_i^{n+1} - \lambda\, u_{i+1}^{n+1} \\ = \lambda\, u_{i-1}^{n} + (2-2\lambda)\, u_i^{n} + \lambda\, u_{i+1}^{n} \qquad i = 1,2 \ldots m-1 \end{aligned} \tag{126}$$

$$\begin{aligned} -\lambda\, u_{m-1}^{n+1} + \big(1+\lambda(1-\Delta r)\big)u_m^{n+1} \\ = \lambda u_{m-1}^{n} + \big(1-\lambda(1-\Delta r)\big)u_m^{n} + \frac{\lambda \Delta r A(\bar{I}^n + \bar{I}^{n+1})}{1 - LAM} \end{aligned} \tag{127}$$

$$u_0^{j+1} = 0 \tag{128}$$

$$\lambda = \frac{\Delta t}{(\Delta \mathrm{r})^2} \tag{129}$$

The above set of equations represent a set of $m + 1$ linear equations which can be solved by Gaussian elimination of the matrix representing the coefficients of the left-hand-side of the set of equations. The matrix representation of the system is given in Eq. (130) where $\mathbf{\Lambda}^{n+1}$ represents the CN matrix coefficients to calculate u^{n+1} at each radius points and is given in Eq. (131). The vector $\vec{d}^n$ represents the right-hand-side of eqs. (126)-(128) and is given in Eq. (132). The CN scheme begins with the initial conditions and then uses Eq. (130) to step through time and simultaneously calculate the values of u at all radial points for the next time step. As a set of simultaneous equations must be solved, the CN scheme is an implicit numerical scheme.

$$\mathbf{\Lambda}^{n+1}\ \vec{u}^{n+1} = \vec{d}^n \tag{130}$$

$$\mathbf{\Lambda}^{n+1} = \begin{pmatrix} 1 & 0 & 0 & 0 & \dots & 0 & 0 & 0 \\ -\lambda & 2+2\lambda & -\lambda & 0 & \dots & 0 & 0 & 0 \\ 0 & -\lambda & 2+2\lambda & -\lambda & \dots & 0 & 0 & 0 \\ \vdots & \vdots & \vdots & \vdots & \ddots & \vdots & \vdots & \vdots \\ 0 & 0 & 0 & 0 & \dots & -\lambda & 2+2\lambda & -\lambda \\ 0 & 0 & 0 & 0 & \dots & 0 & -\lambda & 1+\lambda(1-\Delta r) \end{pmatrix} \tag{131}$$

$$\vec{d}^n = \begin{pmatrix} 0 \\ \lambda\, u_0^n + (2-2\lambda)\, u_1^n + \lambda\, u_2^n \\ \vdots \\ \lambda\, u_{m-2}^n + (2-2\lambda)\, u_{m-1}^n + \lambda\, u_m^n \\ \lambda u_{m-1}^n + \big(1-\lambda(1-\Delta r)\big) u_m^n + \dfrac{\lambda \Delta r A(\bar{I}^n + \bar{I}^{n+1})}{1 - LAM} \end{pmatrix} \tag{132}$$

Once the values for $\vec{u}^{n+1}$ have been calculated, the lithiation fraction, $\vec{x}^{n+1}$, can be calculated. This is required to obtain values of open circuit voltages and entropy coefficients which are defined as functions of x. Using the relationship between u & x given in Eq. (120)

the lithiation fraction can be calculated. By doing this, x becomes undefined at $r = 0$. To account for this, we reinstate the symmetry boundary condition given in Eq. (114). The resulting scheme to calculate lithiation fraction, x, from u is given in eqs. (133) & (134).

$$x_i^n = \frac{u_i^n}{r_i} \quad i = 1 \dots m \tag{133}$$

$$x_0^n = x_1^n \tag{134}$$

5.2.3 Stability of scheme

The CN scheme introduced above is parameterised by the parameter λ, which is defined by the sizes of the radius and time steps. The time step used in solving the diffusion system is the non-dimensional time timestep, which is determined by τ and the size of the real-world time timestep. τ is determined by the parameter A through Eq. (113) and A is the parameter which is adjusted during the optimisation process. This means as the optimisation procedure to find A runs, the size of the timestep used in the numerical scheme changes between optimisation iterations, which changes the value of λ. Therefore, any scheme which is not unconditionally stable for λ would most likely cause the optimisation process to fail.

To evaluate the stability of the CN scheme, Von Neumann stability analysis is performed which is a common approach to evaluate the stability of numerical schemes. The starting point of the stability analysis is the CN numerical scheme in Eq. (126), repeated here for convenience.

$$-\lambda\, u_{i-1}^{n+1} + (2+2\lambda)\, u_i^{n+1} - \lambda\, u_{i+1}^{n+1} = \lambda\, u_{i-1}^{n} + (2-2\lambda)\, u_i^{n} + \lambda\, u_{i+1}^{n} \tag{135}$$

Von Neumann stability analysis involves making the substitutions given in eqs.(136) - (138). The substitutions arise from the Fourier decomposition of the numerical scheme rounding error, the derivation of which is outside of the scope of this thesis. The term $E_k(t)$ represents the amplitude of the error contributed by the k^{th} component of the Fourier decomposition of error at time t. $G(k)$ is the growth rate of the k^{th} component of error at each timestep. For the numerical scheme to remain stable, the growth rate of every component must be less than 1 as stated in Eq. (139) [110].

$$u_{i+m}^{n} = E_k(t) e^{ik(r+m\Delta r)} \tag{136}$$

$$u_{i+m}^{n+1} = E_k(t+\Delta t) e^{ik(r+m\Delta r)} \tag{137}$$

$$G(k) = \frac{E_k(t+\Delta t)}{E_k(t)} \tag{138}$$

$$G(k) \leq 1 \; \forall k \tag{139}$$

The conditions to ensure Eq. (139) is true can be found by substitution of Eqs. (136) - (138) into (126). Doing this and rearranging for $G(k)$ yields Eq. (140). By substitution of $\theta = 2\, k\Delta x$ and using the identity stated in Eq. (141), an expression for $G(\theta)$ is found and is given in Eq. (142). Since $\sin^2(\theta/2)$ can only take values over [0, 1], the maximum value for $G(\theta)$ and hence $G(k)$ is obtained when $\sin^2(\theta/2)$ is 0 as λ is a positive number, this maximum value of $G(k)$ is 1 which satisfies the stability criterion in Eq. (139). This maximum value for $G(k)$ is not a function of λ. Therefore, it can be said that the CN scheme is stable for all values of λ and thus is unconditionally stable.

$$G(k) = \frac{2 - \lambda\left(2 - \ e^{i\,k\Delta x} - e^{-i\,k\Delta x}\right)}{2 + \lambda(2 - \ e^{i\,k\Delta x} - e^{-i\,k\Delta x})} \tag{140}$$

$$\sin^2\left(\frac{\theta}{2}\right) = \frac{2 - e^{i\theta} - e^{-i\theta}}{4} \tag{141}$$

$$G(\theta) = \frac{8 - \lambda \sin^2(\theta/2)}{8 + \lambda \sin^2(\theta/2)} \tag{142}$$

5.2.4 Accuracy of scheme

The accuracy of a numerical scheme gives the size of the truncation error as an order of the step size used. In the CN scheme defined, there is a time dimension with timestep, Δt, and a spacial dimension with step in radius, Δr. By determining the accuracy of the scheme in both dimensions, the amount of error at each step in time and step in space is quantified. The accuracy in each dimension is defined as an order of the step size, for example a "second order accurate in time" would mean that the truncation error is of the order $(\Delta t)^2$. In this section we evaluate the truncation error for the CN scheme in both time and space dimensions.

In general, calculating orders of accuracy of a numerical scheme includes expressing the truncation error as the difference between the numerical scheme and the exact solution. In the CN scheme, the spatial derivative is the easier of the two to understand and so that is the first accuracy that will be calculated. The CN scheme uses a central difference scheme to approximate the spacial second derivative, given in Eq. (143). Here the notation differs slightly to the rest of the chapter, u_{rr}^i is the exact second derivative of u with respect to radius evaluated at the radius grid-point i. Here, the time index is omitted for clarity as all values of u are evaluated at the same timestep. Therefore, the truncation error can be

expressed as the difference between the exact derivative and the approximation. This is given in Eq. (144) where ε_r is the truncation error in the radial dimension.

$$u_{rr}^{i} \approx \frac{u^{i-1} - 2\,u^{i} + u^{i+1}}{(\Delta \mathrm{r})^2} \tag{143}$$

$$\varepsilon_r = \frac{u^{i-1} - 2\,u^{i} + u^{i+1}}{(\Delta \mathrm{r})^2} - u_{rr}^{i} \tag{144}$$

To evaluate this expression, a Taylor series expansion is done for the u^{i-1} and u^{i+1} terms. The general Taylor series expansion for $u^{i+\theta}$ is given in Eq. (145). Applying this formula to Eq. (144) for both $i+1$ and $i-1$ terms and simplifying yields the expression in Eq. (146). The lowest order term for Δr in this expression is second order. Therefore, the scheme is said to be second order accurate in the r dimension.

$$u^{i+\theta} \approx u^{i} + \frac{\theta \Delta \mathrm{r}}{1!}\, u_{r}^{i} + \frac{(\theta\, \Delta r)^2}{2!} u_{rr}^{i} + \frac{(\theta\, \Delta r)^3}{3!} u_{rrr}^{i} + \mathcal{O}(\Delta r^4) \tag{145}$$

$$\varepsilon_r = \frac{\Delta r^2}{12}\, u_{r4}^{i} + \mathcal{O}(\Delta r^4) \tag{146}$$

The above result is well known [111] and its rederivation was probably not necessary, however it does serve as a concrete example of the method to solve the accuracy of the more complicated time dimension which will be addressed now. The approximation of the time derivative in the CN scheme is given in Eq. (147). In the same way as was done for the radial dimension, the Taylor series expansion is written for u_t^{n+1} and u_{rr}^{n+1} using Eq. (145) and is substituted into the expression for the truncation error given in Eq. (148). After substitution and rearranging, an expression for the truncation error is obtained and is given

in Eq. (149). Further simplification of this can be made by noting that the first term on the right-hand-side is the diffusion equation which is equal to 0 as shown in Eq. (150). Furthermore, the second term on the right-hand-side is the time derivative of the first term which must also equal 0. The first two terms on the right-hand-side vanish, leaving only the second order term and the higher order terms as seen in Eq. (151). Therefore, the CN scheme is second order accurate in time as well as in space.

$$\frac{u_t^{n+1} - u_t^n}{\Delta \mathrm{t}} \approx u_t^{n+\frac{1}{2}} = \frac{1}{2}(u_{rr}^{n+1} + u_{rr}^n) \tag{147}$$

$$\varepsilon_t = \frac{u_t^{n+1} - u_t^n}{\Delta t} - \frac{1}{2}(u_{rr}^{n+1} + u_{rr}^n) \tag{148}$$

$$\varepsilon_t = (u_t^n - u_{rr}^n) + \frac{\Delta t}{2}(u_{tt}^n - u_{rrt}^n) + \Delta t^2\left(\frac{u_{(3t)}^n}{6} - \frac{u_{rrtt}^n}{4}\right) + \mathcal{O}(\Delta t^3) \tag{149}$$

$$u_t = u_{rr} \rightarrow u_t - u_{rr} = 0 \tag{150}$$

$$\varepsilon_t = \Delta t^2\left(\frac{u_{(3t)}^n}{6} - \frac{u_{rrtt}^n}{4}\right) + \mathcal{O}(\Delta t^3) \tag{151}$$

5.2.5 Speed of Model

The model and corresponding numerical scheme have been shown to be unconditionally stable and second order accurate in both radial and time dimensions. These are very attractive attributes of a model however the time it takes for the model to solve is yet to be considered. This is especially important as the model is to be used in an optimisation procedure whereby ~1000 evaluations of the model must take place each time the diagnostic technique is run. Typically, the data captured experimentally is at a frequency of 1 Hz and typical experimental time is of the order 1 hour, meaning the model must solve

around 3000 timesteps each time it is run. In all performance tests given here, the number of timesteps evaluated are 3000 and the number of radius points solved for is 100.

The speed of the model is evaluated using MATLAB's "timeit" function which gives the average time for the model to run over a large number of evaluations. On running the model through the "timeit" function, the average time to run is 0.3 s which when considered for two electrodes, is 0.6 s. While this may not seem like a large amount of time, in an optimisation routine, this could mean running times of ~10 minutes. While this is not necessarily a problem as the time between diagnoses is much larger than this, a shorter run time is always desirable especially during the development phase.

The main computationally expensive task in running the model is the inversion of the matrix $\mathbf{\Lambda}$ which is repeated below from Eq. (131) for convenience. The matrix dimensions are M x M where M is the number of radius discretisation points. The matrix inversion is necessary as the scheme is implicit rather than explicit meaning the equations must be solved simultaneously rather than in a 1-by-1 fashion. Explicit schemes have $\mathcal{O}(M)$ calculations per timestep. On the other hand, matrix inversion typically takes $\mathcal{O}(M^3)$ calculations [112] making implicit schemes much slower to solve than explicit ones. This is the penalty that is paid when using an implicit scheme; the increase in accuracy and stability comes at a cost of computational speed.

$$\mathbf{\Lambda}^{n+1} = \begin{pmatrix} 1 & 0 & 0 & 0 & \dots & 0 & 0 & 0 \\ -\lambda & 2+2\lambda & -\lambda & 0 & \dots & 0 & 0 & 0 \\ 0 & -\lambda & 2+2\lambda & -\lambda & \dots & 0 & 0 & 0 \\ \vdots & \vdots & \vdots & \vdots & \ddots & \vdots & \vdots & \vdots \\ 0 & 0 & 0 & 0 & \dots & -\lambda & 2+2\lambda & -\lambda \\ 0 & 0 & 0 & 0 & \dots & 0 & -\lambda & 1+\lambda(1-\Delta r) \end{pmatrix} \quad (131)$$

The matrix $\mathbf{\Lambda}$ does however have a promising property in that it is a tridiagonal matrix. This means only the leading 3 diagonals contain elements and the rest of the elements are zero. The Thomas algorithm is an efficient algorithm for solving linear systems of equations where the matrix to be inverted is tridiagonal [113]. For the Thomas algorithm to be stable, the matrix must be diagonally dominant, that is the magnitude of the leading diagonal term must be greater than or equal to the sum of the magnitude of all other terms in that row or column. It is seen by inspection that this is true for $\mathbf{\Lambda}$ in both the row and column directions and so the Thomas algorithm can be used to solve the system of equations. The implementation details of the Thomas algorithm can be found in [113].

The model's run time is re-evaluated after implementation of the Thomas algorithm using MATLAB's "timeit" function. The average run time of the model is now found to be 30ms, a full order of magnitude faster than before the Thomas algorithm was implemented. This means that the optimisation procedure with ~1000 evaluation of the model for both electrodes would take ~1 minute which makes the model much easier to work with and to use. Figure 52 shows how the model run time varies for different numbers of timesteps and radius points. It is seen that in both cases the Thomas algorithm significantly outperforms the standard matrix inversion algorithm. Both model's runtimes increase linearly with additional timesteps, with the Thomas algorithm increasing as a slower rate than matrix inversion. For increasing number of radius points, both runtimes increase exponentially when plotted on a log scale with the Thomas algorithm increasing at a slower rate. It has therefore been shown that the Thomas algorithm outperforms the standard matrix inversion algorithm in all cases.

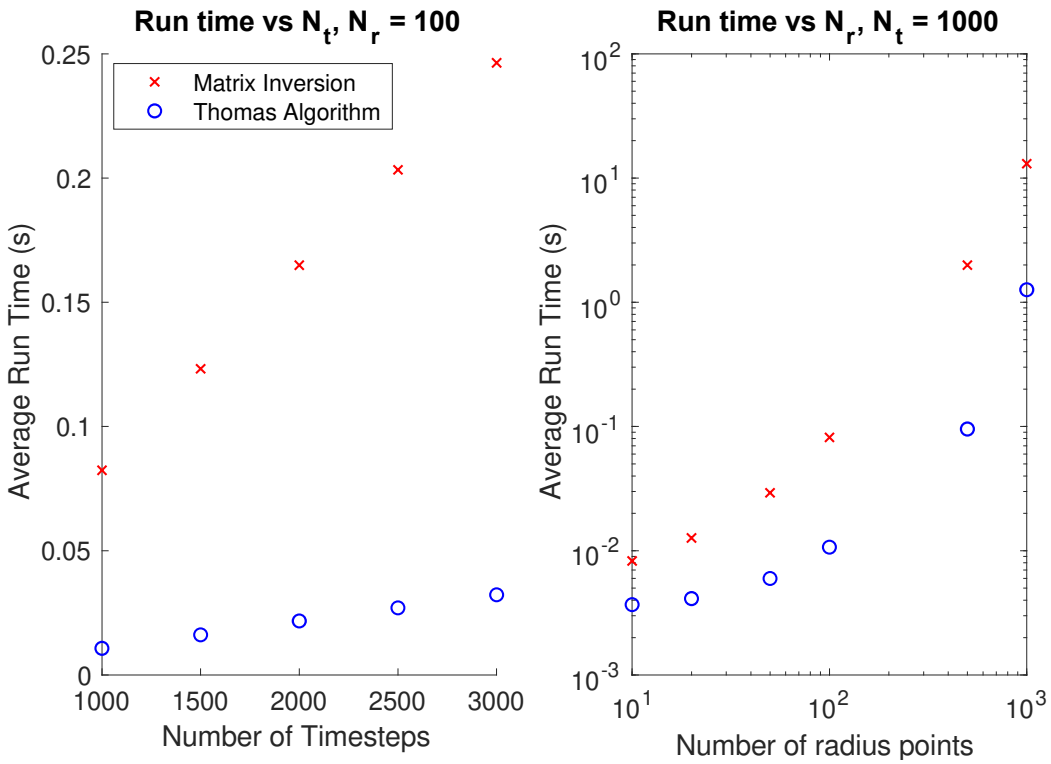

Figure 52: Average model run time for different numbers of timesteps and radius points

5.2.6 Validation of the diffusion model against open-source battery modelling software

To validate the model developed for this thesis, the model can be compared to the open source battery modelling packages from PyBaMM. In this section, the surface lithiation fraction versus time and the lithium fraction distribution throughout the particle are compared for the model developed in this thesis and the single particle model solved using PyBaMM. The PyBaMM code used to generate the data from PyBaMM is taken from the guide in the PyBaMM documentation found in [114] which guides the user to setting up the negative electrode particle domain and sets up the necessary equations, boundary and initial conditions and discretization scheme to find the surface concentration and the spatial distribution of lithium concentration.

The model created in PyBaMM is a spherical diffusion equation without any of the non-dimensional quantities that are present in the model developed in this section. The equations describing the concentration of lithium in a spherical particle is given in Eq. (152) To make these equations comparable to the non-dimensional equations derived in this thesis, the values of D and R are set to equal 1. The initial concentration, c_0, is set to 0.

$$\frac{\partial c}{\partial t} = \frac{1}{r^2}\frac{\partial}{\partial r}\left(r^2 D \frac{\partial r}{dr}\right), \quad 0 \leq r \leq R \tag{152}$$

$$\left.\frac{\partial c}{\partial t}\right|_{r=0} = 0 \tag{153}$$

$$\left.\frac{\partial c}{\partial t}\right|_{r=R} = -\frac{j}{F\ D} \tag{154}$$

$$c(r, 0) = c_0 \tag{155}$$

The next consideration is how the non-dimensional time and seconds equate. The non dimensional time is linked to seconds by the time constant of the system as given in Eq. (106). It can be seen in Eq. (106) that by setting the time constant to 1, the non-dimensional time is equivalent to time in seconds. The time constant is calculated by Eq. (108). It can be seen that as R and D are set to 1, the time constant can be set to 1 by making the gradient of concentration with lithiation fraction, c', also equal to 1. The concentration is related to the lithiation fraction by Eq. (104). As c' is set to 1, the value of c_{lower} can be set to 0 and then the concentration is equal to the lithiation fraction.

Finally, the boundary condition at the surface of the particle must be equated between both models. If j is set to equal $-F$ in Eq. (154) and A is set to 1 in Eq. (115) then the systems of equations are equivalent.

With the systems made equivalent, the models are simulated over 1 second with 100 timesteps and 60 radial elements. The surface lithiations of each models from the simulation are plotted in Figure 53 as well as the difference between the models are given. It is seen that there is very little difference between the models, an error small enough to be attributed to discretization schemes and solving methods. The surface concentration is the key quantity that needs to be correct in the model developed in this thesis as it is the key quantity that is used when calculating the heat generation.

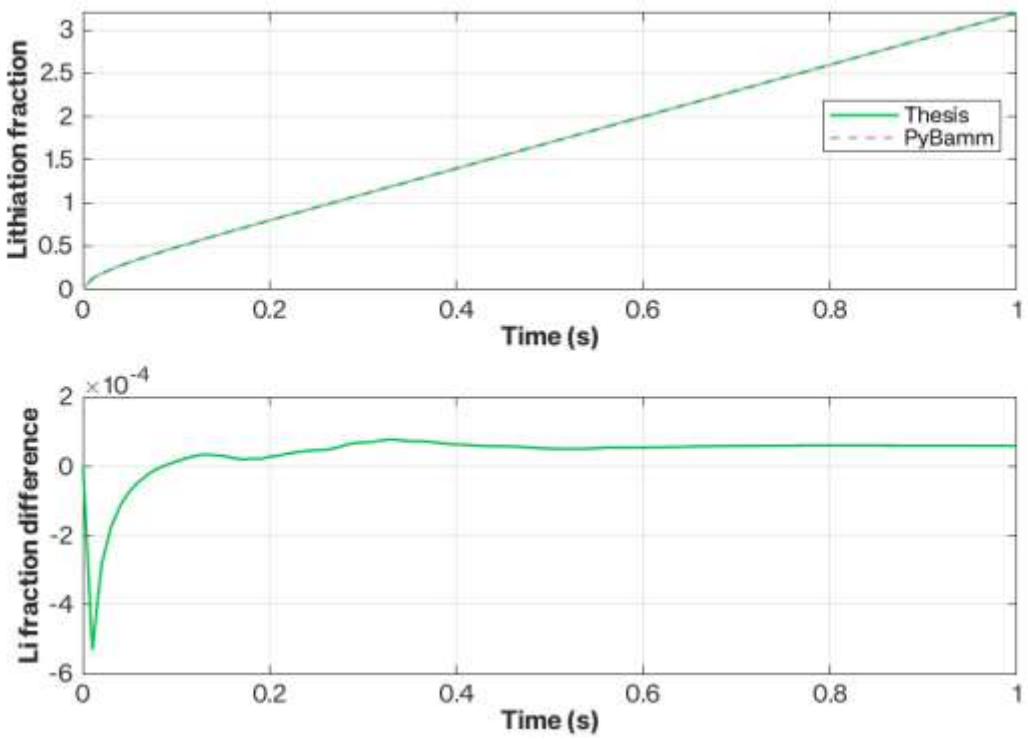

Figure 53: The surface concentration of lithium versus time for the model developed in this thesis and PyBaMM (top) and the difference between both models at each time step (bottom).

To further confirm that the models are equivalent, the lithiation fraction distribution throughout the particle is given in Figure 54. There is a slight difference between both models which gets worse for a smaller number of radial elements. This is due to the model in this thesis calculating the values at the boundaries of the elements whereas PyBaMM uses a finite volume method where the value at the centre of the element is calculated. At higher numbers of elements, both models converge to the same result. With the radial distribution of lithiation and the surface lithiation versus time being very similar in both cases, it is assumed that the model developed in this thesis gives correct results.

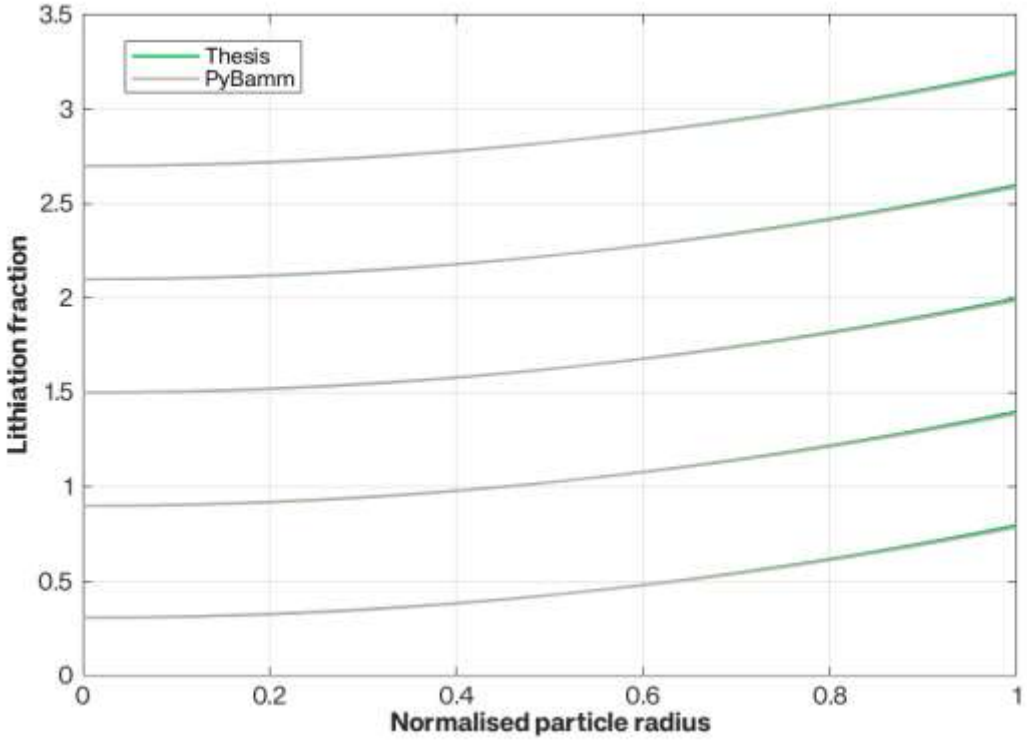

Figure 54: Lithiation fraction versus particle radius position as several timesteps for the model developed in this thesis versus PyBaMM

5.3 Integrating diffusion model with diagnostic technique

Now that the diffusion model is defined and its performance evaluated, it can be integrated with the diagnostic technique. This section first outlines the theory for calculating heat generation with diffusion considerations and what other parameters are necessary in the diagnostic technique. Then the overall algorithm and framework is given for the improved diagnostic technique.

5.3.1 Calculating heat generation with diffusion

Both the irreversible and reversible heat generations are a consequence of the reactions happening at the surface of the electrode particles. This means that the heat generation

with diffusion is calculated with the values of OCV and entropy at the surface of the electrode. Aside from this there are no changes to the way that the heat generation is calculated. The equations used to calculate irreversible and reversible heat generation are given in Eqs. (156) & (157).

$$q_{irr} = \big(V - U(r=1)\big)I \tag{156}$$

$$q_{rev} = I\,T\left(\frac{\partial U}{\partial T}\right)_{r=1} \tag{157}$$

5.3.2 Optimisation algorithm for diagnostic technique

As in the previous chapter, the goal of the diagnostic technique is to be able to predict amounts of LAM and loss of lithium inventory (LLI) by estimating the electrode capacities and their offset. To do this, an optimisation routine has been developed which aims to minimise the error between the measured and modelled heat generation, with electrode capacities and offset as parameters to find. The goal of this version of the diagnostic technique is the same as the previous version, however there are 2 additional parameters: the diffusion parameters, A_{PE} and A_{NE}. Under the assumptions in the model, these parameters do not change and so need only to be parameterised once, most sensibly at the beginning of the cell's life. Once the diffusion parameters are known, the optimisation parameters are only the stoichiometric parameters as is the case in the previous version of the diagnostic technique.

There are two choices for determining the diffusion parameters at beginning of life, the first is to produce heat generation data and run an optimisation procedure for both the stoichiometric parameters and diffusion parameters, optimising 5 parameters and 1 initial

condition for a total of 6 optimisation variables. Alternatively, the beginning of life OCV data for the cell can be used with an OCV model to determine the stoichiometric parameters, a total of 4 optimisation variables - 3 stoichiometric parameters and 1 initial condition. With these parameters determined, heat generation data for the cell can be collected and the diffusion parameters can be estimated given the known stoichiometric parameters for a total of 3 optimisation variables - 1 diffusion parameter for each electrode and 1 initial condition.

Of the two approaches above, the latter may add the need for OCV data at beginning of life but has a lower number of parameters in the optimisation procedures. This means the results obtained from the optimisation are more likely to be closer to the true values as fewer local minima exist in the optimisation search space. It is felt that the increased confidence in the results outweighs the burden added by requiring an OCV dataset at the beginning of life. Oftentimes the OCV data is contained in the cell manufacturers datasheet or is measured as a parameterisation dataset anyway. Therefore, if the dataset is likely to already exist this method of optimisation adds little in the way of experimental burden.

Figure 55 shows a flow chart for how the optimisation procedure and models defined above work together in the optimisation process. The optimisation process is the same for the beginning of life optimisation of the diffusion parameters and the subsequent optimisation for extracting the degradation modes. The only difference between these processes is the parameter vector, $\vec{p}$, that is optimised over.

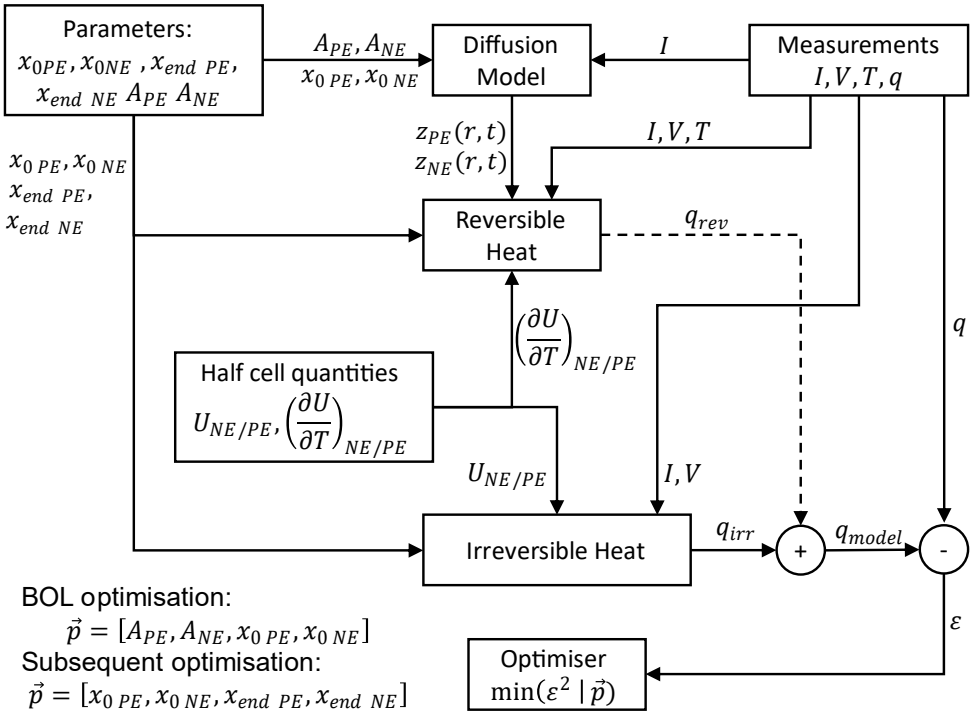

Figure 55: Flowchart of diagnostic optimisation algorithm. Arrows show direction of information flow and boxes represent sub models in the diagnostic technique framework.

5.4 Evaluation of extended technique on high-energy cells

With the framework of the improved technique laid out, its performance is evaluated on a commercial high-energy cell. In this section first the beginning of life parameterisation is performed: The OCV of the cell is used to determine the electrode capacities and offset and then heat generation is measured for a high-rate experiment which is used to determine the diffusion parameters. Next the cell is degraded, and the heat generation of the cell is measured for a range of C-rates under both charge and discharge. With this data the stoichiometric parameters are evaluated using the diagnostic technique both with and without the diffusion addition. The results for both versions of the model are compared to the stoichiometric parameters predicted by an OCV model after degradation. The accuracies of both models are compared and a discussion of the differences between model predictions is given.

5.4.1 Beginning of Life Characterisation & Robustness of Results

The beginning of life characterisation first involves an OCV measurement for the cell whose half-cell OCVs are then manipulated to best match the OCV. The cell used in this work is a 7.5Ah Kokam cell with an NMC-LCO blended positive electrode and a graphite negative electrode. The details of the cell used in the study are given in Table 19. The pseudo OCV of the cell was calculated by conducting a C/25 charge and discharge of the full SOC window of the cell. The average between charge and discharge was taken at each SOC point to give the pseudo OCV. The positive and negative electrode active materials are the same in this cell as in the cell used in the previous chapter and so the same half-cell OCVs and entropies are used in this study as the last. As a reminder, the pseudo OCVs of the half cells were taken at C/100 for both charge and discharge and the average taken in the same way as the full cell.

Table 19: High-energy cell parameters

Parameter	*Value*
Capacity	7.5Ah
Manufacturer	Kokam
Nominal Voltage	3.7V
Negative Electrode	Graphite
Positive Electrode	NMC-LCO blend

From the OCV data, an OCV based diagnostic model is used to determine the stoichiometric parameters of the cell by fitting the half-cell derived OCV to the measured full cell OCV. The results of the best fit half-cell OCV and the measured OCV are plotted in Figure 56. From this figure it can be seen that there is good agreement between the two sets of curves, all major features are captured. Firstly the “knee” at 600mAh is captured by the model and is in a

similar place to the measured OCV. Similarly, the hump at ~3000mAh in the measured data is matched by the model. There is a slight discrepancy at ~4000mAh where the modelled OCV underestimates the measured. However, the shape of the rest of the measured OCV curve is captured by the modelled OCV and so it is assumed that the stoichiometric parameters predicted by the OCV model are accurate.

The stoichiometric parameters predicted are given in Table 20 along with the maximum obtainable cell capacity. The parameters are as expected; excess negative electrode capacity to avoid plating at high SOCs, an offset that is positive meaning the negative electrode is the limiting electrode at low SOCs. The loading ratio between the electrode, the capacity of the positive electrode to the negative electrode is 1.1, lower than the loading ratio of ~1.5 seen for the higher-power cell. This is because the high-energy cell doesn't need as much negative electrode capacity in excess as the cell sees lower currents and hence has less chance of plating by the anode voltage reaching 0V. From these observations, confidence can be placed in the stoichiometric parameters obtained from the OCV model.

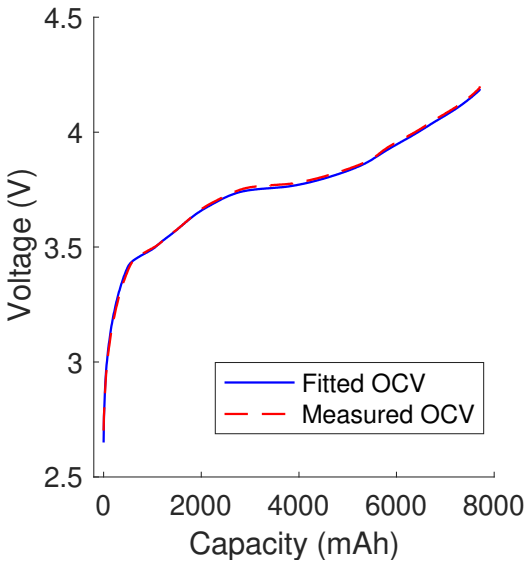

Figure 56: Half-cell fitted and measured OCV curves vs. capacity

Table 20: Stoichiometric parameters of high energy cell predicted by OCV model

Parameter	*Value (mAh)*
Cell Capacity	7709
C_{NE}	9499
C_{PE}	8620
Offset	892

With the stoichiometric parameters calculated by the OCV model, the diffusion related parameters can be estimated from heat generation data. The heat generation test was performed for a 2C constant current discharge. This is because concentration effects are most visible under as high of a C-rate as possible and 2C discharge is the highest rate permitted in the manufacturer's datasheet. The schematic for the experimental set up to measure heat generation is shown in Figure 57. The set up in principle is identical to the set-up used in the previous experiments, adjusted slightly for the shape of the cell. The main heat rejection path is still through the tabs of the cell. The rate of heat generation of the cell is measured by calculating the heat leaving through the tabs and any losses through the insulation plus the heat accumulated in the cell.

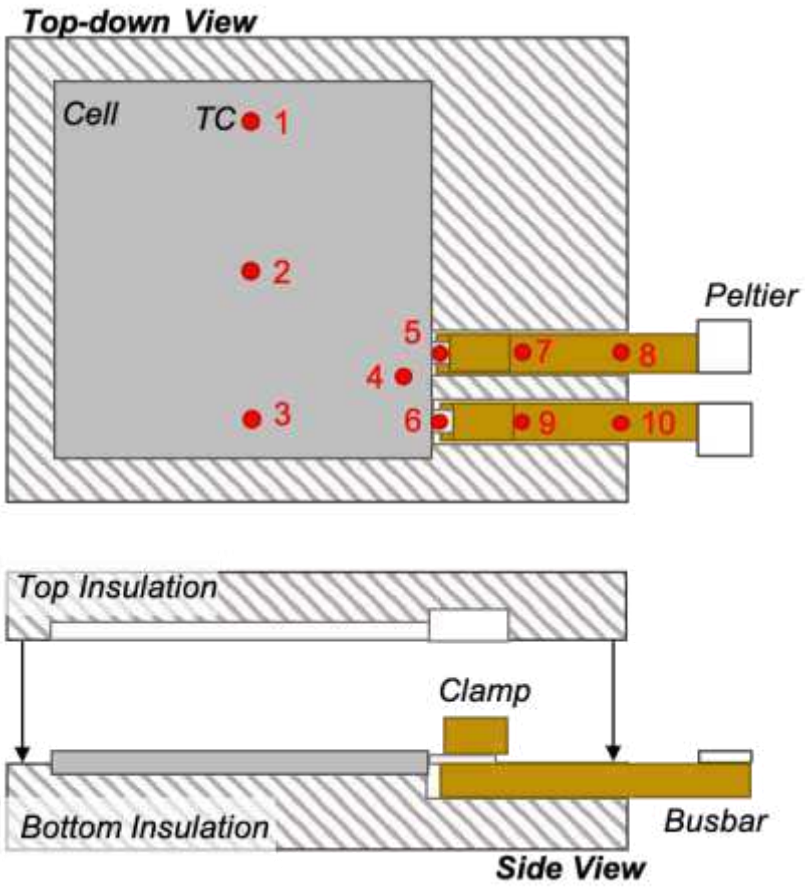

Figure 57: Schematic of experimental set up to measure heat generation, arrows show top insulation sits atop of the cell.

The heat pathway schematic is shown in Figure 58 is operationally identical to that used in the previous experiments. The equations to calculate heat generation are given in eqs. (158) - (161). The values for R_{loss}, R_{tab+} and R_{tab-} are calculated from characterisation experiments where the ends of the busbar are held at a raised temperature compared to ambient and steady state is reached after several hours. The heat transfer through both busbars and hence tabs is then calculated using eqs. (162) & (163) where R_{bb} is the busbar thermal resistance between the thermocouples on each busbar. With the heat flow into each tab known, R_{tab+} and R_{tab-} can be estimated by rearranging eqs. (160) & (161). The heat flows through the tab must be leaving the cell as q_{loss} and so Eq. (159) can be rearranged to estimate R_{loss}.

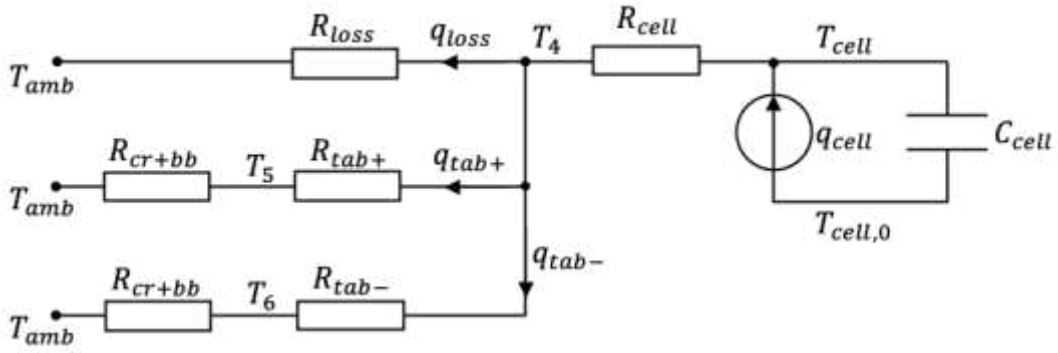

Figure 58: Heat pathway schematic as electrical equivalent circuit

$$q_{cell} = C_{cell}\,\dot{T}_{cell} + q_{tab-} + q_{tab+} + q_{loss} \tag{158}$$

$$q_{loss} = \frac{T_4 - T_{amb}}{R_{loss}} \tag{159}$$

$$q_{tab+} = \frac{T_4 - T_5}{R_{tab+}} \tag{160}$$

$$q_{tab-} = \frac{T_4 - T_6}{R_{tab-}} \tag{161}$$

$$q_{tab+} = \frac{T_8 - T_7}{R_{bb}} \tag{162}$$

$$q_{tab-} = \frac{T_{10} - T_9}{R_{bb}} \tag{163}$$

The heat generation rate is then calculated over the duration of 2C discharge test and the beginning of life optimisation for the diffusion parameters described in section 5.3.2 is then performed. The measured and optimised modelled heat generation for the 2C discharge are plotted. The modelled heat generation is optimised with different initial values which are given in the legend of Figure 59. The resulting values of the diffusion parameters after the optimisation are given in Table 21. It is seen in Figure 59 that the modelled heat generation fit is robust to the initial guess with all modelled heat generation profiles being very similar.

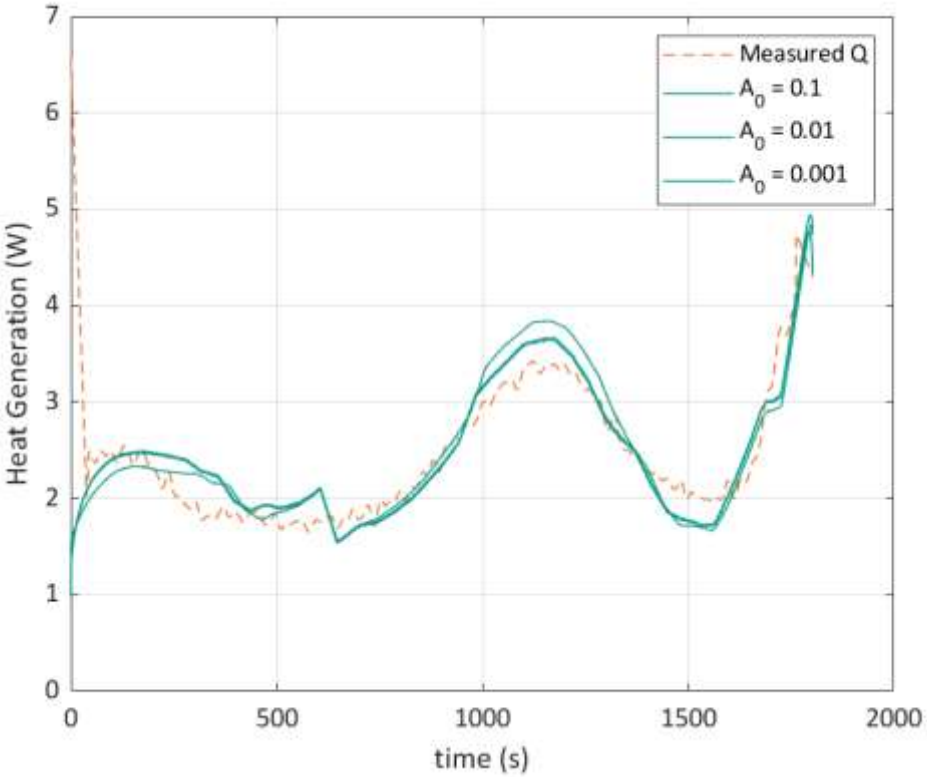

Figure 59: Measured (orange dashed) and modelled (solid teal) heat generation after optimisation for a range of initial guess values for the diffusion parameter A_0.

Table 21: Diffusion parameters obtained from BOL characterisation for different initial guesses

A_0	0.1	0.01	0.001
A_{PE}	0.0583	0.0614	0.0507
A_{NE}	0.0900	0.0107	0.00185

The values the obtained diffusion parameters are given in Table 21. The differences in ranges of values in Table 21 for the final values of the diffusion parameters suggest that the heat generation fit is more sensitive to positive electrode diffusion than negative electrode diffusion. The positive diffusion value has similar values regardless of the optimisation starting point whereas the negative electrode diffusion value varies by an order of magnitude. The Fisher information matrix (FIM), $\mathcal{F}$, can be used to quantify the sensitivity of

the optimisation problem to each parameter. The elements of the FIM are calculated using Eq. (164) where θ_i is the i^{th} parameter and y_n is the n^{th} point in the modelled response evaluated for the parameter set, $\vec{\theta}$. The leading diagonal of $\mathcal{F}$ is the sum of the squared change in y for a small change in θ_i, which can be thought of as the steepness of the optimisation landscape in the direction of θ_i. Therefore, the leading diagonal of $\mathcal{F}$ is the sensitivity of the model to each parameter. This sensitivity is calculated at the different initial points given in Table 21 and the results are given in Table 22.

$$\mathcal{F}_{ij} = \sum_n \left(\frac{\partial y_n}{\partial \theta_i}\right)_{\vec{\theta}} \left(\frac{\partial y_n}{\partial \theta_j}\right)_{\vec{\theta}} \tag{164}$$

Table 22: Fisher sensitivity evaluated at several different parameter set locations

A_0	0.1	0.5	1	2
$\mathcal{F}_{APE}$	0.0739	100	435	4110
$\mathcal{F}_{ANE}$	0.231	25.4	132	793

The values in Table 22 give the sensitivity, the leading diagonal of the FIM, of the model to small changes in each parameter. Here, a larger number means the model is more sensitive to the parameter at the point given by A_0. Around the optimal value, ~0.1, the sensitivity of the model to the parameters is small, this is sensible as it is assumed a minimum exists at this point and so the derivative of the model will be small at this point. In fact, when this point is considered in isolation, the sensitivity of the positive electrode diffusion coefficient, $\mathcal{F}_{APE}$, is smaller which is the opposite of what we would expect given the earlier discussion on the observed variability in the values in Table 21. However, as the initial point moves further away from the location of the minima, the sensitivity of the model to A_{PE} grows

much faster than that to A_{NE}. This makes sense and can be thought of as meaning the slope of the optimisation landscape is gentle in A_{NE} and is steep in A_{PE}. This difference in slope means that the optimisation process is more likely to converge on a solution for A_{PE} than A_{NE} which explains the higher variation for A_{NE} seen in Table 21.

The result explained in the previous paragraph echoes the findings from the evaluation of the 0-D model, that changes in positive electrode related parameters have a much bigger effect on the modelled heat generation than the negative electrode. This does raise the question of how robust the estimates of A_{PE} and A_{NE} are and to answer this question a similar analysis should be performed as in the chapter on the 0-D heat generation model. However, this sort of analysis is very time consuming to perform on a model which takes 1 minute per optimisation – compared to ~1s for the 0-D model. Therefore, in this section a simpler approach is taken.

The optimisation routine has been shown to be robust to initial guess for A_{PE} but less so for A_{NE} which is expected from the discussion in the previous chapter. The next logical step is to examine the robustness of the parameterisation to the load profile used. So far, a 2C discharge has been used to perform the characterisation, however the robustness should at least be explored for other loads. To test this, another set of heat generation experiments are performed. These experiments are a C/2 charge and discharge and a 1C discharge. For each dataset the same set of initial guesses are used which are the same as those given in Table 21.

Figure 60 shows the heat generation fits for several different parameter initial values for each of the load profiles discussed above. Each plot has 4 solid blue lines, however in all cases the lines stack atop of each other. This means that for the 4 load cases given, the optimisation routine is robust to the initial guess of the parameters. Table d gives the average and range of optimal values for A_{PE} & A_{NE} across all initial guess values for each load profile. It is seen that the value for both diffusion parameters varies significantly between the different load profiles, especially when compared to the variability in parameters across the different optimisation initial guesses for each cycle, given as ΔA. This raises the question of how to choose the correct value for the diffusion parameters. To investigate this further, the sensitivity evaluated visually, by plotting the resulting heat generation profile for each set of average values in Table 23.

Table 23: Average and range of diffusion parameters across different optimisation initial values for different load profiles.

	2C Discharge	**1C Discharge**	**C/2 Discharge**	**C/2 Charge**
$\bar{A}_{PE}$	0.0568	0.0884	0.1126	0.0535
ΔA_{PE}	0.0107	4.94E-4	0.0037	0.0160
$\bar{A}_{NE}$	0.0336	0.0282	0.0349	0.0987
ΔA_{NE}	0.0898	0.0774	0.104	0.109

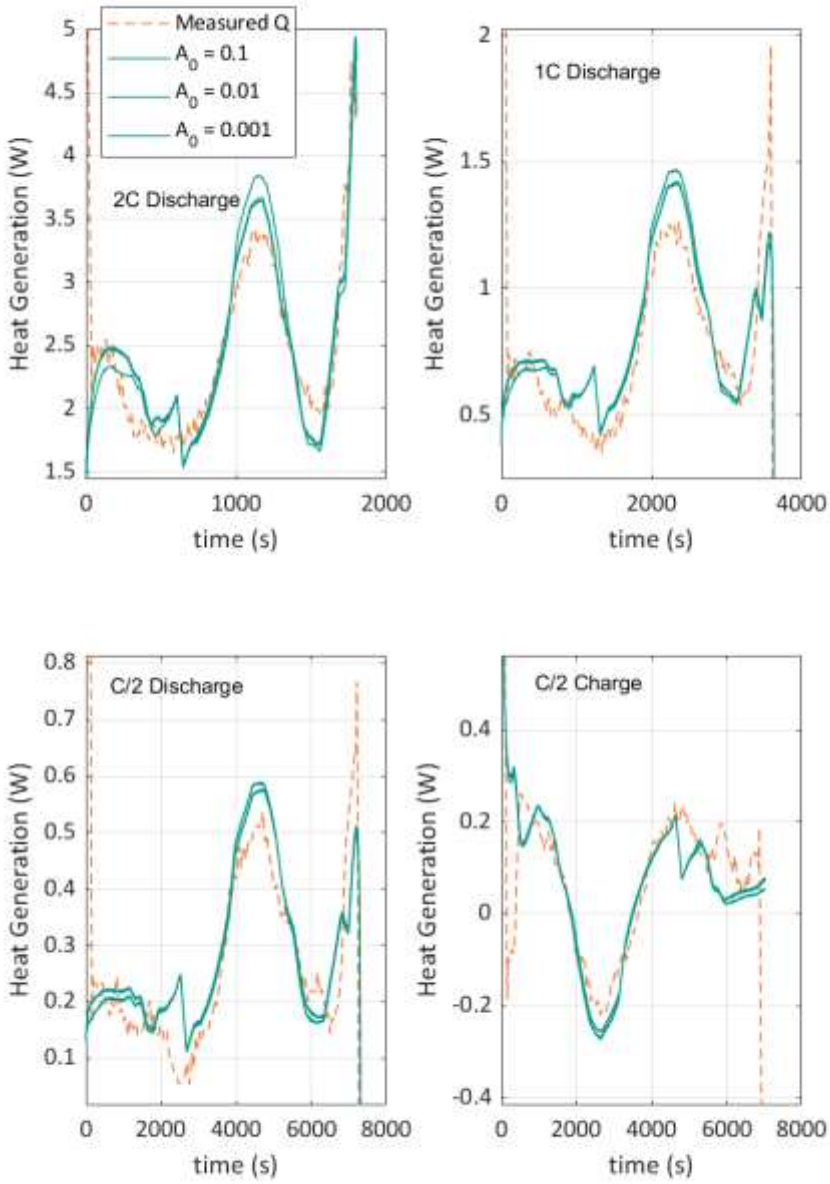

Figure 60: Measured (orange dashed) and optimised modelled (teal solid) heat generations for a range of different loads and optimisation initial conditions

Figure 61 shows the variation in the modelled heat generation profiles when the different sets of values for A are used from Table 23. Clearly, and perhaps unsurprisingly, the highest rate test, a 2C discharge, sees the largest change for the different values of A_{PE} & A_{NE} used. The second highest rate test, 1C discharge, then sees the next largest change. At this point, it would be simple to discard the 1C & C/2 discharge and C/2 charge results and say that the

diffusion parameters are those predicted by the 2C discharge dataset as this is the most sensitive. However, data should never be discarded as any additional measurements will improve confidence in the final results produced. Instead, a pseudo global optimisation technique will be used whereby a weighted average of the optimum parameters for each load is used to calculate the final set of parameters. The weightings are calculated using the FIM diagonal terms.

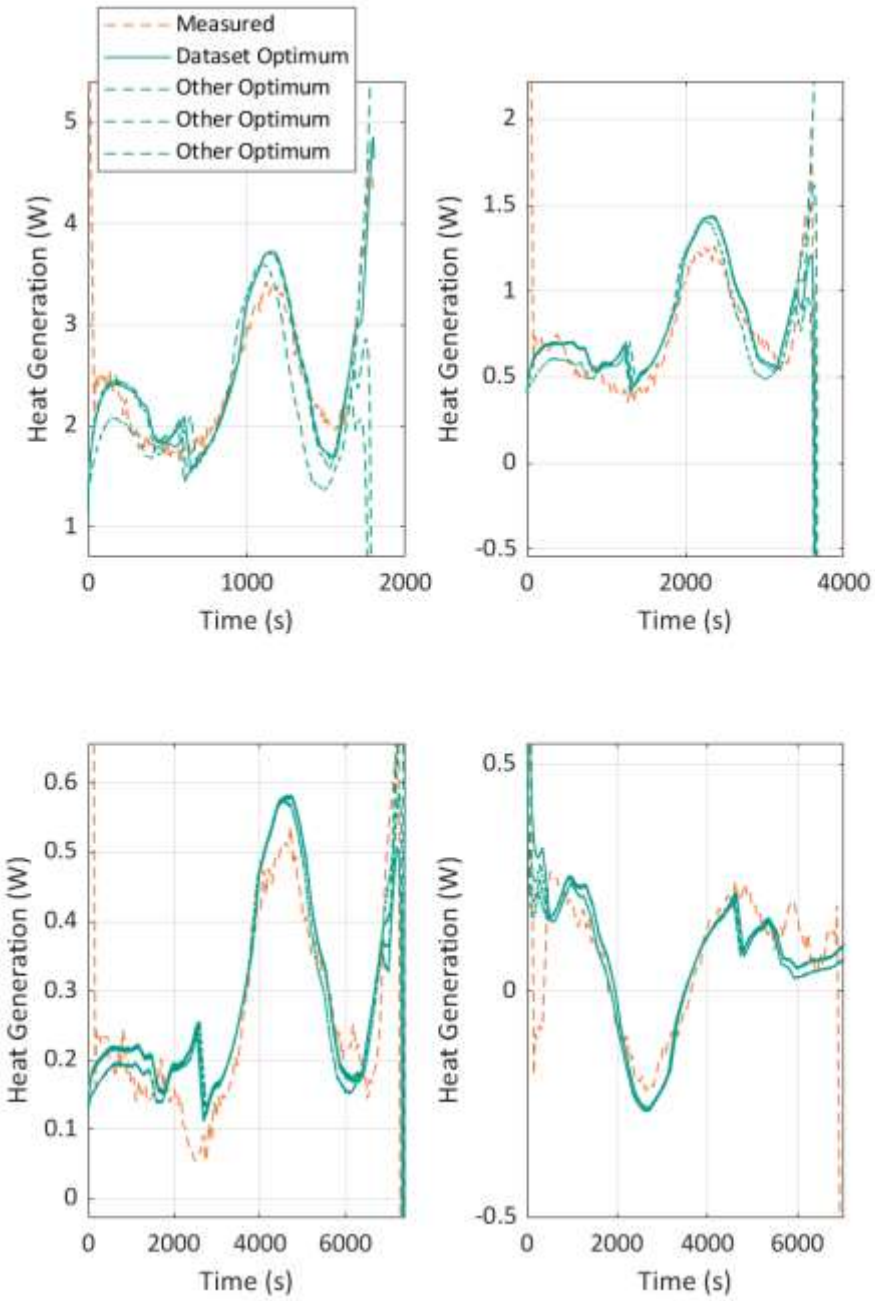

Figure 61: Differences in modelled heat generations (teal) for various average parameter values calculated through optimisation at each load cycle in Table 23. Measured (orange dashed) shown for reference.

The weightings for each load profile's optimum diffusion parameters are calculated as the fraction of that load profile's information content, $\mathcal{F}_j$, of the total information content, $\mathcal{F}$, across the 4 datasets. The weight is expressed mathematically in Eq. (165) and the calculations for $\mathcal{F}$ and $\mathcal{F}_j$ are given in eqs. (166) & (167). $\mathcal{F}_{ij}$ is the average of the squared

sensitivity between the optimum point for dataset, j, and an optimum point for another of the datasets, i. Eq. (168) gives the calculation for $\mathcal{F}_{ij}$ where N_j is the number of datapoints in dataset j. Eq. (169) gives the calculation of the sensitivity term, where $\hat{\theta}$ represents the optimum values of the diffusion parameter for the subscripted dataset. This analysis is done for one parameter at a time, so when calculating each F_j, either A_{PE} or A_{NE} is varied to the optimum of the other datasets while the other stays fixed at the optimum for dataset j. The procedure is then repeated for the other parameter.

$$w_j = \frac{\mathcal{F}_j}{\mathcal{F}}, \qquad j = 1 \dots 4 \tag{165}$$

$$\mathcal{F} = \sum_{j=1}^{4} \mathcal{F}_j \tag{166}$$

$$\mathcal{F}_j = \sum_{i=1}^{3} \mathcal{F}_{ij} \tag{167}$$

$$\mathcal{F}_{ij} = \frac{1}{N_j} \sum_{n=1}^{N_j} \left(\frac{\partial y_n}{\partial \hat{\theta}_i} \right)^2, \quad i = 1 \dots 3 \tag{168}$$

$$\frac{\partial y_n}{\partial \theta_i} = \frac{y_n(\hat{\theta}_j) - y_n(\hat{\theta}_i)}{\hat{\theta}_j - \hat{\theta}_i} \tag{169}$$

Following the methodology laid out in eqs. (165)-(169), the weights for each optimal parameter set can be found. This analysis is done for both A_{PE} and A_{NE} and the results are given in Table 24, containing the weightings and the calculated optimal values for A_{PE} and A_{NE} are given. As expected, the 2C discharge dataset has the largest sensitivity to the change in the positive electrode diffusion parameter and the negative electrode diffusion

parameter. This is most likely due to the magnitude of the heat generation being larger in the case of the 2C discharge and so the sensitivity is higher in magnitude for an equal shift in parameters.

Table 24: Values obtained when performing Fisher sensitivity analysis for parameters across each dataset. Optimal values calculated as weighted sum of each datasets optimum parameters.

		2C Discharge	1C Discharge	C/2 Discharge	C/2 Charge	Optimal Value
A_{PE}	A	0.0336	0.0282	0.0349	0.0987	
	$\mathcal{F}_j$	478E4	151E4	23.9E4	1.60E3	**0.0326**
	w_j	0.731	0.230	3.65E-2	2.50E-3	
A_{NE}	A	0.0568	0.0884	0.113	0.0010	
	$\mathcal{F}_j$	170E3	21.5E3	2.97E3	2.60E3	**0.0604**
	w_j	0.862	0.110	1.51E-2	1.32E-2	

The optimal values obtained through the analysis are also given in Table 24. These optimal values are used in modelling heat generation for each dataset. This is plotted alongside the corresponding measured heat generation in each case in Figure 62. Across all datasets, the modelled heat generation is a good fit to the measured heat generation. Unsurprisingly the best fit dataset is the 2C discharge as this is the dataset which has the highest sensitivity to the positive electrode diffusion however this is not at the cost of deteriorating the other dataset's fits.

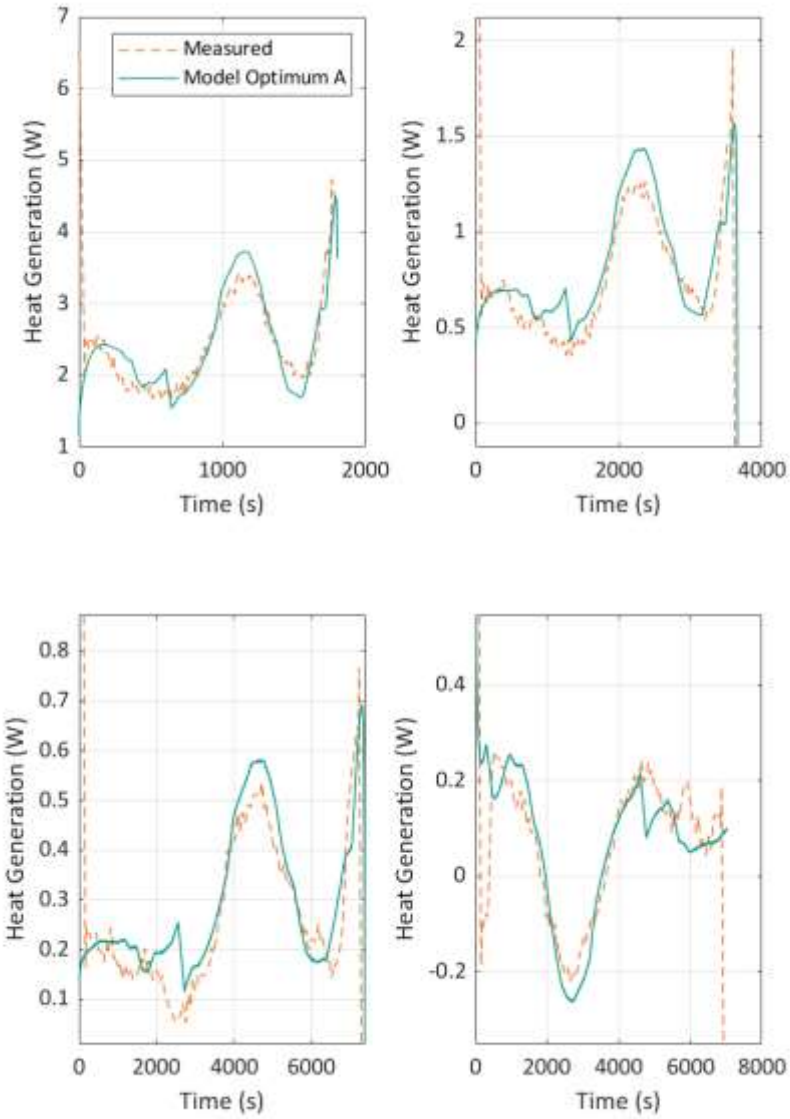

Figure 62: Measured (orange dashed) and modelled (teal solid) heat generation for the optimal diffusion parameters found through fisher sensitivity analysis.

To round off this BOL parameterisation section it is worth summarising what has been accomplished. Firstly, the robustness of the fitting to initial guesses for the diffusion parameters and initial condition was evaluated and it was found that the optimisation routine converged to a set of parameters that were close regardless of initial conditions for the positive electrode diffusion parameter but varied a lot for the negative electrode diffusion parameter. This then allowed an extraction of the optimal parameters for each

dataset which were not consistent between the datasets. To determine how to best decide on what the optimal diffusion parameters were, a sensitivity analysis of each dataset's fit to a variation in each diffusion parameter. This allowed a pseudo global optimal set of parameters to be found which was the weighted sum of each dataset's own optimal parameters. The weightings were determined by each dataset's sensitivity to the parameter values with more sensitive datasets given a higher weighting. Once the optimal set of diffusion parameters had been found, the approach was validated, at least visually, by plotting each datasets modelled heat generation using the optimal parameters and comparing to the measured heat generation. In all cases it was found that the optimum diffusion parameters gave a good fit between measured and modelled heat generation.

5.4.2 Evaluating performance on a degraded cell

So far, the diffusion parameter, A, for both positive and negative electrodes has been determined. This parameter will remain constant for the entirety of the cell's lifetime and will be scaled by the loss of active material in both electrodes which will lead to the changing of the diffusion behaviour of the cell. With the values of A defined for both electrodes, attention is now turned to the stoichiometric parameters and degradation modes for a degraded cell. In this section the stoichiometric parameters obtained by the OCV, 0-D heat generation and heat generation with added diffusion dynamics are compared. The analysis in this section will be performed on a Kokam 7.5Ah cell, as in the previous section, which has been degraded with an unknown degradation history. The profile applied to the cell is a 2C discharge to ensure diffusion has a large impact on the heat generation.

The first insight into the effectiveness of the diffusion model is to observe if it can add the degree of freedom to allow better fit between modelled and measured heat generation when diffusion effects are more pronounced. The 0-D and diffusion augmented models are then fit to the measured heat generation result. The results for this are given in Figure 63. The heat generation with diffusion given in the top subplot fits the peak and trough reasonably well and after multiple runs of the optimisation seems to be robust and give repeatable results. On the other hand, the 0-D model has trouble fitting to the heat generation even with several different starting points for the optimisation. From these results it would appear that the addition of the diffusion model has significantly improved the model. It is not clear why the 0-D model is unable to find a parameter set which gives a reasonable fit between the measured and modelled heat generation.

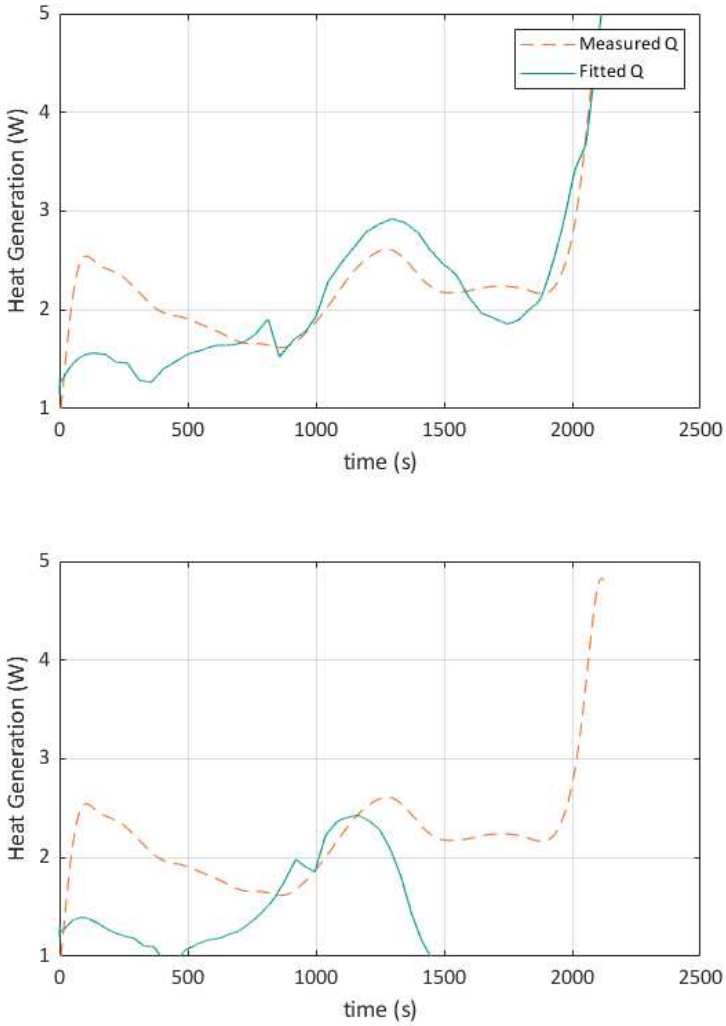

Figure 63: Fits between measured and modelled heat generation for the 2C discharge obtained with model with diffusion (top) and the 0-D heat generation model without diffusion (bottom)

The stoichiometric parameters predicted by the OCV model, 0-D heat generation model and the heat generation with diffusion model are given in Table 25. It is seen that there is significant difference between parameters predicted by all 3 models. The negative electrode capacity and the offset still appear to be difficult to identify owing to the difficulty in identifying the negative electrode start and end lithiation fractions. The heat generation model with diffusion also seems to overestimate the positive electrode capacity.

Table 25: Stoichiometric parameters for the 3 different models.There is a significant difference between all 3 methods

	OCV model	0D Heat generation model	Diffusion heat generation model
C_{NE} (Ah)	8.708	13.29	8.238
C_{PE} (Ah)	7.171	6.970	7.897
OFS (Ah)	0.2431	-3.513E-3	0.954

So far only the fits between measured and modelled heat generation have been explored and the corresponding set of stoichiometric parameters analysed. As is clear from the previous chapter, a single fitness in isolation is not a particularly useful measure of the effectiveness of the diagnostic techniques. The robustness of the 0-D and diffusion augmented models must also be tested using the methodology developed in the last chapter. For this analysis, the optimisation procedure is started from 400 randomly selected initial values of the lithiation fractions. If the technique is robust, it should provide similar results regardless of what the initial points of the optimisation are. To visualise this, the optimal stoichiometric parameters for each set of initial points are plotted using a 'scatter bar' plot where the opacity of the point represents the objective function score where more opaque is a better objective function score.

The scatter bar plot between the 0-D and diffusion augmented heat generation models are given in Figure 64. Plot a) represents the 0-D case and plot b) represents the diffusion augmented model case. Note that the y-axis limit has been set at 16Ah in both cases to improve readability of the graphs. For the 0-D case most of the points are above the 16Ah

axis limit and only a small number of points are visible on the plot. Of the points that are visible, there are no particularly dark clusters of points. This indicates the 0-D model is not robust to the initial conditions for any of the stoichiometric parameters.

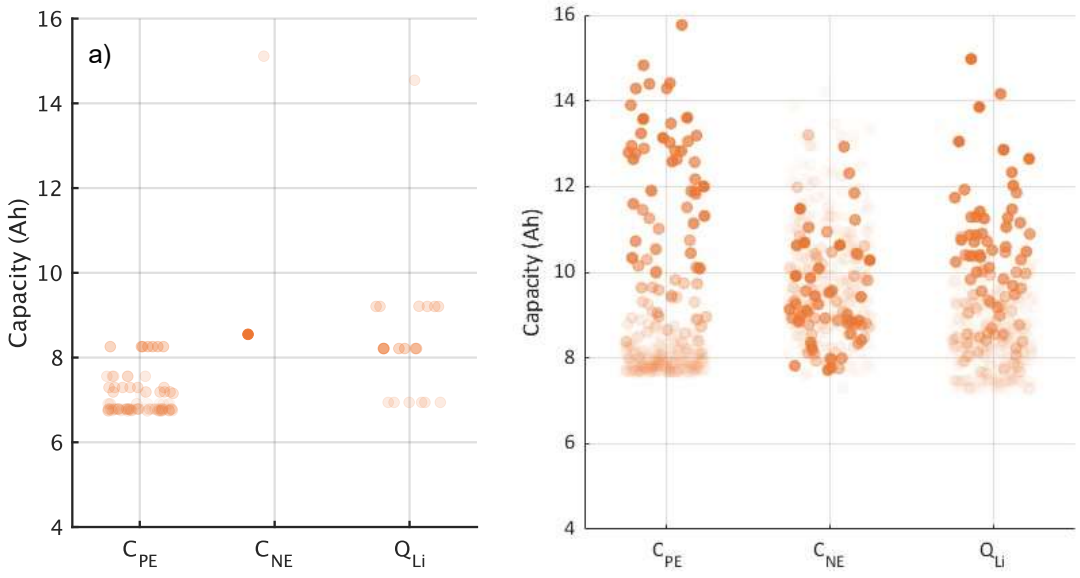

Figure 64: Scatter bar chart showing the robustness of the heat generation diagnostic technique on the degraded 7.5Ah Kokam cell for the 0-D model (left) and the diffusion augmented model (right). Y-axis has been truncated at 16Ah for clarity of plot. 400 samples chosen for both cases, for the 0-D model, most of the points lie above the 16Ah axis limit.

The diffusion augmented model has more points visible in Figure 64 but these points are still spaced out much more than was seen for the previous section. There is a cluster of points for the positive electrode capacity around 8Ah but these are quite faint indicating a relatively weak fitness around this area. The negative electrode capacity and the lithium content both have a spread out set of results with dark dots – indicating parameters of good fitness – across the entire range of values. This further reinforces the conclusions made in the previous section about the negative electrode being difficult to identify due to the near zero gradient and hence very low sensitivity of the objective function to the shifting and scaling of the negative electrode OCV and entropy.

The addition of the diffusion model has improved the robustness of the heat generation diagnostic technique for the case of this high energy degraded cell over the previous 0D model. For completeness attention is turned to the comparison of the results obtained by the diffusion model and the OCV model for the case of the aged 7.5Ah Kokam cell used so far in this section. The results of this analysis are given in Figure 65. The left plot contains the results from the OCV technique and the right plot contains the results obtained from the heat generation technique with added diffusion.

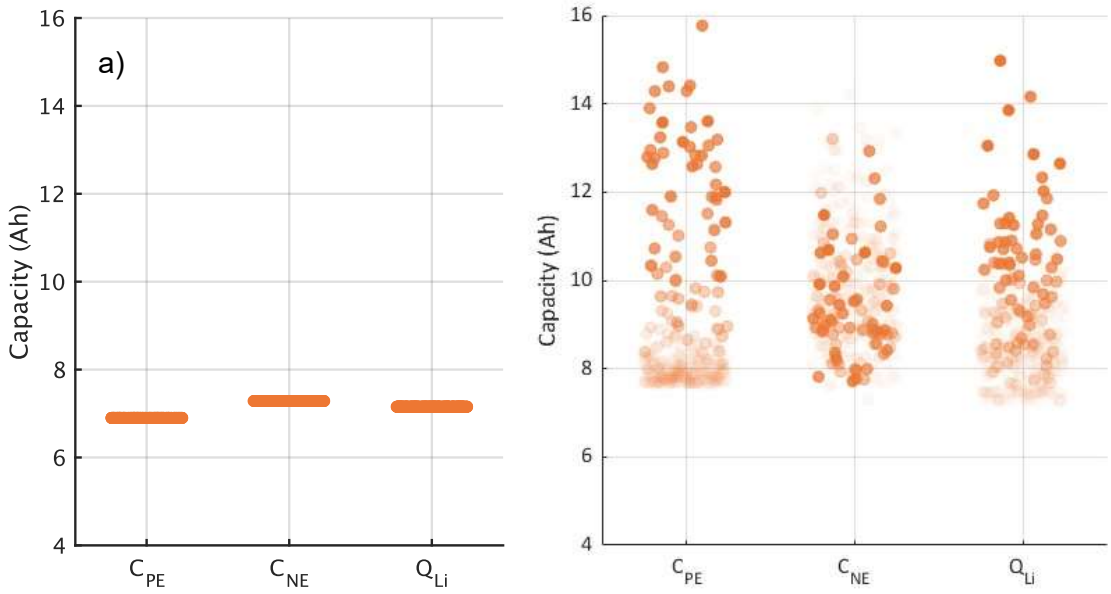

Figure 65: Scatter bar plot of the stoichiometric parameters obtained in the robustness analysis for a) the OCV based technique and b) the heat generation technique with the added diffusion model

Comparing the results for both techniques in Figure 65 it is seen that the OCV technique is far more robust than the heat generation technique. Whilst there are some results for the OCV technique above the 16Ah axis limit, there is clearly good identifiability for this technique. The heat generation technique has poor results in comparison. However, if the distribution of points is examined for the positive electrode then the majority of the points

lie close to the predicted capacity for the positive electrode in the OCV model case. This is a useful result as the benefit of the heat generation technique is that it can be done many times in quick succession using an arbitrary load cycle. Therefore, repeated measurements can be used to refine the distribution to a point where there is much less spread in the distribution. There is less clustering visible for the negative electrode and the total amount of lithium in the system but the same principle would apply.

5.5 Conclusions on the addition of the diffusion model

In this section the 0-D heat generation model was augmented with a computationally efficient diffusion component. The diffusion model implemented is a non-dimensional single particle model. The diffusion coefficient assumed to be constant in both SoC and temperature to minimise the number of added parameters to the diffusion model. The result is a diffusion model that contains a single parameter. This parameter is constant throughout the life of the cell and is independent of the amounts of stoichiometric parameters. This allows the parameter to be found once at beginning of life and is not required in the optimisation in subsequent iterations of the diagnostic algorithm and only the lithiation limits need to be optimised. The boundary condition of the model is related to the loss of active material to reflect the increasing current density with the decrease of active particle surface area.

The heat generation technique with the diffusion model is compared to the 0-D case as well as the OCV technique. The results showed that the addition of the diffusion model had benefit for improving the robustness and the heat generation fit over the 0-D case but still did not have comparable robustness compared to the OCV technique. The problem of

robust fitting to the negative electrode parameters is a mathematically difficult problem as was demonstrated by Bizeray et al. [101]. However, it would be worthwhile to understand exactly what the distribution of the parameters are from a statistical perspective so that quantitative uncertainties on the parameters can then be used. The method used by Aitio et al. [102] where a Markov-Chain Monte Carlo method is used as a Bayesian approach to parameter estimation of a non-linear, non-Gaussian problem has many similarities to the problem faced by this diagnostic technique.

Finally, the results produced by the diffusion augmented heat generation technique are compared to those produced by the OCV technique. It is found that the OCV technique is very robust for the cell used in this study and all stoichiometric parameters are predicted robustly regardless of the starting input parameters. The value for the positive electrode capacity predicted by the heat generation technique with the diffusion model is similar to that predicted by the OCV technique. However, the values for the negative electrode capacity and lithium inventory predicted by the heat generation technique are not robust enough – they contain too much spread in their predicted values – to be useful when compared to the OCV technique for the reasons discussed in the paragraph above.

6 Conclusion

6.1 Overall goals of thesis

The goal set out at the beginning of this thesis is to demonstrate a diagnostic technique which can obtain quantitative degradation mode information under in-operando conditions which is applicable to any form factor and chemistry. The goals are set out to provide an alternative diagnostic technique to the commonly used OCV model techniques used commonly throughout the literature when OCV conditions are not available. The technique should also be robust to the input signal and should only use voltage, temperature and current measurements.

This thesis has achieved those aims by providing the foundation of a technique which has shown effectiveness in extracting degradation mode information for load cycles which are similar to those seen in application. The technique has been demonstrated on high power and high energy cells in chapters 4 & 5 respectively and has show that the heat generation does contain information which can be used to obtain distributions for stoichiometric parameters of a cell. The theory developed in chapter 3 is applicable in theory to any battery system, form factor, chemistry and load cycle which was a key aim of this thesis.

This thesis provides the starting point of the underlying theory and lab based application of a diagnostic technique which can be used to gain quantitative information on degradation modes in batteries. The technique is not as robust as the commonly applied OCV technique but has the advantage that it can be applied in a much wider range of conditions. This could allow for much more common diagnosis. Moreover, the technique could be coupled with

the results from less frequent OCV measurements to obtain a reliable estimate of degradation mode amounts. From here, there are several steps that should be taken next to improve the effectiveness of this technique and make it more applicable to applications outside of the lab.

6.2 Improving the effectiveness of the technique

Firstly, it is clear from the work in this thesis that the output obtained from the diagnostic technique in this work provides a single 'point estimate' of the stoichiometric parameters. It would be much more useful to develop a probability distribution of the stoichiometric parameters. Unfortunately, owing to the non-linearity of the models in this technique, and likely non-gaussian distributions of the parameters there are not many computationally efficient algorithms which can estimate the distribution of the parameters. One work that has stood out to me is that by Aitio et al. when performing parameter identification for the negative electrode diffusion coefficient in [102]. The problem solved in this paper is not too dissimilar to the problem explored in this thesis, a non-linear problem with non-gaussian distributions of parameters. Implementing a similar method for this diagnostic technique may improve the robustness of the results but more importantly would allow the distribution of the estimated parameters to be quantified. This would also allow the noise of the measurements to also be taken into account when generating the estimates which is currently missing from the technique.

The technique developed in this thesis has the advantage of being able to be run more frequently than the OCV technique but at present this thesis does not exploit that advantage. The parameters estimated in this technique have a higher variance than those

obtained from the OCV technique but this uncertainty can most likely be improved by using multiple datasets more closely spaced together and combining the results from each to get a better estimate of the stoichiometric parameters. If the step in the previous paragraph is taken to create a distribution of the parameters for each test, then a recursive Bayesian approach could be taken where the probability distribution of the previous parameter estimates (the prior) can be used to better estimate the present distribution of the parameter estimates.

6.3 Applicability to other battery systems

This work explored the application of the diagnostic technique to a high power cell and then extends the technique for high energy cell applications by incorporating a single particle model to estimate the surface concentration of the electrodes. The theory developed in chapter 3 should be applicable to all form factors, chemistries and load cycles. However, the effectiveness of the technique will be dependent on all of these factors. For example, It is clear in this work that because of the small gradient of the negative electrode OCV and entropy that the negative electrode capacity and lithium inventory are hard to identify. This would be true for any other electrode which are similarly flat in terms of their OCV and entropy profiles such as LFP which has a very flat OCV profile until the extremes of the SoC window.

Further work should investigate the effectiveness of the technique on these different chemistries and form factors. One potential improvement that could be made is to simplify the thermal models used in the technique to only require cell temperature measurement rather than thermal pathway modelling. The rationale behind this is that the temperature

profile should still retain the shape of the heat generation but with a different magnitude and scaling. For example, in the work conducted in this thesis, there is a characteristic peak and trough which can be used as a feature to identify the stoichiometric parameters in this work. With a simplified thermal model which provides the shape and features needed to identify the stoichiometric parameters, a set of features could be identified for the finite amount of positive electrode and negative electrode chemistry combinations that exist. Alternatively, the feature list can be generated during the parameterisation of other models used to design the battery system.

The technique has so far only been demonstrated under conditions where the heat flow out of the cells are carefully controlled and can be measured with a high number of good quality temperature sensors. In pack applications there is a non-constant thermal environment and the quality and quantity of temperature sensors is much lower than that used in this work - typically only a few temperature measurements are available across the entire pack in automotive applications. Therefore, the simplification of the thermal model as discussed above is critical for pack applications. The best that could be hoped for is for the technique to be applied across a module rather than on the individual cell basis. A similar approach could be taken as described above where the module temperature is taken and the features in the temperature profile can be extracted and used for parameter estimation. The big unknown at the pack level is if the local cell to cell variations confuse the signal to the point where the features are no longer identifiable.

To improve the applicability of the technique first the thermal model should be simplified to a single temperature measurement of a cell in laboratory environment and the technique

used as it is with an additional scaling parameter which can account for heat generation magnitude differences. Then, this approach should be tested on for a variety of different form factors and thermal management techniques. If the technique fails then the feature identification approach can be taken. Finally, the technique can be tested on a multi-cell system to see if the overall diagnostic of the cells can be identified.

With the changes made in this section as well as the improved optimisation technique and recursive updating methods described in the previous section would mean a technique which is more applicable in real world environments as well as providing robust statistical estimates of the degradation mode amounts.

References

[1] B. Wang, “World Battery Production.” Accessed: May 06, 2021. [Online]. Available: https://energycentral.com/c/ec/world-battery-production

[2] H. Budde-Meiwes *et al.*, “A review of current automotive battery technology and future prospects,” *Proceedings of the Institution of Mechanical Engineers, Part D: Journal of Automobile Engineering*, vol. 227, no. 5, pp. 761–776, May 2013, doi: 10.1177/0954407013485567.

[3] International Energy Agency, “Global EV Outlook 2020,” 2020.

[4] B. N. E. Finance, “Electric Vehicle Outlook 2020,” 2020.

[5] M. Woodward, B. Walton, and J. Hamilton, “Electric Vehicles: Setting a course for 2030.”

[6] V. Henze, “Battery Pack Prices Cited Below $100/kWh for the First Time in 2020, While Market Average Sits at $137/kWh,” Bloomberg NEF. Accessed: Apr. 13, 2021. [Online]. Available: https://about.bnef.com/blog/battery-pack-prices-cited-below-100-kwh-for-the-first-time-in-2020-while-market-average-sits-at-137-kwh/

[7] World Economic Forum; Global Battery Alliance, “A Vision for a Sustainable Battery Value Chain in 2030,” no. September, pp. 10–11, 2019.

[8] J. Calma, “The UK moves up deadline to ban the sale of combustion-engine vehicles,” The Verge. Accessed: Apr. 15, 2021. [Online]. Available: https://www.theverge.com/2020/11/17/21572312/uk-ban-combustion-engine-vehicles-sale-electric-cars

[9] F. Lambert, “Electric Vehicle Battery Cost Officially Dips Under Critical $100/kWh Price Point but There’s a Catch,” 2020.

[10] G. Berckmans, M. Messagie, J. Smekens, N. Omar, L. Vanhaverbeke, and J. Van Mierlo, “Cost Projection of State of the Art Lithium-Ion Batteries for Electric Vehicles Up to 2030,” 2017, doi: 10.3390/en10091314.

[11] P. Zhu, D. Gastol, J. Marshall, R. Sommerville, V. Goodship, and E. Kendrick, “A review of current collectors for lithium-ion batteries,” *Journal of Power Sources*, vol. 485, p. 229321, Feb. 2021, doi: 10.1016/J.JPOWSOUR.2020.229321.

[12] K. Xu, “Nonaqueous liquid electrolytes for lithium-based rechargeable batteries,” *Chemical Reviews*, vol. 104, no. 10, pp. 4303–4417, 2004, doi: 10.1021/cr030203g.

[13] X. Wu *et al.*, “Safety issues in lithium ion batteries: Materials and cell design,” *Frontiers in Energy Research*, vol. 7, no. JUL. p. 65, 2019. doi: 10.3389/fenrg.2019.00065.

[14] Y. Guo *et al.*, “Solid-state lithium batteries: Safety and prospects,” *eScience*, vol. 2, no. 2, pp. 138–163, Mar. 2022, doi: 10.1016/J.ESCI.2022.02.008.

[15] J. Yang *et al.*, “Rapid Prediction of the Open-Circuit-Voltage of Lithium Ion Batteries Based on an Effective Voltage Relaxation Model”, doi: 10.3390/en11123444.

[16] N. Nitta, F. Wu, J. T. Lee, and G. Yushin, “Li-ion battery materials: present and future,” *Materials Today*, vol. 18, no. 5, pp. 252–264, Jun. 2015, doi: 10.1016/J.MATTOD.2014.10.040.

[17] J. Yan, X. Liu, and B. Li, “Recent progress in Li-rich layered oxides as cathode materials for Li-ion batteries,” 2014, doi: 10.1039/c4ra12454e.

[18] K. Wang *et al.*, “Recent advances and historical developments of high voltage lithium cobalt oxide materials for rechargeable Li-ion batteries,” *Journal of Power Sources*, vol. 460, p. 228062, Jun. 2020, doi: 10.1016/J.JPOWSOUR.2020.228062.

[19] B. Liang, Y. Liu, and Y. Xu, “Silicon-based materials as high capacity anodes for next generation lithium ion batteries,” *Journal of Power Sources*, vol. 267, pp. 469–490, Dec. 2014, doi: 10.1016/J.JPOWSOUR.2014.05.096.

[20] S. Wang, Y. Yang, Y. Dong, Z. Zhang, and Z. Tang, “Recent progress in Ti-based nanocomposite anodes for lithium ion batteries,” *Journal of Advanced Ceramics*, vol. 8, no. 1, pp. 1–18, 2019, doi: 10.1007/s40145-018-0292-2.

[21] J. Newman and K. E. Thomas-Alyea, *Electrochemical Systems*, 3rd ed. 2004.

[22] C. D. Rahn and C.-Y. Wang, *Battery Systems Engineering*. 2013.

[23] J. S. Edge *et al.*, “Lithium ion battery degradation: what you need to know,” *Physical Chemistry Chemical Physics*, vol. 23, no. 14, pp. 8200–8221, 2021, doi: 10.1039/d1cp00359c.

[24] C. Lin, A. Tang, H. Mu, W. Wang, and C. Wang, “Aging Mechanisms of Electrode Materials in Lithium-Ion Batteries for Electric Vehicles,” 2015, doi: 10.1155/2015/104673.

[25] J. Vetter *et al.*, “Ageing mechanisms in lithium-ion batteries,” *Journal of Power Sources*, vol. 147, no. 1–2, pp. 269–281, Sep. 2005, doi: 10.1016/J.JPOWSOUR.2005.01.006.

[26] S. Zhang, K. Zhao, T. Zhu, and J. Li, “Electrochemomechanical degradation of high-capacity battery electrode materials,” *Progress in Materials Science*, vol. 89, pp. 479–521, Aug. 2017, doi: 10.1016/j.pmatsci.2017.04.014.

[27] T. Liu *et al.*, “In situ quantification of interphasial chemistry in Li-ion battery,” *Nature Nanotechnology*, vol. 14, no. 1, pp. 50–56, 2019, doi: 10.1038/s41565-018-0284-y.

[28] A. A. Tahmasbi, T. Kadyk, and M. H. Eikerling, “Statistical Physics-Based Model of Solid Electrolyte Interphase Growth in Lithium Ion Batteries,” *Journal of The Electrochemical Society*, vol. 164, no. 6, pp. A1307–A1313, 2017, doi: 10.1149/2.1581706jes.

[29] M. Safari, M. Morcrette, A. Teyssot, and C. Delacourt, “Multimodal Physics-Based Aging Model for Life Prediction of Li-Ion Batteries,” *Journal of The Electrochemical Society*, vol. 156, no. 3, p. A145, 2009, doi: 10.1149/1.3043429.

[30] M. Ecker *et al.*, “Calendar and cycle life study of Li(NiMnCo)O2-based 18650 lithium-ion batteries,” *Journal of Power Sources*, vol. 248, pp. 839–851, Feb. 2014, doi: 10.1016/J.JPOWSOUR.2013.09.143.

[31] M. Dubarry and D. Beck, “Big data training data for artificial intelligence-based Li-ion diagnosis and prognosis,” *Journal of Power Sources*, vol. 479, p. 228806, Dec. 2020, doi: 10.1016/j.jpowsour.2020.228806.

[32] X. G. Yang, S. Ge, T. Liu, Y. Leng, and C. Y. Wang, “A look into the voltage plateau signal for detection and quantification of lithium plating in lithium-ion cells,” *Journal of Power Sources*, vol. 395, pp. 251–261, Aug. 2018, doi: 10.1016/J.JPOWSOUR.2018.05.073.

[33] I. D. Campbell, M. Marzook, M. Marinescu, and G. J. Offer, “How Observable Is Lithium Plating? Differential Voltage Analysis to Identify and Quantify Lithium Plating Following Fast Charging of Cold Lithium-Ion Batteries,” *Journal of The Electrochemical Society*, vol. 166, no. 4, pp. A725–A739, 2019, doi: 10.1149/2.0821904jes.

[34] Q. Q. Liu, D. J. Xiong, R. Petibon, C. Y. Du, and J. R. Dahn, “Gas Evolution during Unwanted Lithium Plating in Li-Ion Cells with EC-Based or EC-Free Electrolytes,”

Journal of The Electrochemical Society, vol. 163, no. 14, pp. 3010–3015, 2016, doi: 10.1149/2.0711614jes.

[35] X. G. Yang, Y. Leng, G. Zhang, S. Ge, and C. Y. Wang, "Modeling of lithium plating induced aging of lithium-ion batteries: Transition from linear to nonlinear aging," *Journal of Power Sources*, vol. 360, pp. 28–40, Aug. 2017, doi: 10.1016/J.JPOWSOUR.2017.05.110.

[36] M. Ebner, F. Marone, M. Stampanoni, and V. Wood, "Visualization and quantification of Electrochemical and Mechanical," *Science*, vol. 342, no. November, pp. 716–721, 2013.

[37] F. P. McGrogan, S. N. Raja, Y.-M. Chiang, and K. J. Van Vliet, "Electrochemomechanical Fatigue: Decoupling Mechanisms of Fracture-Induced Performance Degradation in LiXMn2O4," *Journal of The Electrochemical Society*, vol. 165, no. 11, pp. A2458–A2466, 2018, doi: 10.1149/2.0191811jes.

[38] X. H. Liu, L. Zhong, S. Huang, S. X. Mao, T. Zhu, and J. Y. Huang, "Size-dependent fracture of silicon nanoparticles during lithiation," *ACS Nano*, vol. 6, no. 2, pp. 1522–1531, 2012, doi: 10.1021/nn204476h.

[39] W. Ai, L. Kraft, J. Sturm, A. Jossen, and B. Wu, "Electrochemical thermal-mechanical modelling of stress inhomogeneity in lithium-ion pouch cells," *Journal of the Electrochemical Society*, vol. 167, no. 1, p. 013512, Oct. 2020, doi: 10.1149/2.0122001JES.

[40] W. J. Zhang, “A review of the electrochemical performance of alloy anodes for lithium-ion batteries,” *Journal of Power Sources*. 2011. doi: 10.1016/j.jpowsour.2010.07.020.

[41] B. A. Boukamp, G. C. Lesh, R. A. Huggins, and J. E. Soc, “All-Solid Lithium Electrodes with Mixed-Conductor Matrix,” *Journal of The Electrochemical Society*, vol. 128, no. 4, pp. 725–729, 1981, doi: 10.1149/1.2127495.

[42] X. Li *et al.*, “Degradation mechanisms of high capacity 18650 cells containing Si-graphite anode and nickel-rich NMC cathode,” *Electrochimica Acta*, 2019, doi: 10.1016/j.electacta.2018.11.194.

[43] S.-K. Jung *et al.*, “Understanding the Degradation Mechanisms of LiNi0.5Co0.2Mn0.3O2 Cathode Material in Lithium Ion Batteries,” *Advanced Energy Materials*, vol. 4, no. 1, p. 1300787, Jan. 2014, doi: 10.1002/aenm.201300787.

[44] R. Jung, M. Metzger, F. Maglia, C. Stinner, and H. A. Gasteiger, “Oxygen Release and Its Effect on the Cycling Stability of LiNi x Mn y Co z O 2 (NMC) Cathode Materials for Li-Ion Batteries,” *Journal of The Electrochemical Society*, vol. 164, no. 7, pp. A1361–A1377, 2017, doi: 10.1149/2.0021707jes.

[45] A. Ghosh, J. M. Foster, G. Offer, and M. Marinescu, “A Shrinking-Core Model for the Degradation of High-Nickel Cathodes (NMC811) in Li-Ion Batteries: Passivation Layer Growth and Oxygen Evolution,” *Journal of The Electrochemical Society*, vol. 168, no. 2, p. 020509, 2021, doi: 10.1149/1945-7111/abdc71.

[46] “Effect of Ambient Storage on the Degradation of Ni-Rich Positive Electrode Materials (NMC811) for Li-Ion Batteries”, doi: 10.1149/2.0401802jes.

[47] D. Li *et al.*, “Temperature-dependent cycling performance and ageing mechanisms of C6/LiNi1/3Mn1/3Co1/3O2 batteries,” *Journal of Power Sources*, vol. 396, pp. 444–452, Aug. 2018, doi: 10.1016/J.JPOWSOUR.2018.06.035.

[48] M. D. Radin *et al.*, “Narrowing the Gap between Theoretical and Practical Capacities in Li-Ion Layered Oxide Cathode Materials,” *Advanced Energy Materials*, vol. 7, no. 20, 2017, doi: 10.1002/aenm.201602888.

[49] E. Zhao *et al.*, “New insight into Li/Ni disorder in layered cathode materials for lithium ion batteries: a joint study of neutron diffraction, electrochemical kinetic analysis and first-principles calculations †,” 2017, doi: 10.1039/c6ta08448f.

[50] “Temperature Dependence of Oxygen Release from LiNi 0.6 Mn 0.2 Co 0.2 O 2 (NMC622) Cathode Materials for Li-Ion Batteries”, doi: 10.1149/2.1261811jes.

[51] G. Sikha, B. N. Popov, and R. E. White, “Effect of Porosity on the Capacity Fade of a Lithium-Ion Battery,” *Journal of The Electrochemical Society*, vol. 151, no. 7, p. A1104, 2004, doi: 10.1149/1.1759972.

[52] C. R. Birkl, M. R. Roberts, E. McTurk, P. G. Bruce, and D. A. Howey, “Degradation diagnostics for lithium ion cells,” *Journal of Power Sources*, vol. 341, pp. 373–386, 2017, doi: 10.1016/j.jpowsour.2016.12.011.

[53] J. Vetter *et al.*, “Ageing mechanisms in lithium-ion batteries,” *Journal of Power Sources*, vol. 147, no. 1–2, pp. 269–281, 2005, doi: 10.1016/j.jpowsour.2005.01.006.

[54] L. Lu, H. Xuebing, L. Jianqui, H. Jianfeng, and O. Minggao, “A review on the key issues for lithium-ion battery management in electric vehicles,” *Journal of Power Sources*, vol. 226, pp. 272–288, 2013.

[55] M. Dubarry, C. Truchot, and B. Y. Liaw, “Synthesize battery degradation modes via a diagnostic and prognostic model,” *Journal of Power Sources*, vol. 219, pp. 204–216, Dec. 2012, doi: 10.1016/J.JPOWSOUR.2012.07.016.

[56] A. Aitio and D. A. Howey, “Predicting battery end of life from solar off-grid system field data using machine learning,” *Joule*, vol. 5, pp. 3204–3220, 2021, doi: 10.1016/j.joule.2021.11.006.

[57] A. Fly and R. Chen, “Rate dependency of incremental capacity analysis (dQ/dV) as a diagnostic tool for lithium-ion batteries,” *Journal of Energy Storage*, vol. 29, p. 101329, Jun. 2020, doi: 10.1016/J.EST.2020.101329.

[58] C. Chang, Q. Wang, J. Jiang, and T. Wu, “Lithium-ion battery state of health estimation using the incremental capacity and wavelet neural networks with genetic algorithm,” *JOURNAL OF ENERGY STORAGE*, vol. 38, Jun. 2021, doi: 10.1016/j.est.2021.102570.

[59] X. Li, C. Yuan, and Z. Wang, “State of health estimation for Li-ion battery via partial incremental capacity analysis based on support vector regression,” *ENERGY*, vol. 203, Jul. 2020, doi: 10.1016/j.energy.2020.117852.

[60] S. Zhang, B. Zhai, X. Guo, K. Wang, N. Peng, and X. Zhang, “Synchronous estimation of state of health and remaining useful lifetime for lithium-ion battery using the incremental capacity and artificial neural networks,” *JOURNAL OF ENERGY STORAGE*, vol. 26, Dec. 2019, doi: 10.1016/j.est.2019.100951.

[61] A. Kuznietsov, T. Happek, and F. L. T. Guefack, “On-board state of health estimation of Li-Ion batteries packs using incremental capacity analysis with principal components,” in *2018 IEEE INTERNATIONAL CONFERENCE ON ELECTRICAL SYSTEMS FOR AIRCRAFT, RAILWAY, SHIP PROPULSION AND ROAD VEHICLES \& INTERNATIONAL TRANSPORTATION ELECTRIFICATION CONFERENCE (ESARS-ITEC)*, 2018.

[62] X. Li, C. Yuan, X. Li, and Z. Wang, “State of health estimation for Li-Ion battery using incremental capacity analysis and Gaussian process regression,” *ENERGY*, vol. 190, Jan. 2020, doi: 10.1016/j.energy.2019.116467.

[63] L. Jing-Yu *et al.*, “Application of in-situ characterization techniques in all-solid-state lithium batteries,” *ACTA PHYSICA SINICA*, vol. 70, no. 19, Oct. 2021, doi: 10.7498/aps.70.20210531.

[64] P. Iurilli, C. Brivio, and V. Wood, “On the use of electrochemical impedance spectroscopy to characterize and model the aging phenomena of lithium-ion

batteries: a critical review," *Journal of Power Sources*, vol. 505, p. 229860, Sep. 2021, doi: 10.1016/J.JPOWSOUR.2021.229860.

[65] M. Dubarry *et al.*, "Evaluation of commercial lithium-ion cells based on composite positive electrode for plug-in hybrid electric vehicle applications. Part I: Initial characterizations," *Journal of Power Sources*, vol. 196, no. 23, pp. 10328–10335, Dec. 2011, doi: 10.1016/J.JPOWSOUR.2011.08.077.

[66] M. Dubarry, V. Svoboda, R. Hwu, B. Yann Liaw, and B. Y. Liaw, "Incremental capacity analysis and close-to-equilibrium OCV measurements to quantify capacity fade in commercial rechargeable lithium batteries," *ELECTROCHEMICAL AND SOLID STATE LETTERS*, vol. 9, no. 10, pp. A454–A457, 2006, doi: 10.1149/1.2221767.

[67] J. R. Dahn and W. R. McKinnon, "Thermodynamics of Lithium Intercalation from High Resolution Electrochemical Measurements," *Journal of The Electrochemical Society*, vol. 131, no. 8, pp. 1823–1828, 1984, doi: 10.1149/1.2115968.

[68] M. Dubarry *et al.*, "Identifying battery aging mechanisms in large format Li ion cells," *Journal of Power Sources*, vol. 196, no. 7, pp. 3420–3425, Apr. 2011, doi: 10.1016/J.JPOWSOUR.2010.07.029.

[69] M. Dubarry *et al.*, "Evaluation of commercial lithium-ion cells based on composite positive electrode for plug-in hybrid electric vehicle applications. Part II. Degradation mechanism under 2 C cycle aging," *Journal of Power Sources*, vol. 196, no. 23, pp. 10336–10343, Dec. 2011, doi: 10.1016/J.JPOWSOUR.2011.08.078.

[70] M. Dubarry and B. Y. Liaw, “Identify capacity fading mechanism in a commercial LiFePO4 cell,” *Journal of Power Sources*, vol. 194, no. 1, pp. 541–549, Oct. 2009, doi: 10.1016/J.JPOWSOUR.2009.05.036.

[71] M. Dubarry, C. Truchot, and B. Y. Liaw, “Synthesize battery degradation modes via a diagnostic and prognostic model,” *Journal of Power Sources*, vol. 219, pp. 204–216, Dec. 2012, doi: 10.1016/J.JPOWSOUR.2012.07.016.

[72] M. Dubarry, A. Devie, and B. Liaw, “The value of battery diagnostics and prognostics,” *J. Energy Power Sources*, vol. 1, no. 5, pp. 242–249, 2014.

[73] M. Dubarry, M. Berecibar, A. Devie, D. Anseán, N. Omar, and I. Villarreal, “State of health battery estimator enabling degradation diagnosis: Model and algorithm description,” *Journal of Power Sources*, vol. 360, pp. 59–69, 2017, doi: 10.1016/j.jpowsour.2017.05.121.

[74] I. Bloom, J. Christophersen, and K. Gering, “Differential voltage analyses of high-power lithium-ion cells 2. Applications,” *JOURNAL OF POWER SOURCES*, vol. 139, no. 1–2, pp. 304–313, Jan. 2005, doi: 10.1016/j.jpowsour.2004.07.022.

[75] I. Bloom, J. Christophersen, D. Abraham, and K. Gering, “Differential voltage analyses of high-power lithium-ion cells - 3. Another anode phenomenon,” *Journal of Power Sources*, vol. 157, no. 1, pp. 537–542, Jun. 2006, doi: 10.1016/j.jpowsour.2005.07.054.

[76] I. Bloom *et al.*, “Differential voltage analyses of high-power, lithium-ion cells 1. Technique and application,” *JOURNAL OF POWER SOURCES*, vol. 139, no. 1–2, pp. 295–303, Jan. 2005, doi: 10.1016/j.jpowsour.2004.07.021.

[77] I. Bloom, L. K. Walker, J. K. Basco, D. P. Abraham, J. P. Christophersen, and C. D. Ho, “Differential voltage analyses of high-power lithium-ion cells. 4. Cells containing NMC,” *JOURNAL OF POWER SOURCES*, vol. 195, no. 3, pp. 877–882, Feb. 2010, doi: 10.1016/j.jpowsour.2009.08.019.

[78] C. R. Birkl, E. McTurk, M. R. Roberts, P. G. Bruce, and D. A. Howey, “A Parametric Open Circuit Voltage Model for Lithium Ion Batteries,” *Journal of The Electrochemical Society*, vol. 162, no. 12, pp. A2271–A2280, 2015, doi: 10.1149/2.0331512jes.

[79] C. R. Birkl, M. R. Roberts, E. McTurk, P. G. Bruce, and D. A. Howey, “Degradation diagnostics for lithium ion cells,” *Journal of Power Sources*, vol. 341, pp. 373–386, 2017, doi: 10.1016/j.jpowsour.2016.12.011.

[80] B. Wu, V. Yufit, Y. Merla, R. F. Martinez-Botas, N. P. Brandon, and G. J. Offer, “Differential thermal voltammetry for tracking of degradation in lithium-ion batteries,” *Journal of Power Sources*, vol. 273, pp. 495–501, Jan. 2015, doi: 10.1016/j.jpowsour.2014.09.127.

[81] Y. Merla, B. Wu, V. Yufit, N. P. Brandon, R. F. Martinez-Botas, and G. J. Offer, “Novel application of differential thermal voltammetry as an in-depth state-of-health

diagnosis method for lithium-ion batteries," *Journal of Power Sources*, vol. 307, pp. 308–319, Mar. 2016, doi: 10.1016/j.jpowsour.2015.12.122.

[82] Y. Merla, B. Wu, V. Yufit, N. P. Brandon, R. F. Martinez-Botas, and G. J. Offer, "Extending battery life: A low-cost practical diagnostic technique for lithium-ion batteries," *Journal of Power Sources*, vol. 331, pp. 224–231, Nov. 2016, doi: 10.1016/j.jpowsour.2016.09.008.

[83] S. Al Hallaj, H. Maleki, J. S. Hong, and J. R. Selman, "Thermal modeling and design considerations of lithium-ion batteries," *J Power Sources*, vol. 83, no. 1–2, pp. 1–8, Oct. 1999, doi: 10.1016/S0378-7753(99)00178-0.

[84] D. Bernardi, E. Pawlikowski, and J. Newman, "General Energy Balance for Battery Systems.," *Electrochemical Society Extended Abstracts*, vol. 84–2, pp. 164–165, 1984, doi: 10.1149/1.2113792.

[85] K. E. Thomas and J. Newman, "Thermal Modeling of Porous Insertion Electrodes," *Journal of The Electrochemical Society*, vol. 150, no. 2, p. A176, 2003, doi: 10.1149/1.1531194.

[86] M. Masmoudi, Z. Moumni, and F. Bidault, "Analysis of the Thermo-Mechanical-Chemical Coupled Response of a Lithium-Ion Battery Particle during a Charge-Discharge Cycle," *Journal of The Electrochemical Society*, vol. 166, no. 3, pp. A5445–A5461, 2019, doi: 10.1149/2.0631903jes.

[87] D. Chalise, W. Lu, V. Srinivasan, and R. Prasher, “Heat of Mixing During Fast Charge/Discharge of a Li-Ion Cell: A Study on NMC523 Cathode,” *Journal of The Electrochemical Society*, vol. 167, no. 9, p. 090560, 2020, doi: 10.1149/1945-7111/abaf71.

[88] B. Yan, C. Lim, L. Yin, and L. Zhu, “Simulation of heat generation in a reconstructed LiCoO2 cathode during galvanostatic discharge,” *Electrochimica Acta*, 2013, doi: 10.1016/j.electacta.2013.03.132.

[89] “Question Video: Calculating the the Enthalpy Change for the Thermal Decomposition of Lithium Carbonate Using Enthalpies of Formation | Nagwa.” Accessed: Dec. 12, 2023. [Online]. Available: https://www.nagwa.com/en/videos/612175340106/

[90] Y. Zhao, Y. Patel, T. Zhang, and G. J. Offer, “Modeling the Effects of Thermal Gradients Induced by Tab and Surface Cooling on Lithium Ion Cell Performance,” *Journal of The Electrochemical Society*, vol. 165, no. 13, pp. A3169–A3178, 2018, doi: 10.1149/2.0901813jes.

[91] Y. Zhao, L. B. Diaz, Y. Patel, T. Zhang, and G. J. Offer, “How to Cool Lithium Ion Batteries: Optimising Cell Design using a Thermally Coupled Model,” *Journal of The Electrochemical Society*, vol. 166, no. 13, pp. A2849–A2859, 2019, doi: 10.1149/2.0501913jes.

[92] A. Hales, M. W. Marzook, L. Bravo Diaz, Y. Patel, and G. Offer, “The Surface Cell Cooling Coefficient: A Standard to Define Heat Rejection from Lithium Ion Battery

Pouch Cells," *Journal of The Electrochemical Society*, vol. 167, no. 2, p. 020524, 2020, doi: 10.1149/1945-7111/ab6985.

[93] A. Hales, L. B. Diaz, M. W. Marzook, Y. Zhao, Y. Patel, and G. Offer, "The Cell Cooling Coefficient: A Standard to Define Heat Rejection from Lithium-Ion Batteries," *Journal of The Electrochemical Society*, vol. 166, no. 12, pp. A2383–A2395, 2019, doi: 10.1149/2.0191912jes.

[94] A. Savitzky and M. J. E. Golay, "Smoothing and Differentiation of Data by Simplified Least Squares Procedures," *Anal Chem*, vol. 36, no. 8, pp. 1627–1639, Jul. 1964, doi: 10.1021/AC60214A047/ASSET/AC60214A047.FP.PNG_V03.

[95] M. Schmid, D. Rath, and U. Diebold, "Why and How Savitzky-Golay Filters Should Be Replaced," *ACS Measurement Science Au*, vol. 2, no. 2, pp. 185–196, Apr. 2022, doi: 10.1021/ACSMEASURESCIAU.1C00054/SUPPL_FILE/TG1C00054_SI_002.ZIP.

[96] S. Särkkä, "Bayesian Filtering and Smoothing," *Bayesian Filtering and Smoothing*, pp. 1–232, Jan. 2013, doi: 10.1017/CBO9781139344203.

[97] X.-F. Zhang *et al.*, "Potentiometric measurement of entropy change for lithium batteries," *Phys. Chem. Chem. Phys.*, vol. 19, no. 15, pp. 9833–9842, 2017, doi: 10.1039/C6CP08505A.

[98] P. J. Osswald, M. Del Rosario, J. Garche, A. Jossen, and H. E. Hoster, "Fast and Accurate Measurement of Entropy Profiles of Commercial Lithium-Ion Cells,"

Electrochimica Acta, vol. 177, pp. 270–276, 2015, doi: 10.1016/j.electacta.2015.01.191.

[99] I. M. Sobol, "Global sensitivity indices for nonlinear mathematical models and their Monte Carlo estimates," *Mathematics and Computers in Simulation*, vol. 55, no. 1–3, pp. 271–280, Feb. 2001, doi: 10.1016/S0378-4754(00)00270-6.

[100] A. Saltelli *et al.*, *Global Sensitivity Analysis. The Primer*. 2008.

[101] A. M. Bizeray, J. H. Kim, S. R. Duncan, and D. A. Howey, "Identifiability and Parameter Estimation of the Single Particle Lithium-Ion Battery Model," *IEEE Transactions on Control Systems Technology*, vol. 27, no. 5, pp. 1862–1877, Sep. 2019, doi: 10.1109/TCST.2018.2838097.

[102] A. Aitio, S. G. Marquis, P. Ascencio, and D. Howey, "Bayesian Parameter Estimation Applied to the Li-ion Battery Single Particle Model with Electrolyte Dynamics," *IFAC-PapersOnLine*, vol. 53, no. 2, pp. 12497–12504, Jan. 2020, doi: 10.1016/J.IFACOL.2020.12.1770.

[103] S. J. Moura, F. B. Argomedo, R. Klein, A. Mirtabatabaei, and M. Krstic, "Battery State Estimation for a Single Particle Model with Electrolyte Dynamics," *IEEE Transactions on Control Systems Technology*, vol. 25, no. 2, pp. 453–468, Mar. 2017, doi: 10.1109/TCST.2016.2571663.

[104] H. E. Perez, S. Dey, X. Hu, and S. J. Moura, “Optimal Charging of Li-Ion Batteries via a Single Particle Model with Electrolyte and Thermal Dynamics,” *J Electrochem Soc*, vol. 164, no. 7, pp. A1679–A1687, 2017, doi: 10.1149/2.1301707jes.

[105] M. Doyle, T. P. Fuller, and J. Newman, “Modeling of Galvanostatic Charge and Discharge of the Lithium/Polymer/Insertion Cell,” 1992.

[106] F. Brosa Planella *et al.*, “A continuum of physics-based lithium-ion battery models reviewed,” *Progress in Energy*, vol. 4, no. 4, Oct. 2022, doi: 10.1088/2516-1083/ac7d31.

[107] M. Andersson *et al.*, “Parametrization of physics-based battery models from input–output data: A review of methodology and current research,” *Journal of Power Sources*, vol. 521. Elsevier B.V., Feb. 15, 2022. doi: 10.1016/j.jpowsour.2021.230859.

[108] R. Mehta and A. Gupta, “An improved single-particle model with electrolyte dynamics for high current applications of lithium-ion cells,” *Electrochim Acta*, vol. 389, Sep. 2021, doi: 10.1016/j.electacta.2021.138623.

[109] S. Cui *et al.*, “Optimized Temperature Effect of Li-Ion Diffusion with Layer Distance in Li(NixMnyCoz)O2 Cathode Materials for High Performance Li-Ion Battery,” *Advanced Energy Materials*, vol. 6, no. 4, pp. 1–9, 2016, doi: 10.1002/aenm.201501309.

[110] K. Chayambuka, G. Mulder, D. L. Danilov, and P. H. L. Notten, “Determination of state-of-charge dependent diffusion coefficients and kinetic rate constants of phase

changing electrode materials using physics-based models," *Journal of Power Sources Advances*, vol. 9, p. 100056, Jun. 2021, doi: 10.1016/J.POWERA.2021.100056.

[111] J. Crank and P. Nicolson, "A practical method for numerical evaluation of solutions of partial differential equations of the heat-conduction type," *Mathematical Proceedings of the Cambridge Philosophical Society*, vol. 43, no. 1, pp. 50–67, Jan. 1947, doi: 10.1017/S0305004100023197.

[112] V. Strassen, "Gaussian elimination is not optimal," *Numerische Mathematik*, vol. 13, no. 4, pp. 354–356, 1969, doi: 10.1007/BF02165411.

[113] J. Jia, T. Sogabe, and S. Li, "A generalized symbolic Thomas algorithm for the solution of opposite-bordered tridiagonal linear systems," *Journal of Computational and Applied Mathematics*, vol. 290, pp. 423–432, Dec. 2015, doi: 10.1016/J.CAM.2015.05.026.

[114] The PyBaMM Group, "A step toward the Single Particle Model," https://docs.pybamm.org/en/latest/source/examples/notebooks/creating_models/3-negative-particle-problem.html#.

Appendix A: table of figure permissions

Item	Source	Copyright holder	Permission requested	Granted
Figure 1	[1] B. Wang	© Next Big Future	N/A	N/A
Figure 2	[2] Budde-Meiwes *et al.*	© Deloitte UK	N/A	N/A
Figure 3	[5] Woodward et al.	© CC-BY	N/A	N/A
Figure 4	[6] V. Henze	© Bloomberg Finance L.P.	28/06/2022	Requested
Figure 5	[7] World Economic Forum; Global Battery Alliance	© CC-BY	N/A	N/A
Figure 6	[10] Berckmans et al.	© CC-BY	N/A	N/A
Figure 7	[15] Yang *et al.*	© CC-BY	N/A	N/A
Figure 8	[22] C. D. Rahn and C.-Y. Wang	© John Wiley & Sons	28/06/2022	Requested
Figure 10	[28] Tahmasbi, Kadyk, and Eikerling	© CC-BY	N/A	N/A
Figure 18	[64] Dubarry et al.	© Elsevier B.V.	28/06/2022	Requested
Figure 19	[73] Bloom et al.	© Elsevier B.V.	28/06/2022	Requested
Figure 21	[84] Chalise et al.	© CC-BY	N/A	N/A